行政院國家科學委員會專題研究計畫　成果報告

奈米結構的空腔量子電動力學及量子傳輸(3/3)

計畫類別：整合型計畫
計畫編號：NSC94-2120-M-009-002-
執行期間：94 年 01 月 01 日至 94 年 12 月 31 日
執行單位：國立交通大學電子物理學系(所)

計畫主持人：褚德三
共同主持人：趙天生，許世英，林俊源，朱仲夏
計畫參與人員：陳岳男、謝振豪、&#63759；志偉、&#63969；耀仁(以上為博士後研究員)、&#63988；高進、廖英彥、簡賸瑞、&#63969；哲明、唐英瓚、邱裕煌、周瑞雯(以上為博士生)、陳柏文、邱奎霖、陳光胤、吳耿榮(以上為碩士生)

報告類型：完整報告
報告附件：出席國際會議研究心得報告及發表論文
處理方式：本計畫可公開查詢

中　華　民　國 95 年 2 月 13 日

行政院國家科學委員會補助專題研究計畫 □ 成 果 報 告
□期中進度報告

Cavity QED and quantum transport in nanostrucrures

奈米結構的空腔量子電動力學及量子傳輸現象之研究

計畫類別：□ 個別型計畫　□ 整合型計畫
計畫編號：NSC 91-2120-M-009-002；NSC 92-2120-M-009-010；NSC 94-2120-M-009-002
執行期間： 91 年 8 月 1 日至 94 年 12 月 31 日

計畫主持人：褚德三
共同主持人：朱仲夏，許世英，趙天生，林俊源
計畫參與人員：陳岳男、謝振豪、羅志偉、李耀仁(以上為博士後研究員)、
林高進、廖英彥、簡賸瑞、李哲明、唐英瓚、邱奕煌、
周瑞雯(以上為博士生)、陳柏文、邱奎霖、陳光胤、
吳耿榮(以上為碩士生)、
成果報告類型(依經費核定清單規定繳交)：□精簡報告 □完整報告

本成果報告包括以下應繳交之附件：
□赴國外出差或研習心得報告一份
□赴大陸地區出差或研習心得報告一份
□出席國際學術會議心得報告及發表之論文各一份(已另外上傳)
□國際合作研究計畫國外研究報告書一份
處理方式：除產學合作研究計畫、提升產業技術及人才培育研究計畫、列管計畫及下列情形者外，得立即公開查詢
□涉及專利或其他智慧財產權，□一年□二年後可公開查詢

執行單位：國立交通大學
中 華 民 國 95 年 2 月 1 日

摘　要

我們在前三年中建議做兩個子題：第一子題是要討論奈米系統的超輻射現象，內容包括提議研究在有或無微空腔的情形下，奈米系統的超輻射激子的光學及傳輸現象，包括考慮量子線、量子井、量子點及量子環上超輻射激子的AB(Aharanov-Bohm)效應及其輻射衰變率隨著系統大小或形狀的變化情形。我們也提議在量子點或環上注入電子及電洞產生再重合，以探討其超輻射受微空腔之影響。探討超輻射激子在微空腔情形下的 Purcell 效應，研究此種奈米微空腔系統的量子電動力學效應，以及建立量子糾纏態之可能性，探討這種量子糾纏態之純化、維持及測量之機制，以及研究有關一個及兩個量子點系統中，光子協助傳輸的效應，並探討強關聯之情形；另外也研究偶極分子受脈衝雷射激發引起轉動及對準效應，並探討產生量子糾纏態之可能性，以及找出這量子糾纏態與熵值之關連性之可能性。我們在過去三年中也提議研究有關研究在有或無微空腔的情形下，奈米系統的 shot noise 現象，並探討以我們的系統完成量子隱形傳輸(quantum teleportation)的可能性。除了上述的理論探討外，我們也著手從實驗來驗証我的想法。在這三年中我們已建立一套 Pump-pro 時間解折光譜系統，並對一些小量子點集團做了研究，目前正改善樣本製作技術及加上低溫量測設備，進行單量子點及單光子測量。

本計畫的第二子題是要建立一個理論模型，來探討高頻電磁波照射於一個受到柵極交流電壓規範下的奈米狹窄電子通道(如量子點接頭)的電子之量子傳輸行為，以及二組從奈米狹窄電子通道通過所電子之間的量子干涉現象，包括其量子電導隨著兩通道的大小及相互距離改變時的行為。在這子題中，我們亦將探討不同材料的自旋電子在奈米狹窄電子通道的量子傳輸行為，這行為可預見也會受到閘極電壓形狀的影響。我們將探討自旋電流的可能性，以及如何在實驗上去測量奈米狹窄電子通道的量子電導，及自旋電流等。在第二子題中另一探討的問題是考慮奈米結構在應變下所引致的自旋電流與奈米級力學振盪之間的關係，並提出未來測量之道。

本計畫已於 2005 年 12 月 31 日結束，在三年的計畫中共發表三篇 PRL 文章 (其中一篇被 PRL 列為 Focus of the Journal，另兩篇正審查中)，及十多篇 PRB，另有多篇在國外知名期刊發表。另由於儀器購置時適值歐元大升值，導致第一、二年之設備經費不足而延誤實驗儀器建立完成之時間，目前實驗儀器大致建立完成，預計完成之實驗測量陸續完成，成果亦已發表於國、內外舉辦之國際會議中，正式論文目前正投稿中。

關鍵詞：空腔量子電動力學，超輻射、量子噪訊，量子糾纏、量子隱形傳輸、量子線、量子井、量子點、量子傳輸、光助量子傳輸、自旋電流、應變引致自旋電流與奈米力學振盪，量子點接頭。

Abstract:

In the past three years, we proposed to study the optical and transport phenomena of superradiant excitons in the nanostructure systems with or without the microcavity. The Aharonov-Bohm effect on superradiant excitons in quantum rings was also proposed to be studied. The decay properties of superradiant excitons in a quantum dot or ring embedded in a microcavity system are believed to change dramatically because of the Purcell effect. We thus proposed to investigate the effect by injecting holes from one side of the cavity which is formed by Bragg mirrors from top and down and electron is attracted by the hole from another side into a double quantum dot system. The electron and hole can recombine in the quantum dot, and thus the Purcell effect can be examined electrically. The frequency shift of the excitons in different structures will be investigated also. We also proposed to study the entanglement generation by the mechanism of superradiance which included the generation, purification and possible application of our system. We also proposed to study the photon assisted quantum transport though a quantum dot system and through a double quantum dot system coupled by the Coulomb force. Actually, in the first subtopic, we proposed to study the cavity quantum electrodynamics of a nanostructure system which included the superradiance and quantum transportation effects.

In the second subtopic, we also proposed to develop a high frequency quantum transport spectroscopy as a tool for the understanding and the probing of the quantum states within the nanostructures. We proposed to study quantum transport in quantum point contacts and quantum narrow channels in the presence of metal gates or an inter-digited metal-gate (IDT) both in theoretical and experiment methods. The quantum transport in quantum rings (or quantum-dots) with a metal-gate which located above one arm of the quantum ring and the effect of the ac signal in the metal-gate to the transport characteristics through the ring will be investigated. We expected eventually to develop a frequency-tunable photon detector that can be operated in the mm-wave regime.

In the processing of the theoretical works as mentioned above, we also proposed to investigated experimentally the effect as we proposed above. In the past 3 years, we have successfully set up a time-resolved single photon detector, and measured the relaxation dynamics of the excitons in quantum well and dots. We have also fabricated the gate-confined nanostructures. The transport properties of the electron with quantum optical effects are observed. Theoretical models with microscopic calculations are proposed and may serve as a guide line for the design of future experiments. Our original proposal are almost finished. Another part is related to the Strain-Induced Coupling of Spin Current to Nanomechanical Oscillations.This work proposes a setup for the detection of spin current. The setup is a free-standing bridge that consists of a semiconductor- metal junction. Strain-induced spin-orbit interaction in the semiconductor couples the electron spin degree of freedom to the twisting motion of the nanomechanical bridge. This work has been reported by the Physical Review Focus.

Keyword: Cavity Quantum electrodynamics, superradiance, quantum dot, quantum ring, quantum transport, spin current, spin-orbit interaction, nanomechanical Oscillation, quantum entanglement, teleportation, reservoir induced entanglement, shot noise, Zeno effect.

報告內容(已發表論文目錄)

Publications (2003-2005)：

(1).Y.N. Chen and D.S.Chuu , “Decay rate of a Wannier exciton in low-dimensional systems”, Europhys. Lett.54(3), 366-372 (2001).

(2).Y.N. Chen, D.S.Chuu , T.Brandes and B.Kramer, “Decay rate and renormalized frequency shift of a quantum wire Wannier exciton in a plannar microcavity”, Phys.Rev. B64, 125307-11 (2001).

(3). K.C.Lin and D.S.Chuu., “The field strength dependent Photon associated tunneling through a quantum dot” , Phys. Rev. B64, 235320-5, (2001).

(4). Y.N. Chen and D.S.Chuu , “Resonant Tunneling into a quantum dot embedded inside a microcavity” Phys. Rev. B 66, 165316-21 (2002).

(5). Y.N. Chen and D.S.Chuu , “Decay rate and renormalized frequency shift of superradiant excitons:in a cylindrical quantum wire”, Physica B 334,175-182 (2003).

(6). Y.N.Chen, D.S.Chuu and T.Brandes,”Current detection of superradiance and induced entanglement of double quantum dot excitons,” Phys. Rev. Lett..90 166802-1 (2004).

(7). Y.N. Chen, and D.S. Chuu ,”Current induced entanglement of double quantum dot excitons”, International Journal of Nanoscience Vol. 2, No.6. 1-8 (2003)

(8) .Y.N. Chen, T. Brandes, C.M. Li, D.S. Chuu ,”Zeno effect and the shot-noise spectrum of superradiant entangled excitons”, Phys. Rev.B. 9,245323-1-245323-4 (2004).

(9).Y.N.Chen and D.S.Chuu , “Superradiant and Aharonov-Bohm effect for the quantum ring exciton” Solid State Comm.130, 491-494 (2004).

(10).Y.K. Lin, K.C. Lin and D.S.Chuu,”Ballistic Transport Through Coupled T-Shaped Quantum Wires”, Physica B 348, 56- 65 (2004).

(11).Y.N. Chen and D.S.Chuu , “Rrenormalized frequency shift of a Wannier exciton in a one-dimensional system”, Phys. Lett.A 324, 86-90 (2004).

(12). A.G. Mal‘shukov, C.S. Tang, C.S. Chu , KA Chao”Spin Current generation and detection in the presence of an ac gate” ,Phys. Rev. B68 (23): Art. No. 233307 (2003).

(13). C.S.Tang, Y.H.Tan, C.S. Chu, “Transport spectroscopy in a time-modulated open quantum dot”, Phy. Rev.B 67 (20): Art. No. 205324 (2003).

(14).C.S.Tang and C.S. Chu, “Nonadiabatic quantum pumping in mesoscopic nanostructures”, Solid state Comm.120 (9-10): 353-357 (2001).

(15). L. Y. Wang, C. S. Tang, and C. S. Chu, cond-mat/0409291 (2004), Accept. by Phys. Rev. B.

(16). S. W. Chung, C. S. Tang, C. S. Chu, and C. Y. Chang, Finger-gate array quantum pumps: Pumping characteristics and mechanisms, Phys. Rev. B **70**, 085315 (2004).

(17). A. G. Mal’ shukov, L. Y. Wang, C. S. Chu, and K. A. Chao, accepted by, Phys. Rev. Lett (2005).

(18). A. G. Mal’ shukov, C. S. Tang, C. S. Chu, and K. A. Chao, Phys. Rev. Lett. **95**, 107203 (2005).

(19). T. H. Fang, S. R. Jian, and D. S. Chuu Nanotribology and fractal analysis of ZnO thin films using scanning probe microscopy , J. Phys. D. 36, 878 (2003),.

(20). S. Y. Hsu and J. Y. Chen. Superconducting behaviors of copper-germanium alloys ,Physica B 329, 1361 (2003),

(21). Y. T. Shih, Y. Y. Liao, and D. S. Chuu Rotational states of an adsorbed dipole molecule in an external electric field , Phys. Rev. B 68, 075402 (2003),.

(22). T.H.Fang, S.R.Jian and D.S.Chuu.," Nanomechanical properties of lead zirchnate titanate thin films by nanoindentation J. of Phys. Condensed Mater 15(30):5253-5259 (2003),

(23). S.R.Jian, T.H.Fang and D.S.Chuu.," Effects of temperature on surface clusters by molecular dynamics simulation, Physica B, 334(3-4):369-374 (2003),

(24). S.R.Jian,T.H.Jian and D.S.Chuu," Analysis of Physical properties of III-nitride thin films by nanoindentation J.Electron Mater 32(6):496-500 (2003).

(25). T.H.Fang,S.R.Jian and D.S.Chuu," Molecular dynamics analysis of effects of velocity and loading on the nanoindentation, J.J. Appl.Phys.,241(11B), L1328-33 (2003),

(26). Lifetime analysis of quasibound states in coupled quantum wells Physica E. 18, 421-428 (2003), M.C. Lin and D.S. Chuu .

(27). Y. N. Chen, T. Brandes, C. M. Li, and D. S. Chuu."Shot-noise spectrum of superradiant entangled excitons , Phys. Rev. B 69, 245323 (2004),

(28). M. C. Kuo, K.C.Chu, T.H.Shih, Y.J.Lai, C.S.Yang, W.K.Chen, D.S.Chuu, M.C.Lee,W.C.Chow, S.Y.Jeng,, Y.T.Shih and W.H.Lan,. Optical properties of Zn1-xCdxSe epilayers grown on (100)GaAs by molecular beam epitaxy J. J. Appl. Phys. 43 5145 (2004),

(29). Y. Y. Liao, Y. N. Chen, and D. S. Chuu Alignment and orientation of absorbed dipole molecules ,Phys. Rev. B 70, 233410 (2004),.

(30). J.Y. Hsieh, J.M. Li and D.S Chuu. A simplification of entanglement purification Physics Letters A328, 94-101 (2004),

(31). Y.K. Lin, K.C. Lin and D.S.Chuu,". Ballistic Transport Through Coupled T-Shaped Quantum Wires, Physica B 348, 56-65 (2004),

(32). J.Y. Hsieh, C.M. Li, J.S. Lin and D.S. Chuu , Formation of a Family of Sure-Success quantum search algorithm,Int. J. of Quantum Information , 2 285-293 (2004),

(33). Jin-Yuan Hsieh, Che-Ming Li,and Der-San Chuu.,An improved phase error tolerance in quantum search algorithm J. of Chinese Physics, (2004),

(34). T.H.Fang,S.R.Jian and D.S.Chuu ,Molecular dynamics for elastic and plastic deformationof a single-walled carbon nanotube under nanoidentation,Chin.Phys. Lett. 21 (6):1117-1119 (2004),

(35). T.H.Fang, S.R.Jian and D.S.Chuu, Nanomechanical properties of TiC,TiN and TiCN thin films using scanning probe microscopy and nanoidentation, Appl.Surface Science 228 (1-4):365-72 (2004),

(36). Y.Y.Liao, Y.N.Chen and D.S.Chuu ,Orientations of two coupled molecule Chemical Physics Lett. 398 418-21 (2004).

(37). K. P. Chang, S. L. Yang, D. S. Chuu, R.S.Hsiao, J.F.Chen, L.Wei, J.S.Wang and J.Y.Chi, Characterization of self-assembled InAs quantum dots with InAlAs/InGaAs strain-reduced layers by photoluminescence spectroscopy ,J. Appl. Phys. 97, 083511 (2005),

(38). R. B. Chen, C.P. Chang , J.S. Hwang , D.S. Chuu and M.F. Lin. , Magnetization of finite carbon nanotubes J. of the Phys. Society of Japan 74 (5): 1404-1407 (2005),

(39). C.W. Chiu, Y.H. Chiu, F.L. Shyu, C.P. Chang, D.S. Chuu, M.F. Lin.," Temperature-Dependent Carrier Dynamics in Metallic Carbon Nanotubes" , Phys. Lett. xxx-xx (2005),

(40). S.R Jian, T.H. Fang and D.S. Chuu," Nanomechanical Characterizations of InGaN Thin Films", Applied Surface Science. xxx-xxx (2005),

(41). S.R Jian, T.H. Fang and D.S. Chuu, "Mechanisms of p-GaAs(100) surface by atomic force microscope nanooxidation", J. of Physics D (Appl.Physics),xxxx- xxx (2005),.

(42). K.C.Lin and D.S. Chuu., Spin-flip transport through an interacting quantum dot Solid State Commun. 134 , 831-835 (2005),

(43). K.C.Lin and D.S. Chuu ,"Anderson model with spin-flip-associated tunneling Phys. Rev. B, B72, 125314-1-11 (2005),.

(44). Y.N. Chen, C.M. Li, D.S. Chuu , T. Brandes," Proposal for teleportation of charge qubits via superradiance" New J. of Physics 7, 172 (2005),.

(45). Y.N. Chen, D.S. Chuu, and T. Brandes,"Current noise of a quantum dot p-i-n junction in a photonic crystal, Phys. Rev.B 72, 153312-1-4 (2005).

(46). Jin-Yuan Hsieh, Che-Ming Li, Der-San Chuu, "Hamiltonian and measuring time for analog quantum search",Accepted by J. OF Phys. Soc. of Japan xx , xxxx-xx (2005).

(47). Y.Y. Liao, Y.N. Chen, C.M. Li and D.S. Chuu ," Entangled rotational states between two coupled molecules" , Accepted by Journal of Physics B: Atomic, Molecular & Optical Physics, xxx, xxxx-xx (2005).

(48). Y.N. Chen, D.S. Chuu, and S.J. Cheng,"Shot noise of a quantum ring exciton in a planar microcavity", Phys. Rev.B 72, 233301-1-4 (2005).

(49). Y.J.Lai,Y.C.Lin,.C.P. Fu, C.S.Yang, C.H.Chia, D.S.Chuu, ,W.K.Chen , M.C.Lee, W.C.Chow,.M.C.Kuo and J.S.Wang, "Growth mode transfer of self-assembled CdSe quantum dots grown by molecular beam epitaxy". J..of Crystal Growth,286, 338-44 (2006).

(50). . Y.Y. Liao, Y.N. Chen , D.S. Chuu and T. Brandes, "Spin relaxation in a GaAs quantum dot embedded inside a suspended phonon cavity" , Phys. Rev. B, xx, xxxxxx-xx (2006).

(51). Y.Y.Liao, Y.N.Chen and D.S.Chuu, " Orientations of adsorbed dipolar molecules" Phys. Rev. B, xx, xxxxxx-xx (2006)..

以下列出數篇論文全文。

Current Detection of Superradiance and Induced Entanglement of Double Quantum Dot Excitons

Y. N. Chen,[1] D. S. Chuu,[1] and T. Brandes[2]

[1]*Department of Electrophysics, National Chiao-Tung University, Hsinchu 30050, Taiwan*
[2]*Department of Physics, UMIST, P.O. Box 88, Manchester, M60 1QD, United Kingdom*

(Received 18 December 2002; published 24 April 2003)

We propose to measure the superradiance effect by observing the current through a semiconductor double-dot system. An electron and a hole are injected separately into one of the quantum dots to form an exciton and then recombine radiatively. We find that the stationary current shows oscillatory behavior as one varies the interdot distance. The amplitude of oscillation can be increased by incorporating the system into a microcavity. Furthermore, the current is suppressed if the dot distance is small compared to the wavelength of the emitted photon. This photon trapping phenomenon generates the entangled state and may be used to control the emission of single photons at predetermined times.

DOI: 10.1103/PhysRevLett.90.166802 PACS numbers: 73.21.La, 03.67.Mn, 42.50.Fx, 71.35.–y

Since Dicke proposed the phenomenon of superradiance [1], the coherent radiation phenomena for atomic systems were intensively investigated. In semiconductor systems, the electron-hole pair is naturally a candidate for examining the spontaneous emission. The decay rate of the exciton is superradiantly enhanced by a factor of $(\lambda/d)^2$ for a 2D exciton-polariton system [2], where λ is the wavelength of the emitted photon and d is the lattice constant of the thin film. In the past decades, the superradiance of excitons in these quantum well structures has been investigated intensively [3]. For lower dimensional systems, the decay rate of the exciton is enhanced by a factor of λ/d in a quantum wire [4]. In the quantum dots, although the decay rate is shown to be proportional to $R^{2.1}$ [5] which confirms the theoretical prediction [6], acceptable experimental data on quantum dot superradiance are still not plentiful owing to the difficulty of techniques in observing the enhanced spontaneous emission optically.

In recent years, great attention has been focused on the entanglement issue since generation of highly entangled states is one of the fundamental requirements for quantum information processing [7]. Many papers have been associated with quantum-optic and atomic systems [8]. However, due to the scalability of the quantum processor, solid-state realizations of such phenomena are the favored choices [9]. In fact, the superradiance effect can also generate entanglement by spontaneous emission. Therefore, a different way is proposed to observe the superradiant effect and generate the entangled states in this work. By injecting electrons and holes into one of the quantum dots of a double-dot system and controlling the gate voltage of one of the dots, a photon is then generated by the coherent recombination of the exciton. This process not only allows one to determine the superradiant effect by measuring the stationary current, but also induces the entangled states in this double-dot system.

In our model, we consider a *p-i-n* junction, similar to the device proposed by Benson *et al.* [10], but with *two spatially separated* quantum dots. The novel feature here is the dissipative creation of entanglement over relatively large distances, and its readout via the stationary current. The device structure is shown in Fig. 1.

One of the obstacles in measuring superradiance between the quantum dots comes from the random size of the dots which result in a random distribution of energy gap and thus diminishes the coherent radiation. This can be overcome by constructing a gate voltage over one of the quantum dots. The energy gap and the orientation of the dipole moments of one of the quantum dots thus can be controlled well. Both the hole and electron reservoirs are assumed to be in thermal equilibrium. For the physical phenomena we are interested in, the current is conducted through dot 1 only, and the Fermi level of the $p(n)$-side hole (electron) is slightly lower (higher) than the hole (electron) subband in the dot. After a hole is injected into the hole subband in the quantum dot, the n-side electron can tunnel into the exciton level because of the Coulomb interaction between the electron and the hole. In our calculation, we also neglect the Forster process which may have some influence on the results if the two dots are close to each other. The validity of this assumption will be discussed later. Thus, we

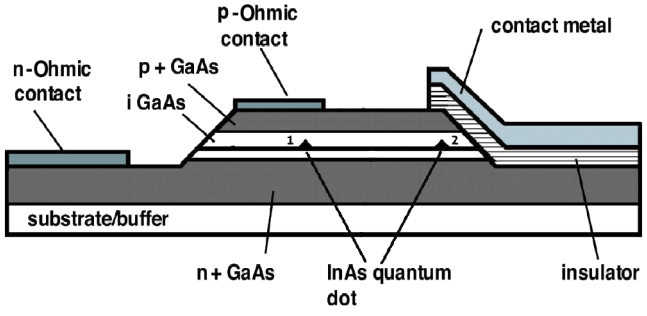

FIG. 1 (color online). Proposed device structure. Two InAs quantum dots are embedded in a *p-i-n* junction. Above dot 2 is a metal gate, which controls the energy gap and orientation of the dipole.

may assume four dot states: $|0\rangle = |0, h; 0, 0\rangle$, $|U_1\rangle = |e, h; 0, 0\rangle$, $|U_2\rangle = |0, 0; e, h\rangle$, and $|D\rangle = |0, 0; 0, 0\rangle$, where $|0, h; 0, 0\rangle$ means there is one hole in dot 1 and $|0, 0; 0, 0\rangle$ represents the ground state with no hole and electron in the quantum dots. The exciton states $|e, h; 0, 0\rangle$ (in dot 1) can be converted to $|0, 0; e, h\rangle$ (in dot 2) through the exciton-photon interactions. One might argue that one cannot neglect the state $|e, 0; 0, 0\rangle$ for real device since the tunable variable is the applied voltage. However, this can be resolved by fabricating a thicker barrier on the electron side so that there is little chance for an electron to tunnel in advance. By transforming $|U_1\rangle$ and $|U_2\rangle$ into Dicke states: $|S_0\rangle = (1/\sqrt{2}) \times (|U_1\rangle - |U_2\rangle)$ and $|T_0\rangle = (1/\sqrt{2})(|U_1\rangle + |U_2\rangle)$, we can now define the dot operators $\hat{n}_S \equiv |S_0\rangle\langle S_0|$, $\hat{n}_T \equiv |T_0\rangle\langle T_0|$, $\hat{n}_D \equiv |D\rangle\langle D|$, $\hat{p}_s \equiv |S_0\rangle\langle D|$, $\hat{p}_T \equiv |T_0\rangle\langle D|$, $\hat{s}_{U_1} \equiv (1/\sqrt{2})(|0\rangle\langle S_0| + |0\rangle\langle T_0|)$, and $\hat{s}_D \equiv |0\rangle\langle D|$. The total Hamiltonian H of the system consists of three parts: H_0 [dot, photon bath H_p, electron (hole) reservoirs $H_{\rm res}$], H_T(dot-photon coupling), and the dot-reservoir coupling H_V:

$$
\begin{aligned}
&H = H_0 + H_T + H_V, \qquad H_0 = \varepsilon_U \hat{n}_S + \varepsilon_U \hat{n}_T + \varepsilon_D \hat{n}_D + H_p + H_{\rm res},\\
&H_T = \sum_{\mathbf{k}} \frac{1}{\sqrt{2}} g\{D_{\mathbf{k}} b_{\mathbf{k}}[\hat{p}_S(1 + e^{i\mathbf{k}\cdot\mathbf{r}}) + \hat{p}_T(1 - e^{i\mathbf{k}\cdot\mathbf{r}})] + \text{c.c.}\} = g(\hat{p}_S X_S + \hat{p}_S{}^{\dagger} X_S^{\dagger} + \hat{p}_T \overline{X}_T + \hat{p}_T{}^{\dagger} p \overline{X}_T{}^{\dagger}),\\
&H_p = \sum_{\mathbf{k}} \omega_{\mathbf{k}} b_{\mathbf{k}}^{\dagger} b_{\mathbf{k}}, \qquad H_V = \sum_{\mathbf{q}} (V_{\mathbf{q}} c_{\mathbf{q}}^{\dagger} \hat{s}_{U_1} + W_{\mathbf{q}} d_{\mathbf{q}}^{\dagger} \hat{s}_D + \text{c.c.}), \qquad H_{\rm res} = \sum_{\mathbf{q}} \varepsilon_{\mathbf{q}}^U c_{\mathbf{q}}^{\dagger} c_{\mathbf{q}} + \sum_{\mathbf{q}} \varepsilon_{\mathbf{q}}^D d_{\mathbf{q}}^{\dagger} d_{\mathbf{q}}.
\end{aligned}
\tag{1}
$$

In the above equation, $b_{\mathbf{k}}$ is the photon operator, $gD_{\mathbf{k}}$ is the dipole coupling strength, $\mathbf{r}$ is the position vector between two quantum dots, $X_S = \sum_{\mathbf{k}}(1 + e^{i\mathbf{k}\cdot\mathbf{r}}) D_{\mathbf{k}} b_{\mathbf{k}}$, $\overline{X}_T = \sum_{\mathbf{k}}(1 - e^{i\mathbf{k}\cdot\mathbf{r}}) D_{\mathbf{k}} b_{\mathbf{k}}$, and $c_{\mathbf{q}}$ and $d_{\mathbf{q}}$ denote the electron operators in the left and right reservoirs, respectively. The dipole approximation is not used in our calculation since we keep the full $e^{i\mathbf{k}\cdot\mathbf{r}}$ terms in the operators X_S and $\overline{X}_T$. Here, g is a constant with a unit of the tunneling rate. The couplings to the electron and hole reservoirs are given by the standard tunnel Hamiltonian H_V, where $V_{\mathbf{q}}$ and $W_{\mathbf{q}}$ couple the channels $\mathbf{q}$ of the electron and the hole reservoirs. If the couplings to the electron and the hole reservoirs are weak, then it is reasonable to assume that the standard Born-Markov approximation with respect to these couplings is valid. In this case, one can derive a master equation from the exact time evolution of the system. The equations of motion can be expressed as (cf. [12])

$$
\begin{aligned}
&\langle \hat{n}_\sigma \rangle_t - \langle \hat{n}_\sigma \rangle_0 = -ig \int_0^t dt' \{\langle \hat{p}_\sigma \rangle_{t'} - \langle \hat{p}_\sigma^{\dagger} \rangle_{t'}\} + \Gamma_U \int_0^t dt' (1 - \langle \hat{n}_S \rangle_{t'} - \langle \hat{n}_T \rangle_{t'} - \langle \hat{n}_D \rangle_{t'}),\\
&\langle \hat{n}_D \rangle_t - \langle \hat{n}_D \rangle_0 = -ig \int_0^t dt' \{\langle \hat{p}_S \rangle_{t'} - \langle \hat{p}_S^{\dagger} \rangle_{t'} + \langle \hat{p}_T \rangle_{t'} - \langle \hat{p}_T^{\dagger} \rangle_{t'}\} - 2\Gamma_D \int_0^t dt' \langle \hat{n}_D \rangle_{t'},\\
&\langle \hat{p}_S \rangle_t - \langle \hat{p}_S \rangle_t^0 = -\Gamma_D \int_0^t dt'\, e^{i\varepsilon(t-t')} \langle X_t X_{t'}^{\dagger} \tilde{p}_S(t') \rangle_{t'} - ig \int_0^t dt'\, e^{i\varepsilon(t-t')} \{\langle \hat{n}_S X_t X_{t'}^{\dagger} \rangle_{t'} - \langle \hat{n}_D X_{t'}^{\dagger} X_t \rangle_{t'}\},\\
&\langle \hat{p}_T \rangle_t - \langle \hat{p}_T \rangle_t^0 = -\Gamma_D \int_0^t dt'\, e^{i\varepsilon(t-t')} \langle \overline{X}_t \overline{X}_{t'}^{\dagger} \tilde{p}_T(t') \rangle_{t'} - ig \int_0^t dt'\, e^{i\varepsilon(t-t')} \{\langle \hat{n}_T \overline{X}_t \overline{X}_{t'}^{\dagger} \rangle_{t'} - \langle \hat{n}_D \overline{X}_{t'}^{\dagger} \overline{X}_t \rangle_{t'}\},
\end{aligned}
\tag{2}
$$

where the index $\sigma = S$ or T, $\Gamma_U = \pi \sum_{\mathbf{q}} V_{\mathbf{q}}^2 \delta(\varepsilon_U - \varepsilon_{\mathbf{q}}^U)$, $\Gamma_D = \pi \sum_{\mathbf{q}} W_{\mathbf{q}}^2 \delta(\varepsilon_D - \varepsilon_{\mathbf{q}}^D)$, and $\varepsilon = \varepsilon_U - \varepsilon_D$ is the energy gap of the quantum dot exciton. Here, $\tilde{p}_S(t') = p_S e^{i\varepsilon t} X_{t'}$, $\tilde{p}_T(t') = p_T e^{i\varepsilon t} \overline{X}_{t'}$, and $X_{t'}$ ($\overline{X}_{t'}$) denotes the time evolution of X ($\overline{X}$) with H_p. The expectation value $\langle \hat{p}_\sigma^{\dagger} \rangle_t^0$ describes the decay of an initial polarization of the system and plays no role for the stationary current. Therefore, we shall assume the initial expectation value of $\hat{p}_\sigma{}^{(\dagger)}$ vanishes at time $t = 0$.

As can be seen from Eq. (2), there are terms such as $\langle \hat{n}_\sigma X_t X_{t'}^{\dagger} \rangle_{t'}$ which contain products of dot operators and photon operators. If we are interested in small coupling parameters here, a decoupling of the reduced density matrix $\tilde{\rho}_\sigma(t')$ can be used: $\tilde{\rho}_\sigma(t') \approx \rho_{\rm ph}^0 Tr_{\rm ph} \tilde{\rho}_\sigma(t')$. Products of these operators can then be obtained. For spontaneous emission, the photon bath is assumed to be in equilibrium. The expectation values $\langle X_t X_{t'}^{\dagger} \rangle_0 \equiv C(t - t')$ and $\langle \overline{X}_t \overline{X}_{t'}^{\dagger} \rangle_0 \equiv \overline{C}(t - t')$ are functions of the time difference only. We can now define the Laplace transformation for real z,

$$
\begin{aligned}
&C_\varepsilon(z) \equiv \int_0^\infty dt\, e^{-zt} e^{i\varepsilon t} C(t),\\
&n_\sigma(z) \equiv \int_0^\infty dt\, e^{-zt} \langle \hat{n}_\sigma \rangle_t \text{ etc.}, \qquad z > 0,
\end{aligned}
\tag{3}
$$

and transform the whole equations of motion into z space. The tunnel current $\hat{I}$ can be defined as the change of the occupation of $\hat{n}_D$ and is given by $\hat{I} \equiv ig \sum_\sigma (\hat{p}_\sigma - \hat{p}_\sigma{}^{\dagger})$, where we have set the electron charge $e = 1$ for convenience. The time dependence of the expectation value $\langle \hat{I} \rangle_t$ can be obtained by performing the inverse Laplace transformation. For time $t \to \infty$, the result is

$$
\langle \hat{I} \rangle_{t \to \infty} = \frac{4g^2 \gamma_+ \gamma_-}{\gamma_- + \gamma_+ [1 + 2\gamma_- (g^2/\Gamma_D + g^2/\Gamma_U + \Gamma_D)]},
\tag{4}
$$

where $g^2\gamma_+$ and $g^2\gamma_-$ are the superradiant and subradiant decay rate of the exciton, respectively [11]. The

derivation of the current equation is closely analogous to the spontaneous emission of phonons in double dots [12], in which the correlation functions $\langle X_t X_{t'}^{\dagger}\rangle_0$ are given by the electron-phonon interaction.

The corresponding decay rate for superradiant and the subradiant channels is given by

$$g^2\gamma_{\pm} = \gamma_0\left(1 \pm \frac{\sin(2\pi d/\lambda_0)}{2\pi d/\lambda_0}\right), \tag{5}$$

where d is the interdot distance and γ_0 is the exciton decay rate in a quantum dot. To display the dependence of the stationary current through the quantum dot on the dot distance d, we present the results of two identical quantum dots in Fig. 2. In plotting the figure, the current is in terms of 100 pA. Furthermore, the tunneling rates, Γ_U and Γ_D, are assumed to be equal to $0.2\gamma_0$ and γ_0, respectively. Here, a value of $1/1.3$ ns for the free-space quantum dot decay rate γ_0 is used in our calculations [13]. As shown in Fig. 2, the current is suppressed as the dot distance d is much smaller than the wavelength (λ_0) of the emitted photon. This corresponds to the trapping state in the two-ion system. As long as we choose only one of the dots to be coupled to reservoirs, the generated photon is reabsorbed immediately by the other dot and vice versa. The current is then blocked by this exchange process. For small rates limit ($g^2\gamma_{\pm}$), one can approximate Eq. (4) by $I \approx 4[1/g^2\gamma_- + 1/g^2\gamma_+]^{-1}$. The rates $\Gamma_{U,D}$ drop out completely and the current is determined only by the (smaller) radiative decay rates. In this approximate form, the current looks identical to the expression for the conductance $G \propto [1/\Gamma_L + 1/\Gamma_R]^{-1}$ from a left lead through a single level to a right lead with tunnel rates $\Gamma_{L,R}$. This implies that the superradiant and the subradiant channel are in series (and not in parallel) in this limit. This is because, once the exciton is formed in dot 1, time evolution of this state is proportional to $e^{-g^2\gamma_+ t} + e^{-g^2\gamma_- t}$ not $e^{-g^2(\gamma_+ + \gamma_-)t}$ [14]. It means the two decay channels in our system are not in parallel. For long time behavior $t \to \infty$ and $\gamma_+ \gg \gamma_-$, the function $e^{-g^2\gamma_+ t} + e^{-g^2\gamma_- t}$ approaches the limit of $e^{-g^2\gamma_- t}$, which is identical to the same limit of the function $e^{-[(g^2\gamma_+\gamma_-)/(\gamma_+ + \gamma_-)]t}$ (in series).

Similar to the two-ion superradiance [11], the current also exhibits oscillatory behavior as a function of dot distance. To observe the interference effect clearly, one may incorporate the system inside a microcavity since semiconductor cavities with strong electron-photon coupling have been realized experimentally by, e.g., Gérard *et al.* [15]. Reduction of the allowed k state is expected to increase the magnitude of the oscillation. For example, if the system is placed inside a rectangular microcavity with length λ_0, the decay rate for the two channels can be worked out straightforwardly:

$$g^2\gamma_{\mathrm{cav},\pm} = \frac{\gamma_0}{\pi}|1 \pm e^{i2\pi d/(\sqrt{2}\lambda_0)}|^2. \tag{6}$$

The stationary current is plotted in the inset of Fig. 2, where a perfect (lossless) cavity is assumed. As we mentioned above, the amplitude of oscillation is larger than that in free space. However, the oscillation period is not half of the wavelength, but $\lambda_0/\sqrt{2}$. This is because the interference term is influenced only by the wave vector in the unconfined direction. Excluding the contributions from fundamental cavity modes, the effective wave vector can be expressed as

$$k_{\mathrm{eff}} = \sqrt{\left(\frac{2\pi}{\lambda_0}\right)^2 - 2 \times \left(\frac{\pi}{\lambda_0}\right)^2} = \frac{k_0}{\sqrt{2}}. \tag{7}$$

The oscillation period of the decay rate and the current is therefore increased by a factor of $\sqrt{2}$.

In Fig. 3, we plot the expectation value of n_S (n_T) as a function of the dot distance. The maximum entangled state ($|S_0\rangle$) is reached as $d \ll \lambda_0$. This is remarkable as the steady state is independent of the initial state. The entanglement is induced by the cooperative decoherence in the system. In a recent paper by Schneider *et al.* [16], the authors consider the behavior of an ion trap with all ions driven simultaneously and coupled collectively to a heat bath. They also found that the steady state of the ion trap can exhibit quantum entanglement. However, the concurrence of their system is below the value of unity

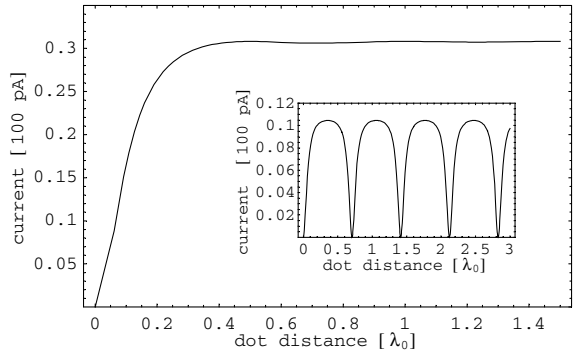

FIG. 2. Stationary tunnel current, Eq. (4), as a function of dot distance d. The interference effect is seen clearly (inset) by incorporating the system inside a rectangular microcavity. The vertical and horizontal units are 100 pA and λ_0, respectively.

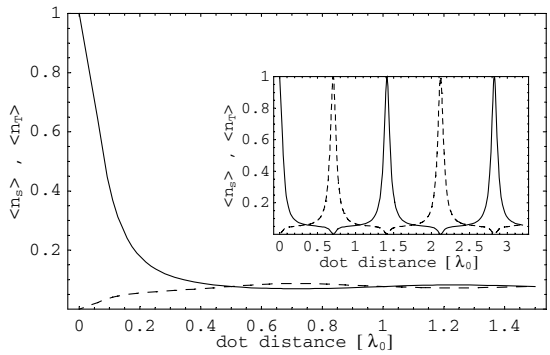

FIG. 3. Occupation probability of the entangled states n_S (solid line) and n_T (dashed line). The inset shows the results inside a rectangular microcavity.

(maximum entanglement). On the contrary, in our system the maximum entangled state can be generated by tuning the band gap of dot 2 (linear stark effect), i.e., control the on/off of the superradiance. Another advantage of our scheme is shown in the inset of Fig. 3. If the double-dot system is incorporated inside a rectangular microcavity, the maximum entangled states repeat as a function of interdot distance. This means, even for remote separation, the entanglement can still be achieved. The reason can be attributed to the fact that the creation of entanglement in our model is governed by the interaction with a common heat bath, while conventional creation of entanglement depends on the direct interaction between two subsystems [17]. When two dots are coupled to the common photon fields, the collective decay process drives the system into the entangled states. The novel feature of the effect predicted here is that entanglement in fact can be controlled electrically (without applying a laser field) and readout in the form of a transport property, i.e., the electron *current* (as a function of the dot distance or, alternatively, the cavity length).

Another possible application of this effect is that, by tuning the coherence of the dots, one can control the emission of single photon at predetermined times, which is important for the field of quantum information technology. However, one should note that the biexciton effect is not included in our present model. Therefore, a low injection limit is required in the experiment [18]. One might argue that for small interdot distance the Forster process may play some role in our system [19]; nevertheless, this causes only small energy splitting between state $|S_0\rangle$ and $|T_0\rangle$. Comparing to the large energy difference in the III-V semiconductor material, its effect on the decay rate $g^2\gamma_{\pm}$ is negligible. As for the problem of dissipation, decoherence due to interaction with other bosonic excitations (phonons and electron-hole pairs in the leads) is inevitable but can in principle be (partly) controlled by variation of the dot energies, or control of the mechanical degree of freedom [20]. In addition, scattering due to impurities is negligible since there is no interdot transport in our system.

In conclusion, we have proposed a method of detecting the superradiant effect in a semiconductor double-dot system. By incorporating the InAs quantum dots between a *p-i-n* junction, the superradiant effect on the stationary tunnel current can be examined by tuning the band gap of the quantum dot. Moreover, the interference effects between two dots can be seen more clearly by incorporating the system inside a microcavity. The oscillation period of the decay rate and current is also increased because of the microcavity. Besides, the maximum entangled state is induced as the interdot distance is much smaller than the wavelength of the emitted photon. Our model provides a new way to generate the entanglement in solid-state systems.

We would like to thank Professor Y. C. Lee at SUNYAB for helpful discussions. This work is supported partially by the National Science Council, Taiwan, under Grant No. NSC 91-2112-M-009-012.

[1] R. H. Dicke, Phys. Rev. **93**, 99 (1954).
[2] K. C. Liu and Y. C. Lee, Physica (Amsterdam) **102A**, 131 (1980); Y. N. Chen and D. S. Chuu, Phys. Rev. B **61**, 10815 (2000).
[3] J. Knoester, Phys. Rev. Lett. **68**, 654 (1992); D. S. Citrin, Phys. Rev. B **47**, 3832 (1993); D. Ammerlahn, J. Kuhl, B. Grote, S. W. Koch, G. Khitrova, and H. Gibbs, Phys. Rev. B **62**, 7350 (2000).
[4] A. L. Ivanov and H. Haug, Phys. Rev. Lett. **71**, 3182 (1993); Y. Manabe, T. Tokihiro, and E. Hanamura, Phys. Rev. B **48**, 2773 (1993); Y. N. Chen, D. S. Chuu, T. Brandes, and B. Kramer, Phys. Rev. B **64**, 125307 (2001).
[5] A. Nakamura, H. Yamada, and T. Tookizaki, Phys. Rev. B **40**, 8585 (1989).
[6] E. Hanamura, Phys. Rev. B **38**, 1228 (1988); F. C. Spano, J. R. Kuklinski, and S. Mukamel, Phys. Rev. Lett. **65,**, 211 (1990).
[7] C. H. Bennett and D. P. DiVincenzo, Nature (London) **404**, 247 (2000).
[8] T. Pellizzari, S. A. Gardiner, J. I. Cirac, and P. Zoller, Phys. Rev. Lett. **75**, 3788 (1995); J. I. Cirac and P. Zoller, Phys. Rev. Lett. **74**, 4091 (1995); K. Molmer and A. Sorensen, Phys. Rev. Lett. **82**, 1835 (1999).
[9] A. T. Costa, Jr. and S. Bose, Phys. Rev. Lett. **87**, 277901 (2001); W. D. Oliver, F. Yamaguchi, and Y. Yamamoto, Phys. Rev. Lett. **88**, 037901 (2002); Oliver Gywat, Guido Burkard, and Daniel Loss, Phys. Rev. B **65**, 205329 (2002).
[10] O. Benson, C. Santori, M. Pelton, and Y. Yamamoto, Phys. Rev. Lett. **84**, 2513 (2000).
[11] R. G. DeVoe and R. G. Brewer, Phys. Rev. Lett. **76**, 2049 (1996).
[12] T. Brandes and B. Kramer, Phys. Rev. Lett. **83**, 3021 (1999).
[13] G. S. Solomon, M. Pelton, and Y. Yamamoto, Phys. Rev. Lett. **86**, 3903 (2001).
[14] Paul S. Lee, Y. C. Lee, and C. T. Chang, Phys. Rev. A **8**, 1722 (1973).
[15] J. M. Gérard, B. Sermage, B. Gayral, B. Legrand, E. Costard, and V. Thierry-Mieg, Phys. Rev. Lett. **81**, 1110 (1998).
[16] S. Schneider and G. J. Milburn, Phys. Rev. A **65**, 042107 (2002).
[17] Daniel Braun, Phys. Rev. Lett. **89**, 277901 (2002).
[18] Z. Yuan, B. E. Kardynal, R. M. Stevenson, A. J. Shields, C. J. Lobo, K. Cooper, N. S. Beattie, D. A. Ritchie, and M. Pepper, Science **295**, 102 (2002).
[19] L. Quiroga and N. Johnson, Phys. Rev. Lett. **83**, 2270 (1999).
[20] S. Debald, T. Brandes, and B. Kramer, Phys. Rev. B **66**, 041301(R) (2002).

Strain-Induced Coupling of Spin Current to Nanomechanical Oscillations

A. G. Mal'shukov,[1] C. S. Tang,[2] C. S. Chu,[3] and K. A. Chao[4]

[1]*Institute of Spectroscopy, Russian Academy of Science, 142190, Troitsk, Moscow oblast, Russia*
[2]*Physics Division, National Center for Theoretical Sciences, P.O. Box 2-131, Hsinchu 30013, Taiwan, Republic of China*
[3]*Department of Electrophysics, National Chiao Tung University, Hsinchu 30010, Taiwan, Republic of China*
[4]*Solid State Theory Division, Department of Physics, Lund University, S-22362 Lund, Sweden*

(Received 6 May 2005; published 1 September 2005)

We propose a setup which allows us to couple the electron spin degree of freedom to the mechanical motions of a nanomechanical system not involving any of the ferromagnetic components. The proposed method employs the strain-induced spin-orbit interaction of electrons in narrow gap semiconductors. We have shown how this method can be used for detection and manipulation of the spin flow through a suspended rod in a nanomechanical device.

DOI: 10.1103/PhysRevLett.95.107203 PACS numbers: 75.40.Gb, 71.70.Ej, 71.70.Fk, 72.25.−b

An ability to control the spin transport in semiconductors is a key problem to be solved towards implementation of semiconductor spintronics into quantum information processing [1–3]. Many methods have been proposed to achieve control of the electron spin degree of freedom using magnetic materials, external magnetic fields, and optical excitation [for a review see Ref. [3]]. Other promising ideas involve the intrinsic spin-orbit interaction (SOI) in narrow gap semiconductors to manipulate the spin by means of electric fields [4] and electric gates [5–7]. Recently, some of these ideas have been experimentally confirmed [8,9].

In semiconductors the spin-orbit effect appears as an interaction of the electron spin with an effective magnetic field whose direction and magnitude depend on the electron momentum. A specific form of this dependence is determined by the crystal symmetry, as well as by the symmetry of the potential energy profile in heterostructures. In strained semiconductors new components of the effective magnetic field appear due to violation of the local crystal symmetry [10]. The effect of the strain-induced SOI on spin transport was spectacularly demonstrated by Kato *et al.* in their Faraday rotation experiment [9]. An interesting property of the strain-induced SOI is that the strain can be associated with mechanical motion of the solid, in particular, with oscillations in nanomechanical systems (NMS), in such a way making possible the spin-orbit coupling of the electron spin to nanomechanical oscillations. At the same time a big progress in fabricating various NMS [11] allows one to reach the required parameter range to observe subtle effects produced by such a coupling.

In this Letter we will consider NMS in the form of a suspended beam with a doped semiconductor film epitaxially grown on its surface (see Fig. 1). An analysis of the SOI in this system shows that the flexural and torsion vibrational modes couple most efficiently to the electron spin. As a simple example, we will focus on the torsion mode. The strain associated with torsion produces the spin-orbit field which is linear with respect to the electron momentum and is directed perpendicular to it. This field varies in time and space according to respective variations of the torsion strain. Because of the linear dependence on the momentum, the SOI looks precisely as interaction with the spin dependent electromagnetic vector potential. An immediate result of this analogy is that the time-dependent torsion gives rise to a motive force on electrons. Such a force, however, acts in different directions on particles with oppositely oriented spins, inducing thus the spin current in the electron gas. The physics of this phenomenon is very similar to the spin-current generation under time-dependent Rashba SOI, where the time dependence of the SOI coupling parameter is provided by the gate voltage variations [6]. In the present work we will focus, however, on the inverse effect. Because of the SOI coupling, the spin current flowing through the beam is expected to create a mechanical torsion. The torque effect on NMS due to spin flow has been previously predicted by Mohanty *et al.* [12] for a different physical realization, where the torque has

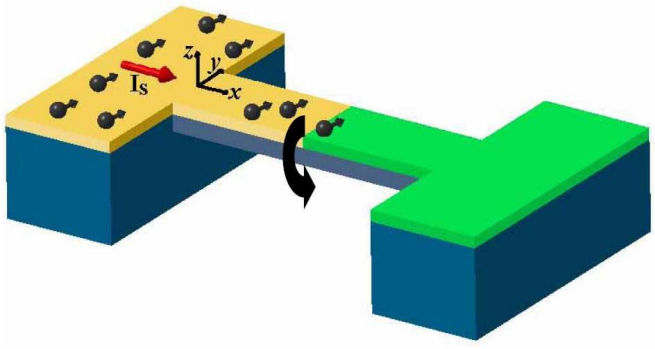

FIG. 1 (color online). Schematic illustration of electromechanical spin-current detector, containing a suspended semiconductor-metal (S-M) rectangular rod atop an insulating substrate (blue). A spin current is injected from the left semiconductor reservoir (yellow) and then diffuses toward the metallic film (green). While passing through the semiconductor film, the spin current induces torque shown by the black arrow.

been created by spin flips at the nonmagnetic-ferromagnetic interface. They also suggested an experimental setup to measure such a small torque. As it will be shown below, the torque due to the strain-induced SOI can be large enough to be measured using the experimental setup proposed in Ref. [12]. Besides this method, other sensitive techniques for displacement measurements can be employed [13].

The system under consideration is a rectangular beam of the total length L_t, width b, and thickness c. The coordinate axes are chosen as shown in Fig. 1. The semiconductor film with the thickness $c/2$ occupies the length L of the beam. The rest part contains a metal film. It can also include some additional elements for detection of the torque, for example, in Ref. [12]. Here we will consider an example when the spin current is created by diffusion of the spin polarization from the left contact in Fig. 1. Therefore, there is no electric current flow through NMS. The spin polarization diffuses towards the metal film which, due to its relatively high conduction, can play an important role as a reservoir for the spin polarization relaxation.

We start from the strain-induced SOI [10] described by the Hamiltonian

$$H_{\mathrm{SO1}} = \alpha[\sigma_x(u_{zx}k_z - u_{xy}k_y) + \sigma_y(u_{xy}k_x - u_{yz}k_z) + \sigma_z(u_{yz}k_y - u_{zx}k_x)] + \beta[\sigma_x k_x(u_{yy} - u_{zz}) + \sigma_y k_y(u_{zz} - u_{xx}) + \sigma_z k_z(u_{xx} - u_{yy})], \quad (1)$$

where u_{ij} are elements of the strain tensor, σ_i stand for Pauli matrices, and k_i denote components of the electron wave vector. In the narrow gap semiconductors the parameter β is usually much smaller than α [10]. Therefore, the term proportional to β will be omitted below. Besides the strain-induced H_{SO1}, the total SOI Hamiltonian also includes the strain independent interaction H_{SO2}. Because of submicron cross-section dimensions of the doped semiconductor film, H_{SO2} will be determined by the bulk Dresselhaus term [14].

$$H_{\mathrm{SO2}} = \delta \sum_{ijn} |\epsilon^{ijn}| k_i(k_j^2 - k_n^2). \quad (2)$$

This interaction, in the range of doping concentrations 10^{17} cm^{-3} and higher, provides the main mechanism for spin relaxation in bulk materials [10].

Since the S-M rod with total length $L_t \gg b$ and c, the major contribution to the strain comes from flexural and torsion motions of the rod [15]. Within the isotropic elastic model, the flexural motions are represented by the diagonal elements u_{xx} and u_{yy} [15] which do not enter into the first square brackets of Eq. (1). On the other hand, due to the crystal anisotropy effects, the u_{xy} components are not zero for such sort of motion and could contribute to Eq. (1). We will consider, however, the simplest example of torsion motions of the rod within an isotropic elastic model. In this case the strain can be represented as [15]

$$u_{yx} = \tau(x)\frac{\partial \chi}{\partial z}; \qquad u_{zx} = -\tau(x)\frac{\partial \chi}{\partial y}; \qquad u_{yz} = 0, \quad (3)$$

where $\tau(x) = \partial\theta/\partial x$ stands for the rate of torsion determined by the torsion angle θ. The function χ depends only on z and y and is uniquely determined by the rod cross-section geometry.

The next step is to derive from the one-particle interaction Eq. (1) a Hamiltonian which describes a coupling of the spin current to the strain. The electron system carrying the spin current can be described by a density matrix $\hat{\rho}$. In the framework of the perturbation theory the leading correction to the electron energy due to the SOI induced strain can be obtained by averaging H_{SO1} with $\hat{\rho}$. In the semiclassical approximation such a procedure can be represented as averaging over the classical phase space with the Boltzmann distribution function $\hat{F}_{\mathbf{k}}(\mathbf{r})$. This function is a 2×2 matrix in the spinor space. One can also define the spin distribution function $P^i_{\mathbf{k}}(\mathbf{r}) = (1/2)\,\mathrm{Tr}\,[\hat{F}_{\mathbf{k}}(\mathbf{r})\sigma^i]$. It is normalized in such a way that the local spin polarization $P^i(\mathbf{r}) = \sum_{\mathbf{k}} \mathbf{P}_{\mathbf{k}}(\mathbf{r})$. We notice that, due to electron confinement in y and z directions, the averages of H_{SO1} containing k_y and k_z turn to zero. Assuming that electron distribution is uniform within the cross section of the semiconductor film one thus obtains, from Eqs. (1) and (3), the SOI energy

$$E_{\mathrm{SO}} = 2\alpha \int_0^L dx \frac{\partial \theta}{\partial x} \sum_{\mathbf{k}} k_x \int dy dz \left(P^y_{\mathbf{k}}(x)\frac{\partial \chi}{\partial z} + P^z_{\mathbf{k}}(x)\frac{\partial \chi}{\partial y} \right). \quad (4)$$

This expression can be further simplified taking into account that χ turns to zero on a free surface [15]. Hence, in the example under consideration $\chi = 0$ on the top and side surfaces of the doped semiconductor film. Consequently, the second term in Eq. (4) vanishes after integration over y. Now Eq. (4) can be expressed in terms of the spin current $J^y(x)$ which is the flux in x direction of y-polarized spins.

$$J^y(x) = S \sum_{\mathbf{k}} v_x P^y_{\mathbf{k}}(x), \quad (5)$$

where $S = bc/2$ is the semiconductor film cross section and v_x is the electron velocity in x direction [16]. Finally, Eq. (4) can be transformed to

$$E_{\mathrm{SO}} = \gamma \int_0^L dx J^y(x) \frac{\partial \theta}{\partial x}. \quad (6)$$

Here the coupling constant γ is given by

$$\gamma = \gamma_0 \int_{-b/2}^{b/2} \chi(y, z = 0) dy, \quad (7)$$

where $\gamma_0 = 2m^*\alpha/\hbar S$.

From the last equation, it is seen that the spin-polarized flow imposes a distributed torque on the rod. In order to study this effect in detail we will neglect, for simplicity, the difference between elastic constants of semiconductor and

metal parts of NMS. As such, the equation of motion for the torsion angle can be then written as

$$I\frac{\partial^2\theta}{\partial t^2} - K\frac{\partial^2\theta}{\partial x^2} - \gamma\frac{\partial}{\partial x}[J^y\eta(L-x)] = 0, \tag{8}$$

where $\eta(x)$ denotes the Heaviside function, K stands for the torsion rigidity, and I is the moment of inertia. It is easy to figure out that the torque imposed by the SOI on NMS can be expressed as

$$\mathcal{T} = \frac{\gamma}{L}\int_0^L dx J^y(x) \equiv \gamma\bar{J}^y, \tag{9}$$

and, for the S-M rod clamped on both ends, the torsion angle at $x = L$

$$\theta_L = \frac{L(L_t - L)}{L_t}\frac{\mathcal{T}}{K}, \tag{10}$$

where L_t is the total length of the rod. From Eq. (8) one can easily see that if the semiconductor film covers the entire length of the beam ($L = L_t$) and the spin current is homogeneous along it, the last term in Eq. (8) turns to 0. Consequently, for a doubly clamped beam the solution of Eq. (8) is $\theta(x) \equiv 0$. In this case, in order to obtain the finite torsion angle, the NMS must include films with different spin-orbit coupling parameters γ, as in Fig. 1 where $\gamma = 0$ in the metal film. On the other hand, if J^y depends on x, as in the example considered below, the metal film is not so necessary. In this example it is shown, however, that such a film can be useful as a reservoir for fast spin relaxation, enhancing thus the diffusive spin-current flow through the beam.

In order to evaluate the torque, let us adopt the following simple model, which is also convenient for an experimental realization. Namely, we assume that the spin current is due to spin diffusion from the left contact. The spin polarization $P^y(0)$ can be created there by various methods ranging from absorption of circularly polarized light to injection from a ferromagnet [3]. One more possibility is the electric spin orientation [9]. For the steady state the diffusion equation reads

$$D_i\frac{d^2P^y}{dx^2} - \frac{P^y}{\tau_i} = 0, \tag{11}$$

where D_i and τ_i are diffusion coefficients and spin relaxation times, with the subscript i indicating the physical quantities in semiconductor ($0 < x < L$) ($i = S$) or metal ($x > L$) ($i = M$) regions. At the semiconductor-metal interface the diffusion current and magnetization $P^y/N_i(0)$ must be continuous, where $N_i(0)$ is the semiconductor or metal density of states at the Fermi energy [17]. We will assume that the length of the metal part of the rod is larger than the spin diffusion length $l_M = \sqrt{D_M\tau_M}$. Therefore, the spin current passes through the semiconductor film and further decays within the metal film. Obviously, in the considered example there is no charge current through the system. Solving the diffusion equation for $l_S \gg L$ and $(\sigma_M L)/(\sigma_S l_M) \gg 1$, where σ_M and σ_S are the 3D conductivities of metal and semiconductor, respectively, we obtain

$$\bar{J}^y = \frac{D_S P^y(0) S}{L}. \tag{12}$$

Since the ratio σ_M/σ_S is very big, Eq. (12) is valid in a broad range of not very small L.

For a numerical evaluation of the spin-orbit torsion effect we take $b = 400$ nm and $c = 200$ nm. The SOI coupling constant $\alpha/\hbar = 4 \times 10^5$ m/sec in GaAs [18]. From Eq. (7) and Ref. [15], it is easy to obtain the spin-current-torsion coupling parameter $\gamma = \gamma_0 k_2 b^3$, where k_2 is a numerical factor depending on the ratio c/b. At $b/c = 2$ the factor $k_2 = 0.03$. For such numerical parameters we find $\gamma = 2.4 \times 10^{-32}$ J sec. It is interesting to compare the torsion effect from the strain-induced SOI with that produced by spin flips at the FM-NM interface [12]. In the latter case $\mathcal{T} = \hbar I_s$, where I_s is of the order of the spin current injected at the FM-NM contact when the electric current passes through it. Comparing this expression with Eq. (9), it is seen that at the *same* spin currents the SOI effect is much stronger, by the factor $\gamma/\hbar \simeq 2.2 \times 10^2$. On the other hand, in [12] the FM-NM contact can be fabricated from all metallic components, while our device must contain the narrow gap semiconductor film. In the former case NMS is able to carry much larger spin current, due to the weaker, by the factor $\sim\sigma_S/\sigma_M$, Joule heating effect. However, the measurement setup suggested by Mohanty *et al.* [12] allows us to measure torsion effects produced by quite weak currents. For example, at $e\bar{J}^y = 10^{-8}$ Amp the torque $\mathcal{T} = 1.5 \times 10^{-21}$ Nm, which is within the sensitivity claimed in [12]. Moreover, the measurement sensitivity can be enhanced [19]. Within our model we can evaluate the spin polarization $P^y(0)$ which can produce a measurable effect on NMS. From Eq. (12), taking $L = 2\ \mu$m, the typical low temperature diffusion constant 300 cm^2/sec, and $n = 10^{17}$ cm^{-3}, one obtains $e\bar{J}^y = 10^4[P^y(0)/n]$ nA. Hence, a measurable 10 nA spin current in NMS can be created by diffusion of spin polarization from an adjacent reservoir containing only 0.1% of spin-polarized carriers. Various methods [3,8,9] are able to provide such and even much larger spin polarization. Higher spin currents are, however, restricted by the heating effects, which depend on the practical design of NMS.

It should be noted that the torsion measurement method of Ref. [12] applies to a time-dependent torque in resonance with a NMS oscillation. For such a measurement the spin current could be modulated in time by a narrow gate between the left contact and the rod, or by varying the spin polarization in the left reservoir, for example, if it is created by absorption of circularly polarized light with modulated intensity.

The static torsion angle at $x = L$ can be found from Eq. (10). On the other hand, the maximum torsion effect is obtained for the time-dependent spin current in resonance with the NMS fundamental oscillation. In this case, the torsion angle θ_L in Eq. (10) must be multiplied by $Q/2$, where Q is the resonance quality factor, which can be quite large in NMS. To observe this torsion angle it must be much larger than the mean amplitude of its thermal fluctuations $\sqrt{\overline{\delta\theta_L^2}}$. For a doubly clamped rod

$$\overline{\delta\theta_L^2} = \frac{k_B T L_t}{\pi^2 K} \sum_{n\geq 1} \frac{1}{n^2} \sin^2\left(\frac{\pi n L}{L_t}\right). \tag{13}$$

For a rectangular cross section with $b/c = 2$, the torsion rigidity $K = 0.057\mu b^3 c$ [15], where $\mu \simeq 3.3 \times 10^{10}$ N/m^2 in GaAs material. Taking $L_t = 5$ μm and all other parameters the same as in the previous paragraph, $Q = 10^4$ and $T = 100$ mK, we obtain the ratio $\delta\theta_L/\theta_L \simeq 4 \times 10^{-2}$ at $e\bar{J}^y = 10$ nA.

We have considered a simple example of the spin-orbit torque effect produced by spin flux in a diffusive 3D semiconductor film. It would be interesting to study other systems, for example, a superlattice of remotely doped high mobility quantum wells in the ballistic regime (L is less than the elastic mean free path). In such a system energy dissipation within the semiconductor film is reduced and, apparently, larger spin currents are allowable.

In summary, we propose a nanomechanical system where due to the strain-induced spin-orbit interaction the electron spin degree of freedom can couple to NMS mechanical motions. We have shown that this coupling is strong enough to induce the measurable torsion in NMS when the spin polarization flows through the suspended nanobeam. Besides a potential for other possible applications, such NMS can be employed as a sensitive detector of spin currents and spin polarizations. The basic structure can be further modified to create devices for eventual use in spintronics as well as spin information processing.

This work was partly funded by the Taiwan National Science Council and RFBR Grant No. 03-02-17452.

[1] *Semiconductor Spintronics and Quantum Computation*, edited by D. D. Awschalom, N. Samarth, and D. Loss (Springer-Verlag, Berlin, 2002).
[2] S. A. Wolf *et al.*, Science **294**, 1488 (2001).
[3] I. Žutić, J. Fabian, and S. Das Sarma, Rev. Mod. Phys. **76**, 323 (2004).
[4] J. Sinova *et al.*, Phys. Rev. Lett. **92**, 126603 (2004); S. Murakami, N. Nagaosa, and S. Zhang, Science **301**, 1348 (2003); V. M. Edelstein, Solid State Commun. **73**, 233 (1990); A. Voskoboynikov, S. S. Liu, and C. P. Lee, Phys. Rev. B **59**, 12514 (1999); L. S. Levitov and E. I. Rashba, Phys. Rev. B **67**, 115324 (2003).
[5] S. Datta and B. Das, Appl. Phys. Lett. **56**, 665 (1990); P. Sharma and P. W. Brouwer, Phys. Rev. Lett. **91**, 166801 (2003); M. Governale, F. Taddei, and R. Fazio, Phys. Rev. B **68**, 155324 (2003).
[6] A. G. Mal'shukov, C. S. Tang, C. S. Chu, and K. A. Chao, Phys. Rev. B **68**, 233307 (2003).
[7] C. S. Tang, A. G. Mal'shukov, and K. A. Chao, Phys. Rev. B **71**, 195314 (2005).
[8] J. Wunderlich, B. Käestner, J. Sinova, and T. Jungwirth, Phys. Rev. Lett. **94**, 047204 (2005).
[9] Y. K. Kato *et al.*, cond-mat/0502627.
[10] G. E. Pikus and A. N. Titkov, in *Optical Orientation*, edited by F. Meier and B. P. Zakharchenya (North-Holland, Amsterdam, 1984).
[11] M. L. Roukes, Phys. World **14**, 25 (2001); H. G. Craighead, Science **290**, 1532 (2000); A. N. Cleland, *Foundations of Nanomechanics* (Springer, New York, 2003).
[12] P. Mohanty, G. Zolfagharkhani, S. Kettemann, and P. Fulde, Phys. Rev. B **70**, 195301 (2004).
[13] R. G. Knobel and A. N. Cleland, Nature (London) **424**, 291 (2003).
[14] G. Dresselhaus, Phys. Rev. **100**, 580 (1955).
[15] L. Landau and E. Lifshitz, *Course of Theoretical Physics* (Pergamon, New York, 1986), 3rd ed., Vol. 7.
[16] We neglected the small correction to the spin current associated with Dresselhaus's term $\frac{\partial H_{SO2}}{\partial \mathbf{k}}$ in the velocity operator, as well as the corresponding correction due to H_{SO1}, within the linear perturbation theory on the strain-induced SOI.
[17] M. Johnson and R. H. Silsbee, Phys. Rev. B **35**, 4959 (1987); **37**, 5312 (1988).
[18] M. I. D'yakonov, V. A. Marushchak, V. I. Perel', and A. N. Titkov, Sov. Phys. JETP **63**, 655 (1986) [Zh. Eksp. Teor. Fiz. **90**, 1123 (1986)].
[19] P. Mohanty (private communication).

Shot-noise spectrum of superradiant entangled excitons

Y. N. Chen,[1] T. Brandes,[2] C. M. Li,[1] and D. S. Chuu[1]
[1]*Department of Electrophysics, National Chiao-Tung University, Hsinchu 300, Taiwan*
[2]*Department of Physics, UMIST, P.O. Box 88, Manchester M60 1QD, United Kingdom*
(Received 10 March 2004; published 28 June 2004)

The shot noise produced by tunneling of electrons and holes into a double dot system incorporated inside a *p-i-n* junction is investigated theoretically. The enhancement of the shot noise is shown to originate from the entangled electron-hole pair created by superradiance. The analogy to the superconducting Cooper pair box is pointed out. A series of Zeno-like measurements is shown to destroy the entanglement, except for the case of maximum entanglement.

DOI: 10.1103/PhysRevB.69.245323 PACS number(s): 73.63.Kv, 72.70.+m, 03.67.Mn, 03.65.Xp

I. INTRODUCTION

Quantum entanglement has become one of the most important issues since the rapid developments in quantum information science.[1] Much research has been devoted to studying entanglement as induced by a direct interaction between the individual subsystems.[2] Very recently, a lot of attention has been focused on reservoir-induced entanglement[3] with the purpose to shed light on the generation of entanglement, and to better understand quantum decoherence.

Furthermore, shot noise[4] has been identified as a valuable indicator of particle entanglement in transport experiments.[5] A well studied example is the doubling of the full shot noise in **S**-**I**-**N** tunnel junctions,[6] where **N** is a normal metal, **S** stands for a superconductor, and **I** is an insulating barrier. The origin of this enhancement comes from the break-up of the spin-singlet state, which results in a quick transfer of two electrical charges.

In this paper, we demonstrate how the dynamics of entangled excitons formed by superradiance can be revealed from the observations of current fluctuations. A doubled zero-frequency shot noise is found for the case of zero subradiant decay rate. We relate the particle noise to photon noise by calculating the first order photon coherence function. Furthermore, strong reservoir coupling acts like a continuous measurement, which is shown to suppress the formation of the entanglement, except for the state of maximum entanglement. These novel features imply that our model provides a new way to examine both the bunching behavior and a Zeno-like effect of the reservoir induced entanglement.

II. DOUBLE DOT MODEL

The effect appears in double quantum dots embedded inside a *p-i-n* junction.[7] It involves superradiant and subradiant decay through two singlet and triplet entangled states, $|S_0\rangle = 1/\sqrt{2}(|U_1\rangle - |U_2\rangle)$ and $|T_0\rangle = 1/\sqrt{2}(|U_1\rangle + |U_2\rangle)$, and one ground state $|D\rangle = |0,0;0,0\rangle$, where $|U_1\rangle = |e,h;0,0\rangle$ ($|U_2\rangle = |0,0;e,h\rangle$) represents one exciton in dot 1 (2). Electron and hole reservoirs coupled to both dots have chemical potentials such that electrons and holes can tunnel into the dot. For the physical phenomena we are interested in, the current is assumed to be conducted through dot 1 only (Fig. 1). Therefore, the exciton states $|0,0;e,h\rangle$ (in dot 2) can only be created via the exciton-photon interactions.

The exciton-photon coupling is described by an interaction Hamiltonian

$$H_I = \sum_{\mathbf{k}} \frac{1}{\sqrt{2}} g\{D_{\mathbf{k}} b_{\mathbf{k}} [(1 + e^{i\mathbf{k}\cdot\mathbf{r}})|S_0\rangle \times \langle D| + (1 - e^{i\mathbf{k}\cdot\mathbf{r}})|T_0\rangle\langle D|] + \text{H.c.}\}, \quad (1)$$

where $b_{\mathbf{k}}$ is the photon operator, $gD_{\mathbf{k}}$ is the coupling strength, $\mathbf{r}$ is the position vector between the two quantum dots. Here, g is a constant with the unit of the tunneling rate. The dipole approximation is not used in our calculation since we keep the full $e^{i\mathbf{k}\cdot\mathbf{r}}$ terms in the Hamiltonian. The coupling of the dot states to the electron and hole reservoirs is described by the standard tunnel Hamiltonian

$$H_V = \sum_{\mathbf{q}} (V_{\mathbf{q}} c_{\mathbf{q}}^{\dagger}|0\rangle\langle U_1| + W_{\mathbf{q}} d_{\mathbf{q}}^{\dagger}|0\rangle\langle D| + \text{H.c.}), \quad (2)$$

where $c_{\mathbf{q}}$ and $d_{\mathbf{q}}$ are the electron operators in the left and right reservoirs, respectively, and $|0\rangle = |0,h;0,0\rangle$ denotes one-hole state in dot 1. $V_{\mathbf{q}}$ and $W_{\mathbf{q}}$ couple the channels $\mathbf{q}$ of the electron and the hole reservoirs. Here we have neglected the state $|e,0;0,0\rangle$ for convenience. This can be justified by fabricating a thicker barrier on the electron side so that there is little chance for an electron to tunnel in advance.[8]

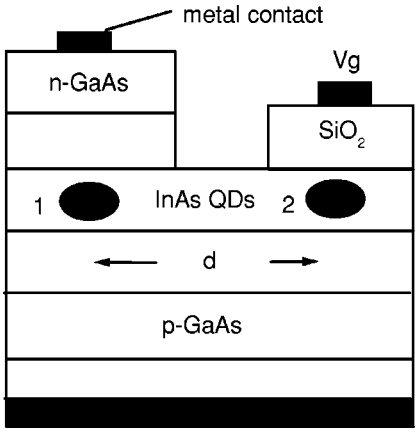

FIG. 1. Schematic view of the structure.

III. RATE EQUATIONS AND NOISE SPECTRUM

The rates Γ_U (electron reservoir) and Γ_D (hole reservoir) for tunneling between the dot and the connected reservoirs can be calculated from H_V by perturbation theory. In double quantum dots, decay of the excited levels is governed by collective behavior, i.e., superradiance and subradiance. The corresponding decay rates for the state $|S_0\rangle$ and $|T_0\rangle$ can be obtained from H_I and are denoted by $g^2\gamma_S$ and $g^2\gamma_T$, respectively. We are then in the position to set up the equations of motion for the time-dependent occupation probabilities $n_j(t)$, $j=0,D,S_0,T_0$, of the double dot states. Together with the normalization condition $\Sigma_j n_j(t)=1$, the equations of motion are Laplace-transformed into z-space[9] for convenience and read

$$z\hat{n}_{S_0}(z) = -ig[\hat{p}_{S_0,D}(z) - \hat{p}_{D,S_0}(z)] + \Gamma_U\left[\frac{1}{z} - \hat{n}_{S_0}(z) - \hat{n}_{T_0}(z) - \hat{n}_D(z)\right],$$

$$z\hat{n}_{T_0}(z) = -ig[\hat{p}_{T_0,D}(z) - \hat{p}_{D,T_0}(z)] + \Gamma_U\left[\frac{1}{z} - \hat{n}_{S_0}(z) - \hat{n}_{T_0}(z) - \hat{n}_D(z)\right],$$

$$z\hat{n}_D(z) = -ig[\hat{p}_{S_0,D}(z) - \hat{p}_{D,S_0}(z) + \hat{p}_{T_0,D}(z) - \hat{p}_{D,T_0}(z)] - \frac{2\Gamma_D}{z}\hat{n}_D(z). \quad (3)$$

Here, $p_{S_0,D}(t)=p^*_{D,S_0}(t)$ and $p_{T_0,D}(t)=p^*_{D,T_0}(t)$ are off-diagonal matrix elements of the reduced density operator of the double dots, whose Laplace-transformed equations of motion close the set (3):

$$\hat{p}_{S_0,D}(z) = ig\gamma_S\hat{n}_{S_0}(z) - \Gamma_D\gamma_S\hat{p}_{S_0,D}(z),$$

$$\hat{p}_{T_0,D}(z) = ig\gamma_T\hat{n}_{T_0}(z) - \Gamma_D\gamma_T\hat{p}_{T_0,D}(z). \quad (4)$$

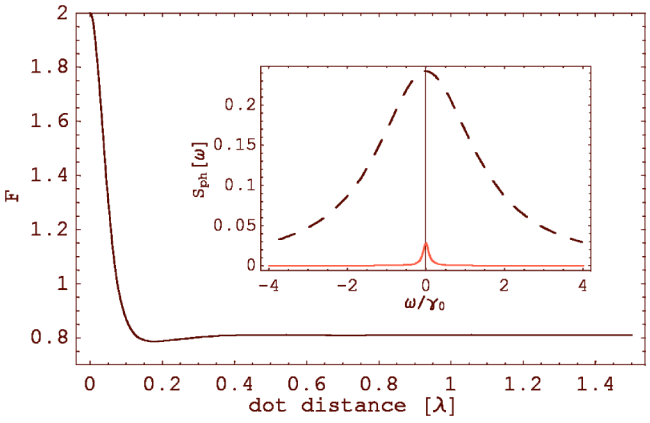

FIG. 2. (Color online) Fano factor as a function of inter-dot distance. The vertical and horizontal units are $S_{I_D}(0)/2eI$ and λ, respectively. The inset shows the value of $S_{\rm ph}(\omega)$ is equal to that of the one-dot limit for $d\to\infty$ (dashed line), while it approaches *zero noise* as $d=0.005\lambda$ (solid line).

Note that in getting the above equations, one has to do a decoupling approximation of dot operators and photon operators. This means we are interested in small coupling parameters here, and a decoupling of the reduced density matrix $\tilde{\rho}(t')$ is used: $\tilde{\rho}(t')\approx\rho^0_{\rm ph}Tr_{\rm ph}\rho(t')$.[9] The stationary tunnel current I can be defined as the change of the occupation of $n_D(t)$ for large times t and is given by

$$I \equiv \lim_{t\to\infty} ig[p_{S_0,D}(t) - p_{D,S_0}(t) + p_{T_0,D}(t) - p_{D,T_0}(t)], \quad (5)$$

where we have set the electron charge $e=1$ for convenience.

In a quantum conductor in nonequilibrium, electronic current noise originates from the dynamical fluctuations of the current being away from its average. To study correlations between carriers, we relate the qubit dynamics with the hole reservoir operators by introducing the degree of freedom n as the number of holes that have tunneled through the hole-side barrier and write

$$\dot{n}^{(n)}_0(t) = -\Gamma_U n^{(n)}_0(t) + \Gamma_D n^{(n-1)}_D(t),$$

$$\dot{n}^{(n)}_{S_0}(t) = \frac{\Gamma_U}{2}n^{(n)}_0(t) + ig[p^{(n)}_{S_0,D}(t) - p^{(n)}_{D,S_0}(t)],$$

$$\dot{n}^{(n)}_{T_0}(t) = \frac{\Gamma_U}{2}n^{(n)}_0(t) + ig[p^{(n)}_{T_0,D}(t) - p^{(n)}_{D,T_0}(t)],$$

$$\dot{n}^{(n)}_D(t) = -\Gamma_D n^{(n)}_0(t) - ig[p^{(n)}_{S_0,D}(t) - p^{(n)}_{D,S_0}(t) + p^{(n)}_{T_0,D}(t) - p^{(n)}_{D,T_0}(t)]. \quad (6)$$

Equations (6) allow us to calculate the particle current and the noise spectrum from $P_n(t)=n^{(n)}_0(t)+n^{(n)}_{S_0}(t)+n^{(n)}_{T_0}(t)\,n^{(n)}_D(t)$ which gives the total probability of finding n electrons in the collector by time t. In particular, the noise spectrum S_{I_D} can be calculated via the MacDonald formula,[10]

$$S_{I_D}(\omega) = 2\omega e^2\int_0^\infty dt\,\sin(\omega t)\frac{d}{dt}[\langle n^2(t)\rangle - (t\langle I\rangle)^2], \quad (7)$$

where $(d/dt)\langle n^2(t)\rangle=\Sigma_n n^2P_n(t)$. Solving Eqs. (6) and (3), we obtain

$$S_{I_D}(\omega) = 2eI\{1 + \Gamma_D[\hat{n}_D(z=-i\omega) + \hat{n}_D(z=i\omega)]\}. \quad (8)$$

In the zero-frequency limit, Eq. (8) reduces to

$$S_{I_D}(\omega=0) = 2eI\left\{1 + 2\Gamma_D\frac{d}{dz}[z\hat{n}_D(z)]_{z=0}\right\}, \quad (9)$$

which is analogous to a recent calculation of noise in dissipative, open two-level systems.[11]

IV. RESULTS

A. Current noise

To display the dependence of carrier correlations on the dot distance d, Fig. 2 shows the result for zero-frequency noise $S_{I_D}(\omega=0)$ as a function of the inter-dot distance. In

plotting the figure, the tunneling rates, Γ_U and Γ_D, are assumed to be equal to $0.1\gamma_0$ and γ_0, respectively. Here, a value of $1/1.3$ ns for the free-space quantum dot decay rate γ_0 is used in our calculations.[12] As shown in Fig. 2, the Fano factor

$$F \equiv \frac{S_{I_D}(0)}{2e\langle I\rangle},$$

is enhanced by a factor of 2 as the dot distance d is much smaller than the wavelength (λ) of the emitted photon. To explain this enhancement, we approximate the Fano factor in the limit of small subradiant decay rate, i.e.,

$$g^2\gamma_S \ll \Gamma_U < \Gamma_D \approx g^2\gamma_T,$$

where we obtain

$$\frac{S_{ID}(0)}{2e\langle I\rangle} \approx 2 - 2g^2\gamma_S\left[\frac{1}{g^2\gamma_T} + 3\left(\frac{1}{\Gamma_D} + \frac{1}{\Gamma_U}\right) + \frac{2\Gamma_D}{g^2}\right]. \tag{10}$$

This is analogous to the case of the single electron transistor near a Cooper pair resonance as discussed recently by Choi and co-workers.[13] In their calculations, the Fano factor is expressed as $S(0)/2e\langle I\rangle = 2-[8E_J^2+(E_J^2+2\Gamma^2)/(3E_J^2+\Gamma^2+4\varepsilon^2)^2]$. In the strong dephasing limit ($E_J \ll \Gamma$, where E_J is the Josephson coupling energy), the zero-frequency shot noise is also enhanced by a factor of 2. Since the doubled shot noise in Josephson junction is attributed to the bunching behavior of Cooper pairs (in singlet state), we then conclude the enhancement in our system is also due to the entanglement induced by the photon reservoir.

B. Photon noise

It is worthwhile to compare the current noise with the *photon noise* generated by the collective decay of the double dot excitons. In order to do so, we have calculated the power spectrum of the fluorescence spectrum,[14] which can be expressed as

$$S_{\rm ph}(\omega) = \frac{1}{\pi}{\rm Re}\int_0^\infty G^{(1)}[\tau]e^{i\omega\tau}d\tau, \tag{11}$$

where $G^{(1)}[\tau]$ is the first order coherence function and reads

$$G^{(1)}[\tau] \propto |1+e^{i2\pi d/\lambda}|^2\langle p_{S_0,D}(0)p_{D,S_0}(\tau)\rangle + |1-e^{i2\pi d/\lambda}|^2\langle p_{T_0,D}(0)p_{D,T_0}(\tau)\rangle. \tag{12}$$

The two time-dependent correlation functions in the above equation can be calculated from the quantum regression theorem, and the numerical result of $S_{\rm ph}(\omega)$ is shown explicitly in the inset of Fig. 2. As can be seen, the value of $S_{\rm ph}(\omega)$ is equal to that of the one-dot case for $d\to\infty$ (dashed line), while it approaches zero as $d=0.005\lambda$ (red line). In the limit of $d=0$, one observes no photon emission from the double dot system since the exciton is now in its maximum entangled state and does not decay. This feature implies that photon noise is suppressed by the bunching of excitons, and its behavior is opposite to that for the electronic case.[15]

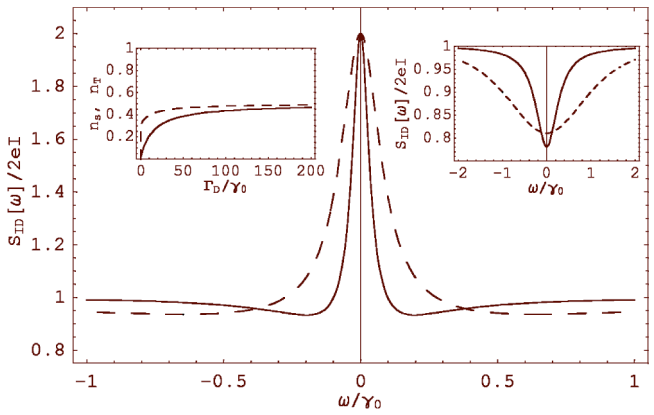

FIG. 3. Effect of measurements on current noise $S_{ID}(\omega)$ ("maximum" superradiance, $g^2\gamma_T=2g^2\gamma_0$, $g^2\gamma_S=0$). Solid and dashed lines correspond to $\Gamma_D=20\gamma_0$ and $\Gamma_D=\gamma_0$, respectively. Right inset: The case of no superradiance. Left inset: Expectation value of the excited states $\langle n_S\rangle$ and $\langle n_T\rangle$ a function of Γ_D.

C. Noise and measurement

Now we investigate how the measurement affects the shot noise spectrum. In the usual Zeno paradox,[16] a two-level system (qubit) is completely frozen under a series of measurements, whose time interval Δt is much smaller than the memory time of the reservoir. In our model, the presence of the exciton state can be viewed as the excited state, and whether or not the next hole can tunnel in is determined by the occupation of this state. Similar to the quantum Zeno effect, the tunneling of holes at the hole-side tunneling rate Γ_D can be thought of as continuous measurements. The "interval time" Δt is then inversely proportional to Γ_D. Figure 3 represents the effects of measurements on the frequency-dependent shot noise spectrum. The numerical results for the tunneling rate $\Gamma_D=20\gamma_0$ and $\Gamma_D=\gamma_0$ are demonstrated by solid and dashed curves, respectively. If the subradiant decay rate is set to zero, one obtains the doubled shot noise as mentioned above. Without superradiance, the values of the Fano factor are always below unity as shown by the right inset of Fig. 3. An interesting feature is that the half-width of the spectrum is narrowed for strong measurements ($\Gamma_D=20\gamma_0$). If one increases the electron-side tunneling rate Γ_U, there exists no such behavior. This implies that the effective decay rate is reduced in the presence of strong measurements.

To investigate thoroughly the underlying physics, we plot the expectation value of the excited states $\langle n_S\rangle$ and $\langle n_T\rangle$ as a function of Γ_D in the left inset of Fig. 3. One clearly finds the occupation probabilities grow with increasing Γ_D, and both of them approach the value of $1/2$. This not only means the measurements tend to localize the exciton in its excited state,[17] but also tells us the entanglement is destroyed under the strong measurements. However, in the limit of no subradiance ($g^2\gamma_S=0$), the occupation probability of the singlet state is always equal to one, i.e., maximum entanglement is robust against strong measurements. This is because once the maximum entangled state is formed, the total probability in the excited states is also maximum. Strong measurements on

the ground state $|D\rangle$ have no influence on the singlet entangled state.

V. DISCUSSION AND CONCLUSION

A few remarks about experimental realizations of the present model should be mentioned here. One should note that biexciton and charged-exciton effects are not included in our present model. Inclusion of these additional states is expected to suppress the enhancement of the shot noise, i.e., degrees of entanglement. However, this can be controlled well by limiting the value of bias voltage so that only the ground-state exciton is present.[18] To produce the maximum entangled state, one can also incorporate the device inside a microcavity.[19] There are two advantages of this design: The maximum entanglement can be generated even for remote separation of the two dots, and Forster process[20] is avoided at this distance.

As for the problem of decoherence due to interactions with phonons, recent experimental data have shown that the exciton-phonon dephasing rate is smaller than the radiative decay one in a quantum dot. This means that due to the discrete energy level scheme in a quantum dot, the *phonon-bottleneck* effect tends to suppress the exciton-phonon interaction.[21] Although the present model describes tunneling of electrons and holes into semiconductor quantum dots, the whole theory can be applied to electron tunneling through coupled quantum dots which are interacting via a common phonon environment.[22]

In conclusion, we have demonstrated that the shot noise of superradiant entangled excitons is enhanced by a factor of two as compared to the Poissonian value. This enhancement was attributed to exciton entanglement, induced by the electromagnetic field (common photon reservoir), and an analogy to the Cooper pair box was made. Second, we found the relaxation behavior of the qubits in the presence of strong measurements, and the Zeno-like effect tends to destroy the entanglement and localize the qubits in the excited states.

ACKNOWLEDGMENT

This work is supported partially by the National Science Council, Taiwan under Grant No. NSC 92-2120-M-009-010.

[1] C. H. Bennett and D. P. DiVincenzo, Nature (London) **404**, 247 (2000); T. Pellizzari, S. A. Gardiner, J. I. Cirac, and P. Zoller, Phys. Rev. Lett. **75**, 3788 (1995); J. I. Cirac and P. Zoller, *ibid.* **74**, 4091 (1995); K. Molmer and A. Sorensen, *ibid.* **82**, 1835 (1999).

[2] A. T. Costa, Jr. and S. Bose, Phys. Rev. Lett. **87**, 277901 (2001); W. D. Oliver, F. Yamaguchi, and Y. Yamamoto, *ibid.* **88**, 037901 (2002); Oliver Gywat, Guido Burkard, and Daniel Loss, Phys. Rev. B **65**, 205329 (2002).

[3] M. S. Kim, Jinhyoung Lee, D. Ahn, and P. L. Knight, Phys. Rev. A **65**, 040101 (2002); Daniel Braun, Phys. Rev. Lett. **89**, 277901 (2002); Fabio Benatti, Roberto Floreanini, and Marco Piani, *ibid.* **91**, 070402 (2003); Rusko Ruskov and Alexander N. Korotkov, Phys. Rev. B **67**, 241305 (2003).

[4] Y. M. Blanter and M. Buttiker, Phys. Rep. **336**, 1 (2000); C. W. J. Beenakker, Rev. Mod. Phys. **69**, 731 (1997).

[5] C. W. J. Beenakker, C. Emary, M. Kindermann, and J. L. van Velsen, Phys. Rev. Lett. **91**, 147901 (2003).

[6] F. Lefloch, C. Hoffmann, M. Sanquer, and D. Quirion, Phys. Rev. Lett. **90**, 067002 (2003).

[7] O. Benson, C. Santori, M. Pelton, and Y. Yamamoto, Phys. Rev. Lett. **84**, 2513 (2000).

[8] In the following calculations, the electron-side tunneling rate Γ_U is always assumed to be much smaller than the hole-side tunneling rate Γ_D.

[9] T. Brandes and B. Kramer, Phys. Rev. Lett. **83**, 3021 (1999).

[10] D. K. C. MacDonald, Rep. Prog. Phys. **12**, 56 (1948); D. Mozyrsky, L. Fedichkin, S. A. Gurvitz, and G. P. Berman, Phys. Rev. B **66**, 161313 (2002).

[11] R. Aguado and T. Brandes, Phys. Rev. Lett. **92**, 206601 (2004).

[12] G. S. Solomon, M. Pelton, and Y. Yamamoto, Phys. Rev. Lett. **86**, 3903 (2001).

[13] Mahn-Soo Choi, F. Plastina, and R. Fazio, Phys. Rev. Lett. **87**, 116601 (2001).

[14] M. O. Scully and M. S. Zubairy, *Quantum Optics* (Cambridge University Press, Cambridge, 1997).

[15] Guido Burkard, Daniel Loss, and Eugene V. Sukhorukov, Phys. Rev. B **61**, R16303 (2000).

[16] B. Misra and E. C. G. Sudarshan, J. Math. Phys. **18**, 756 (1977).

[17] A. N. Korotkov and D. V. Averin, Phys. Rev. B **64**, 165310 (2001); S. A. Gurvitz, L. Fedichkin, D. Mozyrsky, and G. P. Berman, Phys. Rev. Lett. **91**, 066801 (2003).

[18] Z. Yuan, B. E. Kardynal, R. M. Stevenson, A. J. Shields, C. J. Lobo, K. Cooper, N. S. Beattie, D. A. Ritchie, and M. Pepper, Science **295**, 102 (2002).

[19] Y. N. Chen, D. S. Chuu, and T. Brandes, Phys. Rev. Lett. **90**, 166802 (2003).

[20] L. Quiroga and N. Johnson, Phys. Rev. Lett. **83**, 2270 (1999).

[21] N. H. Bonadeo, Gang Chen, D. Gammon, D. S. Katzer, D. Park, and D. G. Steel, Phys. Rev. Lett. **81**, 2759 (1998); D. Birkedal, K. Leosson, and J. M. Hvam, *ibid.* **87**, 227401 (2001); P. Borri *et al.*, *ibid.* **87**, 157401 (2001).

[22] T. Vorrath and T. Brandes, Phys. Rev. B **68**, 035309 (2003).

Alignment and orientation of absorbed dipole molecules

Y. Y. Liao, Y. N. Chen, and D. S. Chuu*
Department of Electrophysics, National Chiao-Tung University, Hsinchu 300, Taiwan
(Received 18 April 2004; revised manuscript received 27 July 2004; published 29 December 2004)

Half-cycle laser pulse is applied on an absorbed molecule to investigate its alignment and orientation behavior. Crossover from field-free to hindered rotation motion is observed by varying the angel of hindrance of potential well. At small hindered angle, both alignment and orientation show sinusoidal-like behavior because of the suppression of higher excited states. However, mean orientation decreases monotonically as the hindered angle is increased, while mean alignment displays a minimum point at certain hindered angle. The reason is attributed to the symmetry of wave function and can be explained well by analyzing the coefficients of eigenstates.

DOI: 10.1103/PhysRevB.70.233410 PACS number(s): 73.20.Hb, 33.55.Be, 33.20.Sn

Alignment and orientation of molecules are important in the investigations of stereodynamics,[1] surface catalysis,[2] molecular focusing,[3] and nanoscale design.[4] The alignment scheme has been demonstrated both in adiabatic and nonadiabatic regimes. A strong laser pulse can adiabatically create pendular states, and the molecular axis is aligned in parallel to the direction of field polarization. The molecule goes back to its initial condition after the laser pulse is switched off, and the alignment can no longer be observed again.[5] To achieve adiabatic alignment, the duration of laser pulse must be longer than the rotational period. However, an ultrashort laser pulse with several cycles is also observed to induce a field-free alignment providing the duration of laser pulse is smaller than the rotational period. In this limit, the alignment occurs periodically in time as long as the coherence of the process is preserved.[6] On the other hand, a femtosecond laser pulse is found to be able to generate field-free orientations.[7] The dipole molecule, kicked by an impulsive pulse, will tend to orient in the direction of laser polarization. Laser-indued molecular orientations have been demonstrated in several experiments.[8–10]

Recently, the rotational motion of a molecule interacting with a solid surface has attracted increasing interest. It is known that molecules can be desorbed by applying UV laser beam along the surface direction, and the quadrupole is a measure of the rotational alignment.[11] To understand molecular-surface interaction, Gadzuk and his co-workers[12] proposed an infinite-conical-well model, in which the adsorbed molecule is only allowed to rotate within the well region. Shih *et al.* further proposed a finite-conical-well model to generalize the study of a finite hindrance.[13] Their results showed that the rotational states of an adsorbed dipole molecule in an external electric field exhibit interesting behaviors, and theoretical calculation of the quadrupole moment based on finite-conical-well model is in agreement with the experimental data.[14] These findings may be very useful for understanding the surface reaction.

In the present work we present a detailed investigation on the rotational motion of a polar diatomic molecule, which is confined by a hindering conical well. Different well-dependent signatures between the alignment and orientation of the hindered molecule under an ultrashort laser pulse are pointed out for the first time. Crossover from field-free to hindered rotation is also observed by varying the hindered angle of potential well. These make our results promising and may be useful in understanding the molecule-surface interactions.

Consider now a laser pulse polarizing in the z direction interacts with the hindered molecule as shown in Fig. 1. The model Hamiltonian can be written as

$$H = \frac{\hbar^2}{2I}J^2 + V_{hin}(\theta,\phi) + H_I, \tag{1}$$

where J^2 and I are angular momentum and momentum of inertia of the molecule. The rotational constant B is set equal to $\hbar^2/2I$. It is reasonable to assume that the surface potential $V_{hin}(\theta,\phi)$ is independent of ϕ since previous calculations have shown that its dependence on ϕ is weaker than that on θ.[15–17] Therefore, in the vertical absorbed configuration, the surface potential can be written as[12]

$$V_{hin}(\theta) = \begin{cases} 0, & 0 \leqslant \theta \leqslant \alpha \\ \infty, & \alpha < \theta \leqslant \pi, \end{cases} \tag{2}$$

where α is the hindered angle of the conical well. In Eq. (1), H_I describes the interaction between the dipole moments (permanent and induced) and laser field:

$$H_I = -\mu E(t)\cos\theta - \tfrac{1}{2}E^2(t)[(\alpha_\parallel - \alpha_\perp)\cos^2\theta + \alpha_\perp], \tag{3}$$

where μ is the dipole moment. The components of the polarizability $\alpha_\parallel$ and $\alpha_\perp$ are parallel and perpendicular to the

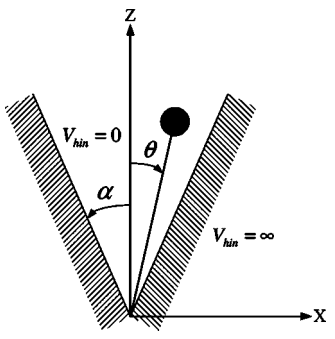

FIG. 1. Schematic view of the hindered rotor.

molecular axis, respectively. The laser field in our consideration is a Gaussian shape: $E(t)=Ee^{-(t-to)^2/\sigma^2}\cos(\omega t)$, where E is the field strength and ω is the laser frequency. To solve the time-dependent Schrödinger equation, the wave function is expressed in terms of a series of eignfunctions as

$$\Psi_{l,m}=\sum c_{l,m}(t)\psi_{l,m}(\theta,\phi), \tag{4}$$

where $c_{l,m}(t)$ are time-dependent coefficients corresponding to the quantum numbers (l,m). For the vertical adsorbed configuration, the wave function can be written as

$$\psi_{l,m}(\theta,\phi)=\begin{cases}A_{l,m}P_{\nu_{l,m}}^{|m|}(\cos\theta)\dfrac{\exp(im\phi)}{\sqrt{2\pi}}, & 0\leqslant\theta\leqslant\alpha\\ 0, & \alpha<\theta\leqslant\pi,\end{cases} \tag{5}$$

where $A_{l,m}$ is the normalization constant and $P_{\nu_{l,m}}^{|m|}$ is the associated Legendre function of arbitrary order. In the above equations, the molecular rotational energy can be expressed as

$$\epsilon_{l,m}=\nu_{l,m}(\nu_{l,m}+1)B. \tag{6}$$

In order to determine $\nu_{l,m}$, one has to match the boundary condition

$$P_{\nu_{l,m}}^{|m|}(\cos\alpha)=0. \tag{7}$$

After determining the coefficients $c_{l,m}(t)$, the orientation $\langle\cos\theta\rangle$ and alignment $\langle\cos^2\theta\rangle$ can be carried out immediately.

We choose ICl as our model molecule, with dipole moment $\mu=1.24$ Debye, rotational constant $B=0.114$ cm^{-1}, polarizability components $\alpha_{\parallel}\approx 18$ Å^3 and $\alpha_{\perp}\approx 9$ Å^3. The peak intensity and frequency of laser pulse are about 5×10^{11} W/cm^2 and 210 cm^{-1}, respectively. For simplicity (zero-temperature case), the rotor is assumed in ground state initially, i.e., $c_{0,0}(t=0)=1$. Besides, in order to keep the simulations promising, the highest quantum number for numerical calculations is $l=15$, such that the results are convergent and the precision is to the order of 10^{-7}.

The solid lines in the insets of Fig. 2 show the dependence of the alignment on hindered angle α. For $\alpha=60°$, sinusoidal-like behavior is presented, and the alignment ranges from 0.63 to 0.91. As the hindered angle increases, the curves become more and more complicated and gradually approach the free rotor limit as shown in the insets of Fig. 2(b) ($\alpha=120°$) and 2(c) ($\alpha=180°$). This can be understood well by studying the populations $|c_{l,m}|^2$ of low-lying states. In the regime of the small hindered angle, there is little chance for electrons to populate in higher excited states since the shrinking of the conical-well angle causes the increasing of energy spacings.

One also notes that the populations of a hindered molecule for $\alpha=60°$ and 120°, shown in Figs. 2(a) and 2(b), are mainly composed of $l=0$, 1 and 2 states, while the population of a free rotor is composed of $l=0$, 2, and 4 states. The underlying physics comes from the reason that $\langle\psi_{l',m'}|\cos^2\theta|\psi_{l,m}\rangle$ is nonzero for all l and l' values in the case of hindered rotation. But it is zero in free rotor limit except for $l=l'$ or $l=l'\pm2$. The dotted lines in the insets represent the first two main contributions of the factors $\Sigma_{l\neq l'}\langle\psi_{l',m'}|\cos^2\theta|\psi_{l,m}\rangle$ summed from low-lying states, i.e., the sum of the largest two values of the off-diagonal term $\langle\psi_{l',m'}|\cos^2\theta|\psi_{l,m}\rangle$. As can be seen, the populations for the small hindered angle are mainly distributed on lower states since the main oscillation feature (e.g., the frequency) of the curve (dotted lines) is quite similar to that from whole contributions (solid lines).

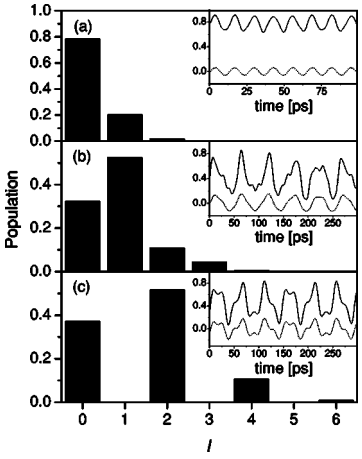

FIG. 2. The populations of the states $(l,m=0)$ for different hindered angles: (a) $\alpha=60°$, (b) $\alpha=120°$, (c) $\alpha=180°$. The insets show the corresponding alignments (solid lines) and the first two main contributions of the factors $\Sigma_{l\neq l'}\langle\psi_{l',m'}|\cos^2\theta|\psi_{l,m}\rangle$ (dotted lines).

Let us now turn our attention to the case of orientation. After applying a short pulse laser, the orientation $\langle\cos\theta\rangle$ of a hindered molecule ($\alpha=60°$) oscillates sinusoidally with time as shown in Fig. 3(a). The value of $\langle\cos\theta\rangle$ is always positive because the rotational wave function is compressed heavily. As the hindered angle α becomes larger, the oscillation fre-

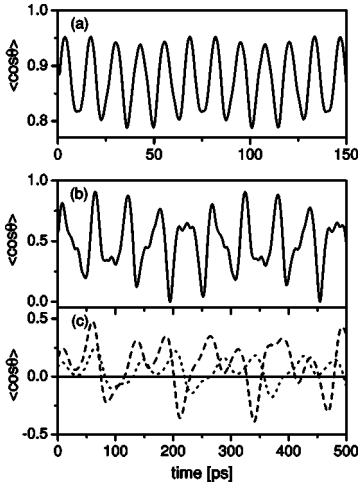

FIG. 3. The orientations $\langle\cos\theta\rangle$ (solid lines) of a hindered molecule confined by an infinite conical-well for different hindered angles: (a) $\alpha=60°$, (b) $\alpha=120°$, and (c) $\alpha=175°$. The dashed and dotted lines in (c) correspond to different potential barrier height, i.e., $V_0=\infty$ and 100, respectively.

quency also decreases as shown in Fig. 3(b). These signatures are quite close to that of the alignment. We then conclude that even at larger hindered angle ($\alpha=120°$) the role of hindered potential still overwhelms the laser pulse, otherwise, the value of $\langle\cos\theta\rangle$ should not always be positive.

Figure 3(c) represents results of orientations in infinite ($V_0=\infty$) or finite ($V_0=100$) conical-well potential for $\alpha=175°$. Dashed and dotted lines correspond to $V_0=\infty$ and 100, respectively. For the case of finite conical-well potential, the wave function is expressed in terms of a series of the basis wave functions obtained in Refs. 13 and 14. As can be seen, the effect of the laser pulse is obvious because a negative value appears. Comparing the results with the free orientation,[7] the angular distributions for the finite well are more isotropic since the wave functions can penetrate into the conical barrier.

Further analysis shows that components of orientation $\langle\cos\theta\rangle$ or alignment $\langle\cos^2\theta\rangle$ can be divided into two parts: diagonal and nondiagonal terms. The nondiagonal term represents the variations of these curves such as those in the insets of Fig. 2. These variations with time are determined by the phase difference coming from various energy levels. To see the contributions from diagonal terms, we evaluate the time-averaged orientation and alignment. In this case, the nondiagonal values will be averaged out, and only contributions from diagonal terms exit. Figure 4 shows the mean orientation and alignment as a function of hindered angle. As α increases, the mean orientation decreases monotonically from 1 to 0. This is because the mean orientation is determined by $|c_{l,m}|^2$ and $\langle\psi_{l,m}|\cos\theta|\psi_{l,m}\rangle$. For a larger angle α, the populations $|c_{l,m}|^2$ is mainly composed of $l=0,2,4$ states. But the value $\langle\psi_{l,m}|\cos\theta|\psi_{l,m}\rangle$ is governed by the selection rule: $l=l'+1$. Thus the net effect is the shrinking of the mean orientation in the large angle limit.

Contrary to orientation, the mean alignment shows a quite different feature. The value of $\langle\cos^2\theta\rangle$ first decreases as α increases. However, it reaches a minimum point about $\alpha=140°$. From the insets of Fig. 4, we know that the values of $(\langle\psi_{l,m}|\cos^2\theta|\psi_{l,m}\rangle)$ do not depend significantly on α. Therefore, the decrease of $\langle\cos^2\theta\rangle$ comes from the decreasing tendency of the population $|c_{l=1,m}|^2$, while its increasing behavior is caused by two other populations $|c_{l=0,m}|^2$ and $|c_{l=2,m}|^2$. Competition between these two effects results in a minimum point.

A few remarks about experimental verifications should be mentioned here. The degree of alignment can be measured

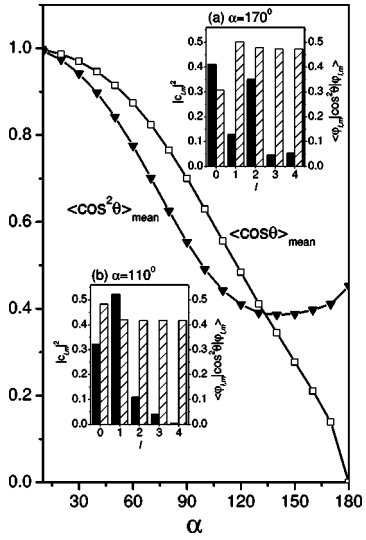

FIG. 4. The mean orientation $\langle\cos\theta\rangle_{\text{mean}}$ and alignment $\langle\cos^2\theta\rangle_{\text{mean}}$ in an infinite conical well. The insets show the populations $|c_{l,m}|^2$ (solid bar) and factors $\langle\psi_{l,m}|\cos^2\theta|\psi_{l,m}\rangle$ (striped bar). Insets (a) and (b) correspond to $\alpha=110°$ and $\alpha=170°$, respectively.

with the techniques of the femtosecond photodissociation spectroscopy and the ion imaging.[8] The alignment is probed by breaking the molecular bond and subsequently measuring the direction of the photofragments by a mass selective position sensitive ion detector. In contrast to alignment, the orientation is probed by Coulomb exploding the molecules with a femtosecond laser pulse.[9] By detecting the fragment ions with the time-of-flight mass spectrometer, a significant asymmetry should be observed in the signal magnitudes of the forward and the backward fragments. Under proper arrangements, orientation and alignment of an absorbed molecule may be examined by these spectroscopic technologies.

In conclusion, we have shown that a short laser pulse can induce alignment and orientation of a hindered molecule. The hindered angle of the hindered potential well plays a key role on the molecular alignment and orientation. Crossover from field-free rotation to a hindered one can be observed by varying the hindered angle of the potential well. Time-averaged alignment and orientation are investigated thoroughly to understand the difference between these two quantities.

This work is supported partially by the National Science Council, Taiwan under Grant No. NSC 92-2120-M-009-010.

*Corresponding author. Email address: dschuu@mail.nctu.edu.tw

[1] Special issue on Stereodynamics of Chemical Reaction [J. Phys. Chem. A **101**, 7461 (1997)].
[2] V. A. Cho and R. B. Bernstein, J. Phys. Chem. **95**, 8129 (1991).
[3] H. Stapelfeldt, H. Sakai, E. Constant, and P. B. Corkum, Phys. Rev. Lett. **79**, 2787 (1997).
[4] T. Seideman, Phys. Rev. A **56**, R17 (1997); R. J. Gordon, L. Zhu, W. A. Schroeder, and T. Seideman, J. Appl. Phys. **94**, 669 (2003).
[5] B. Friedrich and D. Herschbach, Phys. Rev. Lett. **74**, 4623 (1995); L. Cai, J. Marango, and B. Friedrich, Phys. Rev. Lett. **86**, 775 (2001).
[6] J. Ortigoso, M. Rodriguez, M. Gupta, and B. Friedrich, J. Chem. Phys. **110**, 3870 (1999); M. Machholm, *ibid.* **115**, 10724 (2001).
[7] M. Machholm and N. E. Henriksen, Phys. Rev. Lett. **87**, 193001

(2001).
[8] W. Kim and P. M. Felker, J. Chem. Phys. **104**, 1147 (1996); **108**, 6763 (1998); H. Sakai *et al.*, *ibid.* **110**, 10235 (1999); J. J. Larsen *et al.*, *ibid.* **111**, 7774 (1999).
[9] H. Sakai, S. Minemoto, H. Nanjo, H. Tanji, and T. Suzuki, Phys. Rev. Lett. **90**, 083001 (2003); S. Minemoto, H. Nanjo, H. Tanji, T. Suzuki, and H. Sakai, J. Chem. Phys. **118**, 4052 (2003).
[10] V. Renard, M. Renard, S. Guérin, Y. T. Pashayan, B. Lavorel, O. Faucher, and H. R. Jauslin, Phys. Rev. Lett. **90**, 153601 (2003).
[11] I. Beauport, K. Al-Shamery, and H.-J. Freund, Chem. Phys. Lett. **256**, 641 (1996); S. Thiel, M. Pykavy, T. Klüner, H.-J. Freund, R. Kosloff, and V. Staemmler, Phys. Rev. Lett. **87**, 077601 (2001); J. Chem. Phys. **116**, 762 (2002).
[12] J. W. Gadzuk, U. Landman, E. J. Kuster, C. L. Cleveland, and R. N. Barnett, Phys. Rev. Lett. **49**, 426 (1982).
[13] Y. T. Shih, D. S. Chuu, and W. N. Mei, Phys. Rev. B **51**, 14 626 (1995); **54**, 10 938 (1996).
[14] Y. T. Shih, Y. Y. Liao, and D. S. Chuu, Phys. Rev. B **68**, 075402 (2003).
[15] R. P. Pan, R. D. Etters, K. Kobashi, and V. Chandrasekharan, J. Chem. Phys. **77**, 1035 (1982).
[16] J. W. Riehl and C. J. Fisher, J. Chem. Phys. **59**, 4336 (1973).
[17] V. M. Allen and P. D. Pacey, Surf. Sci. **177**, 36 (1986).

Current noise of a quantum dot *p–i–n* junction in a photonic crystal

Y. N. Chen,[1] D. S. Chuu,[1] and T. Brandes[2]
[1]*Department of Electrophysics, National Chiao-Tung University, Hsinchu 300, Taiwan*
[2]*School of Physics and Astronomy, The University of Manchester, P.O. Box 88, Manchester, M60 1QD, United Kingdom*
(Received 18 August 2005; published 26 October 2005)

The shot-noise spectrum of a quantum dot *p–i–n* junction embedded inside a three-dimensional photonic crystal is investigated. Radiative decay properties of quantum dot excitons can be obtained from the observation of the current noise. The characteristic of the photonic band gap is revealed in the current noise with discontinuous behavior. Applications of such a device in entanglement generation and emission of single photons are pointed out, and may be achieved with current technologies.

DOI: 10.1103/PhysRevB.72.153312 PACS number(s): 73.63.−b, 73.50.Td, 71.35.−y, 42.70.Qs

Since Yablonovitch proposed the idea of photonic crystals (PCs),[1] optical properties in periodic dielectric structures have been investigated intensively.[2] Great attention has been focused on these materials not only because of their potential applications in optical devices, but also because of their ability to drastically alter the nature of the propagation of light from a fundamental perspective.[3] Among these, modification of spontaneous emission is of particular interest. Historically, the idea of controlling the spontaneous emission rate was proposed by Purcell,[4] and enhanced and inhibited spontaneous emission rates for atomic systems were intensively investigated in the 1980s (Ref. 5) by using atoms passed through a cavity. In semiconductor systems, the electron-hole pair is naturally a candidate to examine spontaneous emission, where modifications of the spontaneous emission rates of quantum dot (QD) (Ref. 6) or quantum wire (QW) (Ref. 7) excitons inside the microcavities have been observed experimentally.

Recently, the interest in measurements of shot noise in quantum transport has risen owing to the possibility of extracting valuable information not available in conventional dc transport experiments.[8] With the advances of fabrication technologies, it is now possible to embed QDs inside a *p–i–n* structure,[9] such that the electron and hole can be injected separately from opposite sides. This allows one to examine the exciton dynamics in a QD via electrical currents.[10] On the other hand, it is also possible to embed semiconductor QDs in PCs,[11] where modified spontaneous emission of QD excitons is observed over large frequency bandwidths.

In this work, we present nonequilibrium calculations for the quantum noise properties of quantum dot excitons inside photonic crystals. We obtain the current noise of QD excitons via the MacDonald formula,[12] and find that it reveals many of the characteristics of the photonic band gap (PBG). Possible applications of such a device to the generation of entangled states and the emission of single photons are also pointed out.

Model. We assume that a QD *p–i–n* junction is embedded in a three-dimensional PC. A possible structure is shown in Fig. 1. Both the hole and electron reservoirs are assumed to be in thermal equilibrium. For the physical phenomena we are interested in, the Fermi level of the $p(n)$-side hole (electron) is slightly lower (higher) than the hole (electron) subband in the dot. After a hole is injected into the hole subband in the QD, the n-side electron can tunnel into the exciton level because of the Coulomb interaction between the electron and hole. Thus, we may introduce the three dot states: $|0\rangle=|0,h\rangle$, $|\uparrow\rangle=|e,h\rangle$, and $|\downarrow\rangle=|0,0\rangle$, where $|0,h\rangle$ means there is one hole in the QD, $|e,h\rangle$ is the exciton state, and $|0,0\rangle$ represents the ground state with no hole and electron in the QD. One might argue that one cannot neglect the state $|e,0\rangle$ for real devices since the tunable variable is the applied voltage. This can be resolved by fabricating a thicker barrier on the electron side so that there is little chance for an electron to tunnel in advance.[13] Moreover, the charged exciton and biexcitons states are also neglected in our calculations, which means a low injection limit is required.[14]

Derivation of Master equation. We define the dot-operators $\hat{n}_\uparrow\equiv|\uparrow\rangle\langle\uparrow|$, $\hat{n}_\downarrow\equiv|\downarrow\rangle\langle\downarrow|$, $\hat{p}\equiv|\uparrow\rangle\langle\downarrow|$, $\hat{s}_\uparrow\equiv|0\rangle\langle\uparrow|$, $\hat{s}_\downarrow$

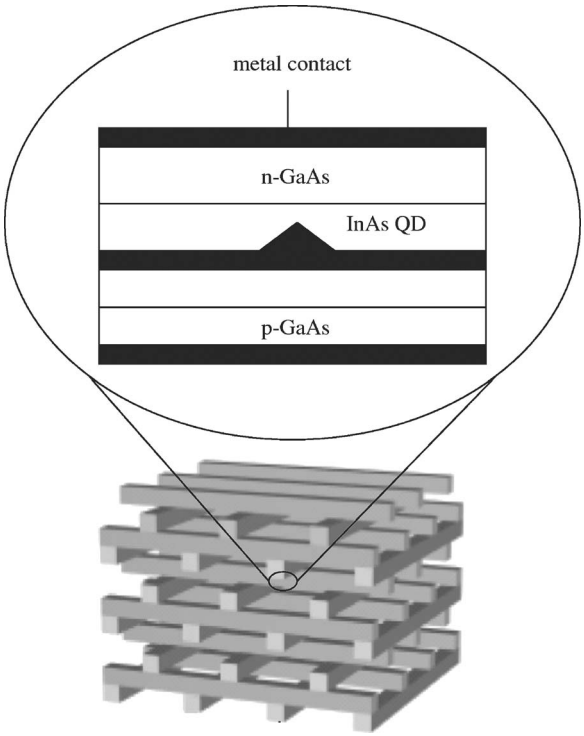

FIG. 1. Illustration of a QD inside a *p–i–n* junction surrounded by a three-dimensional PC.

$\equiv|0\rangle\langle\downarrow|$. The total Hamiltonian H of the system consists of three parts: H_0 [dot, photon bath H_p, and the electron (hole) reservoirs $H_{\rm res}$], H_T (dot-photon coupling), and the dot-reservoir coupling H_V

$$H = H_0 + H_T + H_V,$$

$$H_0 = \varepsilon_\uparrow \widehat{n_\uparrow} + \varepsilon_\downarrow \widehat{n_\downarrow} + H_p + H_{\rm res},$$

$$H_T = \sum_k D_k b_k^\dagger \hat{p} + D_k^* b_k \hat{p}^\dagger = \hat{p}X + \hat{p}^\dagger X^\dagger,$$

$$H_p = \sum_k \omega_k b_k^\dagger b_k$$

$$H_V = \sum_{\mathbf{q}} (V_{\mathbf{q}} c_{\mathbf{q}}^\dagger \widehat{s_\uparrow} + W_{\mathbf{q}} d_{\mathbf{q}}^\dagger \widehat{s_\downarrow} + \text{c.c.}),$$

$$H_{\rm res} = \sum_{\mathbf{q}} \varepsilon_{\mathbf{q}}^\uparrow c_{\mathbf{q}}^\dagger c_{\mathbf{q}} + \sum_{\mathbf{q}} \varepsilon_{\mathbf{q}}^\downarrow d_{\mathbf{q}}^\dagger d_{\mathbf{q}}. \quad (1)$$

In the above equation, $D_k = i\hbar\boldsymbol{\epsilon}\cdot\boldsymbol{\mu}\sqrt{\omega_{\mathbf{k}}/(2\epsilon_0\hbar V)}$ is the dipole coupling strength with $\boldsymbol{\epsilon}$ and $\boldsymbol{\mu}$ being the polarization vector of the photon and the dipole moment of the exciton, respectively. b_k is the photon operator, $X=\Sigma_k D_k b_k^\dagger$, and $c_{\mathbf{q}}$ and $d_{\mathbf{q}}$ denote the electron operators in the left and right reservoirs, respectively.

The couplings to the electron and hole reservoirs are given by the standard tunnel Hamiltonian H_V, where $V_{\mathbf{q}}$ and $W_{\mathbf{q}}$ couple the channels $\mathbf{q}$ of the electron and hole reservoirs. If the couplings to the electron and the hole reservoirs are weak, it is reasonable to assume that the standard Born-Markov approximation with respect to these couplings is valid. In this case, one can derive a master equation from the exact time evolution of the system. The equations of motion can be expressed as (cf. Ref. 15)

$$\frac{\partial}{\partial t}\langle\widehat{n_\uparrow}\rangle_t = -\int dt'[C(t-t') + C^*(t-t')]\langle\widehat{n_\uparrow}\rangle_{t'} + \Gamma_L[1 - \langle\widehat{n_\uparrow}\rangle_t - \langle\widehat{n_\downarrow}\rangle_t], \quad (2)$$

$$\frac{\partial}{\partial t}\langle\widehat{n_\downarrow}\rangle_t = \int dt'[C(t-t') + C^*(t-t')]\langle\widehat{n_\uparrow}\rangle_{t'} - \Gamma_R\langle\widehat{n_\downarrow}\rangle_t,$$

$$\frac{\partial}{\partial t}\langle\hat{p}\rangle_t = -\frac{1}{2}\int dt'[C(t-t') + C^*(t-t')]\langle\hat{p}\rangle_{t'} - \frac{\Gamma_R}{2}\langle\hat{p}\rangle_t,$$

where $\Gamma_L = 2\pi\Sigma_{\mathbf{q}} V_{\mathbf{q}}^2 \delta(\varepsilon_\uparrow - \varepsilon_{\mathbf{q}}^\uparrow)$, $\Gamma_R = 2\pi\Sigma_{\mathbf{q}} W_{\mathbf{q}}^2 \delta(\varepsilon_\downarrow - \varepsilon_{\mathbf{q}}^\downarrow)$, and $\varepsilon = \hbar\omega_0 = \varepsilon_\uparrow - \varepsilon_\downarrow$ is the energy gap of the QD exciton. Here, $C(t-t') \equiv \langle X_t X_{t'}^\dagger\rangle_0$ is the photon correlation function, and depends on the time interval only. We can now define the Laplace transformation for real z

$$C_\varepsilon(z) \equiv \int_0^\infty dt e^{-zt} e^{i\varepsilon t} C(t)$$

$$n_\uparrow(z) \equiv \int_0^\infty dt e^{-zt}\langle\widehat{n_\uparrow}\rangle_t \quad \text{etc.}, \quad z > 0 \quad (3)$$

and transform the whole equations of motion into z space

$$n_\uparrow(z) = -[C_\varepsilon(z) + C_\varepsilon^*(z)]n_\uparrow(z)/z + \frac{\Gamma_L}{z}[1/z - n_\uparrow(z) - n_\downarrow(z)],$$

$$n_\downarrow(z) = [C_\varepsilon(z) + C_\varepsilon^*(z)]n_\downarrow(z)/z - \frac{\Gamma_R}{z} n_\downarrow(z),$$

$$p(z) = -\frac{1}{2}[C_\varepsilon(z) + C_\varepsilon^*(z)]p(z)/z - \frac{\Gamma_R}{2z} p(z). \quad (4)$$

These equations can then be solved algebraically, and the tunnel current from the hole- or electron-side barrier

$$\widehat{I_R} = -e\Gamma_R\langle\widehat{n_\downarrow}\rangle_t, \quad \widehat{I_L} = -e\Gamma_L[1 - \langle\widehat{n_\uparrow}\rangle_t - \langle\widehat{n_\downarrow}\rangle_t] \quad (5)$$

can in principle be obtained by performing the inverse Laplace transformation on Eqs. (4). Depending on the complexity of the correlation function $C(t-t')$ in the time domain, this can be a formidable task which can however be avoided if one directly seeks the quantum noise:

Shot noise spectrum. In a quantum conductor in nonequilibrium, electronic current noise originates from the dynamical fluctuations of the current around its average. To study correlations between carriers, we relate the exciton dynamics with the hole reservoir operators by introducing the degree of freedom n as the number of holes that have tunneled through the hole-side barrier[16] and write

$$\dot{n}_0^{(n)}(t) = -\Gamma_L n_0^{(n)}(t) + \Gamma_R n_\downarrow^{(n-1)}(t),$$

$$\dot{n}_\uparrow^{(n)}(t) + \dot{n}_\downarrow^{(n)}(t) = (\Gamma_L - \Gamma_R) n_0^{(n)}(t). \quad (6)$$

Equations (6) allow us to calculate the particle current and the noise spectrum from $P_n(t) = n_0^{(n)}(t) + n_\uparrow^{(n)}(t) + n_\downarrow^{(n)}(t)$ which gives the total probability of finding n electrons in the collector by time t. In particular, the noise spectrum S_{I_R} can be calculated via the MacDonald formula[12,17]

$$S_{I_R}(\omega) = 2\omega e^2 \int_0^\infty dt \sin(\omega t)\frac{d}{dt}[\langle n^2(t)\rangle - (t\langle I\rangle)^2], \quad (7)$$

where $(d/dt)\langle n^2(t)\rangle = \Sigma_n n^2 \dot{P}_n(t)$. Solving Eqs. (4) and (6), we obtain

$$S_{I_R}(\omega) = 2eI\{1 + \Gamma_R[\hat{n}_\downarrow(z = -i\omega) + \hat{n}_\downarrow(z = i\omega)]\}. \quad (8)$$

In the zero-frequency limit, Eq. (6) reduces to

$$S_{I_R}(\omega = 0) = 2eI\left\{1 + 2\Gamma_R \frac{d}{dz}[z\hat{n}_\downarrow(z)]_{z=0}\right\}. \quad (9)$$

As can be seen, there is no need to evaluate the correlation function $C(t-t')$ in the time domain such that all one has to do is to solve Eq. (4) in z space.

Results and discussions. The above derivation shows that the noise spectrum of the QD excitons depends strongly on

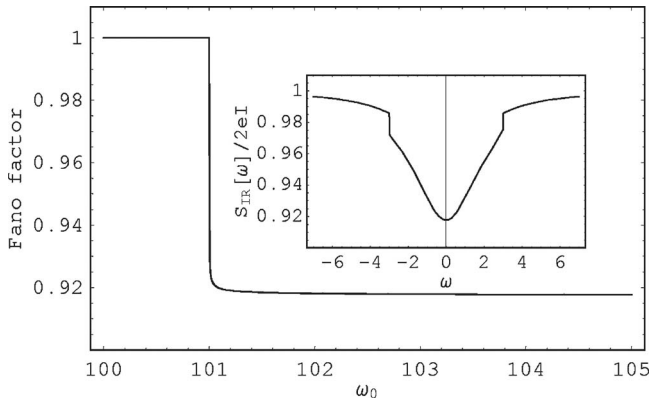

FIG. 2. Current noise (Fano factor) of QD excitons in a one-band PC as a function of the exciton band gap ω_0. The PBG frequency ω_c is set equal to 101β. The inset shows frequency-dependent noise, in which ω_0 is fixed to 104β.

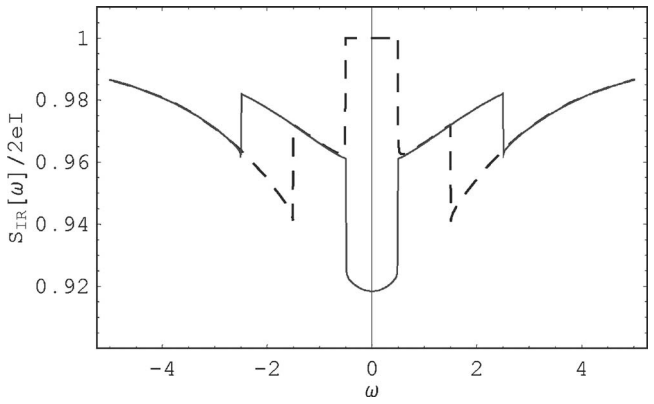

FIG. 3. Shot-noise spectrum of QD excitons in a two-band PC with ω_{c_1} and ω_{c_2} set equal to 101β and 99β, respectively. To demonstrate the ability of extracting information from the PC, the exciton band gap ω_0 in gray and dashed curves is chosen as above ω_{c_2} ($\omega_0=101.5\beta$) and between the two band edge frequencies ($\omega_0=100.5\beta$), respectively.

$C_\varepsilon(z)$. Let us now turn our attention to the spontaneous emission of a QD exciton in a three-dimensional PC, where the vacuum dispersion relation is strongly modified: An anisotropic band-gap structure is formed on the surface of the first Brillouin zone in the reciprocal lattice space. In general, the band edge is associated with a finite collection of symmetrically placed points $\mathbf{k}_0^i$ leading to a three-dimensional band structure.[3] In our study, the transition energy of the QD exciton is assumed to be near the band edge ω_c. The dispersion relation for those wave vectors $\mathbf{k}$ whose directions are near one of the $\mathbf{k}_0^i$ can be expressed approximately by $\omega_\mathbf{k}=\omega_c+A|\mathbf{k}-\mathbf{k}_0^i|^2$, where A is a model dependent constant.[18] Thus, the correlation function $C_\varepsilon(z)=\Sigma_\mathbf{k}|gD_k|^2/[z+i(\omega_\mathbf{k}-\omega_0)]$ can be calculated around the directions of each $\mathbf{k}_0^i$ separately, and is given by

$$C_\varepsilon(z)=\frac{-i\omega_0^2\beta^{3/2}}{\sqrt{\omega_c}+\sqrt{-iz-(\omega_0-\omega_c)}}, \tag{10}$$

with $\beta^{3/2}=d^2\Sigma_i\sin^2\theta_i/8\pi\epsilon_0\hbar A^{3/2}$.[19] Here, $\hbar\omega_0$ is the transition energy of the QD exciton, d is the magnitude of the dipole moment, and θ_i is the angle between the dipole vector of the exciton and the ith $\mathbf{k}_0^i$.

The shot-noise spectrum of QD excitons inside a PC is displayed in Fig. 2, where the tunneling rates Γ_L and Γ_R are assumed to be equal to 0.1β and β, respectively. We see that the Fano factor $[F\equiv S_{I_R}(\omega=0)/2e\langle I\rangle]$ displays a discontinuity as the exciton transition frequency is tuned across the PBG frequency ($\omega_c=101\beta$). It also reflects the fact that below the band edge frequency ω_c, spontaneous emission of the QD exciton is inhibited. To observe this experimentally, a dc electric field (or magnetic field) could be applied in order to vary the band-gap energy of the QD exciton. Another way to examine the PBG frequency is to measure the frequency-dependent noise as shown in the inset of Fig. 2, where the exciton band gap is set equal to 104β. As can be seen, discontinuities also appear as ω is equal to the *detuned* frequency between PBG and QD exciton.

When the atomic resonant transition frequency is very close to the edge of the band and the band gap is relatively large, the above one-band model is a good approximation. If the band gap is narrow, one must consider both upper and lower bands. For a three-dimensional anisotropic PC with point-group symmetry, the dispersion relation near two band edges can be approximated as

$$\omega_k=\begin{cases}\omega_{c_1}+C_1|\mathbf{k}-\mathbf{k}_{10}^i| & (\omega_k>\omega_{c_1}),\\ \omega_{c_2}-C_2|\mathbf{k}-\mathbf{k}_{20}^j| & (\omega_k>\omega_{c_1}).\end{cases} \tag{11}$$

Here, $\mathbf{k}_{10}^i$ and $\mathbf{k}_{20}^j$ are two finite collections of symmetry related points, which are associated with the upper and lower band edges,[20] and C_1 and C_2 are model-dependent constants. Following the derivation for the one-band PC, the correlation function can now be written as

$$C_\varepsilon(z)=\sum_{n=1}^{2}\frac{(-1)^n i\omega_0^2\beta_n^{3/2}}{\sqrt{\omega_{c_n}}+\sqrt{(-1)^n[iz+(\omega_0-\omega_{c_n})]}}, \tag{12}$$

where $\beta_n^{3/2}=d^2\Sigma_i\sin^2\theta_i^{(n)}/8\pi\epsilon_0\hbar C_n^{3/2}$ with the corresponding collections of angles $\theta_i^{(n)}$, $n=1, 2$.

Figure 3 illustrates the frequency-dependent noise of QD excitons embedded inside a two-band PC. The two-band edge frequencies ω_{c_1} and ω_{c_2} are set equal to 101β and 99β, respectively. There are three regimes for the choices of the exciton band gap: $\omega_0>\omega_{c_1}$, $\omega_0<\omega_{c_2}$, and $\omega_{c_1}>\omega_0>\omega_{c_2}$. When ω_0 is tuned above the upper band-edge ω_{c_1} (or below the lower band-edge ω_{c_2}), the QD exciton is allowed to decay, such that the shot noise spectrum (gray curve) is suppressed in the range of $|\omega|<|\omega_0-\omega_{c_1}|$. On the other hand, however, if ω_0 is between the two band edges, spontaneous emission is inhibited. As shown by the dashed curve, the current noise in the central region is increased with its value equal to unity. Similar to the one-band PC, the curves of the shot noise spectrum reveal two discontinuities at $|\omega|=|\omega_0-\omega_{c_1}|$ or $|\omega_0-\omega_{c_2}|$, demonstrating the possibility to extract information from a PC by the current noise.

A few remarks about the application of the QDs inside a PC should be mentioned here. As is known, controlling the

propagation of light (waveguide) is one of the optoelectronic applications of PCs.[21] By controlling the exciton band-gap ω_0 across the PBG frequency with appropriate tunneling rates of the electron and hole, one may achieve the emission of a single photon at predetermined times and directions (waveguides),[22] which are important for the field of quantum information technology. Furthermore, it has been demonstrated recently that a precise spatial and spectral overlap between a single self-assembled quantum dot and a photonic crystal membrane nanocavity can be implemented by a deterministic approach.[23] One of the immediate applications is the coupling of two QDs to a single common cavity mode.[24] Therefore, if two QD *p–i–n* junctions can also be incorporated inside a PC (and on the way of light propagation), the cavitylike effect may be used to create an entangled state between two QD excitons with remote separation.[13] The obvious advantages then would be a suppression of decoherence of the entangled state by the PBG, and the observation of the enhanced shot noise could serve in order to identify the entangled state.[10]

In summary, we have derived the nonequilibrium current noise of QD excitons incorporated in a *p–i–n* junction surrounded by a one-band or two-band PC. We found that characteristic features of the PBG can be obtained from the shot noise spectrum. Generalizations to other types of PCs are expected to be relatively straightforward, which makes QD *p–i–n* junctions good detectors of quantum noise.[25]

This work is supported partially by the National Science Council of Taiwan under Grant Nos. NSC 94-2112-M-009-019 and NSC 94-2120-M-009-002.

[1] E. Yablonovitch, Phys. Rev. Lett. **58**, 2059 (1987).
[2] S. Sakoda, *Optical Properties of Photonic Crystals* (Springer, New York, 2001).
[3] S. John, Phys. Rev. Lett. **58**, 2486 (1987).
[4] E. M. Purcell, Phys. Rev. **69**, 681 (1946).
[5] P. Goy, J. M. Raimond, M. Gross, and S. Haroche, Phys. Rev. Lett. **50**, 1903 (1983); G. Gabrielse and H. Dehmelt, *ibid.* **55**, 67 (1985); R. G. Hulet, E. S. Hilfer, and D. Kleppner, *ibid.* **55**, 2137 (1985); D. J. Heinzen, J. J. Childs, J. E. Thomas, and M. S. Feld, *ibid.* **58**, 1320 (1987).
[6] M. Bayer, F. Weidner, A. Larionov, A. McDonald, A. Forchel, and T. L. Reinecke, Phys. Rev. Lett. **86**, 3168 (2001); G. S. Solomon, M. Pelton, and Y. Yamamoto, *ibid.* **86**, 3903 (2001).
[7] C. Constantin, E. Martinet, D. Y. Oberli, E. Kapon, B. Gayral, and J. M. Gerard, Phys. Rev. B **66**, 165306 (2002).
[8] C. W. J. Beenakker, Rev. Mod. Phys. **69**, 731 (1997); Y. M. Blanter and M. Buttiker, Phys. Rep. **336**, 1 (2000).
[9] G. Kießlich, A. Wacker, E. Schöll, S. A. Vitusevich, A. E. Belyaev, S. V. Danylyuk, A. Förster, N. Klein, and M. Henini, Phys. Rev. B **68**, 125331 (2003).
[10] Y. N. Chen, T. Brandes, C. M. Li, and D. S. Chuu, Phys. Rev. B **69**, 245323 (2004).
[11] P. Lodahl, A. Floris van Driel, Ivan S. Nikolaev, Arie Irman, Karin Overgaag, Daniël Vanmaekelbergh, and Willem L. Vos, Nature (London) **430**, 654 (2004); T. Yoshie, A. Scherer, J. Hendrickson, G. Khitrova, H. M. Gibbs, G. Rupper, C. Ell, O. B. Shchekin, and D. G. Deppe, *ibid.* **432**, 200 (2004).
[12] D. K. C. MacDonald, Rep. Prog. Phys. **12**, 56 (1948).
[13] Y. N. Chen, D. S. Chuu, and T. Brandes, Phys. Rev. Lett. **90**, 166802 (2003).
[14] Z. Yuan, B. E. Kardynal, R. M. Stevenson, A. J. Shields, C. J. Lobo, K. Cooper, N. S. Beattie, D. A. Ritchie, and M. Pepper, Science **295**, 102 (2002).
[15] T. Brandes and B. Kramer, Phys. Rev. Lett. **83**, 3021 (1999); Y. N. Chen and D. S. Chuu, Phys. Rev. B **66**, 165316 (2002).
[16] Actually, the total current noise should be expressed in terms of the spectra of particle currents and the charge noise spectrum: $S_I(\omega)=aS_{I_L}(\omega)+bS_{I_R}(\omega)-ab\omega^2 S_Q(\omega)$, where a and b are capacitance coefficient $(a+b=1)$ of the junctions. Since we have assumed a highly asymmetric setup $(a \ll b)$, it is plausible to consider the hole-side spectra $S_{I_R}(\omega)$ only.
[17] R. Aguado and T. Brandes, Phys. Rev. Lett. **92**, 206601 (2004).
[18] In fact, A is dependent on the structures of the photonic crystals. For a simple three-dimensional periodic dielectric, A can be approximated as $A \simeq \omega_c/(\mathbf{k}_0^i)^2$, where $\mathbf{k}_0^i=\pi/L$ with L being the lattice constant of the photonic crystal (Ref. 18). In order not to lose the generality, we let A being a constant, such that β becomes the unit for the numerical calculations.
[19] S. John and T. Quang, Phys. Rev. A **50**, 1764 (1994); S. Y. Zhu, Y. Yang, H. Chen, H. Zheng, and M. S. Zubairy, Phys. Rev. Lett. **84**, 2136 (2000); N. Vats, S. John, and K. Busch, Phys. Rev. A **65**, 043808 (2002).
[20] Y. Yang, M. Fleischhauer, and S. Y. Zhu, Phys. Rev. A **68**, 043805 (2003).
[21] E. Chow, S. Y. Lin, S. G. Johnson, P. R. Villeneuve, J. D. Joannopoulos, J. R. Wendt, G. A. Vawter, W. Zubrzycki, H. Hou, and A. Alleman, Nature (London) **407**, 983 (2000).
[22] E. Lidorikis, M. L. Povinelli, S. G. Johnson, and J. D. Joannopoulos, Phys. Rev. Lett. **91**, 023902 (2003).
[23] A. Badolato, K. Hennessy, M. Atatüre, J. Dreiser, E. Hu, P. M. Petroff, and A. Imamoglu, Science **308**, 1158 (2005).
[24] A. Imamoglu, D. D. Awschalom, G. Burkard, D. P. DiVincenzo, D. Loss, M. Sherwin, and A. Small, Phys. Rev. Lett. **83**, 4204 (1999).
[25] R. Aguado and L. P. Kouwenhoven, Phys. Rev. Lett. **84**, 1986 (2000).

Shot noise of quantum ring excitons in a planar microcavity

Y. N. Chen, D. S. Chuu, and S. J. Cheng
Department of Electrophysics, National Chiao-Tung University, Hsinchu 300, Taiwan
(Received 25 July 2005; revised manuscript received 5 September 2005; published 1 December 2005)

Shot noise of quantum ring (QR) excitons in a p-i-n junction surrounded by a microcavity is investigated theoretically. Some radiative decay properties of a QR exciton in a microcavity can be obtained from the observation of the current noise, which also gives extra information about one of the tunnel barriers. A different noise feature between the quantum dot (QD) and QR is pointed out, and may be observed in a suitably designed experiment.

DOI: 10.1103/PhysRevB.72.233301 PACS number(s): 71.35.−y, 73.63.−b, 73.50.Td, 42.50.Pq

Since Purcell proposed the idea of controlling the spontaneous emission rate by using a cavity,[1] the enhanced and inhibited SE rate for the atomic system was intensively investigated in the 1980s[2] by using atoms passed through a cavity. In semiconductor systems, the electron-hole pair is naturally a candidate to examine the spontaneous emission. Modifications of the SE rates of the quantum dot (QD),[3] quantum wire,[4] or quantum well[5] excitons inside the microcavities have been observed experimentally.

Interest in measurements of shot noise spectrum has risen owing to the possibility of extracting valuable information not available in conventional dc transport experiments.[6] With the advances of fabrication technologies, it is now possible to embed the QDs inside a p-i-n structure[7] such that the electron and hole can be injected separately from opposite sides. This allows one to examine the exciton dynamics in a QD via electrical currents.[8] On the other hand, it is now possible to fabricate the ring-shaped dots of InAs in GaAs with a circumference of several hundred nanometers.[9] Optical detection of the Aharonov-Bohm effect on an exciton in a single quantum ring (QR) was also reported.[10]

Based on the rapid progress of nanotechnologies, it is not hard to imagine that the QR can be incorporated in a p-i-n junction surrounded by the microcavity. Examinations of the dynamics of the QR excitons by the electrical currents can be realized. We thus present in this work the nonequilibrium calculations of such a device. Current noise of QR excitons in a planar microcavity is obtained via the MacDonald formula[11] and is found to reveal some characteristics of the restricted environment, i.e., the density of states of the confined photons.

The model. Consider now a QR embedded in a p-i-n junction as shown in Fig. 1. Both the hole and electron reservoirs are assumed to be in thermal equilibrium. For the physical phenomena we are interested in, the Fermi level of the $p(n)$-side hole (electron) is slightly lower (higher) than the hole (electron) subband in the dot. After a hole is injected into the hole subband in the QR, the n-side electron can tunnel into the exciton level because of the Coulomb interaction between the electron and hole. Thus, we may introduce the three ring states; $|0\rangle=|0,h\rangle$, $|\uparrow\rangle=|e,h\rangle$, and $|\downarrow\rangle=|0,0\rangle$, where $|0,h\rangle$ means there is one hole in the QR, $|e,h\rangle$ is the exciton state, and $|0,0\rangle$ represents the ground state with no hole and electron in the QR. One might argue that one cannot neglect the state $|e,0\rangle$ for real device since the tunable variable is the applied voltage. This can be resolved by fabricating a thicker barrier on the electron side so that there is little chance for an electron to tunnel in advance. Moreover, the charged exciton and biexcitons states are also neglected in our calculations. This means a low injection limit is required in the experiment.[7]

Derivation of a master equation. We can now define the ring-operators $\hat{n}_\uparrow \equiv |\uparrow\rangle\langle\uparrow|$, $\hat{n}_\downarrow \equiv |\downarrow\rangle\langle\downarrow|$, $\hat{p} \equiv |\uparrow\rangle\langle\downarrow|$, $\hat{s}_\uparrow \equiv |0\rangle\langle\uparrow|$, $\hat{s}_\downarrow \equiv |0\rangle\langle\downarrow|$. The total Hamiltonian H of the system consists of three parts; H_0 [ring, photon bath H_p, and the electron (hole) reservoirs H_{res}], H_T (ring-photon coupling), and the ring-reservoir coupling H_V

$$H = H_0 + H_T + H_V,$$

$$H_0 = \varepsilon_\uparrow \hat{n}_\uparrow + \varepsilon_\downarrow \hat{n}_\downarrow + H_p + H_{res},$$

$$H_T = \sum_k (D_k b_k^\dagger \hat{p} + D_k^* b_k \hat{p}^\dagger) = \hat{p} X + \hat{p}^\dagger X^\dagger,$$

$$H_p = \sum_k \omega_k b_k^\dagger b_k,$$

$$H_V = \sum_{\mathbf{q}} (V_{\mathbf{q}} c_{\mathbf{q}}^\dagger \hat{s}_\uparrow + W_{\mathbf{q}} d_{\mathbf{q}}^\dagger \hat{s}_\downarrow + \text{c.c.}),$$

$$H_{res} = \sum_{\mathbf{q}} \varepsilon_{\mathbf{q}}^\uparrow c_{\mathbf{q}}^\dagger c_{\mathbf{q}} + \sum_{\mathbf{q}} \varepsilon_{\mathbf{q}}^\downarrow d_{\mathbf{q}}^\dagger d_{\mathbf{q}}. \quad (1)$$

In the above equation, b_k is the photon operator, D_k is the dipole coupling strength, $X=\Sigma_k D_k b_k^\dagger$, and $c_{\mathbf{q}}$ and $d_{\mathbf{q}}$ denote the electron operators in the left and right reservoirs, respectively. The couplings to the electron and hole reservoirs are given by the standard tunnel Hamiltonian H_V, where $V_{\mathbf{q}}$ and $W_{\mathbf{q}}$ couple the channels $\mathbf{q}$ of the electron and the hole reservoirs. If the couplings to the electron and the hole reservoirs are weak, then it is reasonable to assume that the standard Born-Markov approximation with respect to these couplings is valid. In this case, one can derive a master equation from the exact time evolution of the system. The equations of motion can be expressed as (cf. Ref. 12)

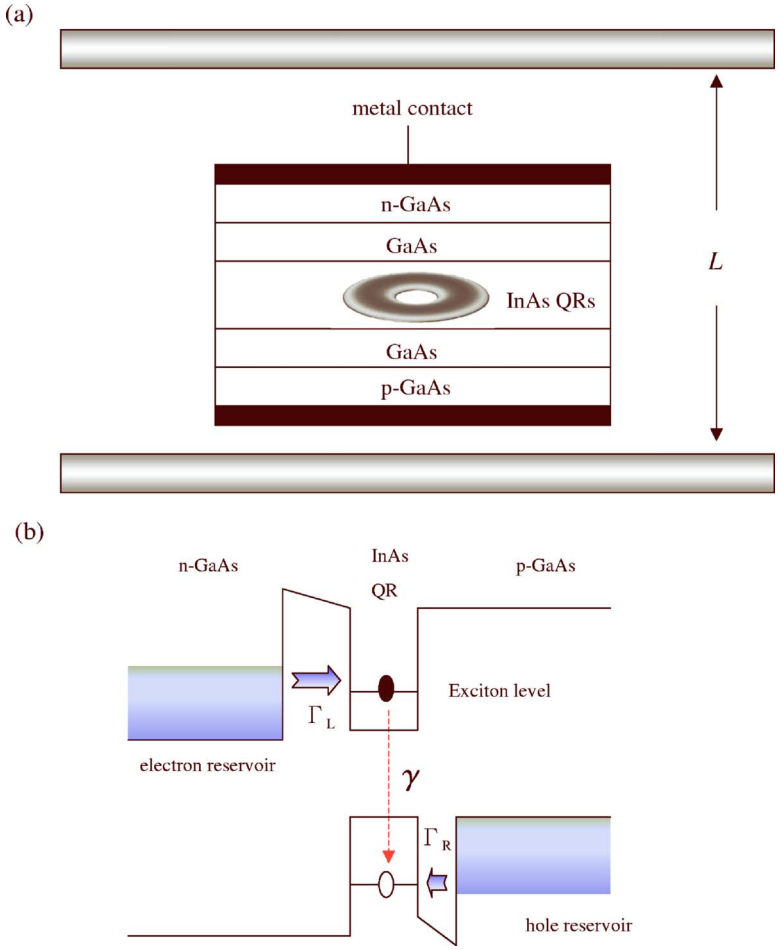

FIG. 1. (Color online) (a) Schematic description of a QR inside a p-i-n junction surrounded by a planar microcavity with length L. (b) Energy-band diagram of a QR in the p-i-n junction.

$$\frac{\partial}{\partial t}\langle \hat{n}_\uparrow\rangle_t = -\int dt'[C(t-t') + C^*(t-t')]\langle \hat{n}_\uparrow\rangle_{t'} + \Gamma_L[1 - \langle \hat{n}_\uparrow\rangle_t - \langle \hat{n}_\downarrow\rangle_t],$$

$$\frac{\partial}{\partial t}\langle \hat{n}_\downarrow\rangle_t = \int dt'[C(t-t') + C^*(t-t')]\langle \hat{n}_\uparrow\rangle_{t'} - \Gamma_R\langle \hat{n}_\downarrow\rangle_t],$$

$$\frac{\partial}{\partial t}\langle \hat{p}\rangle_t = -\frac{1}{2}\int dt'[C(t-t') + C^*(t-t')]\langle \hat{p}\rangle_{t'} - \frac{\Gamma_R}{2}\langle \hat{p}\rangle_t, \tag{2}$$

where $\Gamma_L = 2\pi\Sigma_{\mathbf{q}} V_{\mathbf{q}}^2 \delta(\varepsilon_\uparrow - \varepsilon_{\mathbf{q}}^\uparrow)$, $\Gamma_R = 2\pi\Sigma_{\mathbf{q}} W_{\mathbf{q}}^2 \delta(\varepsilon_\downarrow - \varepsilon_{\mathbf{q}}^\downarrow)$, and $\varepsilon = \varepsilon_\uparrow - \varepsilon_\downarrow$ is the energy gap of the QR exciton. Here, $C(t-t') \equiv \langle X_t X_{t'}^\dagger\rangle_0$ is the photon correlation function, and depends on the time interval only. We can now define the Laplace transformation for real z,

$$C_\varepsilon(z) \equiv \int_0^\infty dt e^{-zt} e^{i\varepsilon t} C(t),$$

$$n_\uparrow(z) \equiv \int_0^\infty dt e^{-zt}\langle \hat{n}_\uparrow\rangle_t \text{ etc.}, \quad z > 0, \tag{3}$$

and transform the whole equations of motion into z space,

$$n_\uparrow(z) = -[C_\varepsilon(z) + C_\varepsilon^*(z)]n_\uparrow(z)/z + \frac{\Gamma_L}{z}[1/z - n_\uparrow(z) - n_\downarrow(z)],$$

$$n_\downarrow(z) = [C_\varepsilon(z) + C_\varepsilon^*(z)]n_\downarrow(z)/z - \frac{\Gamma_R}{z}n_\downarrow(z),$$

$$p(z) = -\frac{1}{2}[C_\varepsilon(z) + C_\varepsilon^*(z)]p(z)/z - \frac{\Gamma_R}{2z}p(z). \tag{4}$$

These equations can then be solved algebraically, and the tunnel current from the hole- or electron-side barrier

$$\hat{I}_R = -e\Gamma_R\langle \hat{n}_\downarrow\rangle_t, \quad \hat{I}_L = -e\Gamma_L[1 - \langle \hat{n}_\uparrow\rangle_t - \langle \hat{n}_\downarrow\rangle_t] \tag{5}$$

can then be obtained by performing the inverse Laplace transformation on Eqs. (4).

Shot noise spectrum. In a quantum conductor in nonequilibrium, electronic current noise originates from the dynamical fluctuations of the current being away from its average. To study correlations between carriers, we relate the exciton dynamics with the hole reservoir operators by introducing the degree of freedom n as the number of holes that have tunneled through the hole-side barrier[13] and write

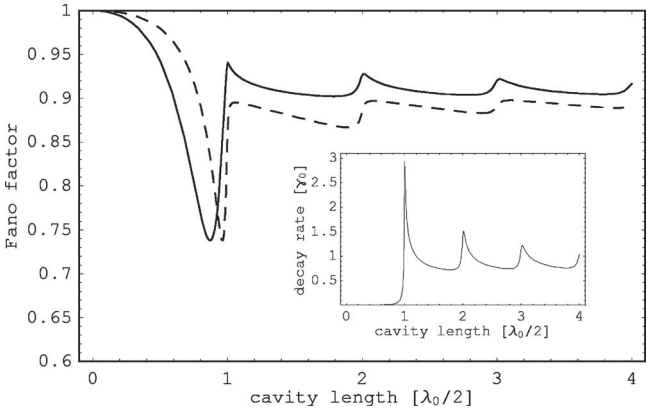

FIG. 2. Fano factor as a function of cavity length L. The vertical and horizontal units are $[S_{I_R}(0)]/(2eI)$ and $\lambda_0/2$, respectively. The inset shows the radiative decay rate of a QR exciton in a planar microcavity.

$$\dot{n}_0^{(n)}(t) = -\Gamma_L n_0^{(n)}(t) + \Gamma_R n_\downarrow^{(n-1)}(t),$$

$$\dot{n}_\uparrow^{(n)}(t) + \dot{n}_\downarrow^{(n)}(t) = (\Gamma_L - \Gamma_R) n_0^{(n)}(t). \tag{6}$$

Equation (6) allows us to calculate the particle current and the noise spectrum from $P_n(t) = n_0^{(n)}(t) + n_\uparrow^{(n)}(t) + n_\downarrow^{(n)}(t)$ which gives the total probability of finding n electrons in the collector by time t. In particular, the noise spectrum S_{I_R} can be calculated via the MacDonald formula.[14] In the zero-frequency limit, the Fano factor can be written as

$$F \equiv \frac{S_{I_R}(\omega = 0)}{2e\langle I \rangle} = 1 - \left. \frac{A(z)\Gamma_L\Gamma_R[A(z) + 2(\Gamma_L + \Gamma_R)]}{\{A(z)\Gamma_R + \Gamma_L[A(z) + 2\Gamma_R]\}^2} \right|_{z=0}, \tag{7}$$

where $A(z) \equiv C_\varepsilon(z) + C_\varepsilon^*(z)$.

Results and Discussions. From Eq. (7), one knows that the noise spectrum of the QR excitons depends strongly on $C_\varepsilon(z)$, which reduces to the radiative decay rate γ in the Markovian limit. The exciton decay rate γ in a microcavity can be obtained easily from the perturbation theory and is given by

$$\gamma = \frac{e^2\hbar}{m^2 c}\frac{\rho}{d}\int |H_0^{(1)} \times (q'\rho)|^2 q' \left(\sum_{k_z'} \frac{\delta(\varepsilon - c\sqrt{q'^2 + k_z'^2})}{\sqrt{k_z'^2 + q'^2}} |\epsilon_{\mathbf{q}'k_z'\lambda} \cdot \chi|^2 \right) dq', \tag{8}$$

where ρ is the ring radius, d is the lattice spacing, $H_0^{(1)}$ is the Hankel function, $\epsilon_{\mathbf{q}'k_z'}$ is the polarization of the photon, and χ is the dipole moment of the QR exciton.[15] The summation of the integer modes in the k_z' direction is determined from the boundary conditions of the planar microcavity.

The radiative decay rate γ of a QR exciton inside a planar microcavity is numerically displayed in the inset of Fig. 2. The tunneling rates, Γ_L and Γ_R, are assumed to be equal to $0.1\gamma_0$ and γ_0, where γ_0 ($\sim 1/1$ ns) is the decay rate of a QR exciton in free space. Also, the planar microcavity is assumed to have a Lorentzian broadening at each resonant mode (with broadening width equal to 1% of each resonant mode).[16] As the cavity length is shorter than one half the wavelength of the emitted photon ($L < \lambda_0/2$), the decay rate is inhibited because of the cut-off frequency of the cavity. When the cavity length exceeds some multiple wavelength, it opens up another decay channel for the quantum ring exciton and turns out that there is an abrupt enhancement on the decay rate. Such a singular behavior also happens in the decay of one dimensional quantum wire polaritons inside a microcavity.[16] This is because the ring geometry preserves the angular momentum of the exciton, rendering the formation of exciton-polariton in the direction of circumference. This kind of behavior can also be found in the calculations of a Fano factor as demonstrated by the solid line in Fig. 2. Comparing to the zero-frequency noise of the QD excitons (dashed line), the Fano factor of the QR excitons shows the "cusp" feature at each resonant mode.

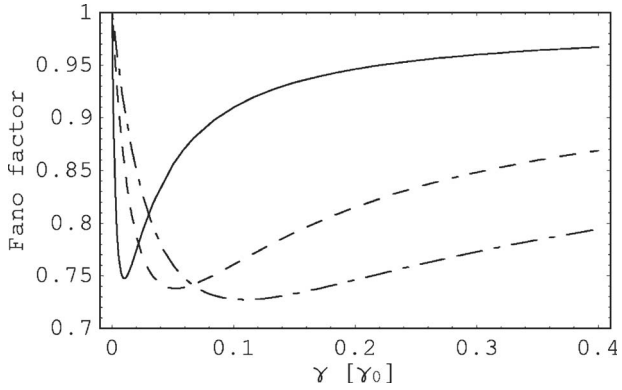

FIG. 3. Fano factor as a function of the decay rate for different electron-side tunneling rate $\Gamma_L = 0.01\gamma_0$ (solid line), $0.05\gamma_0$ (dashed line), and $0.1\gamma_0$ (dashed-dotted line). The hole-side tunneling rate is fixed ($\Gamma_R = \gamma_0$).

Another interesting point is that below the lowest resonant mode ($L = \lambda_0/2$), both the solid and dashed curves have a dip in the Fano factor. It is not seen from the radiative decay rate. To answer this, we have plotted Eq. (7) in Fig. 3 as a function of the decay rate γ. Keeping Γ_R unchanged, the solid, dashed, and dashed-dotted lines correspond to the electron-side tunneling rate $\Gamma_L = 0.01\gamma_0$, $0.5\gamma_0$, and $0.1\gamma_0$, respectively. As can be seen, the Fano factor has a minimum point at $\gamma = \Gamma_L\Gamma_R(\Gamma_L + \Gamma_R)/(\Gamma_L^2 + \Gamma_R^2)$. Comparing this with the inset of Fig. 2, one immediately knows that when the cavity length is increased to $\lambda_0/2$, the abruptly increased decay rate will cross the minimum point and result in a dip in Fig. 2. Furthermore, in the limit of $\Gamma_R \gg \Gamma_L$, the minimum point can be approximated as $\gamma \approx \Gamma_L$. This means by observing the dip in the Fano factor of Fig. 2, the magnitude of the electron-side tunneling rate Γ_L can be obtained.

To further understand the difference between the QD and QR excitons, Fig. 4 illustrates the shot noise as a function of energy gap ε. In plotting the figure, a perfect planar microcavity is assumed for convenience. As can be seen, the shot noise of the QD excitons shows the plateau feature (solid line) with the increasing of ε, while it is a zigzag behavior

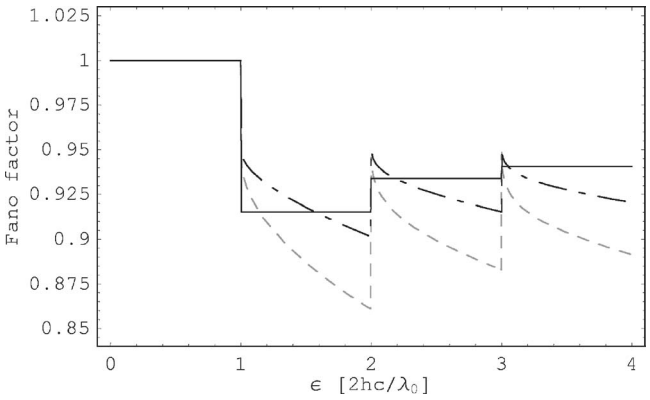

FIG. 4. Fano factor of QD (solid line) and QR (gray dashed line) excitons as a function of energy gap ε. The vertical and horizontal units are $[S_{I_R}(0)]/(2eI)$ and $2hc/\lambda_0$, respectively. The dashed-dotted line represents that if the free-space decay rate of the QR exciton is enhaced by a factor of $2(\gamma_0 \rightarrow 2\gamma_0)$, the shot noise is also enhanced.

(gray-dashed and dashed-dotted lines) for the QR excitons. This is because the decay rate of the QD exciton in a microcavity is given by[16]

$$\gamma_{dot} \propto \sum_{n_c} \frac{e^2\hbar}{m^2c^2L}\theta[(\varepsilon/\hbar c)^2 - (\pi n_c/L)^2]|\epsilon_{\mathbf{q}'k_z'\lambda} \cdot \chi|^2, \quad (9)$$

where θ is the step function, and the summation is over the positive integers. Therefore, when the energy gap ε is tuned above some resonant mode of the cavity, the decay rate is a constant before the next decay channel is opened. On the other hand, however, one knows that the decay rate for the QR exciton is not a constant between two resonant modes. This explains why the decay property for QR exciton is different from that for the QD exciton under the same photonic environment, and the difference may be distinguished by the shot noise measurements. From the experimental point of view, different dependences on ε are easier to be realized since it is almost impossible to vary the cavity length once the sample is prepared. A possible way to observe the mentioned effects is to vary ε around the discontinuous points and measure the corresponding current noise.

A few remarks about the ring radius should be mentioned here. One should note that we do not give the specific value of the ring radius in our model. Instead, a phenomenological value about the free space decay rate γ_0 is used. The magnitudes of the tunnel rates are set relative to it. In general, the changing of radius will certainly affect the shot noise. For example, because of the exciton-polariton (super radiant) effect in the direction of circumference, an increasing of ring radius will enhance the decay rate. In addition, the dipole moment of the QR exciton χ is also altered because of the varying of the wave function. All these can contribute to the variations of the decay rate and shot noise. In our previous study,[15] we have shown that the decay rate is a monotonic increasing function on radius ρ if the exciton is coherent in the quantum ring, i.e., free of scattering from impurities or imperfect boundaries. The dashed-dotted line in Fig. 4 shows the result for *doubled* free-space decay rate, i.e., $\gamma_0 \rightarrow 2\gamma_0$. Although the noise is increased, the zigzag feature remains unchanged.

In conclusion, we have derived in this work the nonequilibrium current noise of QR excitons incorporated in a p-i-n junction surrounded by a planar microcavity. Some radiative decay properties of the one-dimensional QR exciton can be obtained from the observation of shot noise spectrum, which also shows extra information about the electron-side tunneling rate. Different noise features between the QD and QR are pointed out, and deserve to be tested with present technologies.

This work is supported partially by the National Science Council, Taiwan under Grant Nos. NSC 94-2112-M-009-019 and NSC 94-2120-M-009-002.

[1] E. M. Purcell, Phys. Rev. **69**, 681 (1946).
[2] P. Goy *et al.*, Phys. Rev. Lett. **50**, 1903 (1983); G. Gabrielse and H. Dehmelt, *ibid.* **55**, 67 (1985); R. G. Hulet *et al.*, *ibid.* **55**, 2137 (1985); D. J. Heinzen *et al.*, *ibid.* **58**, 1320 (1987).
[3] J. M. Gerard *et al.*, Phys. Rev. Lett. **81**, 1110 (1998); M. Bayer *et al.*, *ibid.* **86**, 3168 (2001); G. S. Solomon *et al.*, *ibid.* **86**, 3903 (2001).
[4] C. Constantin *et al.*, Phys. Rev. B **66**, 165306 (2002).
[5] G. Bjork *et al.*, Phys. Rev. A **44**, 669 (1991); K. Tanaka *et al.*, Phys. Rev. Lett. **74**, 3380 (1995).
[6] C. W. J. Beenakker, Rev. Mod. Phys. **69**, 731 (1997); Y. M. Blanter and M. Buttiker, Phys. Rep. **336**, 1 (2000).
[7] Z. Yuan *et al.*, Science **295**, 102 (2002); G. Kießlich *et al.*, Phys. Rev. B **68**, 125331 (2003).
[8] Y. N. Chen *et al.*, Phys. Rev. B **69**, 245323 (2004).
[9] R. J. Warburton *et al.*, Nature (London) **405**, 926 (2000).
[10] M. Bayer *et al.*, Phys. Rev. Lett. **90**, 186801 (2003).
[11] D. K. C. MacDonald, Rep. Prog. Phys. **12**, 56 (1948).
[12] T. Brandes and B. Kramer, Phys. Rev. Lett. **83**, 3021 (1999); Y. N. Chen *et al.*, *ibid.* **90**, 166802 (2003).
[13] Actually, the total current noise should be expressed in terms of the spectra of particle currents and the charge noise spectrum: $S_I(\omega)=aS_{I_L}(\omega)+bS_{I_R}(\omega)-ab\omega^2S_Q(\omega)$, where a and b are capacitance coefficient $(a+b=1)$ of the junctions. Since we have assumed a highly asymmetric set up $(a \ll b)$, it is plausible to consider the hole-side spectra $S_{I_R}(\omega)$ only.
[14] R. Aguado and T. Brandes, Phys. Rev. Lett. **92**, 206601 (2004).
[15] Y. N. Chen and D. S. Chuu, Solid State Commun. **130**, 491 (2004).
[16] Y. N. Chen *et al.*, Phys. Rev. B **64**, 125307 (2001).

Anderson model with spin-flip-associated tunneling

Kao-Chin Lin and Der-San Chuu
Department of Electrophysics, National Chiao-Tung University, Hsinchu 300, Taiwan
(Received 3 March 2005; revised manuscript received 11 July 2005; published 9 September 2005)

The spin-flip-associated transport through a quantum dot based on the Anderson model in equilibrium and nonequilibrium situations is studied. It is found that electrons are scattered due to the spin-flip effect via the normal and the Kondo channels. Our results show that the conductance is suppressed due to the spin-flip effect, and the suppression due to the spin-flip scattering via the Kondo channel is stronger for temperatures below the Kondo temperature.

DOI: 10.1103/PhysRevB.72.125314 PACS number(s): 73.23.−b, 73.63.−b, 75.25.+z

I. INTRODUCTION

Recently, much theoretical and experimental research related to electron spin has been done. Owing to the progress in nanofabrication and microelectronic techniques, devices based on the electron spin, such as spin memory,[1] spin transistor,[2] and electron-spin-based quantum computers,[3,4] may be realized very soon. These devices are related to the spin-polarization orientation or spin-flip effect. Usually, the spin-flip effect occurs in scattering processes. The scattering processes may be caused by magnetic impurities, magnons, or domain walls at the interface or electrode,[5] or may be due to interactions with phonons[6] or the photon field.[7] In addition to scattering processes, spin flip may occur when the electron is transported between different spin-state regions. One of the instances is that the electron is transported between the Rashba quantum dot and the ferromagnetic lead. The Rashba effect can be observed in InAs semiconductors. The eigenstate of the Rashba Hamiltonian is a superposition of the spin states $|\uparrow\rangle$ and $|\downarrow\rangle$, i.e., $|\pm\rangle=(1/\sqrt{2})(e^{i\theta/2}|\uparrow\rangle\pm e^{-i\theta/2}|\downarrow\rangle)$.[4] It is known that the off-diagonal terms of the tunneling amplitude matrix and coupling constant are nonzero and spin-flip-associated tunneling appears in the system.[8] A sketch of the spin-flip-associated tunneling through a quantum system is shown in Fig. 1.

The spin-flip-associated tunneling effect might cause some special behaviors in the electric properties of the material. The intradot spin-flip effect was found to shift the resonant energy ϵ_0 of the quantum dot to $\epsilon_0\pm R$, where R is the spin-flip scattering amplitude.[8] Sergueev *et al.*[9] studied the spin-flip-associated tunneling through a quantum dot and described the spin-valve effect. The spin-valve effect caused by the transport between different spin states shows that the resistance depends on the direction (parallel or antiparallel) of the magnetization of two ferromagnetic metals.[9–12] Zhu and Balatsky studied the spin-flip-associated tunneling through a local nuclear spin precessing in a magnetic field to simulate the conductance oscillation observed in STM experiments.[13] They included the off-diagonal process and concluded that the conductance of the system can be obviously modified. Guinea pointed out that elastic spin-flip effects give rise to a temperature-independent reduction of the magnetoresistance while inelastic spin-flip processes give rise to temperature-dependent non-Ohmic effects and variation of the conductance.[5] As mentioned above, the spin-flip effect is important in the study of spin electronic devices and thus is worth exploring.

In spin-based devices such as a spin-based quantum computer, which may be operated at low temperature, the correlation between the electron in the quantum dot and the conduction electrons in the reservoir is important because the correlation will cause a peak of the density of states in the vicinity of the Fermi level for temperature $T\leqslant T_K$, where T_K is the Kondo temperature. The Anderson impurity model, which describes the correlation due to on-site Coulomb interaction and the direct tunneling between the conduction band and the local spin state in the magnetic impurity, is also employed to describe the quantum dot (QD) system.[14] The correlation interaction causes a sharp peak in the vicinity of the Fermi level for temperatures below T_K. The electron in the impurity may tunnel out of the impurity site to occupy a "virtual state," and then be replaced by an electron from the metal.[15,16] This process can effectively "flip" the spin of the impurity. Schrieffer and Wolff have shown that, in the limit of strong on-site Coulomb interaction, the Anderson impurity model is equivalent to the *s-d* model when the impurity level ϵ_0 is well below the Fermi level and the Kondo effect is obtained in this limit.[17] In the original Anderson impurity model, the electron spin does not flip during the process of tunneling between the impurity and the electron reservoir. In this work, we consider that the electron spin flips during the tunneling process, i.e., the spin-flip-associated coupling constant $\Gamma_\alpha^{\bar{\sigma}\sigma}=2\pi\Sigma_{k,s,\alpha\in L,R}V^*_{k_\alpha s,\bar{\sigma}2}V_{k_\alpha s,\sigma}\delta(\omega-\epsilon_{k\alpha s})$ where $\sigma(s)$ is the spin state of the electron in the QD (lead) and $\bar{\sigma}\neq\sigma$ is included in our study. The effects on the density of states and the conductance of the quantum dot system versus the strength of the spin-flip coupling will be discussed. Compared to the original Anderson model, the spin-flip-associated tunneling effect is expected to contribute additional self-energy which may modify the local density of state (LDOS), or the diagonal part of the spectral function $-2\,\mathrm{Im}\,G^r_{\sigma\sigma}$. The conductance depends strongly on the profile of the diagonal part of the spectral function $-2\,\mathrm{Im}\,G^r_{\sigma\sigma}$ and the off-diagonal part of the spectral function $-2\,\mathrm{Im}\,G^r_{\bar{\sigma}\sigma}$, which may change sign in the vicinity of the peak position of the LDOS. Therefore, the off-diagonal spectral function is expected to modify the conductance. In other words, the conductance may be modified by spin-flip-associated tunneling.

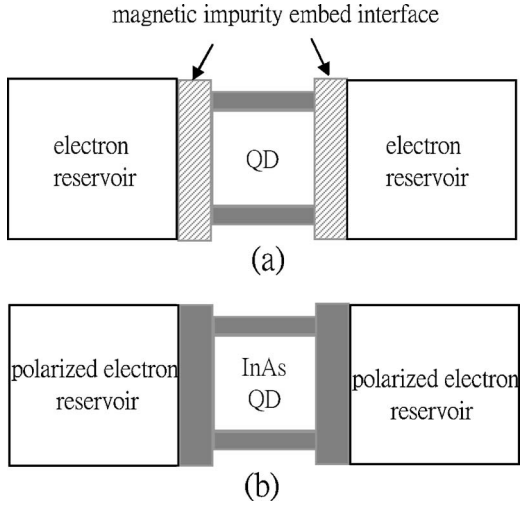

FIG. 1. The schematic plot of the system considered in this work. The spin-flip-associated tunneling is (a) originated by the impurity scattering and (b) due to the tunneling between the different spin states.

Instead of studying the mechanism of the spin-flip effect, we will study the spin-flip effect in a phenomenological way. The tunneling coupling constant will be assumed the same as that proposed in Ref. 13.

II. MODEL AND FORMALISM

The Hamiltonian of the system considered in this work can be written as

$$H_d = \sum_{\sigma} \epsilon_{\sigma} d_{\sigma}^{\dagger} d_{\sigma} + U n_{\sigma} n_{\bar{\sigma}},$$

$$H_C = \sum_{\substack{k_{\alpha} s \\ \alpha \in L,R}} \epsilon_{k_{\alpha} s} c_{k_{\alpha} s}^{\dagger} c_{k_{\alpha} s},$$

$$H_T = \sum_{k_{\alpha} s, \sigma} V_{k_{\alpha} S, \sigma}^{*} d_{\sigma}^{\dagger} c_{k_{\alpha} s} + V_{k_{\alpha} S, \sigma} c_{k_{\alpha} s}^{\dagger} d_{\sigma} \tag{1}$$

where $d_{\sigma}^{\dagger}(d_{\sigma})$ is the creation (annihilation) operator of the electron with spin state σ in the dot, and $c_{k_{\alpha} s}^{\dagger}(c_{k_{\alpha} s})$ is the creation (annihilation) operator of an electron with momentum k and spin state s in the α lead (where $\alpha \in L,R$). Note that the spin states s and σ are not necessary in the same eigenstate, for example, the spin state σ in the QD may be the eigenstate of the Rashba state and the spin state s in the lead may be the pure spin-up or spin-down state. The energy $\epsilon_{k_{\alpha} s}$ is the single-particle energy of the conduction electron in the α lead. U is the intradot Coulomb interaction. The electron tunneling between the lead and dot can be described by the tunneling matrix $V_{k_{\alpha} s, \sigma}$. As shown in Ref. 13, the coupling constant between the QD and the lead can be expressed by $\Gamma_{\alpha}^{\bar{\sigma}\sigma} = 2\pi \Sigma_{k,s,\alpha \in L,R} V_{k_{\alpha} s, \bar{\sigma}}^{*} V_{k_{\alpha} s, \sigma} \delta(\omega - \epsilon_{k\alpha s})$. The spin-flip coupling constant is set to be symmetric for the state $\sigma(\bar{\sigma})$ flipped into the state $\bar{\sigma}(\sigma)$, i.e., $\Gamma_{\alpha}^{\bar{\sigma}\sigma} = \Gamma_{\alpha}^{\sigma\bar{\sigma}} = \Gamma_{\alpha}^{s}$. And the normal coupling constant $\Gamma_{\alpha}^{\sigma\sigma} = 2\pi \Sigma_{k,s,\alpha \in L,R} V_{k_{\alpha} s, \sigma}^{*} V_{k_{\alpha} s, \sigma} \delta(\omega - \epsilon_{k\alpha s})$ is assumed to be spin independent, i.e., $\Gamma_{\alpha}^{\sigma\sigma} = \Gamma_{\alpha}^{\bar{\sigma}\bar{\sigma}} = \Gamma_{\alpha}^{n}$. In this paper, we use the notation $\bar{\sigma}$ to stand for the spin being not equal to σ while σ' is equal or not equal to σ.

The Green's function **G** corresponding to the spin-flip-associated tunneling effect of the noninteracting system can be written as

$$\begin{aligned} \begin{bmatrix} G_{\sigma\sigma} & G_{\sigma\bar{\sigma}} \\ G_{\bar{\sigma}\sigma} & G_{\bar{\sigma}\bar{\sigma}} \end{bmatrix} &= \begin{bmatrix} G_{\sigma\sigma}^{0} & 0 \\ 0 & G_{\bar{\sigma}\bar{\sigma}}^{0} \end{bmatrix} + \begin{bmatrix} G_{\sigma\sigma}^{0} & 0 \\ 0 & G_{\bar{\sigma}\bar{\sigma}}^{0} \end{bmatrix} \begin{bmatrix} \Sigma_{\sigma\sigma} & \Sigma_{\sigma\bar{\sigma}} \\ \Sigma_{\bar{\sigma}\sigma} & \Sigma_{\bar{\sigma}\bar{\sigma}} \end{bmatrix} \begin{bmatrix} G_{\sigma\sigma} & G_{\sigma\bar{\sigma}} \\ G_{\bar{\sigma}\sigma} & G_{\bar{\sigma}\bar{\sigma}} \end{bmatrix} \\ &= \begin{bmatrix} [(G_{\sigma\sigma}^{0})^{-1} - \Sigma_{\sigma\sigma} - \Sigma_{\sigma\bar{\sigma}} \tilde{G}_{\bar{\sigma}\bar{\sigma}}^{0} \Sigma_{\bar{\sigma}\sigma}]^{-1} & \tilde{G}_{\sigma\sigma}^{0} \Sigma_{\sigma\bar{\sigma}} G_{\bar{\sigma}\bar{\sigma}} \\ \tilde{G}_{\bar{\sigma}\bar{\sigma}}^{0} \Sigma_{\bar{\sigma}\sigma} G_{\sigma\sigma} & [(G_{\bar{\sigma}\bar{\sigma}}^{0})^{-1} - \Sigma_{\bar{\sigma}\bar{\sigma}} - \Sigma_{\bar{\sigma}\sigma} \tilde{G}_{\sigma\sigma}^{0} \Sigma_{\sigma\bar{\sigma}}]^{-1} \end{bmatrix} \end{aligned} \tag{2}$$

where the self-energy $\Sigma_{\sigma\sigma}$ is caused by tunneling without an associated spin flip and the self-energy $\Sigma_{\bar{\sigma}\sigma}$ is caused by spin-flip-associated tunneling. $\Sigma_{\bar{\sigma}\sigma}$ flips spin σ to spin $\bar{\sigma}$ during the electron transport between the lead and the dot. $G_{\sigma\sigma}^{0}$ is the free-particle Green's function and $\tilde{G}_{\sigma\sigma}^{0} = (\omega - \epsilon_{\sigma} - \Sigma_{\sigma\sigma})^{-1}$ is the Green's function of the electron in the QD with the spin state σ perturbed by the tunneling effect. The detailed derivation of Eq. (2) is shown in Appendix A.

If the intradot Coulomb interaction is included, the Kondo effect occurs when $T \leqslant T_K$. There are many approaches to solve the problem, such as the noncrossing-approximation approach,[18,11] the equation of motion (EOM) method,[19–22,10] or the renormalization group method.[12,20,23] The equation of motion method will be used to solve the Green's function of the interaction system in this work. In the processes of the EOM, the two-particle correlation function (or Green's function) arises from the two-particle on-site Coulomb interaction and needs to be decoupled. The accuracy of the EOM method depends on the decoupling scheme. One of the compact ways to decouple the two-particle correlation function to the single-particle correlation function is the decoupling scheme introduced by Lacroix for high temperature

(i.e., $T \geqslant T_K$). The high-temperature Lacroix decoupling approximation at low temperatures ($T < T_K$) gives only a qualitative solution and is quantitatively correct at high temperatures ($T \geqslant T_K$).[9,20] The EOM and Lacroix's high-temperature decoupling scheme are popularly adopted by many authors. In this work, we will use the high-temperature Lacroix decoupling approximation to decouple the two-particle Green's function.

Consider the spin-flip-associated tunneling effect where the intradot particle-particle interaction is assumed to be the Coulomb interaction. By using the method of the equation of motion in the Green's function $\mathbf{G}$, one obtains

$$\begin{bmatrix} (\omega-\epsilon_\sigma)G_{\sigma\sigma} & (\omega-\epsilon_\sigma)G_{\sigma\bar{\sigma}} \\ (\omega-\epsilon_{\bar{\sigma}})G_{\bar{\sigma}\sigma} & (\omega-\epsilon_{\bar{\sigma}})G_{\bar{\sigma}\bar{\sigma}} \end{bmatrix} = \begin{bmatrix} 1 & 0 \\ 0 & 1 \end{bmatrix} + \begin{bmatrix} \Sigma^{Tn}_{\sigma\sigma} & \Sigma^{Ts}_{\sigma\bar{\sigma}} \\ \Sigma^{Ts}_{\bar{\sigma}\sigma} & \Sigma^{Tn}_{\bar{\sigma}\bar{\sigma}} \end{bmatrix} \begin{bmatrix} G_{\sigma\sigma} & G_{\sigma\bar{\sigma}} \\ G_{\bar{\sigma}\sigma} & G_{\bar{\sigma}\bar{\sigma}} \end{bmatrix} + U \begin{bmatrix} G^{(2)}_{\sigma\sigma} & G^{(2)}_{\sigma\bar{\sigma}} \\ G^{(2)}_{\bar{\sigma}\sigma} & G^{(2)}_{\bar{\sigma}\bar{\sigma}} \end{bmatrix} \tag{3}$$

where $G_{\sigma\sigma'} \equiv (-i)\langle T\{d_\sigma, d^\dagger_{\sigma'}\}\rangle$ and $G^{(2)}_{\sigma\sigma'} \equiv (-i)\langle T\{d_\sigma n_{\bar{\sigma}}, d^\dagger_{\sigma'}\}\rangle$. The Green's function $G^{(2)}_{\sigma\sigma'}$ is the two-particle Green's function corresponding to particle-particle interaction (Coulomb interaction) and is related to the Kondo effect. Using the EOM in $\mathbf{G}^{(2)}$, we obtain

$$\begin{aligned} \begin{bmatrix} (\omega-\epsilon_\sigma-U)G^{(2)}_{\sigma\sigma} & (\omega-\epsilon_\sigma-U)G^{(2)}_{\sigma\bar{\sigma}} \\ (\omega-\epsilon_{\bar{\sigma}}-U)G^{(2)}_{\bar{\sigma}\sigma} & (\omega-\epsilon_{\bar{\sigma}}-U)G^{(2)}_{\bar{\sigma}\bar{\sigma}} \end{bmatrix} &= \begin{bmatrix} \langle n_{\bar{\sigma}}\rangle & 0 \\ 0 & \langle n_\sigma\rangle \end{bmatrix} + \sum_{k_\alpha s} \begin{bmatrix} V^*_{k\alpha s,\sigma}(-i)\langle T\{c_{k_\alpha s}d^\dagger_{\bar{\sigma}}d_{\bar{\sigma}}, d^\dagger_\sigma\}\rangle & V^*_{k\alpha s,\sigma}(-i)\langle T\{c_{k_\alpha s}d^\dagger_{\bar{\sigma}}d_{\bar{\sigma}}, d^\dagger_{\bar{\sigma}}\}\rangle \\ V^*_{k\alpha s,\bar{\sigma}}(-i)\langle T\{c_{k_\alpha s}d^\dagger_{\sigma}d_{\sigma}, d^\dagger_\sigma\}\rangle & V^*_{k\alpha s,\bar{\sigma}}(-i)\langle T\{c_{k_\alpha s}d^\dagger_{\sigma}d_{\sigma}, d^\dagger_{\bar{\sigma}}\}\rangle \end{bmatrix} \\ &+ \sum_{k_\alpha s} \begin{bmatrix} V_{k\alpha s,\bar{\sigma}}(-i)\langle T\{c^\dagger_{k_\alpha s}d_\sigma d_{\bar{\sigma}}, d^\dagger_\sigma\}\rangle & V_{k\alpha s,\bar{\sigma}}(-i)\langle T\{c^\dagger_{k_\alpha s}d_\sigma d_{\bar{\sigma}}, d^\dagger_{\bar{\sigma}}\}\rangle \\ V_{k\alpha s,\sigma}(-i)\langle T\{c^\dagger_{k_\alpha s}d_{\bar{\sigma}} d_{\sigma}, d^\dagger_\sigma\}\rangle & V_{k\alpha s,\sigma}(-i)\langle T\{c^\dagger_{k_\alpha s}d_{\bar{\sigma}} d_{\sigma}, d^\dagger_{\bar{\sigma}}\}\rangle \end{bmatrix} \\ &- \sum_{k_\alpha s} \begin{bmatrix} V^*_{k\alpha s,\bar{\sigma}}(-i)\langle T\{c_{k_\alpha s}d^\dagger_{\bar{\sigma}}d_{\sigma}, d^\dagger_\sigma\}\rangle & V^*_{k\alpha s,\bar{\sigma}}(-i)\langle T\{c_{k_\alpha s}d^\dagger_{\bar{\sigma}}d_{\sigma}, d^\dagger_{\bar{\sigma}}\}\rangle \\ V^*_{k\alpha s,\sigma}(-i)\langle T\{c_{k_\alpha s}d^\dagger_{\sigma}d_{\bar{\sigma}}, d^\dagger_\sigma\}\rangle & V^*_{k\alpha s,\sigma}(-i)\langle T\{c_{k_\alpha s}d^\dagger_{\sigma}d_{\bar{\sigma}}, d^\dagger_{\bar{\sigma}}\}\rangle \end{bmatrix}. \end{aligned} \tag{4}$$

In general there are four one-particle Green's functions ($G_{\sigma\sigma}$, $G_{\sigma\bar{\sigma}}$, $G_{\bar{\sigma}\sigma}$, and $G_{\bar{\sigma}\bar{\sigma}}$) and four two-particle Green's functions ($G^{(2)}_{\sigma\sigma}$, $G^{(2)}_{\sigma\bar{\sigma}}$, $G^{(2)}_{\bar{\sigma}\sigma}$, and $G^{(2)}_{\bar{\sigma}\bar{\sigma}}$) in our system. In contrast with Eq. (3), the equation of the Green's function $\mathbf{G}^{(2)}$ can be assumed as

$$\begin{aligned} &\begin{bmatrix} (\omega-\epsilon_\sigma-U)G^{(2)}_{\sigma\sigma} & (\omega-\epsilon_\sigma-U)G^{(2)}_{\sigma\bar{\sigma}} \\ (\omega-\epsilon_{\bar{\sigma}}-U)G^{(2)}_{\bar{\sigma}\sigma} & (\omega-\epsilon_{\bar{\sigma}}-U)G^{(2)}_{\bar{\sigma}\bar{\sigma}} \end{bmatrix} \\ &\quad = \begin{bmatrix} \langle n_{\bar{\sigma}}\rangle & 0 \\ 0 & \langle n_\sigma\rangle \end{bmatrix} + \begin{bmatrix} X^{(2)}_{\sigma\sigma} & X^{(2)}_{\sigma\bar{\sigma}} \\ X^{(2)}_{\bar{\sigma}\sigma} & X^{(2)}_{\bar{\sigma}\bar{\sigma}} \end{bmatrix} \begin{bmatrix} G_{\sigma\sigma} & G_{\sigma\bar{\sigma}} \\ G_{\bar{\sigma}\sigma} & G_{\bar{\sigma}\bar{\sigma}} \end{bmatrix} \\ &\quad + \begin{bmatrix} Y^{(2)}_{\sigma\sigma} & Y^{(2)}_{\sigma\bar{\sigma}} \\ Y^{(2)}_{\bar{\sigma}\sigma} & Y^{(2)}_{\bar{\sigma}\bar{\sigma}} \end{bmatrix} \begin{bmatrix} G^{(2)}_{\sigma\sigma} & G^{(2)}_{\sigma\bar{\sigma}} \\ G^{(2)}_{\bar{\sigma}\sigma} & G^{(2)}_{\bar{\sigma}\bar{\sigma}} \end{bmatrix}. \end{aligned} \tag{5}$$

In order to simplify the problem, we consider the infinite-U limit. Under the infinite-U limit, the off-diagonal term of $\mathbf{Y}^{(2)}$ can be ignored (the detailed derivation will be given in Appendix B). Equation (5) can be rewritten as

$$\begin{aligned} &\begin{bmatrix} G^{(2)}_{\sigma\sigma} & G^{(2)}_{\sigma\bar{\sigma}} \\ G^{(2)}_{\bar{\sigma}\sigma} & G^{(2)}_{\bar{\sigma}\bar{\sigma}} \end{bmatrix} \\ &\quad = \begin{bmatrix} g^{0(2)}_{\sigma\sigma}\langle n_{\bar{\sigma}}\rangle & 0 \\ 0 & g^{0(2)}_{\sigma\sigma}\langle n_\sigma\rangle \end{bmatrix} \\ &\quad + \begin{bmatrix} g^{0(2)}_{\sigma\sigma}(X^{(2)}_{\sigma\sigma}G_{\sigma\sigma} + X^{(2)}_{\sigma\bar{\sigma}}G_{\bar{\sigma}\sigma}) & g^{0(2)}_{\sigma\sigma}(X^{(2)}_{\sigma\bar{\sigma}}G_{\bar{\sigma}\bar{\sigma}} + X^{(2)}_{\sigma\sigma}G_{\sigma\bar{\sigma}}) \\ g^{0(2)}_{\bar{\sigma}\bar{\sigma}}(X^{(2)}_{\bar{\sigma}\sigma}G_{\sigma\sigma} + X^{(2)}_{\bar{\sigma}\bar{\sigma}}G_{\bar{\sigma}\sigma}) & g^{0(2)}_{\bar{\sigma}\bar{\sigma}}(X^{(2)}_{\bar{\sigma}\sigma}G_{\sigma\bar{\sigma}} + X^{(2)}_{\bar{\sigma}\bar{\sigma}}G_{\bar{\sigma}\bar{\sigma}}) \end{bmatrix} \end{aligned}$$

where $g^{0(2)}_{\sigma\sigma} \equiv (\omega-\epsilon_\sigma-Y_{\sigma\sigma}-U)^{-1}$ and $g^{0(2)}_{\bar{\sigma}\bar{\sigma}} \equiv (\omega-\epsilon_{\bar{\sigma}}-Y_{\bar{\sigma}\bar{\sigma}}-U)^{-1}$. Substituting $\mathbf{G}^{(2)}$ into $\mathbf{G}$, one obtains

$$\begin{aligned} \begin{bmatrix} (\omega-\epsilon_\sigma)G_{\sigma\sigma} & (\omega-\epsilon_\sigma)G_{\sigma\bar{\sigma}} \\ (\omega-\epsilon_{\bar{\sigma}})G_{\bar{\sigma}\sigma} & (\omega-\epsilon_{\bar{\sigma}})G_{\bar{\sigma}\bar{\sigma}} \end{bmatrix} &= \begin{bmatrix} 1+Ug^{0(2)}_{\sigma\sigma}\langle n_{\bar{\sigma}}\rangle & 0 \\ 0 & 1+Ug^{0(2)}_{\bar{\sigma}\bar{\sigma}}\langle n_\sigma\rangle \end{bmatrix} + \begin{bmatrix} \Sigma^T_{\sigma\sigma}+Ug^{0(2)}_{\sigma\sigma}X^{(2)}_{\sigma\sigma} & \Sigma^T_{\sigma\bar{\sigma}}+Ug^{0(2)}_{\sigma\sigma}X^{(2)}_{\sigma\bar{\sigma}} \\ \Sigma^T_{\bar{\sigma}\sigma}+Ug^{0(2)}_{\bar{\sigma}\bar{\sigma}}X^{(2)}_{\bar{\sigma}\sigma} & \Sigma^T_{\bar{\sigma}\bar{\sigma}}+Ug^{0(2)}_{\bar{\sigma}\bar{\sigma}}X^{(2)}_{\bar{\sigma}\bar{\sigma}} \end{bmatrix} \begin{bmatrix} G_{\sigma\sigma} & G_{\sigma\bar{\sigma}} \\ G_{\bar{\sigma}\sigma} & G_{\bar{\sigma}\bar{\sigma}} \end{bmatrix} \\ &\equiv \begin{bmatrix} 1+Ug^{0(2)}_{\sigma\sigma}\langle n_{\bar{\sigma}}\rangle & 0 \\ 0 & 1+Ug^{0(2)}_{\bar{\sigma}\bar{\sigma}}\langle n_\sigma\rangle \end{bmatrix} + \begin{bmatrix} \Sigma^{tot}_{\sigma\sigma} & \Sigma^{tot}_{\sigma\bar{\sigma}} \\ \Sigma^{tot}_{\bar{\sigma}\sigma} & \Sigma^{tot}_{\bar{\sigma}\bar{\sigma}} \end{bmatrix} \begin{bmatrix} G_{\sigma\sigma} & G_{\sigma\bar{\sigma}} \\ G_{\bar{\sigma}\sigma} & G_{\bar{\sigma}\bar{\sigma}} \end{bmatrix}. \end{aligned}$$

Under the infinite-U limit, $U\mathbf{g}^{0(2)} \sim -1$ and $\mathbf{\Sigma}^{tot} = \mathbf{\Sigma}^T - \mathbf{X}^{(2)}$. Comparing to Eq. (2) (after some algebra), one obtains

$$\begin{bmatrix} G_{\sigma\sigma} & G_{\sigma\bar{\sigma}} \\ G_{\bar{\sigma}\sigma} & G_{\bar{\sigma}\bar{\sigma}} \end{bmatrix} = \begin{bmatrix} (1-\langle n_{\bar{\sigma}}\rangle)[(\tilde{G}^0_{\sigma\sigma})^{-1} - \Sigma^{tot}_{\sigma\bar{\sigma}}\tilde{G}^0_{\bar{\sigma}\bar{\sigma}}\Sigma^{tot}_{\bar{\sigma}\sigma}]^{-1} & \tilde{G}^0_{\sigma\sigma}\Sigma^{tot}_{\sigma\bar{\sigma}}G_{\bar{\sigma}\bar{\sigma}} \\ \tilde{G}^0_{\bar{\sigma}\bar{\sigma}}\Sigma^{tot}_{\bar{\sigma}\sigma}G_{\sigma\sigma} & (1-\langle n_{\sigma}\rangle)[(\tilde{G}^0_{\bar{\sigma}\bar{\sigma}})^{-1} - \Sigma^{tot}_{\bar{\sigma}\sigma}\tilde{G}^0_{\sigma\sigma}\Sigma^{tot}_{\sigma\sigma'}]^{-1} \end{bmatrix}. \quad (6)$$

In Eq. (6) $\tilde{G}^0_{\sigma\sigma} \equiv (\omega - \epsilon_\sigma - \Sigma^{tot}_{\sigma\sigma})^{-1}$ and $\tilde{G}^0_{\bar{\sigma}\bar{\sigma}} \equiv (\omega - \epsilon_{\bar{\sigma}} - \Sigma^{tot}_{\bar{\sigma}\bar{\sigma}})^{-1}$. Comparing $\tilde{G}^0_{\sigma\sigma}$ with Eq. (3) in Ref. 20,

$$G_{\sigma\sigma} = \frac{1-\langle n_{\bar{\sigma}}\rangle}{\omega - \epsilon_\sigma - \Sigma_{0\sigma} - \Sigma_{1\sigma}}, \quad (7)$$

which is the Green's function corresponding to the original Anderson model. Now set $\mathbf{X}^{(2)} \equiv -\mathbf{\Sigma}_{1\sigma}$. $\tilde{\mathbf{G}}^0$ is the same as the Green's function corresponding to the original Anderson Hamiltonian except for the factor $(1-\langle n_{\bar{\sigma}}\rangle)$. $\tilde{\mathbf{G}}^0$ can be regarded as the Green's function of the quasiparticle of the Anderson Hamiltonian without the spin-flip effect. Now, the remaining problem is to obtain $\mathbf{X}^{(2)}$ and $\mathbf{Y}^{(2)}$. The detailed derivation and results are presented in Appendix B.

The form of our result [Eq. (6)] is the same as Eq. (2) except for the self-energy $\mathbf{X}^{(2)}$ which is related to the Kondo effect. The physical picture of the Green's function [Eq. (6)] can be interpreted as follows. $\tilde{\mathbf{G}}^0$ is the Green's function corresponding to the Anderson Hamiltonian without the spin-flip effect, i.e., it is the form of the Green's function as shown in Eq. (3) of Ref. 20. $G_{\sigma\sigma}$ in Eq. (6), for example, represents the corresponding σ-state quasiparticle of the Anderson Hamiltonian, which is scattered between the σ and $\bar{\sigma}$ states and causes the self-energy $\Sigma^{tot}_{\sigma\bar{\sigma}}\tilde{G}^0_{\bar{\sigma}\bar{\sigma}}\Sigma^{tot}_{\bar{\sigma}\sigma}$. $\Sigma^{tot}_{\bar{\sigma}\sigma}$ contains two terms: the self-energy $\Sigma^T_{\bar{\sigma}\sigma}$ corresponding to the scattering via the normal channel and the self-energy $X^{(2)}_{\bar{\sigma}\sigma}$ corresponding to the scattering via the Kondo channel. The normal-channel scattering is energy and temperature independent. Since the Kondo effect is strongly dependent on the temperature and causes a Kondo resonant peak in the vicinity of the Fermi level of the lead, the Kondo-channel scattering is strongly dependent on the temperature and dominates the scattering with energy in the vicinity of the Fermi energy of the lead.

Since the transport problem in a quantum dot system may be a nonequilibrium problem, we will employ the nonequilibrium Green's function method and the transport equation developed by Wingreen *et al.* to calculate the particle number and conductance.[25] To evaluate Eq. (6) numerically, one must determine the particle number $\langle n_\sigma\rangle$ and the expectation value $\langle d^\dagger_\sigma d_{\bar{\sigma}}\rangle$ by a self-consistent method. In order to calculate the expectation values $\langle n_\sigma\rangle$ and $\langle d^\dagger_\sigma d_{\bar{\sigma}}\rangle$, the corresponding lesser Green's functions $G^<_{\sigma\sigma}$ and $G^<_{\bar{\sigma}\sigma}$ must be solved first, i.e., $\langle n_\sigma\rangle = -i\int(d\epsilon/2\pi)G^<_{\sigma\sigma}$ and $\langle d^\dagger_\sigma d_{\bar{\sigma}}\rangle = -i\int(d\epsilon/2\pi)G^<_{\bar{\sigma}\sigma}$. In this work, we use the method proposed by Sun and Guo which is able to solve the lesser Green's function, of the interacting system exactly for the steady-state problem.[24] The detailed derivation processes are shown in Appendix C.

III. RESULTS AND DISCUSSION

In the following discussion, all energy scales are normalized to the normal-tunneling coupling constant $\Gamma^n_\alpha = 1$. The resonant energy of the quantum dot is set as $\epsilon_0 = -5$. The Fermi level of the lead E_F is set to be zero for the equilibrium situation. The temperature is normalized to the Kondo temperature T_K, which is calculated by the exact expression obtained by Haldane, $T_K \approx (D\Gamma)^{1/2}\exp[\pi(\epsilon_0 - E_F)/(2\Gamma)] \approx 0.004$,[26] with the half-width $D=100$ and $\Gamma = \Gamma^n_L + \Gamma^n_R$.

Since the high temperature Lacroix decoupling approximation at low temperatures ($T < T_K$) gives only a qualitative solution and is quantitatively correct at high temperatures ($T > T_K$), we consider the situation with the temperature near the Kondo temperature, i.e., $T = 10T_K$, $1T_K$, and $0.1T_K$, and the normal limit $T = 100T_K$, for which the Kondo effect can be ignored for comparison.[27] The spectral function $A_{\sigma'\sigma}(\omega) = -2\,\mathrm{Im}\,G^r_{\sigma'\sigma}$ (or local density of states when $\sigma' = \sigma$) in the equilibrium situation is calculated in terms of the strength of spin-flip-associated tunneling, which is described by the spin-flip coupling constant Γ^s. As in the previous discussion, the quasiparticle of the Anderson Hamiltonian is scattered by the normal and the Kondo channels. The self-energy $\mathbf{\Sigma}^T$ due to normal-channel scattering is independent of the energy and the temperature; thus the electron can be scattered by the normal channel at arbitrary energy and temperature. In contrast to the normal channel, the Kondo-effect channel is energy dependent and the strength increases logarithmically in the vicinity of the Fermi level when $T \leqslant T_K$. Thus, the self-energy corresponding to the Kondo channel $\mathbf{X}^{(2)}$ is sensitive to temperature and energy. It can be expected that the Kondo channel dominates the scattering due to spin-flip-associated tunneling in the vicinity of the Fermi level when $T \leqslant T_K$. The normal-channel scattering dominates the spin-flip effect for electrons with energies far away from the Fermi level or $T > T_K$. As shown in Fig. 2, the LDOS in the region far away from the Fermi level is temperature independent. It implies that an electron with energy far away from the Fermi level is mainly scattered by the normal channel. Figure 3 shows a detailed plot of the LDOS with energy in the vicinity of the Fermi level. The spectral functions for $T = 100T_K$, i.e., the normal case, are shown in Figs. 3(a) and 3(b) (dashed lines). The spin-flip scattering via the normal channel affects the diagonal part of the spectrum function $A_{\sigma\sigma}$ (or LDOS) very slightly for the case of $T = 100T_K$ (normal limit). But the dependence of the off-diagonal spectrum function $A_{\bar{\sigma}\sigma}$ on spin-flip scattering via the classical channel is stronger than for $A_{\sigma\sigma}$. When the temperature is decreased to the order of the Kondo temperature ($T = 10T_K$ and $1T_K$ in our case), the Kondo effect becomes obvious and the Kondo resonance peak grows logarithmically. As Figs. 3(a) and 3(b) (solid line) and Figs. 3(c) and 3(d) show, it is obvious that the

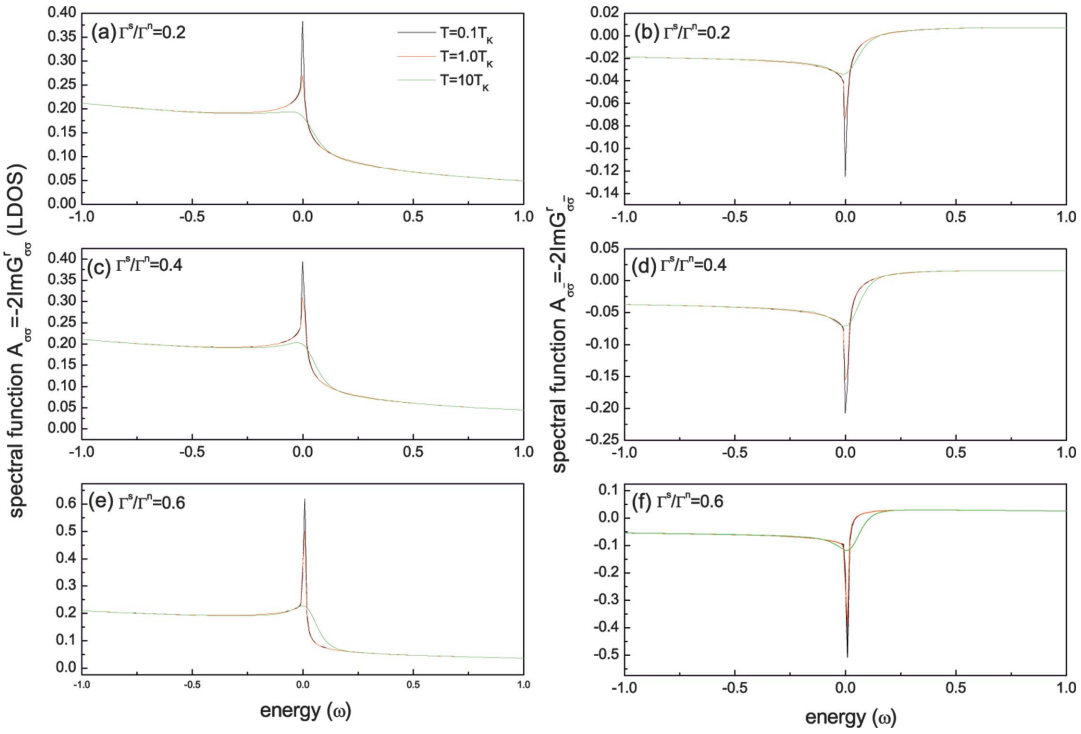

FIG. 2. (Color) The plot of spectral function as a function of ω with temperature $T=10T_K$, $1T_K$, and $T=0.1T$.

LDOS with energy near the Fermi level is strongly dependent on temperature when the temperature is close to the Kondo temperature. Therefore, it implies that the scattering in the region near the Fermi level is dominated by the Kondo channel. When the temperature is below the Kondo temperature ($T=0.1T_K$ in our case), the scattering via the Kondo channel is prominent. As shown in Figs. 3(e) and 3(f), there are two major effects due to the spin-flip-associated tunneling via the Kondo channel. The amplitude of the Kondo resonance peak is increased as Γ^s is increased, i.e., the

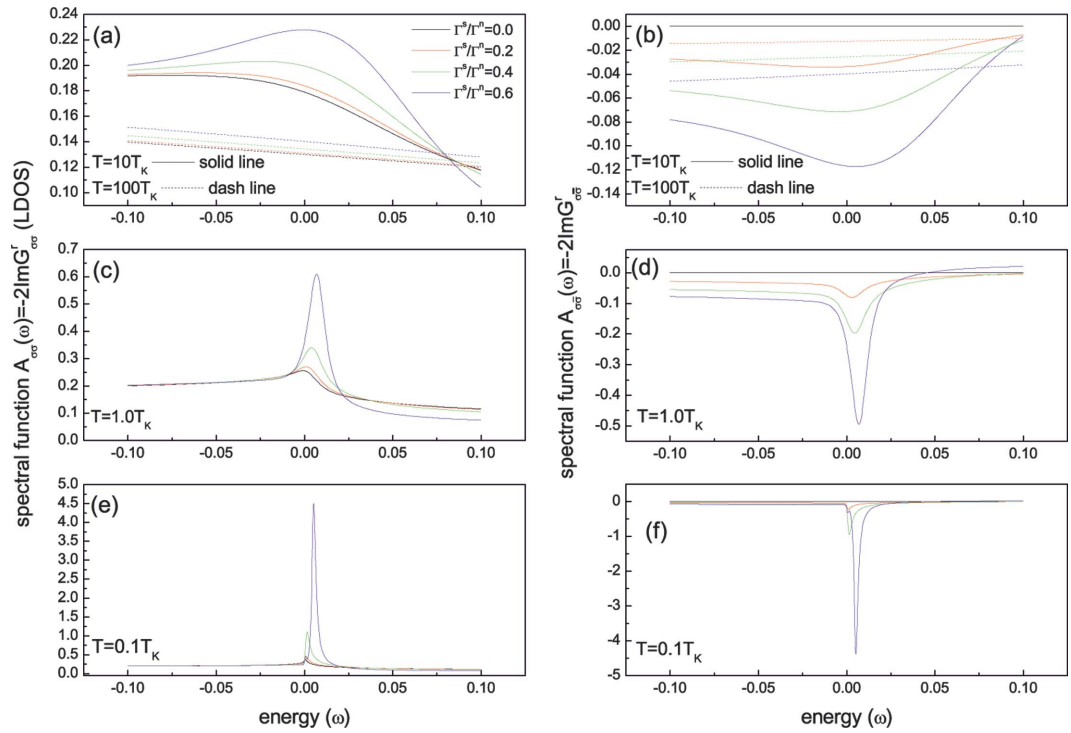

FIG. 3. (Color) The detailed plot of the spectral function in the vicinity of the Fermi level as a function of ω. $T=$(a)$100T_K$ and $10T_K$, (b) $1T_K$, and (c) $0.1T_K$ with various $\Gamma^s_\alpha/\Gamma^n_\alpha$.

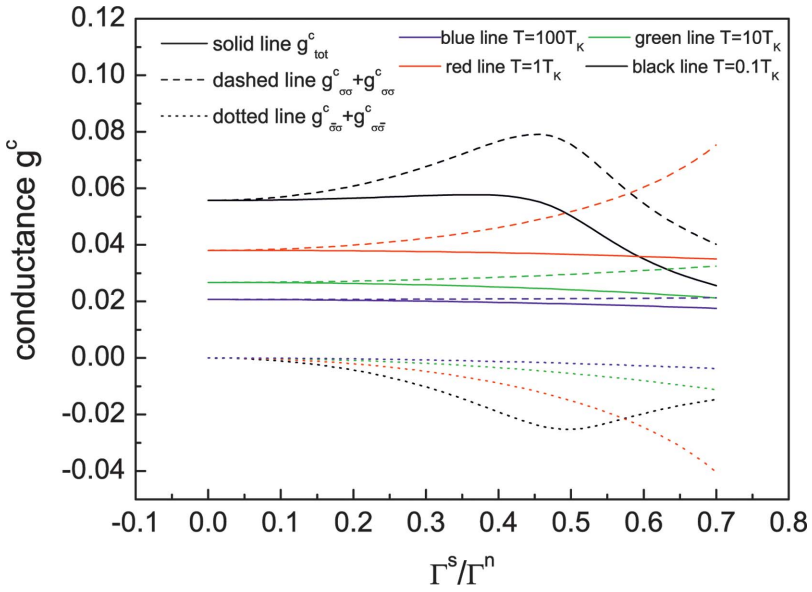

FIG. 4. (Color) The equilibrium conductance versus $\Gamma^s_\alpha/\Gamma^n_\alpha$ at various temperatures. The dashed line is the diagonal part. The dotted line is the off-diagonal part. The solid line is the total conductance. The blue line is $T=100T_K$, the green line $T=10T_K$, the red line is $T=1T_K$, and the black line is $T=0.1T_K$

Kondo resonance peak is enhanced by the spin-flip-associated tunneling effect. In addition to the increasing of the peak height, the spin-flip tunneling also causes a blue-shift of the Kondo resonance. These effects become stronger as the temperature is decreased. Note that the enhancement and shift of the Kondo resonance peak due to spin-flip-associated tunneling will affect the conductance. Since the off-diagonal Green's function is $G_{\bar{\sigma}\sigma}=\tilde{G}^0_{\sigma\sigma}\Sigma^{tot}_{\bar{\sigma}\sigma}G_{\sigma\sigma}$, the profile of the off-diagonal spectral function $A_{\bar{\sigma}\sigma}$ is similar to that of the diagonal spectral function $A_{\sigma\sigma}$ but with opposite sign. It is worth noting that for the case of $T \geqslant T_K$, the decrease (to more negative values) of $A_{\bar{\sigma}\sigma}$ is faster than the increase of $A_{\sigma\sigma}$. This phenomenon is the main reason for suppression of the conductance for $T \geqslant T_K$.

The conductance g^c for the equilibrium case is calculated by Eq. (3) of Ref. 13. For the equilibrium situation, the current is contributed by the electrons with energy near the Fermi level of the leads. Thus, the equilibrium conductance reflects the properties of the Kondo resonance peak with energy in the vicinity of the Fermi level of the leads. Figure 4 shows the equilibrium conductance versus the spin-flip coupling constant Γ^s. One can find that for $\Gamma^s=0$, the total conductance g^c_{tot} is increased as the temperature is decreased, since the Kondo resonance peak is enhanced as the temperature is decreased. For the case of $T=100T_K$, the Kondo effect can be ignored and the scattering is dominated by the normal channel. As in previous discussion, the decrease of $A_{\bar{\sigma}\sigma}$ is faster than the increase of $A_{\sigma\sigma}$ as Γ^s is increased; hence the total conductance g^c_{tot} is dominated by the off-diagonal part conductance $g^c_{\sigma\bar{\sigma}}$ and decreased as Γ^s is increased. For the cases of $T=10T_K$ and $1.0T_K$ the Kondo effect appears; however, it is not obvious. One can find that $g^c_{\sigma\sigma}$ is increased slightly as Γ^s is increased for $\Gamma^s > 0.3\Gamma^n(0.1\Gamma^n)$. This phenomenon reflects the enhancement of the Kondo resonance peak due to the spin-flip effect via the Kondo channel as discussed previously. Similar to the case of $T=100T_K$, the total conductance is dominated by the off-diagonal conductance and decreased as Γ^s is increased. For the case of $T=0.1T_K$, the effect due to spin-flip scattering via the Kondo channel becomes more prominent. The diagonal part $g^c_{\sigma\sigma}$ contains peak-enhancement and peak-shift effects due to spin-flip via the Kondo channel. For $\Gamma^s < 0.48$, the peak-enhancement effect is dominant and $g^c_{\sigma\sigma}$ increases as Γ^s is increased. For $\Gamma^s > 0.48$, the peak-shift effect is dominant and thus the peak height is shifted out of the vicinity of the Fermi level of the leads, and thus there are fewer electrons contributing to the conductance; hence $g^c_{\sigma\sigma}$ is decreased. The profile of the off-diagonal spectral function $A_{\bar{\sigma}\sigma}$ is similar to that of $A_{\sigma\sigma}$ except with the opposite sign; thus the behavior of the off-diagonal part of the conductance is similar to the diagonal part except for the sign. For $T=0.1T_K$ the total conductance is dominated by $g^c_{\sigma\sigma}$. In the region dominated by the peak-enhancement effect, i.e., $\Gamma^s < 0.48$, the total conductance is slightly increased as Γ^s is increased. In the region dominated by the peak-shift effect, the total conductance decreases as Γ^s is increased. Note that the conductance is suppressed rapidly for the case of $T=0.1T_K$ when $\Gamma^s > 0.48$. The rapid decrease of conductance is caused by the peak-shift effect due to spin-flip scattering.

For the nonequilibrium case, a quantum dot connected to two leads with different Fermi levels is studied. The Fermi levels of leads are set to be zero when the bias voltage is zero. When the bias voltage V_{bias} is applied, the Fermi levels of the leads are $E^R_F=-V_{bias}/2$ and $E^L_F=V_{bias}/2$. The nonequilibrium differential conductance is defined as $g^c=\Delta J/\Delta V_{bias}$, where the current J is calculated by the method of Ref. 25. The nonequilibrium differential conductance is shown in Fig. 5. Since the applied bias is symmetry, the conductance is symmetry for $V_{bias}>0$ and $V_{bias}<0$, as shown in Figs. 5(a) and 5(b). Following the same reasoning, the nonequilibrium differential conductance is decreased as Γ_s is increased for the cases of $T \geqslant T_K$. In the region $|V_{bias}|>0.25$ the conductance is temperature insensitive. It implies that the nonequilibrium differential conductance for $|V_{bias}|>0.25$ is dominated by the scattering via the normal channel, the behavior of the differential conductance is similar to the equilibrium case for $T > T_K$. Hence, for $|V_{bias}|>0.25$, the differential conductance is decreased as Γ^s is increased. In the region with energy near the Fermi level, i.e., $|V_{bias}|<0.25$, the Kondo

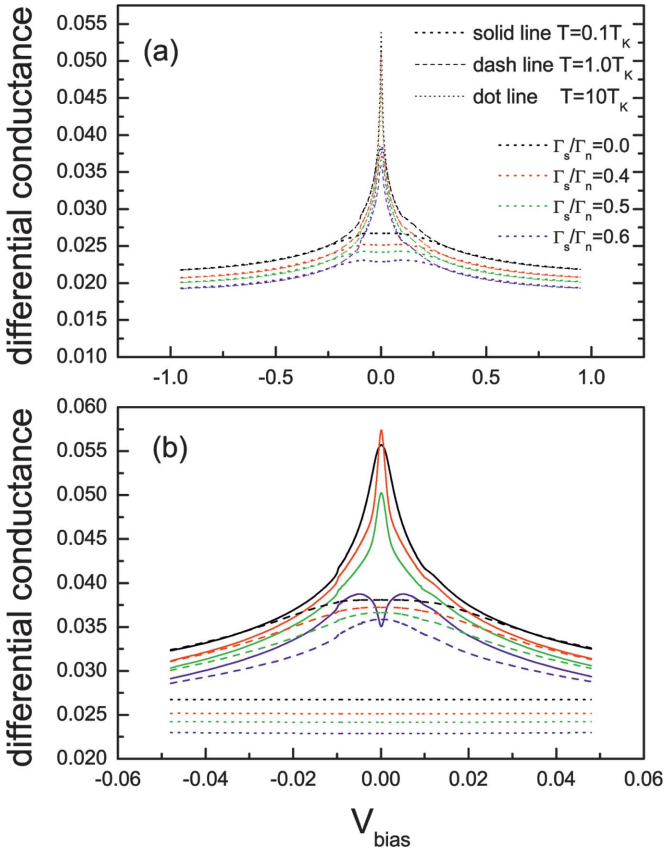

FIG. 5. (Color) (a) The differential conductance versus bias voltage with various $\Gamma^s_\alpha/\Gamma^n_\alpha$ for different temperature. (b) A detailed plot of (a) with energy almost equal to zero bias voltage.

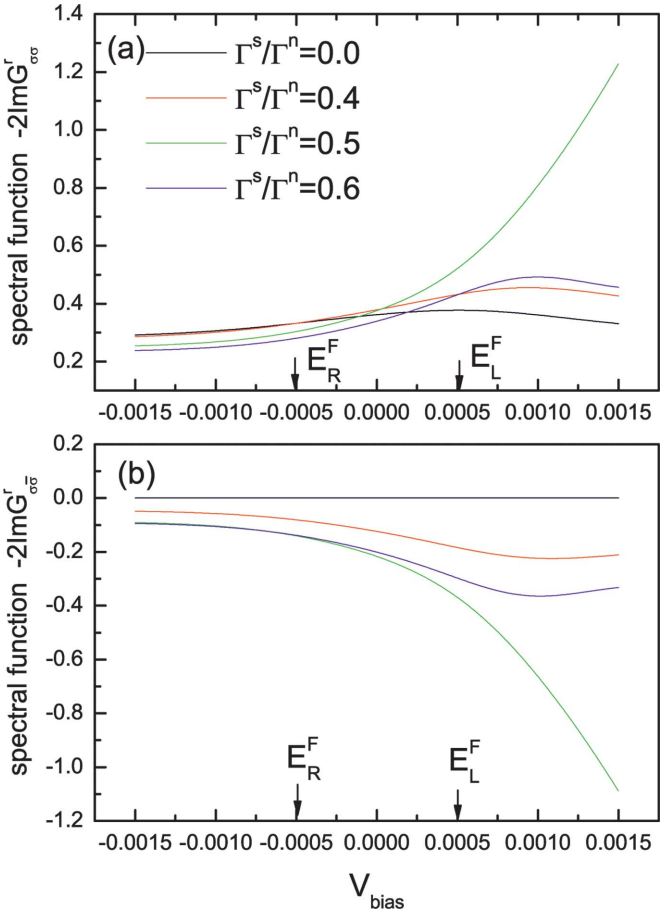

FIG. 6. (Color) (a) The nonequilibrium diagonal and (b) off-diagonal spectral functions for the case of $V_{bias}=10^{-3}$ and $T=0.1T_K$ with various $\Gamma^s_\alpha/\Gamma^n_\alpha$.

effect is more important when $T<T_k$. This is because the Kondo effect influences the LDOS only when the electron energy is near the Fermi level. The nonequilibrium differential conductance is influenced strongly by the Kondo effect when the bias voltage $|V_{bias}|\sim 0$ for $T\leqslant T_k$. Figure 5(b) shows a detailed plot of the nonequilibrium differential conductance with bias voltage $|V_{bias}|<0.05$. The variation of the conductance for $|V_{bias}|\sim 0$ is similar to the case of $|V_{bias}|\gg 0$ when $T>T_k$ (the dotted line in Fig. 5) and the scattering is via the normal channel. As the temperature is decreased to $T\sim T_k$, the influence due to the Kondo effect becomes important and the Kondo resonance peak is prominent. Hence, the conductance is larger than the one for $T>T_k$. For $T=T_k$ (the dashed line in Fig. 5), the quantity of conductance suppression due to the spin-flip-associated tunneling is similar to that in the large-bias-voltage region. The suppression of conductance is due to the decrease of $g^c_{\sigma\bar{\sigma}}$ as Γ^s is increased. The prominence of the conductance reflects the prominent Kondo resonance peak of the LDOS. When $T\leqslant T_k$ (the solid line in Fig. 5), the influence of the peak shift of the Kondo resonance becomes important. As in the case of equilibrium, the $g^c_{\sigma\sigma}$ is strongly suppressed by the shift of the Kondo resonance peak when Γ_s is large. As a result, the total conductance is suppressed rapidly when $\Gamma^s>0.4$ and causes a valley when $\Gamma^s=0.6$. Figures 6(a) and 6(b) show the spectral function for $T=0.1T_K$ and $V_{bias}=10^{-3}$. One can find that the LDOS within the Fermi level of the leads is increased as Γ^s is increased when $\Gamma^s<0.6$. This explains why the differential conductance is increased as Γ^s is increased when $\Gamma^s<0.6$ and $T=0.1T_K$ in the vicinity of $V_{bias}=0$. For $\Gamma^s=0.6$, the peak-shift effect shifts the peak height out of the region between the Fermi level of the leads and the total LDOS within the Fermi level of the leads is smaller than the LDOS for $\Gamma^s<0.6$. Hence, the differential conductance appears slightly when $V_{bias}\sim 0$ for $T=0.1T_K$ and $\Gamma^s=0.6$. This tip of the conductance occurs when $T<T_k$ in the vicinity of the Fermi level of the leads, therefore, this phenomenon mainly originates from the scattering via the Kondo channel.

IV. SUMMARY

In summary, we study the spin-flip-associated tunneling in the Anderson model. The total effect can be interpreted as follows. As Eq. (6) shows, the quasiparticle described by the Anderson Hamiltonian is scattered via the normal and the Kondo channels. The normal channel dominates the scattering of the electrons with energy far away from the Fermi level of the lead. The electrons with energy near the Fermi level of the leads are mainly scattered by the Kondo channel when $T\leqslant T_k$. Note that only the infinite-U limit approximation is used in Eq. (6), i.e., Eq. (6) is a general form for the

Anderson model with spin-flip-associated tunneling in the infinite-U limit and does not relate to the decoupling method. The spin-flip-associated tunneling via the Kondo channel causes two main effects. One is the enhancement of the Kondo resonance peak; the other is the blueshift of the Kondo resonance peak. When the temperature $T=10T_K$ and $1.0T_K$, the Kondo resonance peak is obviously enhanced by spin-flip-associated tunneling effect, but the blueshift of the Kondo resonance peak is not obvious. This effect is reflected in the conductance. The enhancement of the Kondo resonant peak causes an increase of the diagonal part of the conductance $g_{\sigma\sigma}$ and decreases the off-diagonal part of the conductance $g_{\bar{\sigma}\sigma}$ (to more negative values). Since the decrease of the off-diagonal part of the conductance is stronger than the increase of the diagonal part of the conductance; as a result the total conductance is suppressed by spin-flip-associated tunneling. The conductance due to off-diagonal processes is negative and cannot be neglected. As the temperature gets lower, the blueshift of the Kondo resonance peak becomes important. When $T \leqslant T_k$ and the spin-flip-associated coupling constant Γ_s is large enough, the blueshift of the Kondo resonance peak will cause a strong suppression of the diagonal part of the conductance and the total conductance is suppressed rapidly. The conductance suppression due to the shift of the Kondo resonance peak is ascribed to the Kondo channel mainly, since the effect occurs as $T<T_K$. The high-temperature Lacroix decoupling approximation is used to decouple the two-particle correlation function (or Green's function). Our result is quantitatively correct when $T>T_K$. The Kondo resonance peak is slightly enhanced and blueshifted as $T \geqslant T_K$. On the contrary, the Kondo resonance peak is enhanced prominently and blueshifted obviously in the case of $T=0.1T_k$. Although the decoupling approximation only gives a qualitative result for $T<T_K$, the conductance can be suppressed strongly by the spin-flip-associated tunneling effect for $T<T_K$.

ACKNOWLEDGMENT

This work is supported by the National Science Council of Taiwan under Grant No. NSC 94-2120-M-009-002.

APPENDIX A

First, we derive the general form of the Green's function for the spin-flip system. Assume that the lowest-order self-energies corresponding to the non-spin-flip transition processes $\sigma \to \sigma$ and $\bar{\sigma} \to \bar{\sigma}$ (the diagonal terms) are $\Sigma_{\sigma\sigma}$ and $\Sigma_{\bar{\sigma}\bar{\sigma}}$. And the lowest-order self-energies corresponding to the spin-flip transition processes $\bar{\sigma} \to \sigma$ and $\sigma \to \bar{\sigma}$ (the diagonal terms) are $\Sigma_{\sigma\bar{\sigma}}$ and $\Sigma_{\bar{\sigma}\sigma}$. The typical Dyson equation can be expressed as

$$\begin{bmatrix} G_{\sigma\sigma} & G_{\sigma\bar{\sigma}} \\ G_{\bar{\sigma}\sigma} & G_{\bar{\sigma}\bar{\sigma}} \end{bmatrix} = \begin{bmatrix} G^0_{\sigma\sigma} & 0 \\ 0 & G^0_{\bar{\sigma}\bar{\sigma}} \end{bmatrix} + \begin{bmatrix} G^0_{\sigma\sigma} & 0 \\ 0 & G^0_{\bar{\sigma}\bar{\sigma}} \end{bmatrix} \begin{bmatrix} \Sigma_{\sigma\sigma} & \Sigma_{\sigma\bar{\sigma}} \\ \Sigma_{\bar{\sigma}\sigma} & \Sigma_{\bar{\sigma}\bar{\sigma}} \end{bmatrix} \begin{bmatrix} G_{\sigma\sigma} & G_{\sigma\bar{\sigma}} \\ G_{\bar{\sigma}\sigma} & G_{\bar{\sigma}\bar{\sigma}} \end{bmatrix} = \begin{bmatrix} G^0_{\sigma\sigma} & 0 \\ 0 & G^0_{\bar{\sigma}\bar{\sigma}} \end{bmatrix} + \begin{bmatrix} G^0_{\sigma\sigma}\Sigma_{\sigma\sigma}G_{\sigma\sigma} + G^0_{\sigma\sigma}\Sigma_{\sigma\bar{\sigma}}G_{\bar{\sigma}\sigma} & G^0_{\sigma\sigma}\Sigma_{\sigma\sigma}G_{\sigma\bar{\sigma}} + G^0_{\sigma\sigma}\Sigma_{\sigma\bar{\sigma}}G_{\bar{\sigma}\bar{\sigma}} \\ G^0_{\bar{\sigma}\bar{\sigma}}\Sigma_{\bar{\sigma}\sigma}G_{\sigma\sigma} + G^0_{\bar{\sigma}\bar{\sigma}}\Sigma_{\bar{\sigma}\bar{\sigma}}G_{\bar{\sigma}\sigma} & G^0_{\bar{\sigma}\bar{\sigma}}\Sigma_{\bar{\sigma}\sigma}G_{\sigma\bar{\sigma}} + G^0_{\bar{\sigma}\bar{\sigma}}\Sigma_{\bar{\sigma}\bar{\sigma}}G_{\bar{\sigma}\bar{\sigma}} \end{bmatrix}. \tag{A1}$$

The off-diagonal terms can be rewritten as $G_{\sigma\bar{\sigma}}=\tilde{G}^0_{\sigma\sigma}\Sigma_{\sigma\bar{\sigma}}G_{\bar{\sigma}\bar{\sigma}}$ and $G_{\bar{\sigma}\sigma}=\tilde{G}^0_{\bar{\sigma}\bar{\sigma}}\Sigma_{\bar{\sigma}\sigma}G_{\sigma\sigma}$ where $\tilde{G}^0_{\sigma\sigma} \equiv [(G^0_{\sigma\sigma})^{-1}-\Sigma_{\sigma\sigma}]^{-1}$ and $\tilde{G}^0_{\bar{\sigma}\bar{\sigma}} \equiv [(G^0_{\bar{\sigma}\bar{\sigma}})^{-1}-\Sigma_{\bar{\sigma}\bar{\sigma}}]^{-1}$. Substitute these expressions for $G_{\sigma\bar{\sigma}}$ and $G_{\bar{\sigma}\sigma}$ into the diagonal term, Eq. (8) becomes

$$\begin{bmatrix} G_{\sigma\sigma} & G_{\sigma\bar{\sigma}} \\ G_{\bar{\sigma}\sigma} & G_{\bar{\sigma}\bar{\sigma}} \end{bmatrix} = \begin{bmatrix} [(G^0_{\sigma\sigma})^{-1} - \Sigma_{\sigma\sigma} - \Sigma_{\sigma\bar{\sigma}}\tilde{G}^0_{\bar{\sigma}\bar{\sigma}}\Sigma_{\bar{\sigma}\sigma}]^{-1} & G_{\sigma\bar{\sigma}} = \tilde{G}^0_{\sigma\sigma}\Sigma_{\sigma\bar{\sigma}}G_{\bar{\sigma}\bar{\sigma}} \\ \tilde{G}^0_{\bar{\sigma}\bar{\sigma}}\Sigma_{\bar{\sigma}\sigma}G_{\sigma\sigma} & [(G^0_{\bar{\sigma}\bar{\sigma}})^{-1} - \Sigma_{\bar{\sigma}\bar{\sigma}} - \Sigma_{\bar{\sigma}\sigma}\tilde{G}^0_{\sigma\sigma}\Sigma_{\sigma\bar{\sigma}}]^{-1} \end{bmatrix}. \tag{A2}$$

Equation (9) is the same as Eqs. (5a) and (5b) in Ref. 13 exactly.

APPENDIX B

In order to solve Eq. (4), one has to decouple the two correlation functions $\langle T\{c_{k_\alpha s}d^\dagger_{\bar{\sigma}}d_{\bar{\sigma}}, d^\dagger_\sigma\}\rangle$, $\langle T\{c^\dagger_{k_\alpha s}d_\sigma d_{\bar{\sigma}}, d^\dagger_\sigma\}\rangle$, and $\langle T\{c_{k_\alpha s}d^\dagger_{\bar{\sigma}}d_{\bar{\sigma}}, d^\dagger_\sigma\}\rangle$, etc. The decoupling scheme proposed by Lacroix in the high-temperature limit

$$\langle T\{c^\dagger_{k_\alpha s}(t)c_{k_\beta s'}(t)d_{\bar{\sigma}}(t), d^\dagger_\sigma(t')\}\rangle = \delta_{k_\alpha, k_\beta}\delta_{s,s'}f(\epsilon_{k\alpha s})\langle T\{d_{\bar{\sigma}}(t), d^\dagger_\sigma(t')\}\rangle,$$

$$\langle T\{c^\dagger_{k_\alpha s}(t)c_{k_\beta s'}(t)d_\sigma(t), d^\dagger_\sigma(t')\}\rangle = \delta_{k_\alpha, k_\beta}\delta_{s,s'}f(\epsilon_{k\alpha s})\langle T\{d_\sigma(t), d^\dagger_\sigma(t')\}\rangle,$$

$$\langle T\{c_{k_\alpha s}(t)c_{k_\beta s'}(t)d^\dagger_\sigma(t), d^\dagger_\sigma(t')\}\rangle = \langle T\{c_{k_\alpha s}(t)c_{k_\beta s'}(t)d^\dagger_{\bar{\sigma}}(t), d^\dagger_\sigma(t')\}\rangle = 0 \tag{B1}$$

is used. For example, consider the term $\langle c_{k_\alpha s}d^\dagger_{\bar{\sigma}}d_\sigma, d^\dagger_\sigma\rangle$ of Eq. (4). Using the EOM method, and Lacroix's high-temperature decoupling approximation, one obtains

$$
\begin{aligned}
&(\omega-\epsilon_{k\alpha s}-\epsilon_{\sigma}+\epsilon_{\bar{\sigma}})\langle T\{c_{k_{\alpha^s}s}d_{\bar{\sigma}}^{\dagger}d_{\sigma},d_{\sigma}^{\dagger}\}\rangle\\
&=V_{k_{\alpha^s},\sigma}\langle T\{d_{\sigma}d_{\bar{\sigma}}^{\dagger}d_{\sigma},d_{\bar{\sigma}}^{\dagger}\}\rangle+V_{k_{\alpha^s},\bar{\sigma}}\langle T\{d_{\bar{\sigma}}d_{\bar{\sigma}}^{\dagger}d_{\sigma},d_{\sigma}^{\dagger}\}\rangle\\
&\quad-\sum_{q\alpha s'}V_{q_{\alpha^{s'}},\bar{\sigma}}\langle T\{c_{k_{\alpha^s}s}c_{q_{\alpha^{s'}}}^{\dagger}d,d_{\sigma}^{\dagger}\}\rangle\\
&=-\langle d_{\bar{\sigma}}^{\dagger}d_{\sigma}\rangle V_{k_{\alpha^s},\sigma}(i)G_{\sigma\sigma}+V_{k_{\alpha^s},\bar{\sigma}}(i)(G_{\sigma\sigma}-G_{\sigma\sigma}^{(2)})\\
&\quad-\sum_{q\alpha s'}V_{q_{\alpha^{s'}},\bar{\sigma}}\langle c_{k_{\alpha^s}}c_{q_{\alpha^{s'}}}^{\dagger}\rangle(i)G_{\sigma\sigma}\delta_{k_{\alpha^s},q_{\alpha^{s'}}};
\end{aligned}
\tag{B2}
$$

thus

$$
\begin{aligned}
&-\sum_{k_{\alpha^s}}V_{k\alpha s,\bar{\sigma}}^{*}(-i)\langle c_{k_{\alpha^s}}d_{\bar{\sigma}}^{\dagger}d_{\sigma},d_{\sigma}^{\dagger}\rangle\\
&=\langle d_{\bar{\sigma}}^{\dagger}d_{\sigma}\rangle\sum_{k_{\alpha^s}}\frac{V_{k\alpha s,\bar{\sigma}}^{*}V_{k\alpha s,\sigma}}{\omega-\epsilon_{k\alpha s}-\epsilon_{\sigma}+\epsilon_{\bar{\sigma}}}G_{\sigma\sigma}\\
&\quad+\sum_{k_{\alpha^s}}\frac{|V_{k\alpha s,\bar{\sigma}}|^2}{\omega-\epsilon_{k\alpha s}-\epsilon_{\sigma}+\epsilon_{\bar{\sigma}}}(G_{\sigma\sigma}^{(2)}-G_{\sigma\sigma})\\
&\quad+\sum_{k_{\alpha^s}}\frac{|V_{k\alpha s,\bar{\sigma}}|^2}{\omega-\epsilon_{k\alpha s}-\epsilon_{\sigma}+\epsilon_{\bar{\sigma}}}[1-f_{\alpha}(\epsilon_{k\alpha s})]G_{\sigma\sigma}.
\end{aligned}
\tag{B3}
$$

In the same way, the $\langle T\{c_{k_{\alpha^s}}d_{\bar{\sigma}}^{\dagger}d_{\sigma},d_{\bar{\sigma}}^{\dagger}\}\rangle$ term of Eq. (4) is

$$
\begin{aligned}
&\sum_{k_{\alpha^s}}V_{k\alpha s,\sigma}^{*}(-i)\langle T\{c_{k_{\alpha^s}}d_{\bar{\sigma}}^{\dagger}d_{\sigma},d_{\sigma}^{\dagger}\}\rangle\\
&=\sum_{k_{\alpha^s}}\frac{|V_{k\alpha s,\sigma}|^2}{\omega-\epsilon_{k\alpha s}}G_{\sigma\sigma}^{(2)}-\langle n_{\bar{\sigma}}\rangle\frac{V_{k\alpha s,\sigma}^{*}V_{k\alpha s,\bar{\sigma}}}{\omega-\epsilon_{k\alpha s}}G_{\bar{\sigma}\sigma}\\
&\quad+\frac{V_{k\alpha s,\sigma}^{*}V_{k\alpha s,\bar{\sigma}}}{\omega-\epsilon_{k\alpha s}}f_{\alpha}(\epsilon_{k\alpha s})G_{\bar{\sigma}\sigma}
\end{aligned}
\tag{B4}
$$

and the $\langle T\{c_{k_{\alpha^s}}^{\dagger}d_{\sigma}d_{\bar{\sigma}},d_{\sigma}^{\dagger}\}\rangle$ term is

$$
\begin{aligned}
&\sum_{k_{\alpha^s}}V_{k\alpha s,\bar{\sigma}}^{*}(-i)\langle T\{c_{k_{\alpha^s}}^{\dagger}d_{\sigma}d_{\bar{\sigma}},d_{\sigma}^{\dagger}\}\rangle\\
&=\sum_{k_{\alpha^s}}-\frac{|V_{k\alpha s,\sigma}|^2}{\omega+\epsilon_{k\alpha s}-\epsilon_{\sigma}-\epsilon_{\bar{\sigma}}-U}G_{\bar{\sigma}\sigma}^{(2)}\\
&\quad-\frac{|V_{k\alpha s,\sigma}|^2}{\omega+\epsilon_{k\alpha s}-\epsilon_{\sigma}-\epsilon_{\bar{\sigma}}-U}G_{\sigma\sigma}^{(2)}\\
&\quad+\sum_{k_{\alpha^s}}\frac{|V_{k\alpha s,\sigma}|^2}{\omega+\epsilon_{k\alpha s}-\epsilon_{\sigma}-\epsilon_{\bar{\sigma}}-U}f_{\alpha}(\epsilon_{k\alpha s})G_{\bar{\sigma}\sigma}\\
&\quad+\frac{V_{k\alpha s,\bar{\sigma}}^{*}V_{k\alpha s,\sigma}}{\omega+\epsilon_{k\alpha s}-\epsilon_{\sigma}-\epsilon_{\bar{\sigma}}-U}f_{\alpha}(\epsilon_{k\alpha s})G_{\sigma\sigma}.
\end{aligned}
\tag{B5}
$$

Under the infinite-U limit, the Eq. (14) is zero. Compare to Eq. (5), The self-energy $Y_{\sigma\bar{\sigma}}^{(2)}$ transfers $G_{\bar{\sigma}\sigma}^{(2)}$ to $G_{\sigma\sigma}^{(2)}$, we can recognize that $Y_{\sigma\bar{\sigma}}^{(2)}=\Sigma_{k_{\alpha^s}}-|V_{k\alpha s,\sigma}|^2/(\omega+\epsilon_{k\alpha s}-\epsilon_{\sigma}-\epsilon_{\bar{\sigma}}-U)$ and can be ignored under the infinite-U limit. Hence the Green's function $G_{\sigma\sigma}^{(2)}$ is found as

$$
\begin{aligned}
&(\omega-\epsilon_{\sigma}-U)G_{\sigma\sigma}^{(2)}(\omega)\\
&=n_{\bar{\sigma}}+\sum_{k_{\alpha^s}}\frac{|V_{k\alpha s,\sigma}|^2}{\omega-\epsilon_{k\alpha s}}G_{\sigma\sigma}^{(2)}-\langle n_{\bar{\sigma}}\rangle\frac{V_{k\alpha s,\sigma}^{*}V_{k\alpha s,\bar{\sigma}}}{\omega-\epsilon_{k\alpha s}}G_{\bar{\sigma}\sigma}\\
&\quad+\frac{V_{k\alpha s,\sigma}^{*}V_{k\alpha s,\bar{\sigma}}}{\omega-\epsilon_{k\alpha s}}f_{\alpha}(\epsilon_{k\alpha s})G_{\bar{\sigma}\sigma}+\langle d_{\bar{\sigma}}^{\dagger}d_{\sigma}\rangle\\
&\quad\sum_{k_{\alpha^s}}\frac{V_{k\alpha s,\bar{\sigma}}^{*}V_{k\alpha s,\sigma}}{\omega-\epsilon_{k\alpha s}-\epsilon_{\sigma}+\epsilon_{\bar{\sigma}}}G_{\sigma\sigma}+\frac{|V_{k\alpha s,\bar{\sigma}}|^2}{\omega-\epsilon_{k\alpha s}-\epsilon_{\sigma}+\epsilon_{\bar{\sigma}}}(G_{\sigma\sigma}^{(2)}\\
&\quad-G_{\sigma\sigma})+\frac{|V_{k\alpha s,\bar{\sigma}}|^2}{\omega-\epsilon_{k\alpha s}-\epsilon_{\sigma}+\epsilon_{\bar{\sigma}}}[1-f_{\alpha}(\epsilon_{k\alpha s})]G_{\sigma\sigma}\equiv Y_{\sigma\sigma}^{(2)}G_{\sigma\sigma}^{(2)}\\
&\quad+X_{\sigma\sigma}^{(2)}G_{\sigma\sigma}+X_{\sigma\bar{\sigma}}^{(2)}G_{\bar{\sigma}\sigma}
\end{aligned}
\tag{B6}
$$

where

$$
Y_{\sigma\sigma}^{(2)}\equiv\sum_{k_{\alpha^s}}\frac{|V_{k\alpha s,\sigma}|^2}{\omega-\epsilon_{k\alpha s}}+\frac{|V_{k\alpha s,\bar{\sigma}}|^2}{\omega-\epsilon_{k\alpha s}-\epsilon_{\sigma}+\epsilon_{\bar{\sigma}}},
$$

$$
\begin{aligned}
X_{\sigma\sigma}^{(2)}&\equiv\sum_{k_{\alpha^s}}\langle d_{\bar{\sigma}}^{\dagger}d_{\sigma}\rangle\frac{V_{k\alpha s,\sigma}^{*}V_{k\alpha s,\bar{\sigma}}}{\omega-\epsilon_{k\alpha s}-\epsilon_{\sigma}+\epsilon_{\bar{\sigma}}}\\
&\quad-\frac{|V_{k\alpha s,\bar{\sigma}}|^2}{\omega-\epsilon_{k\alpha s}-\epsilon_{\sigma}+\epsilon_{\bar{\sigma}}}f_{\alpha}(\epsilon_{k\alpha s}),
\end{aligned}
$$

$$
X_{\sigma\bar{\sigma}}^{(2)}=\sum_{k_{\alpha^s}}-\langle n_{\bar{\sigma}}\rangle\frac{V_{k\alpha s,\sigma}^{*}V_{k\alpha s,\bar{\sigma}}}{\omega-\epsilon_{k\alpha s}}+\frac{V_{k\alpha s,\sigma}^{*}V_{k\alpha s,\bar{\sigma}}}{\omega-\epsilon_{k\alpha s}}f_{\alpha}(\epsilon_{k\alpha s}).
\tag{B7}
$$

APPENDIX C

In this appendix, we will show the detailed derivation of the expressions for $\langle n_{\sigma}\rangle$ and $\langle n_{\bar{\sigma}\sigma}\rangle$. We follow the derivation proposed by Sun and Guo. Since the system considered in this paper is in steady state, the first derivation of the expectation values of $\langle d_{\sigma}^{\dagger}d_{\sigma}\rangle$ and $\langle d_{\bar{\sigma}}^{\dagger}d_{\sigma}\rangle$ over time is zero, i.e., $\langle i(\partial/\partial t)[d_{\sigma}^{\dagger}d_{\sigma}]\rangle=0$. Using the equation of motion method, one can find the time evolution of particle number $\langle d_{\sigma}^{\dagger}d_{\sigma}\rangle$ as

Hence,

$$
\left\langle i\frac{\partial}{\partial t}[d_{\sigma}^{\dagger}d_{\sigma}]\right\rangle=\sum_{k\alpha s}-V_{k\alpha s,\sigma}\langle c_{k\alpha s}^{\dagger}d_{\sigma}\rangle+V_{k\alpha s,\sigma}^{*}\langle d_{\sigma}^{\dagger}c_{k\alpha s}\rangle=0
\tag{C1}
$$

where $\langle c_{k\alpha s}^{\dagger}d_{\sigma}\rangle=-i\int(d\epsilon/2\pi)G_{\sigma,k\alpha s}^{<}(\varepsilon)$ and $\langle d_{\sigma}^{\dagger}c_{k\alpha s}\rangle=-i\int(d\epsilon/2\pi)G_{k\alpha s,\sigma}^{<}(\varepsilon)$. The lesser Green's functions $G_{\sigma,k\alpha s}^{<}(\varepsilon)$ and $G_{k\alpha s,\sigma}^{<}(\varepsilon)$ can be easily calculated by the Dyson expansion and Langreth theorem. In order to calculate the lesser Green's function, the contour-ordered Green's function must be found first. The contour Green's function $G_{k\alpha s,\sigma}(t,t')$ is

$$G_{k\alpha s,\sigma}(t,t') = -iT\langle c_{k\alpha s}(t)d^{\dagger}_{\sigma}(t')\rangle$$
$$= (-i)^2 T\int d\tau[V_{k\alpha s,\sigma}\langle c_{k\alpha s}(t)c^{\dagger}_{k\alpha s}(\tau)\rangle\langle d_{\sigma}d^{\dagger}_{\sigma}(t')\rangle$$
$$+ V_{k\alpha s,\bar{\sigma}}\langle c_{k\alpha s}(t)c^{\dagger}_{k\alpha s}(\tau)\rangle\langle d_{\bar{\sigma}}d^{\dagger}_{\sigma}(t')\rangle]$$
$$= T\int d\tau[V_{k\alpha s,\sigma}g_{k\alpha s}(t,\tau)G_{\sigma\sigma}(\tau,t')$$
$$+ V_{k\alpha s,\bar{\sigma}}g_{k\alpha s}(t,\tau)G_{\bar{\sigma}\sigma}(\tau,t')]. \quad \text{(C2)}$$

Then, using the Fourier transformation and Langreth theorem, the lesser Green's function $G^{<}_{k\alpha s,\sigma}$ is obtained:

$$G^{<}_{k\alpha s,\sigma} = V_{k\alpha s,\sigma}(g^{r}_{k\alpha s}G^{<}_{\sigma\sigma} + g^{<}_{k\alpha s}G^{a}_{\sigma\sigma}) + V_{k\alpha s,\bar{\sigma}}(g^{r}_{k\alpha s}G^{<}_{\bar{\sigma}\sigma}$$
$$+ g^{<}_{k\alpha s}G^{a}_{\bar{\sigma}\sigma}). \quad \text{(C3)}$$

In the same way, the lesser Green's function $G^{<}_{\sigma,k\alpha s}$ is

$$G^{<}_{\sigma,k\alpha s} = V^{*}_{k\alpha s,\sigma}(G^{r}_{\sigma\sigma}g^{<}_{k\alpha s} + G^{<}_{\sigma\sigma}g^{a}_{k\alpha s}) + V^{*}_{k\alpha s,\bar{\sigma}}(G^{r}_{\sigma\bar{\sigma}}g^{<}_{k\alpha s}$$
$$+ G^{<}_{\sigma\bar{\sigma}}g^{a}_{k\alpha s}). \quad \text{(C4)}$$

Substituting Eqs. (C3) and (C4) into Eq. (C1), one can obtain

$$\sum_{k_{\alpha}s}\int\frac{d\epsilon}{2\pi}V^{*}_{k_{\alpha}s,\sigma}V_{k_{\alpha}s,\sigma}[G^{r}_{\sigma\sigma}g^{<}_{k_{\alpha}s}(\epsilon) + G^{<}_{\sigma\sigma}(\epsilon)g^{a}_{k_{\alpha}s}(\epsilon)]$$
$$+ V^{*}_{k_{\alpha}s,\bar{\sigma}}V_{k_{\alpha}s,\sigma}[G^{r}_{\sigma\bar{\sigma}}(\epsilon)g^{<}_{k_{\alpha}s} + G^{<}_{\sigma\bar{\sigma}}(\epsilon)g^{a}_{k_{\alpha}s}]$$
$$= \sum_{k_{\alpha}s}\int\frac{d\epsilon}{2\pi}V^{*}_{k_{\alpha}s,\sigma}V_{k_{\alpha}s,\sigma}(g^{r}_{k_{\alpha}s}G^{<}_{\sigma\sigma} + g^{<}_{k_{\alpha}s}G^{a}_{\sigma\sigma})$$
$$+ V^{*}_{k_{\alpha}s,\bar{\sigma}}V_{k_{\alpha}s,\sigma}(g^{r}_{k_{\alpha}s}G^{<}_{\bar{\sigma}\sigma} + g^{<}_{k_{\alpha}s}G^{a}_{\bar{\sigma}\sigma}). \quad \text{(C5)}$$

Using the relations $\Sigma_{k_{\alpha}s}V^{*}_{k_{\alpha}s,\sigma}V_{k_{\alpha}s,\sigma}g^{r,a}_{k_{\alpha}s} = \Sigma_{\alpha}\mp i(\Gamma^{\alpha}_{n}/2)$, $\Sigma_{k_{\alpha}s}V^{*}_{k_{\alpha}s,\bar{\sigma}}V_{k_{\alpha}s,\sigma}g^{r,a}_{k_{\alpha}s} = \Sigma_{\alpha}\mp i(\Gamma^{\alpha}_{s}/2)$, $\Sigma_{k_{\alpha}s}V^{*}_{k_{\alpha}s,\sigma}V_{k_{\alpha}s,\sigma}g^{<}_{k_{\alpha}s}(\epsilon) = i\Sigma_{\alpha}\Gamma^{\alpha}_{n}f_{\alpha}(\epsilon)$, and $\Sigma_{k_{\alpha}s}V^{*}_{k_{\alpha}s,\bar{\sigma}}V_{k_{\alpha}s,\sigma}g^{<}_{k\alpha s}(\epsilon) = i\Sigma_{\alpha}\Gamma^{\alpha}_{s}f_{\alpha}(\epsilon)$, and after some simple algebra, one finds

$$(\Gamma^{2}_{n} - \Gamma^{2}_{s})\int\frac{d\epsilon}{2\pi}G^{<}_{\sigma\sigma}(\epsilon)$$
$$= \Gamma_{n}\left(\sum_{\alpha} -i\Gamma^{\alpha}_{n}\int\frac{d\epsilon}{2\pi}f_{\alpha}(\epsilon)[2\ \mathrm{Im}\ G^{r}_{\sigma\sigma}(\epsilon)]\right.$$
$$\left. - i\Gamma^{\alpha}_{s}\int\frac{d\epsilon}{2\pi}f_{\alpha}(\epsilon)[2\ \mathrm{Im}\ G^{r}_{\bar{\sigma}\sigma}(\epsilon)]\right)$$
$$- \Gamma_{s}\left(\sum_{\alpha} -i\Gamma^{\alpha}_{s}\int\frac{d\epsilon}{2\pi}f_{\alpha}(\epsilon)[2\ \mathrm{Im}\ G^{r}_{\sigma\sigma}(\epsilon)]\right.$$
$$\left. - i\Gamma^{\alpha}_{n}\int\frac{d\epsilon}{2\pi}f_{\alpha}(\epsilon)[2\ \mathrm{Im}\ G^{r}_{\bar{\sigma}\sigma}(\epsilon)]\right) \quad \text{(C6)}$$

where $\Gamma_{n} = \Sigma_{\alpha}\Gamma^{\alpha}_{n}$ and $\Gamma_{s} = \Sigma_{\alpha}\Gamma^{\alpha}_{s}$. In Eq. (C6), we have used the relation $G^{r,a,<}_{\bar{\sigma}\sigma}(\epsilon) = G^{r,a,<}_{\sigma\bar{\sigma}}(\epsilon)$ since the spin states are degenerate in the QD. In the same way for treating $\langle i(\partial/\partial t)\times[d^{\dagger}_{\sigma}d_{\sigma}]\rangle = 0$, with the condition $\langle i(\partial/\partial t)[d^{\dagger}_{\bar{\sigma}}d_{\sigma}]\rangle = 0$, one obtains the relation

$$(\Gamma^{2}_{n} - \Gamma^{2}_{s})\int\frac{d\epsilon}{2\pi}G^{<}_{\bar{\sigma}\sigma}(\epsilon)$$
$$= \Gamma_{n}\left(\sum_{\alpha} -i\Gamma^{\alpha}_{s}\int\frac{d\epsilon}{2\pi}f_{\alpha}(\epsilon)[2\ \mathrm{Im}\ G^{r}_{\sigma\sigma}(\epsilon)]\right.$$
$$\left. - i\Gamma^{\alpha}_{n}\int\frac{d\epsilon}{2\pi}f_{\alpha}(\epsilon)[2\ \mathrm{Im}\ G^{r}_{\bar{\sigma}\sigma}(\epsilon)]\right)$$
$$- \Gamma_{s}\left(\sum_{\alpha} -i\Gamma^{\alpha}_{n}\int\frac{d\epsilon}{2\pi}f_{\alpha}(\epsilon)\big[2\ \mathrm{Im}\ G^{r}_{\sigma\sigma}(\epsilon)\big]\right.$$
$$\left. - i\Gamma^{\alpha}_{s}\int\frac{d\epsilon}{2\pi}f_{\alpha}(\epsilon)[2\ \mathrm{Im}G^{r}_{\bar{\sigma}\sigma}(\epsilon)]\right). \quad \text{(C7)}$$

Since the retarded (advanced) Green's functions have been solved, the equations for $\int(d\epsilon/2\pi)G^{<}_{\sigma\sigma}(\epsilon)$ and $\int(d\epsilon/2\pi)G^{<}_{\bar{\sigma}\sigma}(\epsilon)$ can be solved also. The results can be checked by taking the equilibrium limit, i.e., $f_{R}(\epsilon) = f_{L}(\epsilon) = f(\epsilon)$,

$$\langle n_{\sigma}\rangle = -i\int\frac{d\epsilon}{2\pi}G^{<}_{\sigma\sigma}(\epsilon) = \int\frac{d\epsilon}{2\pi}f_{\alpha}(\epsilon)[-2\ \mathrm{Im}\ G^{r}_{\sigma\sigma}(\epsilon)] \quad \text{(C8)}$$

and

$$\langle d^{\dagger}_{\bar{\sigma}}d_{\sigma}\rangle = -i\int\frac{d\epsilon}{2\pi}G^{<}_{\bar{\sigma}\sigma}(\epsilon) = \int\frac{d\epsilon}{2\pi}f_{\alpha}(\epsilon)[-2\ \mathrm{Im}\ G^{r}_{\bar{\sigma}\sigma}(\epsilon)]. \quad \text{(C9)}$$

Equations (C8) and (C9) show that Eqs. (C6) and (C7) obey the fluctuation-dissipation theorem at the equilibrium limit:

$$\Gamma_{n}\int\frac{d\epsilon}{2\pi}G^{<}_{\sigma\sigma}(\epsilon) + \Gamma_{s}\int\frac{d\epsilon}{2\pi}G^{<}_{\sigma\bar{\sigma}}(\epsilon)$$
$$= \sum_{\alpha} -\Gamma^{\alpha}_{n}\int\frac{d\epsilon}{2\pi}f_{\alpha}(\epsilon)[G^{r}_{\sigma\sigma}(\epsilon) - G^{a}_{\sigma\sigma}(\epsilon)]$$
$$- \Gamma^{\alpha}_{s}\int\frac{d\epsilon}{2\pi}f_{\alpha}(\epsilon)[G^{r}_{\bar{\sigma}\sigma}(\epsilon) - G^{a}_{\bar{\sigma}\sigma}(\epsilon)], \quad \text{(C10)}$$

$$\Gamma_{s}\int\frac{d\epsilon}{2\pi}G^{<}_{\sigma\sigma}(\epsilon) + \Gamma_{n}\int\frac{d\epsilon}{2\pi}G^{<}_{\sigma\bar{\sigma}}(\epsilon)$$
$$= \sum_{\alpha} -\Gamma^{\alpha}_{s}\int\frac{d\epsilon}{2\pi}f_{\alpha}(\epsilon)[G^{r}_{\sigma\sigma}(\epsilon) - G^{a}_{\sigma\sigma}(\epsilon)]$$
$$- \Gamma^{\alpha}_{n}\int\frac{d\epsilon}{2\pi}f_{\alpha}(\epsilon)[G^{r}_{\sigma\sigma}(\epsilon) - G^{a}_{\sigma\bar{\sigma}}(\epsilon)]. \quad \text{(C11)}$$

[1] M. Dax, Semicond. Int. **20**, 84 (1997).
[2] H. X. Tang, F. G. Monzon, Ron Lifshitz, M. C. Cross, and M. L. Roukes, Phys. Rev. B **61**, 4437 (2000); X. F. Wang, P. Vasilopoulos and F. M. Peeters, *ibid.* **65**, 165217 (2002).
[3] B. E. Kane, Nature (London) **393**, 133 (1998).
[4] S. Bandyopadhyay, Phys. Rev. B **61**, 13813 (2000).
[5] F. Guinea, Phys. Rev. B **58**, 9212 (1998).
[6] A. V. Akimov, A. V. Scherbakov, D. R. Yakovlev, W. Ossau, L. W. Molenkamp, T. Wojtowicz, J. Kossut, S. Tatarenko, and J. Cibert, Physica B **316-317**, 41 (2002).
[7] F. T. Vasko and O. Keller, Phys. Rev. B **58**, 15666 (1998).
[8] P. Zhang, Q. K. Xue, Y. P. Wang, and X. C. Xie, Phys. Rev. Lett. **89**, 286803 (2002).
[9] N. Sergueev, Qing-feng Sun, Hong Guo, B. G. Wang, and Jian Wang, Phys. Rev. B **65**, 165303 (2002).
[10] J. Martinek, Y. Utsumi, H. Imamura, J. Barnas, S. Maekawa, J. Konig, and G. Schon, Phys. Rev. Lett. **91**, 127203 (2003).
[11] Bing Dong, H. L. Cui, S. Y. Liu, and X. L. Lei, J. Phys.: Condens. Matter **15**, 8435 (2003).
[12] J. Martinek, M. Sindel, L. Borda, J. Barnas, J. Konig, G. Schon, and J. von Delft, Phys. Rev. Lett. **91**, 247202 (2003).
[13] Jian-Xin Zhu and A. V. Balatsky, Phys. Rev. Lett. **89**, 286802 (2002).
[14] L. I. Glazman and M. E. Raikh, Pis'ma Zh. Eksp. Teor. Fiz. **47**, 378 (1988) [JETP Lett. **47**, 452 (1988)]; Tai Kai Ng and Patrick A. Lee, Phys. Rev. Lett. **61**, 1768 (1988).
[15] P. W. Anderson, Phys. Rev. **124**, 41 (1961).
[16] L. Kouwenhoven and L. Glazman, Phys. World **14** (1), 33 (2001).
[17] J. R. Schrieffer and P. A. Wolff, Phys. Rev. **149**, 491 (1966).
[18] Ned S. Wingreen, and Yigal Meir, Phys. Rev. B **49**, 11040 (1994).
[19] C. Lacroix, J. Phys. F: Met. Phys. **11**, 2389 (1981).
[20] Yigal Meir, Ned S. Wingreen, and Patrick A. Lee, Phys. Rev. Lett. **70**, 2601 (1993).
[21] Kicheon Kang and B. I. Min, Phys. Rev. B **52**, 10689 (1995).
[22] H.-G. Luo, Z.-J. Ying, and S.-J. Wang, Phys. Rev. B **59**, 9710 (1999).
[23] T. A. Costi, A. C. Hewson, and V. Zlatic, J. Phys.: Condens. Matter **6**, 2519 (1994).
[24] Qing-feng Sun and Hong Guo, Phys. Rev. B **66**, 155308 (2002).
[25] Antti-Pekka Jauho, Ned S. Wingreen, and Yigal Meir, Phys. Rev. B **50**, 5528 (1994).
[26] F. D. M. Haldane, Ph.D. thesis, University of Cambridge, 1987; Phys. Rev. Lett. **40**, 416 (1978).
[27] The temperature of interest in Ref. 20 is an order of 2 lower than the Kondo temperature; however, the temperature considered in our work is about one-tenth of the Kondo temperature, Therefore, our decoupling approach sounds reasonable.

Rotational states of an adsorbed dipole molecule in an external electric field

Y. T. Shih*
Graduate Institute of Opto-electronic Engineering, National Changhua University of Education, Changhua, Taiwan 50058, Republic of China

Y. Y. Liao and D. S. Chuu†
Institute of Electrophysics, National Chiao Tung University, Hsinchu, Taiwan 30050, Republic of China
(Received 15 February 2002; revised manuscript received 3 March 2003; published 7 August 2003)

The rotational states of an adsorbed dipole molecule in an external electric field were investigated. The surface hindering potential was modeled as a finite conical well and a dipole-field interaction was added to the hindering potential. The molecular wave functions were expressed in terms of the eigenfunctions of molecular hindered rotation in the absence of electric field. Eigenenergies were determined by the matrix diagonalization procedures. Our results showed that, for both vertically and horizontally adsorbed molecules, there is avoided crossing between two adjacent rotational energy levels, as the field strength is increased, and finally all state energies decrease rapidly as the field strength is strong enough. The avoided crossing is due to the redistribution of wave function between different potential well regions. By employing the sudden unhindrance approximation, the rotational-state distributions of molecules desorbing from a solid surface in the presence of external electric field were calculated. Our results showed that the rotational-state distributions are significantly influenced by the external electric field. Since the electric field increases the ground-state energy of adsorbed molecule, the distribution shifts towards the high-J region if the electric field is applied to orient the molecular axis against the molecular preferred orientation. On the contrary, the distribution shifts towards the low-J region if the electric field is applied to orient the molecular axis towards molecular preferred orientation because the electric field decreases the ground-state energy of adsorbed molecule. The solutions to the finite conical well were also used to calculate the rotational alignment in the photodesorption of CO from $Cr_2O_3(0001)$. Our results showed that at low-J values the CO molecules desorb like a helicopter, while at high-J values a cartwheel-like motion is preferred. This result is in qualitative agreement with the experimental observation.

DOI: 10.1103/PhysRevB.68.075402 PACS number(s): 73.20.Hb, 33.55.Be, 33.20.Sn

I. INTRODUCTION

The rotational motion of a molecule that interacts with a solid surface has attracted increasing interest. Experimental and theoretical investigations of the rotational distribution of scattering or desorbing molecules have been an active research field.[1–18] The measured rotational-state distributions of molecules scattering or desorbing from surfaces were found to exhibit a substrate temperature-independent non-Boltzmann feature.[1–3] On the other hand, the theoretical studies on the rotational motion of adsorbed molecules have been also reported. Gadzuk and his co-workers[4–7] proposed an infinite-conical-well model, in which the adsorbed molecule is only allowed to rotate within the well region, to mimic the surface hindering potential. Rotational-state energy spectra for both vertical and horizontal adsorption configurations were obtained. Together with the sudden unhindrance approximation, the non-Boltzmann property of the rotational-state distributions can be attributed to the hindered rotations of adsorbed molecules. In our previous works,[8–10] we proposed a finite-conical-well model to generalize the study of a finite hindrance. Our results showed that the rotational-state distributions of desorbing molecules are non-Boltzmann and display oscillatory structures with alternate drops and plateaus. A similar structure was observed in a gas-surface scattering experiment and was interpreted in terms of rotational rainbows.[19] The oscillatory structure obtained in our previous studies is a general result of a system transiting from hindered states to free states, and can be regarded as the manifestation of the rotational invariance. Our calculated results have been found in good agreement with the previously measured data.[3]

The surface physics and chemistry in high electric fields have attracted great interest since the inventions of field emission microscope (FEM)[20] and field ion microscope (FIM).[21] In these microscopes, a strong electric field of the order of 1 V/Å is applied to the tip of a sharp metal wire. In such high electric field, many effects can occur. For example, the tunneling through a field-deformed barrier at the surface of the metal is possible. This is responsible for the field emission, field ionization, and field desorption/evaporation processes.[22,23] On the other hand, in a strong electric field of the order of 10^{-1} V/Å, the electronic orbitals may be distorted so that the chemical characteristics of atoms or molecules are affected. Therefore, the chemical effects by establishing new bonding orbitals may occur. In this way, molecules that are unstable in field free situations may be stabilized by strong electric field. Also, new pathways of chemical reaction may be established.[24]

It is well known that the rotational energy levels of a free molecule placed in an electric field are split due to the interaction between molecular dipole moment and electric field.[25] In addition to the splittings, theoretical investigation[26] showed that, when the applied electric field is strong, mo-

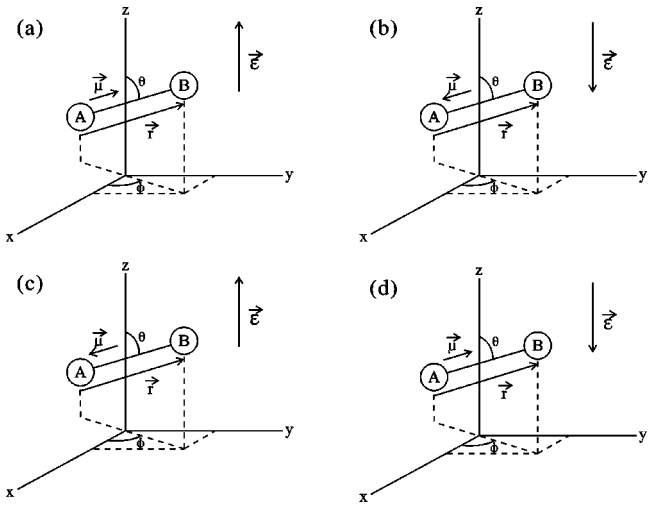

FIG. 1. An adsorbed diatomic molecule with a dipole moment $\vec{\mu}$ in the presence of perpendicular electric field $\vec{\varepsilon}$.

lecular rotational energies have large negative shifts. On the other hand, in our previous work,[9] we have investigated the external electric field effect on the ground-rotational-state energy of an adsorbed dipole molecule. We considered that an dipole-field interaction was added to the finite-conical-well potential. Our results showed that the Stark shift of ground-rotational-state energy will be suppressed by the conical-well potential if the field strength is smaller than the hindering potential. However, when the applied field is very strong, large Stark shift may take place.

In our previous investigation, the variational method was utilized and only the Stark shift of ground-state energy of horizontally adsorbed molecule was considered. In this work, we extended the investigation to the Stark shift of the excited rotational states for both cases of vertically and horizontally adsorbed molecules. Instead of using variational wave functions, the molecular wave functions we used in this work were expressed in terms of the eigenfunctions of molecular hindered rotation in the absence of electric field. Therefore, ground state and excited state energies can be determined simultaneously. One can see that the Stark shifts of rotational energies of adsorbed molecules show interesting behaviors. Besides, the rotational-state distributions of molecules desorbing from a solid surface in the presence of external electric field can be calculated. One can see the distributions are significantly influenced by the applied electric field.

II. MODEL AND FORMULISM

Figure 1 shows the situations that an adsorbed diatomic molecule with a dipole moment $\vec{\mu}$ in the presence of perpendicular electric field $\vec{\varepsilon}$. The Hamiltonian of such system is

$$H=\frac{\hbar^2}{2I}L^2+U^{\mathrm{rot}}(\theta,\phi)-\mu\varepsilon\cos\gamma, \tag{1}$$

where I is the molecular moment of inertia, $\hbar L$ is the angular momentum operator, γ is the angle between $\vec{\mu}$ and $\vec{\varepsilon}$, and $U^{\mathrm{rot}}(\theta,\phi)$ is the surface potential energy to which the molecule is subjected. As a first approximation we assume that $U^{\mathrm{rot}}(\theta,\phi)$ is independent of ϕ. Calculation indicates that the dependence on ϕ is weaker than that on θ.[27–29] We express the energy in the unit of the molecular rotational constant $B=\hbar^2/2I$; thus, Eq. (1) can be written as

$$H=L^2+V^{\mathrm{hin}}(\theta)-\omega\cos\theta, \tag{2}$$

where $V^{\mathrm{hin}}(\theta)$ is the polar hindering potential energy to which the molecule is subjected. According to the finite-conical-well model,[8–10] we assume

$$V^{\mathrm{hin}}(\theta)=\begin{cases}0, & 0\leqslant\theta\leqslant\alpha\\ V_0, & \alpha<\theta\leqslant\pi,\end{cases} \tag{3}$$

for the vertical adsorption configuration, and

$$V^{\mathrm{hin}}(\theta)=\begin{cases}0, & \alpha\leqslant\theta\leqslant\beta\\ V_0, & 0\leqslant\theta<\alpha \ \text{ or } \ \beta<\theta\leqslant\pi,\end{cases} \tag{4}$$

for the horizontal adsorption configuration. The parameter ω in Eq. (2) presents the strength of the dipole-field interaction:

$$\omega=\begin{cases}+\mu\varepsilon/B, & \gamma=\theta\\ -\mu\varepsilon/B, & \gamma=\pi-\theta.\end{cases} \tag{5}$$

The positive sign is for the cases of Figs. 1(a) and 1(b), while the negative sign is for the cases of Figs. 1(c) and 1(d). Therefore, $\omega>0$ means the electric field orients the molecular axis toward molecular preferred orientation, while $\omega<0$ means the electric field orients the molecular axis against molecular preferred orientation.

For the case that the applied electric field is absent, the Hamiltonian of the system is

$$H_0=L^2+V^{\mathrm{hin}}(\theta). \tag{6}$$

There are analytic eigenfunctions for this system:[8–10]

$$\Psi^{(0)}_{l,m}(\theta,\phi)=\Theta^{(0)}_{l,m}(\cos\theta)\frac{\exp(im\phi)}{\sqrt{2\pi}}, \quad m=0,\pm1,\pm2,\ldots, \tag{7}$$

where

$$\Theta^{(0)}_{l,m}(\xi)=\begin{cases}C_{\mathrm{I},l,m}\mathcal{P}_{(+1)}(\nu_{l,m},m,\xi), & \cos\alpha<\xi\leqslant1\\ C_{\mathrm{II},l,m}\mathcal{P}_{(-1)}(\nu'_{l,m},m,\xi), & -1\leqslant\xi<\cos\alpha,\end{cases} \tag{8}$$

for vertical adsorption configuration, and

$$\Theta^{(0)}_{l,m}(\xi)=\begin{cases}C_{\mathrm{I},l,m}\mathcal{P}_{(+1)}(\nu'_{l,m},m,\xi), & \cos\alpha<\xi\leqslant1\\ C_{\mathrm{II},l,m}\mathcal{P}_{(+1)}(\nu_{l,m},m,\xi)+D_{\mathrm{II},\nu,,m}\mathcal{Q}_{(+1)}(\nu_{l,m},m,\xi), & \cos\beta\leqslant\xi\leqslant\cos\alpha\\ C_{\mathrm{III},l,m}\mathcal{P}_{(-1)}(\nu'_{l,m},m,\xi), & -1\leqslant\xi<\cos\beta,\end{cases} \tag{9}$$

for horizontal adsorption configuration. The functions $\mathcal{P}_{(\pm 1)}$ and $\mathcal{Q}_{(+1)}$ in the above equations are defined as

$$\mathcal{P}_{(\pm 1)}(\nu_{l,m},m,\xi)=(1-\xi^2)^{|m|/2}F\left(|m|-\nu_{l,m},1+|m|+\nu_{l,m},1+|m|;\frac{1\mp\xi}{2}\right), \tag{10}$$

$$\begin{aligned}\mathcal{Q}_{(+1)}(\nu'_{l,m},m,\xi)=(1-\xi^2)^{|m|/2}\Bigg\{ & F\left(|m|-\nu'_{l,m},1+|m|+\nu'_{l,m},1+|m|;\frac{1-\xi}{2}\right)\ln\left(\frac{1-\xi}{2}\right)\\ & +\sum_{n=1}^{\infty}\frac{(|m|-\nu'_{l,m})_n(1+|m|+\nu'_{l,m})_n}{(1+|m|)_n n!}\left(\frac{1-\xi}{2}\right)^n\\ & \times[\psi(|m|-\nu'_{l,m}+n)-\psi(|m|-\nu'_{l,m})+\psi(1+|m|+\nu'_{l,m}+n)-\psi(1+|m|+\nu'_{l,m})\\ & -\psi(1+|m|+n)+\psi(1+|m|)-\psi(1+n)+\psi(1)]\\ & -\sum_{n=1}^{|m|}\frac{(n-1)!(-|m|)_n}{(1-|m|+\nu'_{l,m})_n(-|m|-\nu'_{l,m})_n}\left(\frac{1-\xi}{2}\right)^{-n}\Bigg\},\end{aligned} \tag{11}$$

where $F(a,b,c;z)$ is the hypergeometric function.[30] In above equations, the molecular rotational energy has been expressed as

$$E^{(0)}_{l,m}=\nu_{l,m}(\nu_{l,m}+1), \tag{12}$$

and $\nu'_{l,m}$ is defined as

$$\nu'_{l,m}(\nu'_{l,m}+1)=\nu_{l,m}(\nu_{l,m}+1)-V_0. \tag{13}$$

In order to determine $\nu_{l,m}$, one has to match the boundary conditions at $\xi_1=\cos\alpha$ and $\xi_2=\cos\beta$.

When the electric field is applied, there are no analytic eigenfunctions to the Hamiltonian, as shown in Eq. (2). However, consider that the system is still symmetric about z axis, we can express the eigenfunctions in terms of Eq. (7) for specific azimuthal quantum number m:

$$\Psi^{\rm hin}_m(\theta,\phi)=\sum_{l'=m}^{\infty}c_{l',m}\Psi^{(0)}_{l',m}(\theta,\phi). \tag{14}$$

Substitute Eq. (14) into the Schrödinger wave equation, and multiply both sides of the equation by $\Psi^{(0)}_{l,m}{}^*$ and then integrate it. We get

$$[E^{(0)}_{l,m}-E_m]c_{l,m}-\omega\sum_{l'}c_{l',m}\langle\Psi^{(0)}_{l,m}|\cos\theta|\Psi^{(0)}_{l',m}\rangle=0. \tag{15}$$

The condition for nontrivial coefficients $c_{l',m}$ is, therefore,

$$\begin{vmatrix} E^{(0)}_{m,m}-E_m-\omega a^{m,m}_{m,m} & -\omega a^{m+1,m}_{m,m} & -\omega a^{m+2,m}_{m,m} & \cdots\\ -\omega a^{m,m}_{m+1,m} & E^{(0)}_{m+1,m}-E_m-\omega a^{m+1,m}_{m+1,m} & -\omega a^{m+2,m}_{m+1,m} & \cdots\\ -\omega a^{m,m}_{m+2,m} & -\omega a^{m+1,m}_{m+2,m} & E^{(0)}_{m+2,m}-E_m-\omega a^{m+2,m}_{m+2,m} & \cdots\\ \vdots & \vdots & \vdots & \ddots \end{vmatrix}=0, \tag{16}$$

where $a^{l',m}_{l,m}=\langle\Psi^{(0)}_{l,m}|\cos\theta|\Psi^{(0)}_{l',m}\rangle$. The eigenenergy E_m to Eq. (2) for specific azimuthal quantum number m can be obtained from solving this equation.

III. RESULTS AND DISCUSSION

A. Vertical adsorption configuration

For a vertically adsorbed molecule, the hindering potential energy can be modeled by Eq. (3). Figure 2 shows the rotational-state energies of a vertically adsorbed dipole molecule in an external electric field as functions of field strength parameter $\omega>0$ for azimuthal quantum number $m=0$ and potential barrier heights $V_0=20$ and 80. The hindrance angle is set as $\alpha=30°$. From Fig. 2, one can see that an applied electric field can induce shifts of adsorbed molecular rotational energies. When the electric field is increased, the ground-state energy decreases monotonously while the excited-state energies increase to a maximum and then decrease. The rate of the energy variation depends on

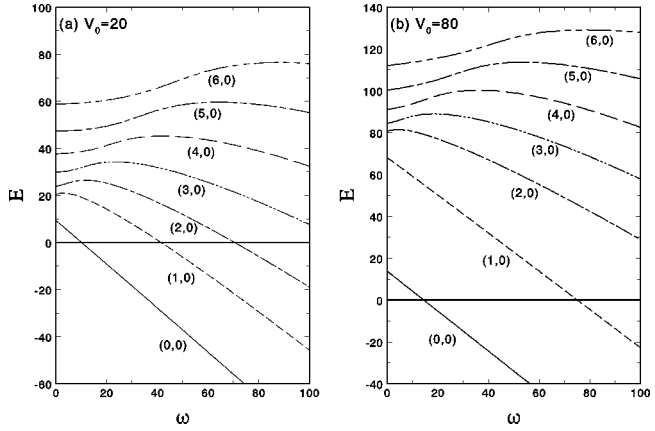

FIG. 2. Rotational-state energies of a vertically adsorbed dipole molecule in an external electric field as functions of field strength parameter $\omega>0$ for azimuthal quantum number $m=0$ and potential barrier heights $V_0=20$ and 80. The hindrance angle is set as $\alpha=30°$.

the rotational state. The lower the state, the larger the rate. The behaviors of the rotational energies shown in Fig. 2 are similar to those of free dipole molecule in an electric field.[26] However, if the potential barrier is high enough, even the lower excited-state energies, e.g., the energy of (1, 0) state of the $V_0=80$ case, show direct decreasing as the electric field is increased. This is different from that of a free dipole molecule.

Figure 3 shows the rotational-state energies of a vertically adsorbed dipole molecule in an external electric field as functions of field strength parameter $\omega<0$ for azimuthal quantum number $m=0$ and potential barrier heights $V_0=20$ and 80. From Fig. 3 one can see that the variations of rotational energies for the case of $\omega<0$ are very different from those for the case of $\omega>0$. When the electric field is applied, the ground-state energy increases initially and then decreases as the field strength is stronger than some critical value. However, for the first excited (1, 0) state of the $V_0=20$ case, the energy decreases initially and then increases to avoid the crossing of two energy levels at the same field strength. The avoided crossing between two levels also makes the ground-state energy to start to decrease at the same field strength. Finally, the energy of the (1, 0) state decreases again for field strength stronger than another critical value. On the other hand, for the first excited (1, 0) state of the $V_0=80$ case, the energy increases initially and then decreases at some critical field strength and then increases again to avoid crossing with the ground-state energy level. The avoided crossing also makes the ground-state energy to start to decrease at the same field strength. Finally, further decrease occurs for field strength stronger than another critical value. In Fig. 3, there are two or more avoided crossings for the other excited-state energies. The avoided crossing of two energy levels is a general result for the case of two very close levels with small perturbation where the Hamiltonian contains some parameter and its eigenvalues are consequently functions of that parameter.[31]

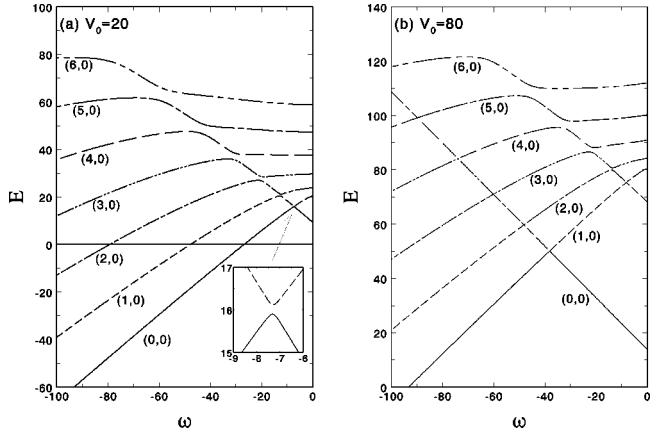

FIG. 3. Rotational-state energies of a vertically adsorbed dipole molecule in an external electric field as functions of field strength parameter $\omega<0$ for azimuthal quantum number $m=0$ and potential barrier heights $V_0=20$ and 80. The hindrance angle is set as $\alpha=30°$.

For the adsorbed molecule with higher potential barrier, there are more avoided crossings. Besides, for the adsorbed molecule with lower potential barrier height, their avoided crossings of higher energy levels become more smooth while compared with those with higher barrier height. Furthermore, the energies of two adjacent energy levels at the avoided crossing are very close to each other, especially for the lower states.

To analyze the variation of rotational energy with applied electric field, one may reexamine the potential energy for which an adsorbed molecule is subjected:

$$V(\theta)=V^{\mathrm{hin}}(\theta)-\omega\cos\theta. \tag{17}$$

For the case of $\omega>0$, when the external electric field is applied, the potential well is tilted to the $\theta=0°$ side and the potential energy $V(\theta)$ has a minimum at $\theta=0°$. That is, the electric field as well as conical well tend to concentrate molecular wave functions about $\theta=0°$. For the (0, 0) state of the $V_0=20$ case or the (0, 0) and (1, 0) states of the $V_0=80$ case, since the vertical conical well confines the major part of molecular wave functions about $\theta=0°$ even the electric field is absent, an applied electric field will result in more concentration of the wave functions about $\theta=0°$ and then rotational energies are decreased rapidly. On the other hand, for other excited states, when the electric field is absent, the rotational energies are higher than the barrier height. Their wave functions are similar to those of free molecule and the major part of the wave functions distributes outside the conical well.[8] An applied electric field will result in initially increasing the state energy. However, if the applied field is so large that molecular wave functions are forced to concentrate about $\theta=0°$, the rotational energies will decrease as the applied field is increased.

However, the case of $\omega<0$ shows very different situation. Figures 4 and 5 show the potential energy $V(\theta)$ and the angular distributions of molecular wave functions $|\Psi|^2$ for a vertically adsorbed molecule as functions of θ for different electric field strengths. For comparison, the energy levels $E_{0,0}$ and $E_{1,0}$ are also indicated. From Figs. 4 and 5, one can

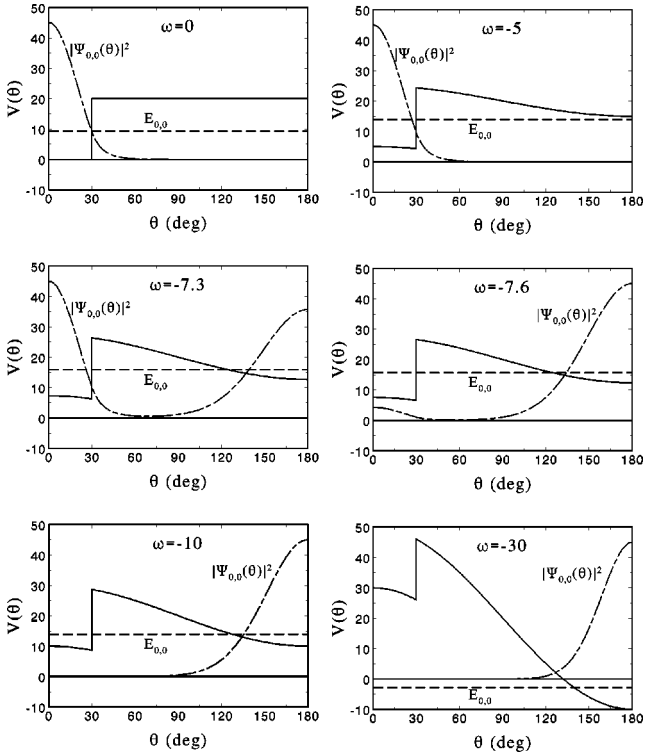

FIG. 4. Potential energy $V(\theta)=V^{\mathrm{hin}}(\theta)-\omega\cos\theta$ and angular distribution of molecular wave function $|\Psi_{0,0}|^2$ for a vertically adsorbed molecule as functions of θ for different electric field strengths. $V^{\mathrm{hin}}(\theta)$ is the vertical-conical-well hindering potential with $V_0=20$ and $\alpha=30°$.

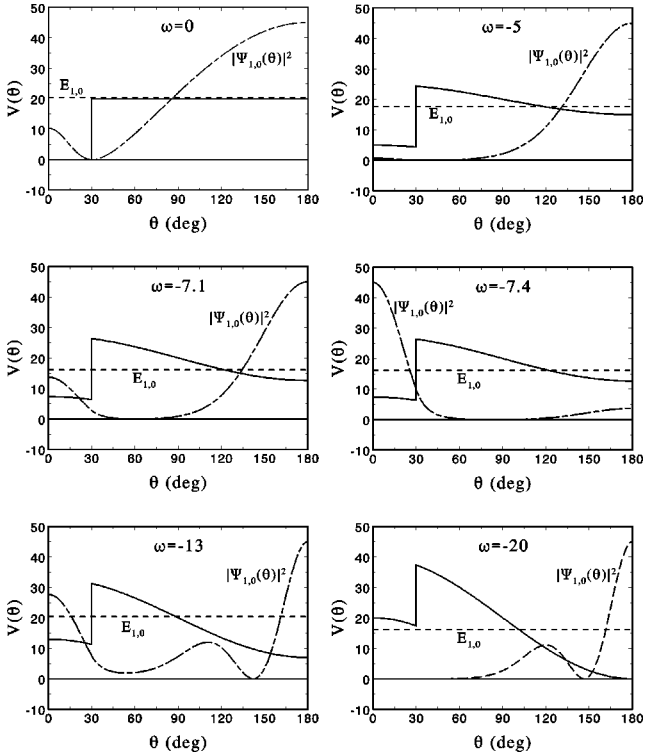

FIG. 5. Potential energy $V(\theta)=V^{\mathrm{hin}}(\theta)-\omega\cos\theta$ and angular distribution of molecular wave function $|\Psi_{1,0}|^2$ for a vertically adsorbed molecule as functions of θ for different electric field strengths. $V^{\mathrm{hin}}(\theta)$ is the vertical-conical-well hindering potential with $V_0=20$ and $\alpha=30°$.

see that, for the case of $\omega<0$, the electric field not only tilts the conical potential well but also creates a new potential minimum at $\theta=180°$. That is, the applied electric field tends to turn over the vertically adsorbed molecule. Therefore, in fact, the problem treated in this work, for the polar space region $0°\leqslant\theta\leqslant180°$, is equivalent to a double-well problem. This is absolutely different from the situation of a Cartesian square well subjected to an external electric field,[32,33] and is the manifestation of the rotational invariance.

Employing Figs. 4 and 5, one can understand that the avoided crossing of two energy levels in Fig. 3 are due to the redistributions of molecular wave functions between two potential wells. For the ground-state, if the electric field is absent, the molecular wave function is confined initially in the $0°\leqslant\theta<\alpha$ region by the vertical conical well. Therefore, the energy increases initially as the electric field is applied. However, when the electric field strength is increased up to the critical value so that $E_{0,0}$ is higher than the energy minimum about $\theta=180°$, it becomes energetically favorable to concentrate the wave function at $\theta=180°$. Hence the ground-state solution has now the character of the field-free (1, 0) state solution and its energy decreases as the applied field strength is increased.

On the other hand, for the excited (1, 0) state of the $V_0=20$ case, its energy decreases initially as an electric field is applied. However, when the ground-state wave function tunnels into the conical barrier region, the wave function of the excited (1, 0) state will tunnel into the conical well region to keep the orthogonality of wave functions. Hence it has now the character of the field-free ground-state solution and its energy increases as the applied field is increased. When the electric field strength is increased further to another critical value, the wave function of the (1, 0) state will tunnel back the region about $\theta=180°$ and then its energy decreases again. For the (1, 0) state of the $V_0=80$ case, when the electric field is absent, the wave function concentrates at $\theta=0°$ due to the higher potential barrier. Thus, as the field strength is increased, there is an additional energy change other than the (1, 0) state of the $V_0=20$ case. Similar discussions can be issued to other higher excited states. For larger field strengths more avoided crossings with the higher states occur. Beside, for the higher excited states whose energies are much higher than the potential barrier height, their wave function can smoothly redistribute over the polar space by an electric field. Thus their avoided crossings become smoother.

B. Horizontal adsorption configuration

For a horizontal adsorbed molecule, the hindering potential energy can be modeled by Eq. (4). Figure 6 shows the rotational-state energies of a horizontally adsorbed dipole molecule in an external electric field as functions of field strength parameter ω for azimuthal quantum number $m=0$

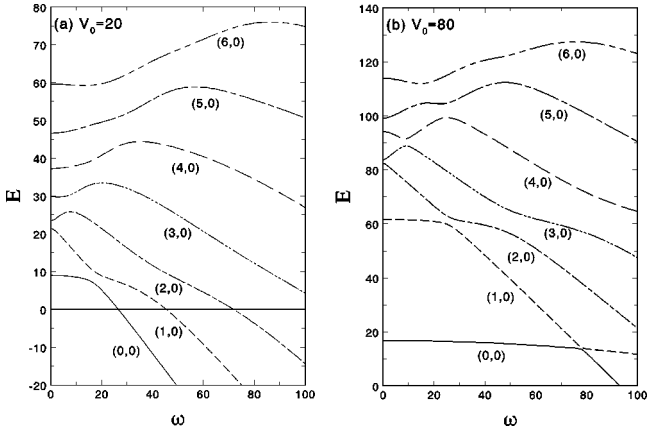

FIG. 6. Rotational-state energies of a horizontally adsorbed dipole molecule in an external electric field as functions of field strength parameter ω for azimuthal quantum number $m=0$ and potential barrier heights $V_0=20$ and 80. The hindrance angle is set as $\alpha=75°$ and $\beta=180°-\alpha$.

and potential barrier heights $V_0=20$ and 80. The hindrance angles are chosen as $\alpha=75°$ and $\beta=180°-\alpha$. Since the hindering potential is symmetric about the $\theta=90°$ plane, the electric field effects on the rotational energies for $\omega>0$ case and $\omega<0$ case are the same. Therefore, we show the results for the $\omega>0$ case only. From Fig. 6, one can see that the ground-state energies of both $V_0=20$ and 80 cases decrease slowly as the electric field is applied and then rapid decrease occurs as the field strength is stronger than some critical value. However, the variation of excited-state energy is different. For $V_0=20$, the energy of (1, 0) state decreases rapidly as the field is applied. When the state energy has decreased closely to the ground-state energy, the decrease rate becomes gentle to avoid the crossing of two energy levels. For further stronger electric field, the energy of the (1,0) state decreases rapidly again. For the other excited states of the $V_0=20$ case, their energy variations shown in Fig. 6(a) are similar to those in Fig. 2(a).

On the other hand, for the $V_0=80$ case, the energy of (1, 0) state decreases slowly and then rapidly. Finally, it decreases slowly again when the field strength is larger than the strength at which the energy of (0, 0) state begins to decrease rapidly. For the other excited states of the $V_0=80$ case, the energy variations show in Fig. 6(b) are somewhat similar to those in Fig. 3. However, the avoided crossings are smoother and the gaps between two adjacent levels at these avoided crossings are larger than those in Fig. 3.

Figures 7 and 8 show the potential energy $V(\theta)$ and the angular distributions of molecular wave function $|\Psi|^2$ for a horizontally adsorbed molecule as functions of θ for different electric field strengths. The polar space is divided into three regions. When ω increases, the value of $V(\theta)$ decreases in region I ($0°\leqslant\theta<\alpha$), and increases in region III ($\beta<\theta\leqslant180°$), but changes slightly in region II ($\alpha<\theta<\beta$).

For the ground (0, 0) state, if the electric field is absent, molecular wave function is confined initially in the $\alpha<\theta<\beta$ region by the vertical conical well. Therefore, the state energy varies gently as the field is applied, or one can say that the Stark shift of the rotational energy is suppressed by the conical well potential. However, when the electric field strength increases so that $E_{0,0}$ is higher than the energy minimum about $\theta=0°$, the major part of the molecular wave function begins to distribute about $\theta=0°$; therefore, the decrease of the state energy becomes rapid. When the electric field strength is very large, most of the molecular wave function will concentrate about $\theta=0°$. This implies that the adsorption configuration changes from horizontal to vertical.

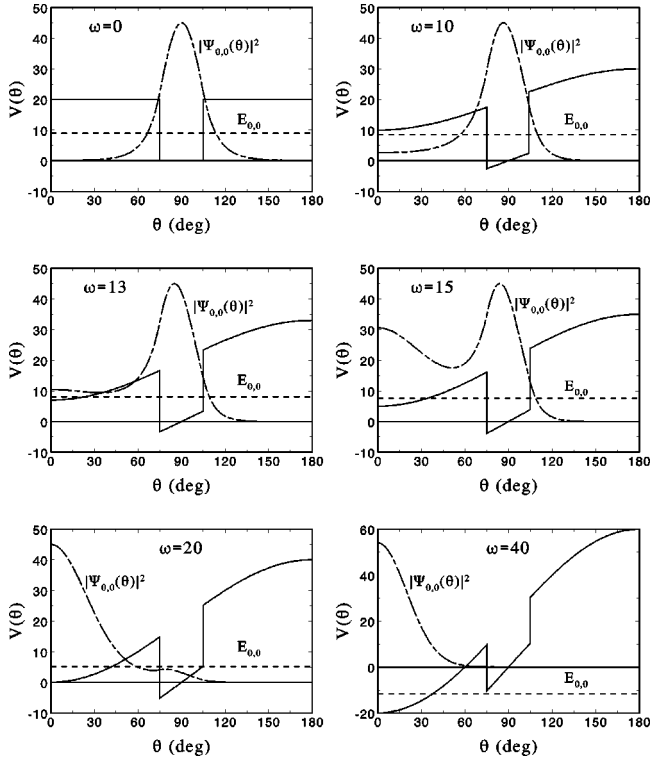

FIG. 7. Potential energy $V(\theta)=V^{\rm hin}(\theta)-\omega\cos\theta$ and angular distribution of molecular wave function $|\Psi_{0,0}|^2$ for a horizontally adsorbed molecule as functions of θ for different electric field strengths. $V^{\rm hin}(\theta)$ is the horizontal-conical-well hindering potential with $V_0=20$, $\alpha=75°$, and $\beta=180°-\alpha$.

For the excited (1, 0) state of the $V_0=20$ case, when the electric field is absent, the major part of the molecular wave function distributes in region I ($0°\leqslant\theta<\alpha$) and region III ($\beta<\theta\leqslant180°$). When the electric field is applied, molecular wave function redistributes. The distribution in region I increases, and the distribution in region III decreases. Therefore, the energy decreases rapidly. If the applied electric field is further increased, considerable part of the wave function will concentrate in region II ($\alpha<\theta<\beta$), and the energy decreases slowly. When the electric field is so strong that most of the wave function concentrates in region I, the energy will decrease rapidly again. Similar discussions can be issued to other higher excited states. However, for those excited states whose rotational energies are much higher than the potential barrier height V_0, the confinement potential is no longer

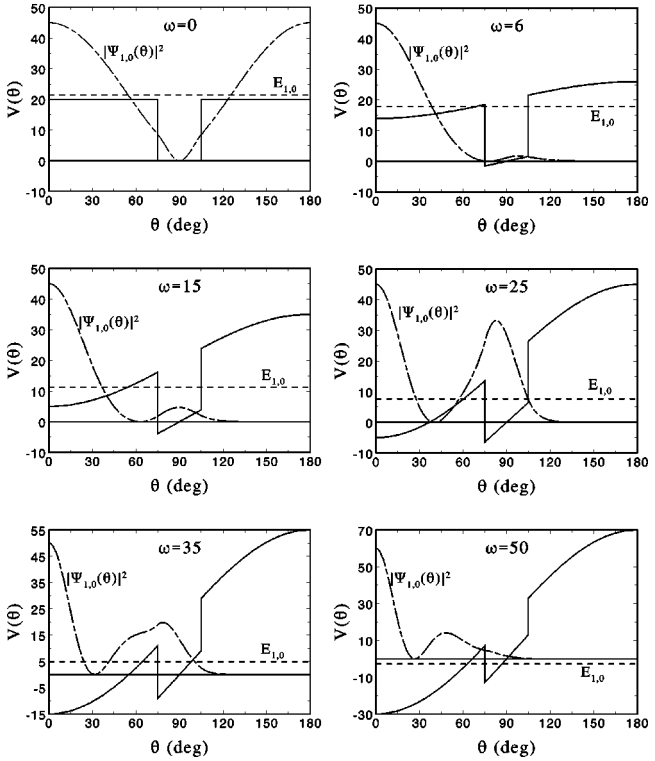

FIG. 8. Potential energy $V(\theta)=V^{\mathrm{hin}}(\theta)-\omega\cos\theta$ and angular distribution of molecular wave function $|\Psi_{1,0}|^2$ for a horizontally adsorbed molecule as functions of θ for different electric field strengths. $V^{\mathrm{hin}}(\theta)$ is the horizontal-conical-well hindering potential with $V_0=20$, $\alpha=75°$, and $\beta=180°-\alpha$.

dominant. Therefore, the variations of energy are similar to those of free dipole molecule in an external electric field.

C. Rotational-state distributions

The measurement of final rotational-state distributions of molecules desorbing from a surface is one of the familiar experimental methods to study rotational motion of adsorbed molecules. To compare with the experimental data, we employ the sudden unhindrance approximation to calculate the final rotational-state distributions as proposed in the works of Gadzuk and his co-workers.[4–6] We assumed that the desorption is induced by a fast process, i.e., the hindering potential is suddenly switched off and, thus, the pure hindered-to-free rotational transition takes place without changing the wave function. If the external electric field persists during the desorption process, the free-rotational states of a desorbing dipole molecule in an electric field can be expressed in terms of spherical harmonics:[26]

$$\Psi_m^{\mathrm{free}}(\theta,\phi)=\sum_{j'=m}^{\infty} c_{j',m}Y_{j',m}(\theta,\phi). \tag{18}$$

The probability of ending up in the Jth free-rotational state is the sum of rotational Franck-Condon factors between the final state $\Psi_{J,m}^{\mathrm{free}}$ and the hindered-rotational state $\Psi_{L,m'}^{\mathrm{hin}}$, weighted by appropriate thermal factors; that is,

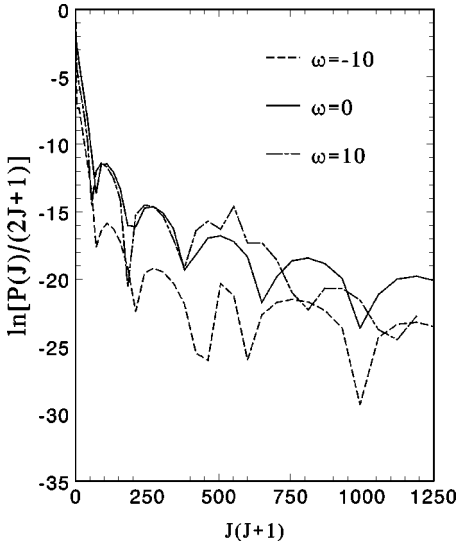

FIG. 9. Rotational-state distributions of suddenly desorbing molecule for various field strength parameters. In the calculation, we set $B/k_BT=1$ and the molecule was assumed vertically adsorbed with hindrance parameters $V_0=20$ and $\alpha=30°$.

$$P(J)=\frac{1}{Z_{\mathrm{hin}}}\sum_{m,L,m'}\exp(-E_{L,m'}/k_BT)\left|\langle\Psi_{J,m}^{\mathrm{free}}|\Psi_{L,m'}^{\mathrm{hin}}\rangle\right|^2, \tag{19}$$

where T is the surface temperature, k_B is the Boltzmann constant, and Z_{hin} is the partition function of the hindered rotor.

Figure 9 shows the calculated rotational-state distributions based on Eq. (19) for various field strength parameters. In the calculation, we set $B/k_BT=1$, and the molecule was assumed vertically adsorbed with hindrance parameters $V_0=20$ and $\alpha=30°$. In Fig. 9, the curves are plotted in the form $\ln[P(J)/(2J+1)]$ vs $J(J+1)$. It is known that for a Boltzmann distribution a straight line with slope$=-B/k_BT$ should be obtained. From Fig. 9 one can see that the non-Boltzmann feature and oscillatory structure with alternate drops and plateaus of the rotational-state distributions still display when an external electrical field is present. However, the positions of the dips and the maxima are displaced.

To apply our calculation to a more realistic system, let us consider the Cs-CN adsorption system. Figure 10 shows the calculated rotational distribution for CN* desorbing from Cs surface based on Eq. (19) for various field strength parameters. The measured distribution for Cs-CN adsorption system in the absence of electric field[3] is presented for comparison. In our calculation, the hindering potential was modeled as a vertical conical well with cone opening angle $\alpha=11.36°$ and potential barrier height $V_0=10\,030$ (i.e., $V_0\approx 2.45$ eV). These hindrance parameters for Cs-CN adsorption system have been determined in our previous work.[10] Since the electric field strength parameters we used in the calculation are much less than the potential barrier height V_0, the electronic wave functions of the adsorbed molecule on a surface in the presence of an external electrical field are expected to undergo a mild variation during the desorption

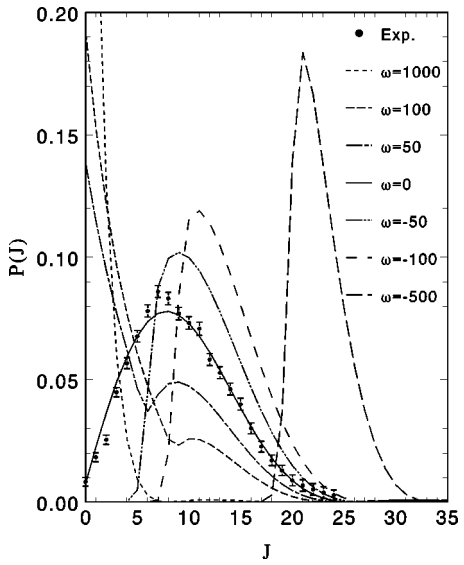

FIG. 10. Rotational-state distribution for CN* desorbing from Cs surface for various field strength parameters. In the calculation, the molecule was assumed vertically adsorbed with hindrance parameters $V_0 = 10\,030$ and $\alpha = 11.36°$.

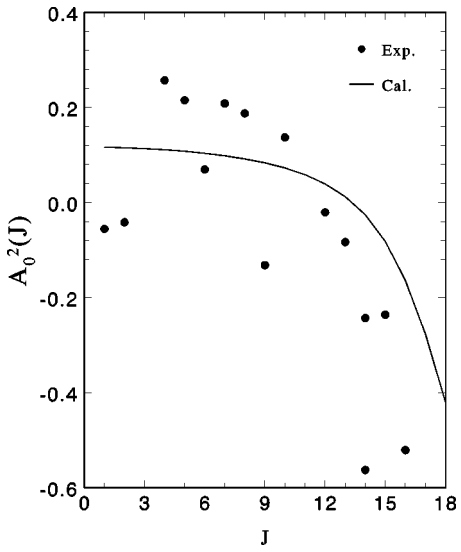

FIG. 11. Quadrupole moments for the desorption of CO from $Cr_2O_3(0001)$ as a function of quantum number J. Filled circles: experimental data points.

process. Furthermore, the bond length and dipole moment of adsorbed molecule can be assumed not to be affected.

Figure 10 shows that the rotational-state distributions are significantly influenced by the external electric field. One can note that, for the $\omega<0$ case, when the field strength is increased, the distribution shifts towards the high-J region. However, for the $\omega>0$ case, the distribution shifts towards the low-J region as the field strength is increased. The shift of rotational-state distribution with electric field can be realized by the fact that, at low enough temperature, the final free-state distribution is mainly due to the conversion of initial ground-hindered-rotational-state energy. For the case of $\omega<0$, as we gradually increase the electric field strength, the energy of ground-hindered-rotational state starts to increase because ω is still much less than V_0 (see Fig. 3), and thus the overlaps of ground-hindered-rotational state with high-J free-rotational states become more prominent. This causes the distribution to shift towards the high-J region. However, for the $\omega>0$ case, as the field strength is increased, the energy of ground-hindered-rotational state starts to decrease (see Fig. 2), and the overlaps of ground-hindered-rotational state with low-J free-rotational states become more prominent. Therefore, the distribution shifts towards the low-J region.

Finally, an additional remark on the finite-conical-well model is made. Certainly, using a simplified analytical potential is not state of the art. Molecule-surface interaction potentials can nowadays be mapped out in great detail by *ab initio* electronic structure methods. However, as we have seen in our previous[8–10] and present works, the simplified model shows interesting results. Furthermore, qualitative concepts and mechanisms can also be derived from the investigations. For example, we can justify our model by the performance of calculations on the rotational alignment of the desorbing molecules.

When a molecule desorbs from a solid surface,[11–14,16,18] the quadrupole moment $A_0^2(J)$ is a measure of the rotational alignment and is defined as $A_0^2(J) = \langle J|(3\mathbf{J}_z^2 - \mathbf{J}^2)/\mathbf{J}^2|J\rangle$.[34] In the classical limit, the value of $A_0^2(J)$ represents the ensemble average of $(3\cos^2\chi - 1)$ where χ is the angle between the angular momentum vector $\mathbf{J}$ of the molecule and the surface normal. The value of $A_0^2(J)$ ranges from $+2$ to -1, where positive values present helicopterlike motion ($\mathbf{J}$ vector prefers to parallel to the surface normal), negative values correspond cartwheel-like motion ($\mathbf{J}$ vector prefers to perpendicular to the surface normal).

To compare with the possible observed data, we calculate the quadrupole moment $A_0^2(J)$ by the results obtained in our model of finite conical well. According to the sudden unhindrance approximation, the quadrupole moment of the alignment distribution can be evaluated by the following equation:

$$A_0^2(J) = \frac{\sum_{m,L,m'} \exp(-E_{L,m'}/k_BT)\langle Y_{J,m}|\dfrac{3\mathbf{J}_z^2 - \mathbf{J}^2}{\mathbf{J}^2}|Y_{J,m}\rangle|\langle Y_{J,m}|\Psi_{L,m'}^{\text{hin}}\rangle|^2}{\sum_{m,L,m'} \exp(-E_{L,m'}/k_BT)|\langle Y_{J,m}|\Psi_{L,m'}^{\text{hin}}\rangle|^2}. \tag{20}$$

Figure 11 shows our calculated results compared with the experimental results of the rotational alignment in the photodesorption of CO from $Cr_2O_3(0001)$.[16,18] The hindrance parameters we used here are $V_0=2000$ and $\alpha=120°$.

It was observed experimentally the quadrupole moment of desorbing CO changes its sign from positive to negative with increasing rotational quantum number J. Theoretically we could reproduce a positive quadrupole moment for small quantum number J and thus corresponds to the helicopterlike desorbing, while a negative quadrupole moment of desorbing CO can be obtained and thus corresponds to the cartwheel-like desorbing for larger quantum number J. This result agrees qualitatively with the experimental observations as can be noted from Fig. 11.

To see more profoundly that our calculated results can yield positive values of quadrupole momentum for small angular momentum and negative values for large J states, we examine the expectation value $\langle Y_{J,m}|(3\mathbf{J}_z^2-\mathbf{J}^2)/\mathbf{J}^2|Y_{J,m}\rangle$ in Eq. (20). For a specific quantum number J, this expectation value is positive for high $|m|$ values and is negative for low $|m|$ values. In the summation of Eq. (20), only the low-lying hindered-rotational states $\Psi_{L,m}^{\mathrm{hin}}$, dominate due to the thermal factor. We calculated the overlapping factors $|\langle Y_{J,m}|\Psi_{L,m'}^{\mathrm{hin}}\rangle|^2$ between the free-rotational states $Y_{J,m}$ and the low-lying hindered-rotational states $\Psi_{L,m'}^{\mathrm{hin}}$. Our results showed that, when J is small, the calculated value of $|\langle Y_{J,m}|\Psi_{L,m'}^{\mathrm{hin}}\rangle|^2$ for a specific L is larger for $\Psi_{L,m}^{\mathrm{hin}}$, states with larger $|m|$, which correspond to more horizontally distributed wave functions. This makes the hindered molecule pernt to the helicopterlike desorption and yield a positive quadrupole moment. On the contrary, when J is larger, the low-lying $\Psi_{L,m}^{\mathrm{hin}}$, states correspond smaller $|m|$ and then negative expectation values $\langle Y_{J,m}|(3\mathbf{J}_z^2-\mathbf{J}^2)/\mathbf{J}^2|Y_{J,m}\rangle$. Our results also showed that, when J is larger, the calculated value of $|\langle Y_{J,m}|\Psi_{L,m'}^{\mathrm{hin}}\rangle|^2$ for a specific L is larger for $\Psi_{L,m}^{\mathrm{hin}}$, states with smaller $|m|$, which correspond to more vertically distributed wave functions. This makes the hindered molecule tend to the cartwheel-like desorption in larger J states and yield a negative quadrupole moment.

IV. CONCLUSIONS

We have investigated the electric field effect of adsorbed dipole molecules. The surface hindering potential to which the adsorbed molecule is subjected was modeled as a finite conical well and an dipole-field interaction was added to the hindering potential. The molecular wave functions were expressed in terms of the eigenfunctions of adsorbed molecule in the free field situation.

Our results show that for the vertically adsorbed dipole molecules, if the external electric field orients the molecular axis toward molecular preferred orientation, the ground-state energy decreases as the electric field is increased, while the excited-state energies increase to a maximum and then decrease as the field is increased. While, if the external electric field orients the molecular axis against molecular preferred orientation, there are avoided crossings of two energy levels as the field is increased and finally all state energies decrease rapidly as the field strength is strong enough. On the other hand, for the horizontally adsorbed molecules, there are smoother avoided crossings of two adjacent levels as the field strength is increased and finally all state energies decrease rapidly for very strong field. The avoided crossing of two adjacent energy levels is due to the redistribution of wave function between different potential well regions.

By employing the sudden unhindrance approximation, the rotational-sate distributions of molecules desorbing from a solid surface in the presence of external electric field were calculated. When the calculated distributions were plotted semilogarithmically, the non-Boltzmann feature and oscillatory structure with alternate drops and plateaus of distributions displayed. We applied our calculation to more realistic Cs-CN adsorption system. Our results showed that the rotational-state distributions are significantly influenced by the external electric field. When the electric field is applied to orient the molecular axis against the molecular preferred orientation, the distribution shifts towards the high-J region, since the electric field increases the ground-state energy of adsorbed molecule. However, when the electric field is applied to orient the molecular axis towards the molecular preferred orientation, the distribution shifts towards the low-J region, since the electric field decreases the ground-state energy of adsorbed molecule.

We have calculated the rotational alignment in the photodesorption of CO from $Cr_2O_3(0001)$ by the solutions to the finite conical well. Our calculated results showed that at low-J values the CO molecules desorb like a helicopter, while at high J values a cartwheel-like motion is preferred. This result is in qualitative agreement with the experimental observation.

ACKNOWLEDGMENTS

This work was supported by the National Science Council, Taiwan, Republic of China under the Grants Nos. NSC 91-2112-M-018-014 and NSC 91-2120-M-009-002.

*Author to whom correspondence should be addressed. Electronic mail: ytshih@cc.ncue.edu.tw

†Electronic mail: dschuu@cc.nctu.edu.tw

[1] A.W. Kleyn, A.C. Luntz, and D.J. Auerbach, Phys. Rev. Lett. **47**, 1169 (1981).

[2] R.R. Cavanagh and D.S. King, Phys. Rev. Lett. **47**, 1829 (1981).

[3] J. Xu, A. Barnes, R. Albridge, C. Ewig, N. Tolk, and L.D. Hulett, Jr., Phys. Rev. B **48**, 8222 (1993).

[4] J.W. Gadzuk, U. Landman, E.J. Kuster, C.L. Cleveland, and R.N. Barnett, Phys. Rev. Lett. **49**, 426 (1982).

[5] U. Landman, Isr. J. Chem. **22**, 239 (1982).

[6] J.W. Gadzuk, U. Landman, E.J. Kuster, C.L. Cleveland, and R.N. Barnett, J. Electron Spectrosc. Relat. Phenom. **30**, 103 (1983).

[7] U. Landman, G.G. Kleiman, C.L. Cleveland, E. Kuster, R.N. Barnett, and J.W. Gadzuk, Phys. Rev. B **29**, 4313 (1984).

[8] Y.T. Shih, D.S. Chuu, and W.N. Mei, Phys. Rev. B **51**, 14 626

(1995).
[9] Y.T. Shih, D.S. Chuu, and W.N. Mei, Solid State Commun. **99**, 819 (1996).
[10] Y.T. Shih, D.S. Chuu, and W.N. Mei, Phys. Rev. B **54**, 10 938 (1996).
[11] D.C. Jacobs, K.W. Kolasinski, R.J. Madix, and R.N. Zare, J. Chem. Phys. **87**, 5038 (1987).
[12] H. Hou, S.J. Gulding, C.T. Rettner, A.M. Wodtke, and D.J. Auerbach, Science **277**, 80 (1997).
[13] D. Wetzig, R. Dopheide, M. Rutkowski, R. David, and H. Zacharias, Phys. Rev. Lett. **76**, 463 (1996).
[14] M. Rutkowski, D. Wetzig, and H. Zacharias, Phys. Rev. Lett. **87**, 246101 (2001).
[15] A. Eichler, J. Hafner, A. Groß, and M. Scheffler, Chem. Phys. Lett. **311**, 1 (1999).
[16] I. Beauport, K. Al-Shamery, and H.-J. Freund, Chem. Phys. Lett. **256**, 641 (1996).
[17] S. Thiel, M. Pykavy, T. Klüner, H.-J. Freund, R. Kosloff, and V. Staemmler, Phys. Rev. Lett. **87**, 077601 (2001).
[18] S. Thiel, M. Pykavy, T. Klüner, H.-J. Freund, R. Kosloff, and V. Staemmler, J. Chem. Phys. **116**, 762 (2002).
[19] R. Schinke, J. Chem. Phys. **76**, 2352 (1982).
[20] E.W. Müller, Z. Phys. A **106**, 541 (1937).
[21] E.W. Müller, Z. Physik **131**, 136 (1951).
[22] R. Gomer, Surf. Sci. **299/300**, 129 (1994).
[23] T.T. Tsong, Surf. Sci. **299/300**, 153 (1994).
[24] H. J. Kreuzer, in *Chemistry and Physics of Solid Surfaces*, edited by R. Vanselow and R. Howe (Springer-Verlag, New York, 1990), Vol. VIII.
[25] G. Herzberg, *Molecular Spectra and Molecular Structure. I. Spectra of Diatomic Molecules*, 2nd ed. (Van Nostrand, New York, 1950).
[26] K. von Meyenn, Z. Phys. A **231**, 154 (1970).
[27] R.P. Pan, R.D. Etters, K. Kobashi, and V. Chandrasekharan, J. Chem. Phys. **77**, 1035 (1982).
[28] J.W. Riehl and C.J. Fisher, J. Chem. Phys. **59**, 4336 (1973).
[29] V.M. Allen and P.D. Pacey, Surf. Sci. **177**, 36 (1986).
[30] *Handbook of Mathematical Functions*, edited by M. Abramowitz and I. A. Stegun (Dover, New York, 1970).
[31] L. D. Landau and E. M. Lifshitz, *Quantum Mechanics*, 3rd ed. (Pergamon, New York, 1977).
[32] G. Bastard, E.E. Mendez, L.L. Chang, and L. Esaki, Phys. Rev. B **28**, 3241 (1983).
[33] D. Ahn and S.L. Chuang, Appl. Phys. Lett. **49**, 1450 (1986).
[34] C.H. Greene and R.N. Zare, J. Chem. Phys. **78**, 6741 (1983).

Spin Hall Effect on Edge Magnetization and Electric Conductance of a 2D Semiconductor Strip

A. G. Mal'shukov,[1] L. Y. Wang,[2] C. S. Chu,[2] and K. A. Chao[3]

[1]*Institute of Spectroscopy, Russian Academy of Science, 142190, Troitsk, Moscow oblast, Russia*
[2]*Department of Electrophysics, National Chiao Tung University, Hsinchu 30010, Taiwan*
[3]*Solid State Theory Division, Department of Physics, Lund University, S-22362 Lund, Sweden*

(Received 7 July 2005; published 27 September 2005)

The intrinsic spin Hall effect on spin accumulation and electric conductance in a diffusive regime of a 2D electron gas has been studied for a 2D strip of a finite width. It is shown that the spin polarization near the flanks of the strip, as well as the electric current in the longitudinal direction, exhibit damped oscillations as a function of the width and strength of the Dresselhaus spin-orbit interaction. Cubic terms of this interaction are crucial for spin accumulation near the edges. As expected, no effect on the spin accumulation and electric conductance have been found in case of Rashba spin-orbit interaction.

DOI: 10.1103/PhysRevLett.95.146601 PACS numbers: 72.25.Dc, 71.70.Ej, 73.40.Lq

Spintronics is a fast developing area to use electron spin degrees of freedom in electronic devices [1]. One of its most challenging goals is to find a method for manipulating electron spins by electric fields. The spin-orbit interaction (SOI), which couples the electron momentum and spin, can be a mediator between the charge and spin degrees of freedom. Such a coupling gives rise to the so-called spin Hall effect (SHE) which attracted much interest recently. Because of SOI the spin flow can be induced perpendicular to the dc electric field, as has been predicted for systems containing spin-orbit impurity scatterers [2]. Later, similar phenomenon was predicted for noncentrosymmetric semiconductors with spin split electron and hole energy bands [3]. It was called the *intrinsic* spin Hall effect, in contrast to the *extrinsic* impurity induced effect, because in the former case it originates from the electronic band structure of a semiconductor sample. Since the spin current carries the spin polarization, one would expect a buildup of the spin density near the sample boundaries. In fact, this accumulated polarization is a first signature of SHE which has been detected experimentally, confirming thus the extrinsic SHE [4] in semiconductor films and intrinsic SHE in a 2D hole gas [5]. On the other hand, there was still no experimental evidence of intrinsic SHE in 2D electron gases. The possibility of such an effect in macroscopic samples with a finite elastic mean free path of electrons caused recently much debates. It has been shown analytically [6–11] and numerically [12] that in such systems SHE vanishes at arbitrary weak disorder in dc limit for isotropic as well as anisotropic [10] impurity scattering when SOI is represented by the so-called Rashba interaction [13]. As one can expect in this case, there is no spin accumulation at the sample boundaries, except for the pockets near the electric contacts [7]. At the same time, the Dresselhaus SOI [14], which dominates in symmetric quantum wells, gives a finite spin Hall conductivity [11]. The latter can be of the order of its universal value $e/8\pi\hbar$. The same has been shown for the cubic Rashba interaction in hole systems [12,15]. In this connection an important question is what sort of the spin accumulation could Dresselhaus SOI induce near sample boundaries. Another problem which, as far as we know, was not discussed in literature, is how the *electric* current along the applied electric field will change under SHE. In the present work we will use the diffusion approximation for the electron transport to derive the drift-diffusion equations with corresponding boundary conditions for the spin and charge densities coupled to each other via SOI of general form. Then the spin density near the flanks of an infinite 2D strip and the correction to its longitudinal electric resistance will be calculated for Dresselhaus and Rashba SOI.

Let us consider two-dimensional electron gas (2DEG) confined in an infinite 2D strip. The boundaries of the strip are at $y = \pm d/2$. The electric field E drives the dc current in the x direction and induces the spin Hall current in the y direction. This current leads to spin polarization buildup near boundaries. Since $d \gg k_F^{-1}$, where k_F is the Fermi wave vector, this problem can be treated within the semiclassical approximation. Moreover, we will assume that d is much larger than the electron elastic mean free path l, so that the drift-diffusion equation can be applied for description of the spin and charge transport. Our goal is to derive this equation for SOI of general form

$$H_{so} = \boldsymbol{h}_{\boldsymbol{k}} \cdot \boldsymbol{\sigma}, \tag{1}$$

where $\boldsymbol{\sigma} \equiv (\sigma^x, \sigma^y, \sigma^z)$ is the Pauli matrix vector, and the effective magnetic field $\boldsymbol{h}_{\boldsymbol{k}} = -\boldsymbol{h}_{-\boldsymbol{k}}$ is a function of the two-dimensional wave vector $\boldsymbol{k}$.

We start from determining linear responses to the magnetic $\boldsymbol{B}(\boldsymbol{r}, t)$ and electric $V(\boldsymbol{r}, t)$ potentials. The magnetic potentials are introduced in order to derive the diffusion equation and play an auxiliary role. The corresponding one-particle interaction with the spin density is defined as $H_{sp} = \boldsymbol{B}(\boldsymbol{r}, t) \cdot \boldsymbol{\sigma}$. These potentials induce the spin and charge densities, $\boldsymbol{S}(\boldsymbol{r}, t)$ and $n(\boldsymbol{r}, t)$, respectively. Because of SOI the charge and spin degrees of freedom are coupled, so that the electric potential can induce the spin density [16] and *vice versa*. Therefore, it is convenient to introduce

the four vector of densities $D_i(\boldsymbol{r}, t)$, such that $D_0(\boldsymbol{r}) = n(\boldsymbol{r}, t)$ and $D_{x,y,z}(\boldsymbol{r}, t) = S_{x,y,z}(\boldsymbol{r}, t)$. The corresponding four vector of potentials will be denoted as $\Phi_i(\boldsymbol{r}, t)$. Accordingly, the linear response equations can be written in the form

$$D_i(\boldsymbol{r}, t) = \int d^2r' dt' \sum_j \Pi_{ij}(\boldsymbol{r}, \boldsymbol{r}', t - t')\Phi_j(\boldsymbol{r}', t') + D_i^0(\boldsymbol{r}, t). \quad (2)$$

The response functions $\Pi_{ij}(\boldsymbol{r}, \boldsymbol{r}', t - t')$ can be expressed in a standard way [17] through the retarded and advanced Green functions $G^r(\boldsymbol{r}, \boldsymbol{r}', t)$ and $G^a(\boldsymbol{r}, \boldsymbol{r}', t)$. In the Fourier representation we get

$$\Pi_{ij}(\boldsymbol{r}, \boldsymbol{r}', \omega) = i\omega \int \frac{d\omega'}{2\pi} \frac{\partial n_F(\omega')}{\partial \omega'} \langle \mathrm{Tr}[G^a(\boldsymbol{r}', \boldsymbol{r}, \omega') \times \Sigma_i G^r(\boldsymbol{r}, \boldsymbol{r}', \omega' + \omega)\Sigma_j]\rangle, \quad (3)$$

where $\Sigma_0 = 1$, $\Sigma_i = \sigma_i$ at $i = x, y, z$, and $n_F(\omega)$ is the Fermi distribution function. The time Fourier components of densities $D_i^0(\boldsymbol{r}, t)$ at $\omega \ll E_F$ are defined as

$$D_i^0(\boldsymbol{r}, \omega) = i \int d^2r' \sum_j \Phi_j(\boldsymbol{r}', \omega) \int \frac{d\omega'}{2\pi} n_F(\omega') \times \langle \mathrm{Tr}[G^r(\boldsymbol{r}, \boldsymbol{r}', \omega')\Sigma_i G^r(\boldsymbol{r}', \boldsymbol{r}, \omega')\Sigma_j - G^a(\boldsymbol{r}, \boldsymbol{r}', \omega')\Sigma_i G^a(\boldsymbol{r}', \boldsymbol{k}, \omega')\Sigma_j]\rangle. \quad (4)$$

The trace in Eqs. (3) and (4) runs through the spin variables, and the angular brackets denote the average over the random distribution of impurities. Within the semiclassical approximation the average of the product of Green functions can be calculated perturbatively. Ignoring the weak localization effects, the perturbation expansion consists of the so-called ladder series [17,18]. At small ω and large $|\boldsymbol{r} - \boldsymbol{r}'|$ they describe the particle and spin diffusion processes. The building blocks for the perturbation expansion are the average Green functions $\mathcal{G}^r$ and $\mathcal{G}^a$, together with the pair correlator of the impurity scattering potential $U_{sc}(\boldsymbol{r})$. A simple model of the short-range isotropic potential gives $\langle U_{sc}(\boldsymbol{r})U_{sc}(\boldsymbol{r}')\rangle = \Gamma\delta(\boldsymbol{r} - \boldsymbol{r}')/\pi N_0$, where N_0 is the electron density of states at the Fermi energy and $\Gamma = 1/2\tau$. Within the semiclassical approach the explicit behavior of the electron wave functions near the boundaries of the strip is not important. Therefore, the bulk expressions can be used for the average Green functions. Hence, in the plane wave representation

$$\mathcal{G}^r(\boldsymbol{k}, \omega) = [\mathcal{G}^a(\boldsymbol{k}, \omega)]^\dagger = (\omega - E_{\boldsymbol{k}} - \boldsymbol{h}_{\boldsymbol{k}} \cdot \boldsymbol{\sigma} + i\Gamma)^{-1}, \quad (5)$$

where $E_{\boldsymbol{k}} = k^2/(2m^*) - E_F$. Since the integral in (4) rapidly converges at $|\boldsymbol{r} - \boldsymbol{r}'| \lesssim k_F^{-1}$, $D_i^0(\boldsymbol{r}, \omega)$ are given by the local values of potentials. From (4) and (5) one easily obtains the local equilibrium densities

$$D_i^0(\boldsymbol{r}, \omega) = -2N_0\Phi_i(\boldsymbol{r}, \omega). \quad (6)$$

In their turn, the nonequlibrium spin and charge densities are represented by the first term in Eq. (2). Within the diffusion approximation this term is given by the gradient expansion of (3) [18]. Such an expansion is valid as far as spatial variations of $D_i(\boldsymbol{r}, \omega)$ are relatively small within the length of the order of the mean free path l. The length scale for spin density variations near the boundaries of the strip is given by $v_F/h_{\boldsymbol{k}_F}$. Hence, the diffusion approximation can be employed only in the dirty limit $h_{\boldsymbol{k}_F} \ll 1/\tau$. The diffusion equation is obtained after the ladder summation in the first term of Eq. (3) and multiplying this equation by the operator inverse to $\Pi_{ij}(\boldsymbol{r}, \boldsymbol{r}', \omega)$, as it has been previously done in [19,20]. After some algebraic manipulations one gets

$$\sum_j \mathcal{D}^{ij}(D_j - D_j^0) = -i\omega D_i, \quad (7)$$

where the diffusion operator $\mathcal{D}^{ij}$ can be written as

$$\mathcal{D}^{ij} = \delta^{ij}D\boldsymbol{\nabla}^2 - \Gamma^{ij} + R^{ijm}\nabla_m + M^{ij}. \quad (8)$$

The first term represents the usual diffusion of the spin and charge densities, while the second one describes the D'akonov-Perel' [21] spin relaxation

$$\Gamma^{ij} = 4\tau\overline{h_{\boldsymbol{k}}^2[\delta^{ij} - n_{\boldsymbol{k}}^i n_{\boldsymbol{k}}^j]}, \quad (9)$$

where $i, j \neq 0$, the overline denotes the average over the Fermi surface, and $\boldsymbol{n}_{\boldsymbol{k}} = \boldsymbol{h}_{\boldsymbol{k}}/h_{\boldsymbol{k}}$. The third term gives rise to precession of the inhomogeneous spin polarization in the effective field of SOI [19]

$$R^{ijm} = 4\tau \sum_l \varepsilon^{ijl}\overline{h_{\boldsymbol{k}}^l v_F^m}. \quad (10)$$

The nondiagonal elements of the form $\mathcal{D}^{i0}$ appear due to spin-orbit mixing of spin and charge degrees of freedom. They are collected in M^{ij}. For Rashba SOI M^{i0} have been calculated in [7,8]. In general case

$$M^{i0} = \overline{\frac{h_{\boldsymbol{k}}^3}{\Gamma^2} \frac{\partial n_{\boldsymbol{k}}^i}{\partial \boldsymbol{k}}} \cdot \boldsymbol{\nabla}. \quad (11)$$

When a time independent homogeneous electric field is applied to the system one has $\Phi_0 = eEx$ and $D_0^0 = -2N_0eEx$. At the same time, $\Phi_i = 0$ and, hence, $D_i^0 = 0$ at $i = x, y, z$. Because of charge neutrality the induced charge density $eD_0 = 0$. It should be noted that in the system under consideration the charge neutrality cannot be fulfilled precisely. The spin polarization accumulated at the strip boundaries gives rise to charge accumulation via the M^{0i} terms in (7) and (8). The screening effect will, however, strongly reduce this additional charge, because the screening length of 2DEG is much less than the typical length scale of spin density variations. We will ignore such a small correction and set $D_0 = 0$ in (7). In this way one

arrives to the closed diffusion equation for three components of the spin density. This equation coincides with the usual equation describing diffusive propagation of the spin density [19], for exception of the additional term $-M^{i0}D_0^0 = 2N_0eE\overline{h_{\boldsymbol{k}}^3\nabla_{\boldsymbol{k}}^x n_{\boldsymbol{k}}^i}/\Gamma^2$ due to the external electric field. Its origin becomes more clear in an infinite system where the spin density is constant in space and only Γ^{ij} and M^{ij} are retained in (7) and (8). Hence, the corresponding solution of (8) at $\omega = 0$ is $S_i \equiv S_i^{\rm b}$, with

$$S_i^{\rm b} \equiv D_i^0/2 = \frac{N_0eE}{\Gamma^2}\sum_j(\Gamma^{-1})^{ij}\overline{h_{\boldsymbol{k}}^3\frac{\partial n_{\boldsymbol{k}}^j}{\partial k_x}}, \qquad (12)$$

where $(\Gamma^{-1})^{ij}$ is the matrix inverse to (9). Such a phenomenon of spin orientation by the electric field was predicted in Ref. [16] and recently observed in [22]. In the special case of Rashba SOI $\boldsymbol{h}_{\boldsymbol{k}} = \alpha(k)(\boldsymbol{k}\times z)$ it is easily to get from (12) the result of Ref. [16] $S_y^{\rm b} = -N_0eE\alpha\tau$.

In addition to the diffusion equation one needs the boundary conditions. These conditions are that the three components of the spin flux I_x^y, I_y^y, I_z^y flowing in the y direction turn to 0 at $y = \pm d/2$. The linear response theory, similar to (2), gives

$$I_i^l(\boldsymbol{r}, t) = \int d^2r'dt'\sum_j \Xi_{ij}^l(\boldsymbol{r}, \boldsymbol{r}', t-t')\Phi_j(\boldsymbol{r}', t'), \qquad (13)$$

where the response function Ξ is given by

$$\Xi_{ij}^l(\boldsymbol{r}, \boldsymbol{r}', \omega) = i\omega\int\frac{d\omega'}{2\pi}\frac{\partial n_F(\omega')}{\partial\omega'}\langle{\rm Tr}[G^a(\boldsymbol{r}', \boldsymbol{r}, \omega') \times J_i^l G^r(\boldsymbol{r}, \boldsymbol{r}', \omega'+\omega)\Sigma_j]\rangle, \qquad (14)$$

with the one-particle spin-current operator defined by $J_i^l = (\sigma^i {\rm v}_l + {\rm v}_l\sigma^i)/4$ and the particle velocity

$${\rm v}_l = \frac{k_l}{m^*} + \frac{\partial}{\partial k_l}(\boldsymbol{h}_{\boldsymbol{k}}\cdot\boldsymbol{\sigma}). \qquad (15)$$

Taking into account (7) and (6), we obtain from (13) and (14)

$$I_i^y(\boldsymbol{r}) = -D\frac{\partial S_i}{\partial y} - \frac{1}{2}R^{ijy}(S_j - S_j^{\rm b}) + \delta_{iz}I_{sH}. \qquad (16)$$

The first two terms represent the diffusion spin current and the current associated with the spin precession. The third term is the uniform spin Hall current polarized along the z axis. It is given by

$$I_{sH} = -\frac{1}{2}R^{zjy}S_j^{\rm b} + eE\frac{N_0}{\Gamma^2}\overline{v_F^y\left(\frac{\partial\boldsymbol{h}_{\boldsymbol{k}}}{\partial k^x}\times\boldsymbol{h}_{\boldsymbol{k}}\right)_z}. \qquad (17)$$

From (10) and (12) it is easy to see that for Rashba SOI both terms in (17) cancel each other making $I_{sH} = 0$, in accordance with [6–12]. Therefore, in case of the strip the solution of the diffusion equation satisfying the boundary condition is $S_j = \delta_{jy}S_y^{\rm b}$. Hence, the spin density is uniform and does not accumulate near boundaries. It should be noted that such accumulation can, however, take place in the ballistic regime of electron scattering [23]. At the same time, as shown in Ref. [11], even in the diffusive regime $I_{sH} \neq 0$ for the Dresselhaus SOI. This inevitably leads to the spin accumulation. Taking Dresselhaus SOI in the form

$$h_{\boldsymbol{k}}^x = \beta k_x(k_y^2 - \kappa^2); \qquad h_{\boldsymbol{k}}^y = -\beta k_y(k_x^2 - \kappa^2), \qquad (18)$$

one can see that the bulk spin polarization (12) has a nonzero $S_x^{\rm b}$ component, $R^{zxy} \neq 0$, while $R^{zyy} = 0$. Hence, the solution of the diffusion Eq. (7) with the boundary condition $I_x^y(\pm d/2) = I_z^y(\pm d/2) = 0$ is S_x, $S_z \neq 0$ $S_y = 0$. Let us define $\Delta S_i(y) = S_i(y) - S_i^{\rm b}$. The dependence of $\Delta S_i(\pm d/2)$ from the strip width, as well as an example of ΔS_z coordinate dependence, are shown in Fig. 1. The damped oscillation in the d-dependence of the spin accumulation on the flanks of the strip can be seen for the S_z polarization. Similar oscillations take place also in the coordinate dependence. The length scale of these oscillations is determined by the spin precession in the effective spin-orbit field.

The arbitrary units have been used in Fig. 1. For a numerical evaluation let us take $E = 10^4$ V/m, $\sqrt{\overline{h_{\boldsymbol{k}_F}^2}}\tau/\hbar = 0.1$, and $\kappa/k_F = 0.8$ for a GaAs quantum

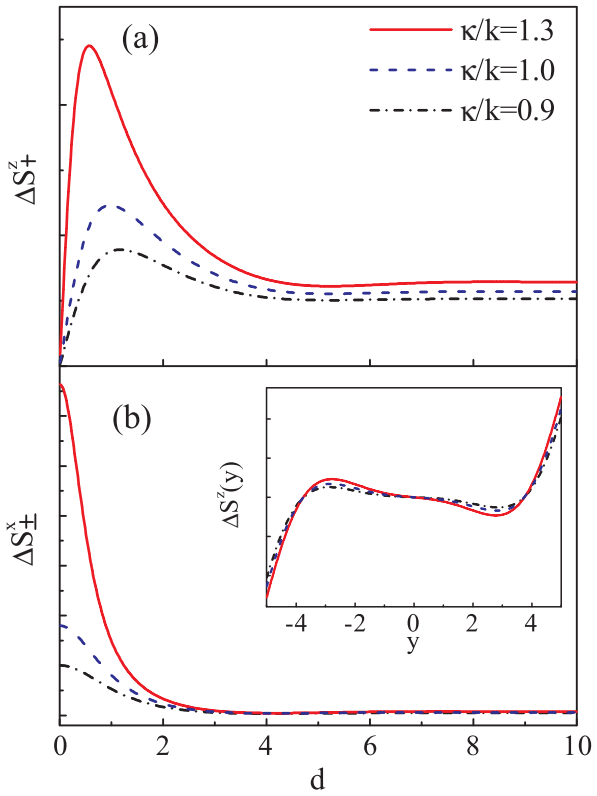

FIG. 1 (color online). Spin densities $\Delta S_i(\pm d/2) \equiv \Delta S_{\pm}^i$ for $i = x, z$ on the boundaries of the strip, as functions of its width d, for $\kappa/k = 0.9$, 1.0, and 1.3, respectively. The inset shows the dependence of $\Delta S_z(y)$ on the transverse coordinate y. Lengths are measured in units of $l_{so} = v_F^2\hbar/2(\overline{v_{Fy}h_{\boldsymbol{k}y}})$.

well of the width $w = 100$ Å doped with 1.5×10^{15} m^{-2} electrons. We thus obtain $|\Delta S_z(\pm d/2)| \simeq 5 \times 10^{11}$ m^{-2}. The corresponding volume density $\Delta S_z/w \simeq 5 \times 10^{19}$ m^{-3}, which is within the sensitivity range of the Faraday rotation method [4].

It should be noted that in the considered here "dirty" limit $\sqrt{\overline{h_{\boldsymbol{k}_F}^2}}\tau/\hbar \ll 1$ the spin Hall current is suppressed by the impurity scattering. As shown in [11,12] for Dresselhaus and cubic Rashba SOI, this current decreases as $\overline{h_{\boldsymbol{k}_F}^2}\tau^2/\hbar^2$ down from its highest universal value. At the same time, an analysis of the diffusion equation shows that the accumulated at the flanks of the strip spin density decreases slower, as $\sqrt{\overline{h_{\boldsymbol{k}_F}^2}}\tau/\hbar$. This explains why for the considered above realistic numerical parameters, even in the dirty case, the noticeable spin polarization can be accumulated near the boundary.

Usually, the spin Hall effect is associated with the spin polarization flow, or the spin density accumulation on the sample edges, in response to the electric field. On the other hand, this effect can show up in the *electric* conductance as well. To see such an effect we take 0-projection of (13), which by definition is the electric current. The current flows along the x axis. The corresponding response function Ξ_{0j}^x is given by (14) with $J_0^x = \mathrm{v}_x$. Using Eqs. (14), (15), and (7), and expressing Φ_i from (6) one gets the electric current density

$$I^x = \sigma E + A\frac{\partial S_z}{\partial y}, \tag{19}$$

where σ is the Drude conductivity and

$$A = e\frac{1}{2\Gamma^2}\left[2\overline{v_F^y\left(\frac{\partial \boldsymbol{h}_{\boldsymbol{k}}}{\partial k^x}\times \boldsymbol{h}_{\boldsymbol{k}}\right)_z} + \overline{v_F^x\left(\frac{\partial \boldsymbol{h}_{\boldsymbol{k}}}{\partial k^y}\times \boldsymbol{h}_{\boldsymbol{k}}\right)_z}\right]. \tag{20}$$

The total current is obtained by integrating (19) over y. Therefore, the spin Hall correction to the strip conductance

$$\Delta G = \frac{A}{E}[S_z(d/2) - S_z(-d/2)] = \frac{2A}{E}S_z(d/2). \tag{21}$$

Hence, the dependence of ΔG on the strip width coincides with that of the spin density shown in Fig. 1(a).

In conclusion, we employed the diffusion approximation to study the spin Hall effect in an infinite 2D strip. In case of the Dresselhaus spin-orbit interaction this effect leads to spin accumulation near the flanks of the strip, as well as to a correction to the longitudinal electric conductance. Both the spin accumulation and the conductance exhibit damped oscillations as a function of the strip width.

This work was supported by the Taiwan National Science Council NSC93-2112-M-009-036, NSC94-2811-M-009-010, and RFBR Grant No. 03-02-17452.

[1] G. A. Prinz, Science **282**, 1660 (1998); S. A. Wolf *et al.*, Science **294**, 1488 (2001); *Semiconductor Spintronics and Quantum Computation*, edited by D. D. Awschalom, D. Loss, and N. Samarth (Springer-Verlag, Berlin, 2002); I. Zutić, J. Fabian, and S. Das Sarma, Rev. Mod. Phys. **76**, 323 (2004).
[2] M. I. Dyakonov and V. I. Perel, Phys. Lett. **35A**, 459 (1971); J. E. Hirsch, Phys. Rev. Lett. **83**, 1834 (1999).
[3] S. Murakami, N. Nagaosa, and S.-C. Zhang, Science **301**, 1348 (2003); J. Sinova *et al.*, Phys. Rev. Lett. **92**, 126603 (2004); D. Culcer *et al.*, Phys. Rev. Lett. **93**, 046602 (2004).
[4] Y. K. Kato *et al.*, Science **306**, 1910 (2004).
[5] J. Wunderlich *et al.*, Phys. Rev. Lett. **94**, 047204 (2005).
[6] J. I. Inoue, G. E. W. Bauer, and L. W. Molenkamp, Phys. Rev. B **70**, 041303 (2004); E. I. Rashba, Phys. Rev. B **70**, 201309 (2004); O. Chalaev and D. Loss, Phys. Rev. B **71**, 245318 (2005).
[7] E. G. Mishchenko, A. V. Shytov, and B. I. Halperin, Phys. Rev. Lett. **93**, 226602 (2004).
[8] A. A. Burkov, A. S. Nunez, and A. H. MacDonald, Phys. Rev. B **70**, 155308 (2004).
[9] O. V. Dimitrova, Phys. Rev. B **71**, 245327 (2005).
[10] R. Raimondi and P. Schwab, Phys. Rev. B **71**, 033311 (2005).
[11] A. G. Mal'shukov and K. A. Chao, Phys. Rev. B **71**, 121308(R) (2005).
[12] B. A. Bernevig and S. C. Zhang, Phys. Rev. Lett. **95**, 016801 (2005); K. Nomura *et al.*, cond-mat/0506189 [Phys. Rev. B (to be published)].
[13] Yu. A. Bychkov and E. I. Rashba, J. Phys. C **17**, 6039 (1984).
[14] G. Dresselhaus, Phys. Rev. **100**, 580 (1955).
[15] The cubic Rashba interaction should not be confused with the conventional linear Rashba SOI with the wave-vector-dependent coupling constant $\alpha(k)$. In the latter case SHE $\propto \alpha(k)k/E_F \ll 1$ [9,12].
[16] V. M. Edelstein, Solid State Commun. **73**, 233 (1990); J. I. Inoue, G. E. W. Bauer, and L. W. Molenkamp, Phys. Rev. B **67**, 033104 (2003).
[17] A. A. Abrikosov, L. P. Gorkov, and I. E. Dzyaloshinskii, *Methods of Quantum Field Theory in Statistical Physics* (Dover, New York, 1975).
[18] B. L. Altshuler and A. G. Aronov, in *Electron-Electron Interactions in Disordered Systems*, edited by A. L. Efros and M. Pollak (North-Holland, Amsterdam, 1985).
[19] A. G. Mal'shukov and K. A. Chao, Phys. Rev. B **61**, R2413 (2000).
[20] A. G. Mal'shukov, K. A. Chao, and M. Willander, Phys. Rev. Lett. **76**, 3794 (1996); Phys. Scr. **T66**, 138 (1996).
[21] M. I. D'yakonov and V. I. Perel', Sov. Phys. JETP **33**, 1053 (1971) [Zh. Eksp. Teor. Fiz. **60**, 1954 (1971)].
[22] Y. K. Kato *et al.*, Appl. Phys. Lett. **87**, 022503 (2005).
[23] B. K. Nikolić *et al.*, Phys. Rev. Lett. **95**, 046601 (2005); Q. Wang, L. Sheng, and C. S. Ting, cond-mat/0505576.

Finger-gate array quantum pumps: Pumping characteristics and mechanisms

S. W. Chung,[1] C. S. Tang,[2] C. S. Chu,[3] and C. Y. Chang[1]
[1]*Department of Electronics, National Chiao-Tung University, Hsinchu 30010, Taiwan*
[2]*Physics Division, National Center for Theoretical Sciences, P.O. Box 2-131, Hsinchu 30013, Taiwan*
[3]*Department of Electrophysics, National Chiao-Tung University, Hsinchu 30010, Taiwan*
(Received 7 June 2003; revised manuscript received 19 March 2004; published 27 August 2004)

We study the pumping effects, in both the adiabatic and nonadiabatic regimes, of a pair of *finite* finger-gate array (FGA) on a narrow channel. Connection between the pumping characteristics and associated mechanisms is established. The pumping potential is generated by ac biasing the FGA pair. For a single pair ($N=1$) of finger gates (FG's), the pumping mechanism is due to the coherent inelastic scattering of the traversing electron to its subband threshold. For a pair of FGA with pair number $N>2$, the dominant pumping mechanism becomes that of the time-dependent Bragg reflection. The contribution of the time-dependent Bragg reflection to the pumping is enabled by breaking the symmetry in the electron transmission when the pumping potential is of a predominant propagating type. This propagating wave condition can be achieved both by an appropriate choice of the FGA pair configuration and by the monitoring of a phase difference ϕ between the ac biases in the FGA pair. The robustness of such a pumping mechanism is demonstrated by considering a FGA pair with only pair number $N=4$.

DOI: 10.1103/PhysRevB.70.085315 PACS number(s): 72.10.−d, 72.30.+q, 72.90.+y

I. INTRODUCTION

Quantum charge pumping (QCP) has become an active field in recent years.[1–21] This is concerned with the generation of net transport of charges across an unbiased mesoscopic structure by cyclic deformation of two structure parameters. Original proposal of QCP, in the adiabatic regime, was due to Thouless[1,2] and Niu.[2] They considered the current generated by a slowly varying traveling wave in an isolated one-dimensional system. The number of electrons transported per period was found to be quantized if the Fermi energy lies in a gap of the spectrum of the instantaneous Hamiltonian. Aiming at this quantized pumped charge nature of the adiabatic pumping, Niu proposed various one-dimensional periodic potentials for the adiabatic quantum pumping (AQP),[2] and pointed out the importance of the quantized charge pumping in utilizing it for a direct-current standard.[2]

Another way to achieve the AQP was suggested by Hekking and Nazarov,[3] who studied the role of inelastic scattering in the quantum pumping of a double-oscillating barrier in a one-dimensional system. Intended to stay in the adiabatic regime, they invoked a semiclassical approximation and had assumed that the Fermi energy $\varepsilon_F \gg \hbar\Omega$, where Ω is the pumping frequency. This semiclassical treatment of the inelastic scattering is known to be inappropriate for the regime when either the initial or the final states are in the vicinity of the energy band edge. Such a regime, however, is our major focus in this work. It is because the coherent inelastic scattering becomes resonant when the traversing electron can make transitions to its subband threshold by emitting $m\hbar\Omega$.[22,23] Depending on the system configuration, this and another resonant inelastic scatterings will be shown to dominate the pumping characteristics.[10]

A recent experimental confirmation of AQP has been reported by Switkes *et al.*[4] Two metal gates that defined the shape of an open quantum dot were ac biased[24] with voltages of the same frequency but differed by a tunable phase difference.[5] DC response across the source and drain electrodes is the signature of the AQP. This has prompted further intensive studies on AQP in quantum dots,[6–8] double-barrier quantum wells,[9] pumped voltage,[12] noiseless AQP,[13] heat current,[14] incoherent processes,[15,16] quantum rings,[19,20] and interacting wires.[21]

An alternate experimental effort in generating AQP involves surface acoustic wave (SAW).[25–29] Generated by an interdigitated SAW transducer located deep on an end-region of a narrow channel, the SAW propagates to the other end-region of the narrow channel while inducing a wave of electrostatic potential inside the channel. Electrons trapped in the potential minima are thus transported along the narrow channel. Both Mott-Hubbard electron-electron repulsion in each such trap and the adiabaticity in the transport are needed to give rise to quantization in the pumped current.[26] As such, the channel has to be operated in the pinch-off regime.[27]

In this work, we propose to study yet another experimental configuration for QCP in a narrow channel. The proposed configuration consists of a pair of *finite* finger-gate array (FGA), with the number N of FG's in each FGA being kept to a small number. In contrast to the SAW configuration, the FGA pair sits on top of the narrow channel, rather than locating at a distance far away from it and the most significant QCP occurs in regimes other than the pinch-off regime. The FG's orient transversely and line up longitudinally with respect to the narrow constriction. As is shown in Fig. 1, pumping potential can be generated by ac biasing the FGA pairs with the same frequency but maintaining a phase difference ϕ between them. Since the wave of electrostatic potential induced in the narrow channel is directly from the FG's, rather than via the SAW, our proposed structure has the obvious advantage that the working frequency is not restricted to the frequency of the SAW, $\omega_S = 2\pi v_S/d$. Here v_S is the phase velocity of the SAW, and d is the pitch in the FGA. Furthermore, when the working frequency is different from

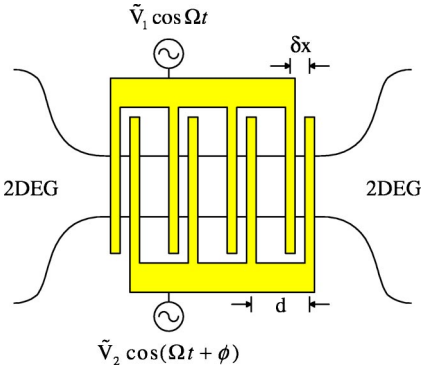

FIG. 1. (Color online) Top view of the proposed system structure for the case of pair number $N=4$. A FGA pair is located on top of a narrow channel. $\tilde{V}_i$ denotes the amplitude of the potential energy, and ϕ is the phase difference.

ω_S, the contribution from SAW to the pumped current will be negligible.

Below we shall show how the ac biased FGA pair plays a subtle role in the generation of QCP. In Sec. II, we present our theoretical model for the FGA pair calculation of the pumped current generated by the FGA pair configuration. In Sec. III, we present the pumping characteristics and demonstrate that resonant coherent inelastic scatterings are the underlying pumping mechanisms. Finally, in Sec. IV, we present our discussion and summary.

II. FGA PAIR MODEL

The potential $V(x,t)$ in a narrow constriction induced by a FGA pair is represented by

$$V(x,t) = \sum_{i=1}^{N} V_{1i}(x)\cos(\Omega t) + V_{2i}(x)\cos(\Omega t + \phi), \qquad (1)$$

where N is the number of FG's per FGA. We assume that the ac biased FGA pair are localized, respectively, at positions x_i and $x_i+\delta x_i$, namely, that $V_{1i}(x)=V_1\delta(x-x_i)$ and $V_{2i}(x)=V_2\delta(x-x_i-\delta x)$ with a relative phase difference ϕ. These FG's are evenly spaced, with a pitch d, and are located at $x_i=(i-1)d$ for one FGA and $x_i+\delta x$ for the other. The relative shift between the FGA pair is $\delta x=\alpha\, d$, where the fractional shift $0<\alpha<1$. In the following, we consider the case of the same modulation amplitude $V_1=V_2=V_0$. Depending on the choice of the values for ϕ and α, $V(x,t)$ will either be predominantly of a propagating or a standing wave type. A sensible choice can be made from considering the lowest order Fourier component of $V(x,t)$, given by

$$\mathcal{V}_1 = \frac{2V_0}{d}\{\cos Kx \cos \Omega t + \cos[K(x-\delta x)]\cos(\Omega t + \phi)\}, \qquad (2)$$

where $K=2\pi/d$. For our purposes in this work, an optimal choice is $\phi=\pi/2$ and $\alpha=1/4$, in which $V(x,t)$ is a predominant left-going wave.

The Hamiltonian of the system is $H=H_y+H_x(t)$, in which $H_y=-\partial^2/\partial y^2+\omega_y^2 y^2$ contains a transverse confinement, leading to subband energies $\varepsilon_n=(2n+1)\omega_y$. The time-dependent part of the Hamiltonian $H_x(t)$ is of the dimensionless form $H_x(t)=-\partial^2/\partial x^2+V(x,t)$. Here appropriate units have been used such that all physical quantities presented are in dimensionless form.[24]

In the QCP regime, the chemical potential μ is the same in all reservoirs. Thus the pumped current, at zero temperature, can be expressed as[10]

$$I = -\frac{2e}{h}\int_0^{\mu} dE\,[T_{\rightarrow}(E) - T_{\leftarrow}(E)]. \qquad (3)$$

Here the total current transmission coefficients include the contributions by electrons with incident energy E in incident subband n, which may absorb or emit $m\Omega$ to energy $E_m=E+m\Omega$ by the FG pumping potentials, given by

$$T_{\rightarrow(\leftarrow)}(E) = \sum_{n=0}^{\mathcal{N}_S-1}\sum_{m=-\infty}^{\infty} T_{n\rightarrow(\leftarrow)}(E_m,E), \qquad (4)$$

where $\mathcal{N}_S$ stands for the number of occupied subbands. The summations are over all the propagating components of the transmitted electrons, and includes both the subband index n and the sideband index m. The subscripted arrow in the total current transmission coefficient indicates the incident direction. These coefficients are calculated numerically by a time-dependent scattering-matrix method.[10,30,31]

III. NUMERICAL RESULTS

In this section we present the numerical results for the pumping characteristics of either a single FG pair ($N=1$) or a *finite* FGA pair ($N>2$). In these two cases the pumping characteristics are due to different resonant inelastic scattering processes. For definiteness, the parameter values in our numerical results are taken from the FaAs-$Al_xGa_{1-x}As$ based heterostructure. The values that we choose for our configuration parameters are $\omega_y=0.007$, subband level spacing $\Delta\varepsilon=2\omega_y(\simeq 0.13$ meV), $d=40$ ($\simeq 0.32$ μm), and $V0=0.04$ ($\simeq 28.7$ meV Å). From the value of V_0, and the assumed FG width ~ 0.05 μm, the amplitude of the potential induced by a FG is ~ 0.057 mV.

A. Single FG pair case

In this subsection we investigate the pumping characteristics for the case of a single FG pair. Figure 2 presents the dependence of the total current transmission coefficients on the incident electron energy μ. We replace the chemical potential μ by

$$X_\mu = \frac{\mu}{\Delta\varepsilon} + \frac{1}{2}, \qquad (5)$$

which integral value corresponds to the number of propagating subbands $\mathcal{N}_S$ in the narrow channel. The pumping frequency is higher in Fig. 2(a), with $\Omega=0.6\Delta\varepsilon(\Omega/2\pi \simeq 18$ GHz), than that in Fig. 2(b), where $\Omega=0.1\Delta\varepsilon(\Omega/2\pi \simeq 3$ GHz). We select the phase shift $\phi=\pi/2$ and $\alpha=1/4$.

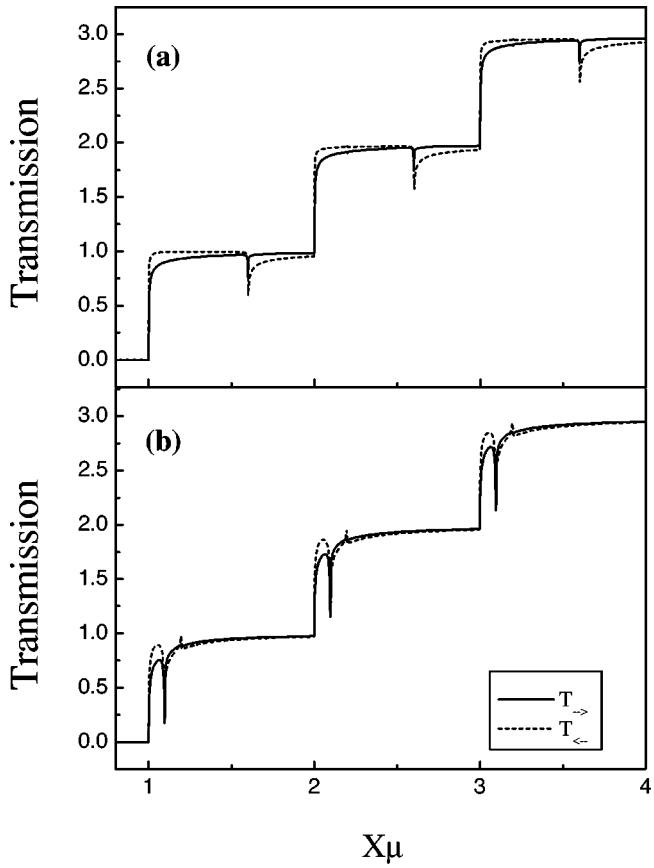

FIG. 2. Total current transmission coefficient versus X_μ for a pair of FG; (a) $\Omega=0.6\Delta\varepsilon$ and (b) $\Omega=0.1\Delta\varepsilon$. The transmission of the right-going (left-going) electrons are represented by the solid (dotted) curve. The subband level spacing is $\Delta\varepsilon$. Parameters $\alpha=1/4$ and $\phi=\pi/2$ are chosen to meet the optimal condition.

At integral values of X_μ, the total current transmission coefficients $T_{\rightarrow\,(\leftarrow)}(X_\mu)$ exhibit abrupt changes. This is due to the changes in the number of propagating subbands in the narrow channel. Between integral X_μ values, $T_{\rightarrow\,(\leftarrow)}$ both show dip structures. The dip structures are located at $X_{\rm dip}=\mathcal{N}_S+0.6$ in Fig. 2(a), and at $X_{\rm dip}=\mathcal{N}_S+0.1$ in Fig. 2(b). These dip structure locations are the same for both $T_\rightarrow$ and $T_\leftarrow$, and are resonant structures associated with inelastic scattering that causes an electron to jump into a quasibound state (QBS) just beneath a subband bottom.[22] The peak structures in $T_\leftarrow$ of Fig. 2(b), and at $X_\mu=\mathcal{N}_S+0.2$, are 2Ω resonant structures.

In Fig. 2, we can see that $T_\leftarrow(X_\mu)$ does not equal to $T_\rightarrow(X_\mu)$, this allows the occurrence of the pumped current. Moreover, between integral X_μ values, $T_\leftarrow > T_\rightarrow$ on the left region of a dip structure, while $T_\leftarrow < T_\rightarrow$ on the right region of the dip structure. This has an important bearing on the dependence of the pumped current on μ, as is shown in Fig. 3. The pumped current rises, and drops, on the left, and right, region of a $X_{\rm dip}$, respectively, in accordance with the relative changes in $T_\rightarrow$ and $T_\leftarrow$ about the same $X_{\rm dip}$. Hence the peaks of the pumped current depend on the pumping frequency, at

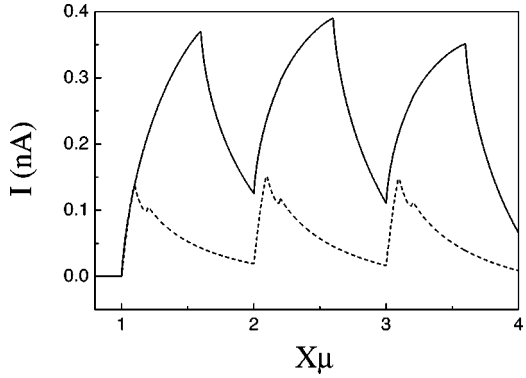

FIG. 3. The pumped currents versus X_μ with the same parameters used in Fig. 2. The solid and dashed curves correspond, respectively, to $\Omega=0.6\Delta\varepsilon$ and $\Omega=0.1\Delta\varepsilon$.

$$X_\mu^{(\rm peak)}=\mathcal{N}_S+\frac{\Omega}{\Delta\varepsilon}, \tag{6}$$

reassuring us that the pumping is dominated by the aforementioned resonant inelastic process.

Besides the trend that the pumped current in Fig. 3 drops with the pumping frequency, we would like to remark on a more interesting result: that both the adiabatic and nonadiabatic behaviors can be found in the same curve. Since the adiabatic condition is given by $\mu \gg \Omega$, the curve for $\Omega=0.1\Delta\varepsilon$ in the regions $\mathcal{N}_s+\Omega/\Delta\varepsilon < X_\mu \leqslant \mathcal{N}_s+1$ corresponds to the adiabatic regimes, while the other X_μ regions are nonadiabatic regimes. This is checked also with our other calculation, which is not shown here, using the Brouwer expression.[5] For the higher pumping frequency, $\Omega=0.6\Delta\varepsilon$, the adiabatic condition is not satisfied in the entire X_μ region, even though the pumping characteristics resemble that of the adiabatic one in the regions $\mathcal{N}_s+\Omega/\Delta\varepsilon < X_\mu \leqslant \mathcal{N}_s+1$.

B. Finite FGA case

In this subsection we present the numerical results for the pumping characteristics of a *finite* FGA pair. QCP for two prominent modes of tuning the system are considered. These are (i) tuning of the electron density by the *back-gate* technique, and (ii) tuning of the channel width by *split-gate* technique.

1. Tuning back-gate

We present the numerical results for the pumping characteristics of a FGA pair with $N=4$ that is realized by the *back-gate technique*. The dependence of the total current transmission coefficients on X_μ is shown in Fig. 4, in which the pumping frequencies are (a) $\Omega=0.6\Delta\varepsilon$ and (b) $\Omega=0.1\Delta\varepsilon$. The choice of the parameters d, ϕ, and α is the same as in the previous subsection, but the latter two parameters give rise here to an equivalent left-going wave in the pumping potential $V(x,t)$.

The curves in Fig. 4 show additional structures, other than the dip structures that has been discussed in the last subsection. These additional structures are valley structures that occur at different X_μ values for $T_\rightarrow(X_\mu)$ and $T_\leftarrow$. In a region

between two integral values of X_μ, the valley structure of $T_{\rightarrow}(X_\mu)$ occurs at a lower X_μ. This shows clearly the breaking of the transmission symmetry by the pumping potential. Furthermore, the valleys are separated by $\Delta X_\mu = \Omega/\Delta\varepsilon$. This can be understood from resonant coupling conditions $\varepsilon_k = \varepsilon_{k-K} - \Omega$ and $\varepsilon_{k+K} = \varepsilon_k - \Omega$ for, respectively, the right-going and the left-going k. From these conditions, the valley locations are at

$$k_{\pm}^2 = \left[\frac{K}{2}\left(1 \mp \frac{\Omega}{K^2}\right)\right]^2, \tag{7}$$

where the upper sign is for positive, or right-going, k. These locations, expressed in terms of X_μ, are given by

$$X_\mu = \mathcal{N}_S + \frac{k_{\pm}^2}{\Delta\varepsilon}, \tag{8}$$

and are at $X_\mu = 1.19$, 1.79, 2.19, 2.79, 3.19, and 3.79 for the case of Fig. 4(a), and $X_\mu = 1.39$, 1.49, 2.39, 2.49, 3.39, and 3.49 for the case of Fig. 4(b). The matching between these numbers and our numerical results in Fig. 4 is remarkable. In addition, energy gaps open up at these $k_{\pm}^2$ locations, causing the drop in the transmission and the formation of the valley structures.[10] All these results reassure us that the time-dependent Bragg's reflection is the dominant resonant inelastic scattering in our FGA pair structure.

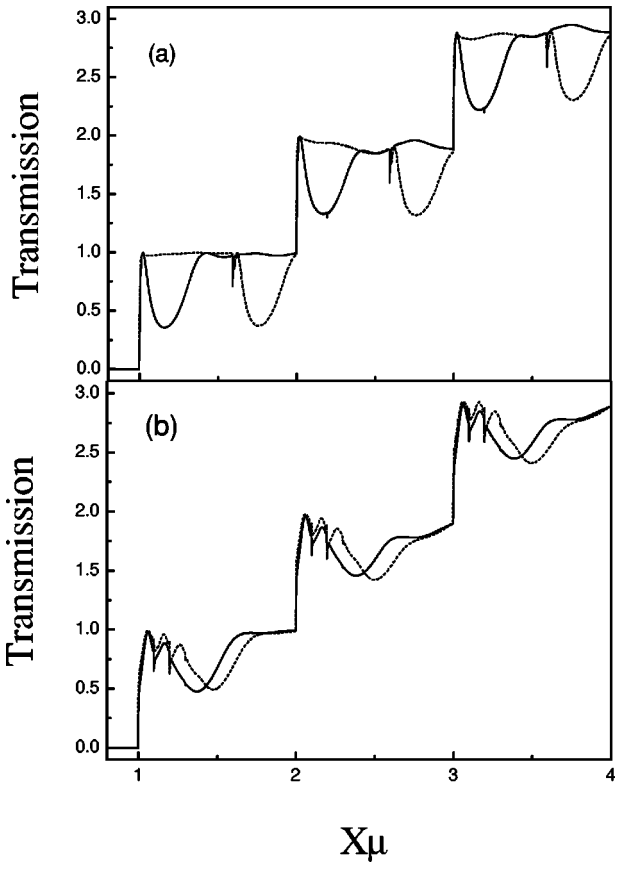

FIG. 4. Total current transmission coefficient versus X_μ for $N = 4$; (a) $\Omega = 0.6\Delta\varepsilon$ and (b) $\Omega = 0.1\Delta\varepsilon$. The transmission of the right-going (left-going) electrons are represented by the solid (dotted) curve. The parameters $\alpha = 1/4$ and $\phi = \pi/2$.

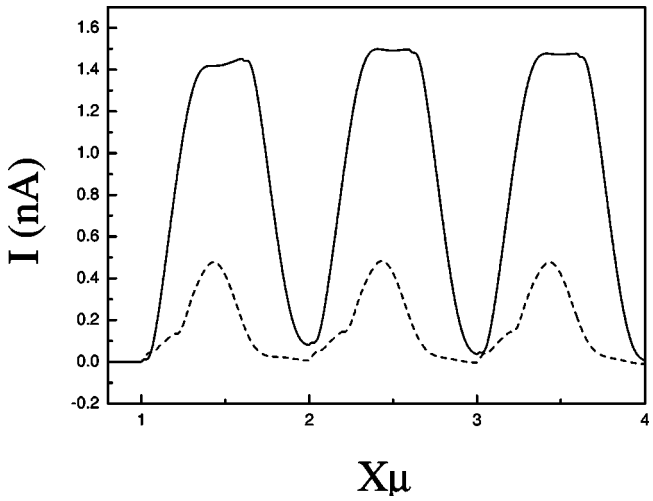

FIG. 5. Pumped current versus X_μ. The choices of parameters are the same as in Fig. 4. The solid and dashed curves correspond, respectively, to $\Omega = 0.6\Delta\varepsilon$ and $\Omega = 0.1\Delta\varepsilon$.

On the other hand, the adiabatic condition is here given by $\varepsilon_{\text{gap}} \gg \Omega$, where ε_{gap} is the *effective* energy gap of the *instantaneous* Hamiltonian.[2] Since ε_{gap} is given by the widths of the valley structures, therefore contributions of the valleys to the pumped current is nonadiabatic in Fig. 4(a), because the valleys are well separated, and adiabatic in Fig. 4(b), because the valleys overlap.

In Fig. 5, we present the X_μ dependence of the pumped current for the cases in Fig. 4. The pumped current peaks at X_μ that lies in the middle between a valley in $T_{\rightarrow}(X_\mu)$ and the corresponding valley in $T_{\leftarrow}(X_\mu)$. The locations are around

$$X_\mu = \mathcal{N}_S + \frac{K^2}{4\Delta\varepsilon}\left(1 + \frac{\Omega^2}{K^4}\right), \tag{9}$$

which depend on both the pitch d and the pumping frequency Ω. The peaks have flat tops for the solid curve, when $\Omega = 0.6\Delta\varepsilon$. Comparing with the total current transmission curves in Fig. 4(a), we see that the flat-topped peak profile is associated with the complete separation between the valleys in $T_{\rightarrow}$ and $T_{\leftarrow}$. This is in the nonadiabatic regime. In contrast, for the case when the valleys overlap, such as in Fig. 4(b), the pumped current peaks no longer carry a flat-top profile, as is shown by the dashed curve in Fig. 5. This is in the adiabatic regime. Meanwhile, their peak values are lowered. It is because cancellation sets in when the valleys overlap. We note that the pumped currents are of order nA.

The robustness of the time-dependent Bragg reflection, on the other hand, is demonstrated most convincingly by the number of charge pumped per cycle at the maximum I_{Max} of the pumped current. In the dashed curve of Fig. 5, the pumped charge per cycle per spin state $Q_P = (2\pi/\Omega) I_{\text{Max}}/2e = 0.495$, where $I_{\text{Max}} = 0.48$ nA and $\Omega = 0.1\Delta\varepsilon = 3.03$ GHz. To get a unity, or quantized, charge pumped per cycle per spin state, one can fix the pumping frequency $\Omega = 0.1\Delta\varepsilon$, $N = 4$, $\phi = \pi/2$, and $d = 40$, then tune the

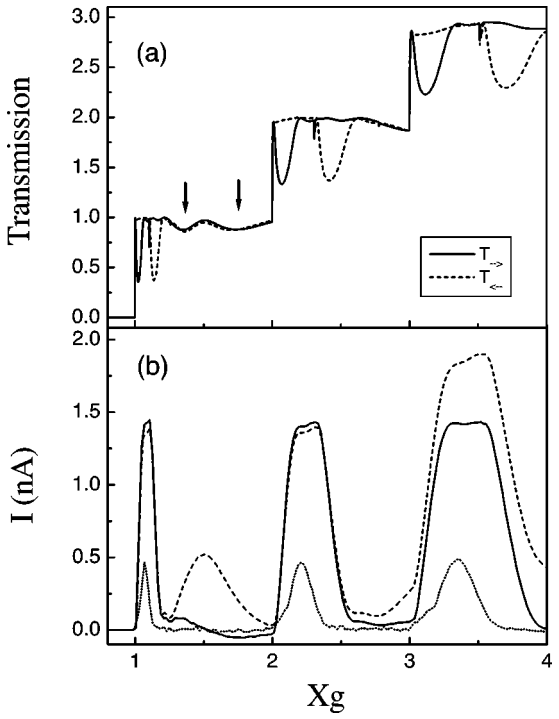

FIG. 6. The dependence on subband level spacing $\Delta\varepsilon$ of (a) the total current transmission coefficient, and (b) the pumped current. The abscissa is depicted by Eq. (10) where $\mu=0.049$ and $N=4$. Pumping frequency $\Omega=0.0084$ in all curves except for the dotted curve in (b), where $\Omega=0.0014$. Parameters $\phi=\pi/2$ and $\alpha=1/4$ for all curves except for the dashed curve in (b), where $\alpha=1/5$. In (a), the solid (dashed) curve is for $T_{\rightarrow}(X_g)[T_{\leftarrow}(X_g)]$, and contributions from the second Fourier component of $V(x,t)$ are indicated by arrows.

other pumping parameters $V_0=0.09$ and $\alpha=0.15$ to obtain $Q_P=0.992$ at $X_\mu=3.465$ (not shown here). In this frequency regime, the pumping would be expected to be adiabatic, according to Thouless[1] and Niu[2] when $\varepsilon_{\text{gap}} \gg \Omega$. However, in our case here, the energy gap is at best only partially opened, as we can see from the nonzero transmission in Fig. 4(b), because we have only $N=4$ FG pairs. Thus our result shows that the condition of occurrence of the AQP is less stringent than we would have expected originally.[2] In other words, the pumping effect of our FGA configuration is robust.

It is also worth pointing out that the pumped currents are positive in Fig. 5, showing that the net number flux of the pumped electrons is from right to left. This is consistent with the propagation direction of the electrostatic wave in $V(x,t)$.[10]

2. Tuning split-gate

Thus far, we have explored the dependence of the FGA pair's QCP characteristics on X_μ by the use of the *back-gate technique*. Another way of tuning the QCP characteristics is via the modulation of the channel width (or subband level spacing $\Delta\varepsilon$). This can be realized experimentally by the use of the so-called *split-gate technique*. Hence we present, in Fig. 6, the transverse confinement dependence of both the total current transmission coefficients and the pumped current. The transverse confinement is depicted by

$$X_g = \frac{\mu}{\Delta\varepsilon} + \frac{1}{2}, \tag{10}$$

which is linearly related to the effective channel width, and that its integral value corresponds to the number of propagating subbands in the channel. In this mode of tuning the QCP characteristics, μ is kept fixed.

In Fig. 6(a), except for μ, which is fixed at 0.049, and ω_y, which varies with X_g, other parameters such as $\Omega=0.0084$, $\phi=\pi/2$, and $\alpha=1/4$ are the same as in Fig. 4(a). The solid (dashed) curve is for $T_{\rightarrow}$ ($T_{\leftarrow}$). Both the QBS and the time-dependent Bragg reflection features are found. The expected locations of the QBS, given by the expression

$$X_g = \frac{1}{2} + \left(n + \frac{1}{2}\right)\frac{\mu}{\mu - \Omega}, \tag{11}$$

are at 1.1, 2.3, and 3.5, and they match the QBS locations in Fig. 6(a) perfectly. Here n is the subband index. The expected locations of the valleys, associated with the time-dependent Bragg reflection, are given by the expression

$$X_g = \frac{1}{2} + \left(n + \frac{1}{2}\right)\frac{\mu}{\mu - k_\pm^2}, \tag{12}$$

thus they should be at $X_g=1.03,2.1,3.14$ for $T_{\rightarrow}(X_g)$, and at $X_g=1.15,2.4,3.73$ for $T_{\leftarrow}(X_g)$. Again, they match the valley locations in Fig. 6(a) remarkably.

Besides, there are in Fig. 6(a) two additional valley structures, indicated by arrows, at which $T_{\rightarrow}(X_g)$ and $T_{\leftarrow}(X_g)$ fall one on top of the other. These structures do not contribute to the pumped current, and they are due to the time-dependent Bragg reflection from the second order Fourier component of $V(x,t)$. The second Fourier component of $V(x,t)$ is in the form of a standing wave, given by $\cos(2Kx)[\cos\Omega t + \sin\Omega t]$. That both of the additional valleys all appear in $T_{\rightarrow}(X_g)$ and $T_{\leftarrow}(X_g)$ can be understood from the fact that more resonant coupling conditions come into play for the case of standing wave. The resonant coupling conditions are $\varepsilon_k=\varepsilon_{k\pm 2K}\pm\Omega$, and $\varepsilon_k=\varepsilon_{k\pm 2K}\mp\Omega$. As such, the valley locations are given by the expression

$$X_g = \frac{1}{2}\left[1 + \frac{\mu}{\mu - \epsilon_\pm}\right] \tag{13}$$

for $n=0$, and for $\epsilon_\pm=[K(1\mp\Omega/(2K)^2)]^2$. Accordingly, these $2K$ time-dependent Bragg reflection valley locations are expected to be at 1.36 and 1.73, which coincide with the two additional valleys in Fig. 6(a), and are indicated by arrows. We note, in passing, that contributions from higher Fourier components diminish, as is seen by comparing the valleys from the first and the second Fourier components of $V(x,t)$.

The X_g dependence of the pumped current for the case in Fig. 6(a) is represented by the solid curve in Fig. 6(b). The peaks have flat tops because the valleys in the corresponding $T_{\rightarrow}(X_g)$, $T_{\leftarrow}(X_g)$ are well separated. The pumped current for $\Omega=0.0014$, the same frequency as in the case of Fig. 4(b), is depicted by the dotted curve in Fig. 6(b). The peaks are not flat-topped and the magnitudes are much smaller because the

transmission valleys overlap. For comparison, we also present the case when parameter values differ slightly from that of the optimal choice. As is shown by the dashed curve in Fig. 6(b), where all parameters are the same as for the solid curve except that α is changed from 1/4 to 1/5, the basic pumped current peaks in the solid curve remain intact. This demonstrates the robustness of the QCP against the deviation in values of the configuration parameters from the optimal choice.

Interestingly, there are two additional features in the dashed curve of Fig. 6(b): namely, an additional pumped current peak at $X_g=1.5$, and an increase in the peak value for the pumped current near $X_g=3.5$. That both of these features are found to arise from the second Fourier component of $V(x,t)$ is supported by the outcome of our analysis performed upon the Fourier component of $V(x,t)$. This method of analysis has thus far been successful in providing us insights on the pumping characteristics presented in this work. The m-th Fourier component of $V(x,t)$, apart from a constant factor, is given by the form

$$V_m = \{[\cos(m\pi\alpha) - \sin(m\pi\alpha)]\cos[mKx' - \Omega t - \pi/4] + [\cos(m\pi\alpha) + \sin(m\pi\alpha)]\cos[mKx' + \Omega t + \pi/4]\}, \tag{14}$$

where $x'=x-\delta x/2$. $\mathcal{V}_m$ consists, in general, of waves propagating in both left and right directions. But when $\alpha=1/4$, as we have discussed before, $\mathcal{V}_1$ becomes a pure left-going wave and $\mathcal{V}_2$ becomes a pure standing wave. The case of $\alpha=1/5$, however, have both $\mathcal{V}_1$ and $\mathcal{V}_2$ consisting of waves in opposite propagation directions. Therefore, in contrast with the $\alpha=1/4$ result, additional contributions from the $2K$ Bragg reflection are expected for the case $\alpha=1/5$. This additional contribution should peak at the mid-point between two transmission valleys for the $2K$ Bragg reflections, and the expression for X_g is given by

$$X_g = \frac{1}{2} + \left(n + \frac{1}{2}\right)\frac{\mu}{\mu - \epsilon_M}, \tag{15}$$

where $\epsilon_M=K^2+(\Omega/2K)^2$. For the case of the dashed curve in Fig. 6(b), the values of $X_g = 1.54$ and 3.6 are shown to match the locations of the additional features nicely. Finally, we can extract information of the sensitivity of the pumped current characteristics to α by looking at the coefficients of the left-going and right-going waves in $\mathcal{V}_m$. For $\alpha=1/5$, the coefficients of $\mathcal{V}_1$ for, respectively, the right-going and the left-going waves are 0.22 and 1.4. This shows that $\mathcal{V}_1$ is still dominated by the left-going wave and thus explains the tiny modifications to the pumped current peaks at $X_g=1.1$, and 2.3. But for $\mathcal{V}_2$, the coefficients for, respectively, the right-going and the left-going waves are -0.95 and 1.57. This shows that $\mathcal{V}_2$ deviates quite significantly from that of a standing wave, and so explains that the additional peaks from the $2K$ Bragg reflections are quite large.

IV. DISCUSSION AND SUMMARY

It is interesting to note in passing that our proposal of the FGA pair configuration is different, in three aspects, from the voltage lead pattern proposed earlier by Niu.[2] First of all, the pumping mechanisms to which the configurations are catering to are different. It is the mechanism of translating the Wannier functions in a given Bloch band in Ref. 2, while it is the mechanism of the time-dependent Bragg reflection in this work. The former mechanism is adiabatic by nature but the latter mechanism is shown, in this work, to hold in both the adiabatic and non-adiabatic regimes.

Second, the configurations are different in the number of sets of voltage leads invoked. A third set of voltage leads was instituted by Niu to fix the Fermi energy at the middle of the *instantaneous energy gap* in order to maintain the adiabaticity of the pumping. Since our interest here is on the general pumping characteristics, including, in particular, their dependence on the Fermi energy, it suffices us to consider a simpler configuration—the FGA pair configuration. Third, the number of voltage lead expected, and needed, in a voltage lead set is different. Our results demonstrate the resonant nature of the time-dependent Bragg reflection, and that the pumping characteristic is robust—requiring only a FGA pair with small N. Hence the FGA pair configuration proposed in this work should be more accessible experimentally.

In conclusion, we have proposed a finger-gate array pair configuration for the generation of quantum charge pumping. Detail pumping characteristics have been analyzed, the robustness of the time-dependent Bragg reflection in QCP has been demonstrated, and the pumping mechanism is understood.

ACKNOWLEDGMENT

This work was funded by the National Science Council of Taiwan under Grant Nos. NSC92-2112-M-009-035, NSC92-2120-M-009-010 (CSC), and NSC91-2119-M-007-004 (NCTS).

[1] D. J. Thouless, Phys. Rev. B **27**, 6083 (1983).
[2] Q. Niu, Phys. Rev. Lett. **64**, 1812 (1990).
[3] F. Hekking and Yu. V. Nazarov, Phys. Rev. B **44**, 9110 (1991).
[4] M. Switkes, C. M. Marcus, K. Campman, and A. C. Gossard, Science **283**, 1905 (1999).
[5] P. W. Brouwer, Phys. Rev. B **58**, R10135 (1998).
[6] I. L. Aleiner and A. V. Andreev, Phys. Rev. Lett. **81**, 1286 (1998).
[7] F. Zhou, B. Spivak, and B. Altshuler, Phys. Rev. Lett. **82**, 608 (1999).
[8] O. Entin-Wohlman and A. Aharony, Phys. Rev. B **66**, 035329 (2002).
[9] Y. Wei, J. Wang, and H. Guo, Phys. Rev. B **62**, 9947 (2000).
[10] C. S. Tang and C. S. Chu, Solid State Commun. **120**, 353 (2001).

[11] S. Zhu and Z. D. Wang, Phys. Rev. B **65**, 155313 (2002).
[12] M. L. Polianski and P. W. Brouwer, Phys. Rev. B **64**, 075304 (2001).
[13] J. E. Avron, A. Elgart, G. M. Graf, and L. Sadun, Phys. Rev. Lett. **87**, 236601 (2001).
[14] B. Wang and J. Wang, Phys. Rev. B **66**, 125310 (2002).
[15] M. Moskalets and M. Büttiker, Phys. Rev. B **64**, 201305(R) (2001).
[16] M. Moskalets and M. Büttiker, Phys. Rev. B **66**, 035306 (2002).
[17] S. W. Kim, Phys. Rev. B **68**, 085312 (2003); S. W. Kim, Phys. Rev. B **66**, 235304 (2002).
[18] M. Moskalets and M. Büttiker, Phys. Rev. B **68**, 075303 (2003).
[19] M. Moskalets and M. Büttiker, Phys. Rev. B **68**, 161311 (2003).
[20] D. Cohen, Phys. Rev. B **68**, 201303(R) (2003).
[21] P. Sharma and C. Chamon, Phys. Rev. B **68**, 035321 (2003).
[22] The fact that a coherent inelastic scattering becomes resonant when the traversing electron can make transitions to its band edge by emitting $m\hbar\Omega$ was studied by P. F. Bagwell and R. K. Lake in Phys. Rev. B **46**, 15329 (1992), where they considered the transmission through a single oscillating barrier.
[23] D. F. Martinez and L. E. Reichl, Phys. Rev. B **64**, 245315 (2001).
[24] C. S. Tang, Y. H. Tan, and C. S. Chu, Phys. Rev. B **67**, 205324 (2003).
[25] J. M. Shilton, V. I. Talyanskii, M. Pepper, D. A. Ritchie, J. E. F. Frost, C. J. B. Ford, C. G. Smith, and G. A. C. Jones, J. Phys.: Condens. Matter **8**, L531 (1996); J. M. Shilton, D. R. Mace, V. I. Talyanskii, Yu. Galperin, M. Y. Simmons, M. Pepper, and D. A. Ritchie, J. Phys.: Condens. Matter **8**, L337 (1996).
[26] V. I. Talyanskii, J. M. Shilton, M. Pepper, C. G. Smith, C. J. B. Ford, E. H. Linfield, D. A. Ritchie, and G. A. C. Jones, Phys. Rev. B **56**, 15180 (1997).
[27] Y. Levinson, O. Entin-Wohlman, and P. Wölfle, Phys. Rev. Lett. **85**, 634 (2000).
[28] O. Entin-Wohlman, Y. Levinson, and P. Wölfle, Phys. Rev. B **64**, 195308 (2001).
[29] A. Aharony and O. Entin-Wohlman, Phys. Rev. B **65**, 241401(R) (2002).
[30] A time-dependent transfer matrix method was discussed by M. Wagner, Phys. Rev. A **51**, 798 (1995); Phys. Rev. B **49**, 16544 (1994); M. Henseler, T. Dittrich, and K. Richter, Phys. Rev. E **64**, 046218 (2001).
[31] A detail presentation of a time-dependent scattering matrix method was given by C. S. Tang and C. S. Chu in Physica B **292**, 127 (2000).

Spin-current generation and detection in the presence of an ac gate

A. G. Mal'shukov,[1] C. S. Tang,[2] C. S. Chu,[3] and K. A. Chao[4]
[1]*Institute of Spectroscopy, Russian Academy of Science, 142190, Troitsk, Moscow oblast, Russia*
[2]*Physics Division, National Center for Theoretical Sciences, P.O. Box 2-131, Hsinchu 30013, Taiwan*
[3]*Department of Electrophysics, National Chiao-Tung University, Hsinchu 30010, Taiwan*
[4]*Solid State Theory Division, Department of Physics, Lund University, S-22362 Lund, Sweden*
(Received 15 August 2003; published 24 December 2003)

We predict that in a narrow gap III-V semiconductor quantum well or quantum wire, an observable electron spin current can be generated with a time-dependent gate to modify the Rashba spin-orbit coupling constant. Methods to rectify the so generated ac current are discussed. An all-electric method of spin-current detection is suggested, which measures the voltage on the gate in the vicinity of a two-dimensional electron gas carrying a time-dependent spin current. Both the generation and detection do not involve any optical or magnetic mediator.

DOI: 10.1103/PhysRevB.68.233307 PACS number(s): 73.63.−b, 71.70.Ej, 72.25.Dc

One key issue in spintronics based on semiconductor is the efficient control of the spin degrees of freedom. Datta and Das[1] suggested the use of gate voltage to control the strength of Rashba spin-orbit interaction (SOI)[2] which is strong in narrow gap semiconductor heterostructures. In InAs-based quantum wells a variation of 50% of the SOI coupling constant was observed experimentally.[3,4] Consequently, much interest has been attracted to the realization of spin-polarized transistors and other devices based on using electric gate to control the spin-dependent transport.[5]

In addition to using a static gate to control the SOI strength and so control the stationary spin transport, new physical phenomena can be observed in time-dependent spin transport under the influence of a fast varying gate voltage. Along this line, in this article we will consider a mechanism of ac spin current generation using time-dependent gate. This mechanism employs a simple fact that the time variation of Rashba SOI creates a force which acts on opposite spin electrons in opposite directions. Inversely, when a gate is coupled to a nearby electron gas, the spin current in this electron gas also induces a variation of the gate voltage, and hence affects the electric current in the gate circuit. We will use a simple model to clarify the principle of such a new detection mechanism without any optical or magnetic mediator. The systems to be studied will be 1D electron gas in a semiconductor quantum wire (QWR) and 2D electron gas in a semiconductor quantum well (QW).

We consider a model in which the Rashba SOI is described by the time-dependent Hamiltonian $H_{\mathrm{SO}}(t)=\hbar\alpha(t)\times(\vec{k}\times\hat{\nu})\cdot\vec{s}$, where $\vec{k}$ is the wave vector of an electron, $\hbar\vec{s}$ is the spin operator, and $\hat{\nu}$ is the unit vector. For a QWR $\hat{\nu}$ is perpendicular to the wire axis, and for a QW perpendicular to the interfaces. The time dependence of the coupling parameter $\alpha(t)$ is caused by a time-dependent gate.[6] To explain clearly the physical mechanisms leading to the spin-current generation, we will first consider the 1D electron gas in a QWR, and assume $\alpha(t)$ to be a constant α for $t<0$, and $\alpha(t)=0$ for $t>0$. For the 1D system we choose the x direction as the QWR axis and y axis parallel to $\hat{\nu}$, to write the SOI coupling in the form $H_{\mathrm{SO}}(t)=\hbar\alpha(t)k_x s_z$. For $t<0$ the spin degeneracy of conduction electrons is lifted by SOI, producing a splitting $\Delta=\hbar\alpha k_x$ between $s_z=1/2$ and $s_z=-1/2$ bands, as shown in Fig. 1 by solid curves together with the Fermi energy E_F. The spin current in this state is zero, as it should be under thermal equilibrium.

Indeed, the spin current is defined as $I_s(t)=I_\uparrow(t)-I_\downarrow(t)$, where $I_\uparrow(t)$ [or $I_\downarrow(t)$] is the partial current associated with the spin projections $s_z=1/2$ (or $s_z=-1/2$). Hence,

$$I_s(t)=\frac{\hbar}{2L}\sum_{E(k_x)<E_F}[v_\uparrow(k_x)-v_\downarrow(k_x)], \tag{1}$$

where L is the length of the QWR. Taking the momentum derivative of the Hamiltonian, we obtain the velocity as

$$v_{\uparrow,\downarrow}(k_x)=\hbar k_x/m^*\pm\alpha(t)/2. \tag{2}$$

The spin current is then readily obtained as

$$I_s(t)=(\hbar n/4m^*)(\hbar k_\uparrow-\hbar k_\downarrow)+\hbar\alpha(t)n/4, \tag{3}$$

where n is the 1D electron density, and $k_\uparrow$ (or $k_\downarrow$) is the average momentum in the $\uparrow$-spin (or $\downarrow$-spin) band.

For a parabolic band $\hbar k_\uparrow=-m^*\alpha/2$ and $\hbar k_\downarrow=m^*\alpha/2$. Although $\hbar k_\uparrow-\hbar k_\downarrow$ gives a finite contribution to $I_s(t)$ in Eq. (3), for $t<0$ where $\alpha(t)=\alpha$, this contribution is compensated by the contribution $\hbar\alpha n/4$ due to the SOI. Hence, the total spin current $I_s(t)=0$ for $t<0$. However, when the SOI is switched off at $t=0$, $\alpha(t)=0$ and so the spin current is finite, because the average electron momenta retain the same as they were at $t<0$. As time goes on, the electron momenta relax with a relaxation time τ. Therefore, $I_s(t)=-(\hbar\alpha n/4)\exp(-t/\tau)$ for $t>0$.

It is instructive to make a Fourier transform of $I_s(t)$ to obtain a Drude-like expression

$$I_s(\Omega)=\left[\frac{\tau\hbar n}{2m^*(i\Omega\tau-1)}\right]\left[\frac{m^*}{2}i\Omega\alpha(\Omega)\right]. \tag{4}$$

Since the units of our spin current is $\hbar/2$, the above expression is a complete analogy to the electric conductivity. Instead of an electric driving force eE, here we have an

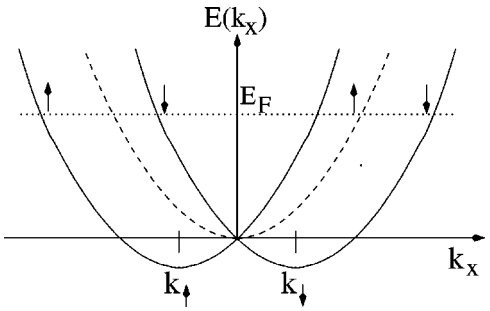

FIG. 1. The dashed curve is the electron energy band without SOI. The SOI splits the energy band into the ↑-spin and the ↓-spin bands, as shown by the solid curves, with corresponding average wave vectors $k_\uparrow$ and $k_\downarrow$.

equivalent driving force $(m^*/2)[d\alpha(t)/dt]$, the Fourier component of which is $(m^*/2)i\Omega\alpha(\Omega)$. Under this driving force we have the classic equation of motion

$$m^*\frac{dv_{\uparrow,\downarrow}}{dt}=\pm\frac{m^*}{2}\frac{d\alpha(t)}{dt}. \tag{5}$$

This force acts in opposite directions on electrons with opposite spin projections. When such a force creates a spin current, it does not induce an electric current.

The above conclusion of spin-current generation can be demonstrated with a rigorous linear response analysis, which will be performed on a 2D electron gas (2DEG). The simple Drude expression (4) will then appear as a general result. Let the 2DEG be in the xy plane with the unit vector $\hat{\nu}$ along the z axis, which is the spin-quantization axis. We will use the equation of motion for the spin-density operator to generalize the 1D expressions (1), (2) for the spin current. For a homogeneous system the spin-current density operators can be expressed in terms of the electron creation operator $c^\dagger_{\vec{k},\gamma}$ and destruction operator $c_{\vec{k},\gamma}$, where γ labels the spin projection onto the z axis. This current is then derived as

$$\mathcal{J}^i_j=J^i_j+J^i_{j,\mathrm{SOI}}, \tag{6}$$

where the superscript $i=x,y,z$ specifies the direction of spin polarization, and the subscript $j=x,y$ refers to the direction of the spin-current flow. The partial current

$$J^i_j=\sum_{\vec{k}}\sum_{\gamma\beta}\frac{\hbar^2k_j}{m^*}c^\dagger_{\vec{k},\gamma}s^i_{\gamma\beta}c_{\vec{k},\beta} \tag{7}$$

is the ordinary kinematic term and

$$J^i_{j,\mathrm{SOI}}=\varepsilon^{ijz}\hbar\alpha n/4 \tag{8}$$

is the contribution of SOI.[7] Here ε^{ijz} denotes the Levy-Civita symbol. The SOI induced current resembles the diamagnetic current of electrons under the action of an external electromagnetic vector potential.

We note that the SOI Hamiltonian can be conveniently written in terms of the kinematic current as

$$H_{\mathrm{SO}}(t)=[m^*\alpha(t)/\hbar](J^x_y-J^y_x). \tag{9}$$

When an ac bias with frequency Ω is applied to the front or the back gate of a 2DEG,[3,4] the Rashba coupling constant contains two terms $\alpha(t)=\alpha_0+\delta\alpha(t)$, where α_0 is constant in time and $\delta\alpha(t)=\delta\alpha e^{i\Omega t}$. We assume that the only effect of the ac bias is to add a time-dependent component to the SOI coupling constant, although in practice it is not simple to avoid the bias effect on the electron density.[4] The SOI Hamiltonian is separated correspondingly into two parts $H_{\mathrm{SO}}(t)=H^0_{\mathrm{SO}}+H'_{\mathrm{SO}}(t)$. The time-independent part H^0_{SO} does not produce a net spin current in the thermodynamically equilibrium state. However, as pointed out in the above analysis on the 1DEG system, the time-dependent $H_{\mathrm{SO}}(t)$ can give rise to a spin current.

We will incorporate H^0_{SO} into our unperturbed Hamiltonian and treat $H'_{\mathrm{SO}}(t)$ within the linear response regime. The so-generated ac spin current $\langle\mathcal{J}^i_j(t)\rangle$ has the form

$$\langle\mathcal{J}^i_j(t)\rangle=\frac{i}{\hbar}\int_{-\infty}^{t}dt'\langle[H'_{\mathrm{SO}}(t'),J^i_j(t)]\rangle+\varepsilon^{ijz}\hbar\,\delta\alpha(t)n/4. \tag{10}$$

In the above equation the first term can be written in the form $\delta\alpha(t)\mathcal{R}^i_j(\Omega)$. For zero temperature and with $\Omega>0$, the response function $\mathcal{R}^i_j(\Omega)$ can be represented as the Fourier transform of the correlator

$$\mathcal{R}^i_j(t)=-i\frac{\hbar^2}{m^*}\sum_{\vec{k}'\alpha'\beta'}k'_j s^i_{\alpha'\beta'}\times\sum_{k\alpha\beta}\vec{h}_{\vec{k}}\cdot\vec{s}_{\alpha\beta}\overline{\langle T\{c^\dagger_{\vec{k}'\alpha'}(t)c_{\vec{k}\beta}\}\rangle\langle T\{c_{\vec{k}'\beta'}(t)c^\dagger_{\vec{k}\alpha}\}\rangle}, \tag{11}$$

where $\vec{h}_{\vec{k}}=\vec{k}\times\hat{\nu}$. In the above equation, the bar over the product of two one-particle Green functions means an ensemble average over impurity positions.

We will use the standard perturbation theory[9] to calculate this ensemble average, which is valid when the elastic scattering time τ due to impurities is sufficiently long such that $E_F\tau\gg\hbar$. We will assume that the electron Fermi energy E_F is much larger than both $\hbar\Omega$ and $\hbar\alpha_0 h_{\vec{k}}$. To the first-order approximation, we neglect the weak localization corrections to the correlator (11), since these corrections simply renormalize the spin-diffusion constant.[8] Consequently, the configuration average of the pair product of Green functions is expressed in the so-called ladder series.[9] We found that since $\vec{h}_{\vec{k}}=-\vec{h}_{-\vec{k}}$ many of such ladder diagrams vanish after angular integration in Eq. (11), similar to suppression of ladders in the electric current driven by the vector potential.[9] At the same time, some of nondiagonal on spin indice diagrams do not turn to 0 after the angular integration. Employing the analysis of similar diagrams done in it can be shown that they cancel each other.[8] Hence, the configuration average in Eq. (11) decouples into a product of average Green functions and Eq. (11) becomes

$$\mathcal{R}^i_j(\Omega) = -i\frac{\hbar^2}{m^*}\sum_{l,n}\varepsilon^{lnz}\sum_{\vec{k}} k_j k_n \times \int \frac{d\omega}{2\pi}\mathrm{Tr}[s^l G(\vec{k},\omega) s^i G(\vec{k},\omega+\Omega)], \quad (12)$$

where $G(\vec{k},\omega)$ is the average Green's function which contains fully the effect of H^0_{SO}. This function is represented by the 2×2 matrix

$$G(\vec{k},\omega) = [\omega - E_{\vec{k}}/\hbar - \alpha_0 \vec{h}_{\vec{k}}\cdot\vec{s} + i\Gamma\,\mathrm{sgn}(\omega)]^{-1}, \quad (13)$$

where $\Gamma = 1/2\tau$, and $E_{\vec{k}}$ is defined with respect to E_F. Substituting Eq. (13) into Eq. (12), and then into Eq. (10), we obtain the spin current

$$\langle \mathcal{J}^i_j(\Omega)\rangle = \varepsilon^{ijz}\frac{\hbar}{4}\delta\alpha n\frac{\Omega}{\Omega + 2i\Gamma}. \quad (14)$$

It is important to point out that the spin density under the gate area is zero. This is the reason why even in a 2DEG the D'yakonov-Perel spin relaxation[10] does not appear in Eq. (14) for the generated spin current, although this spin current is determined by the response function (12) which involves spin degrees of freedom. Hence, in the homogeneous system with zero spin density, only electron momentum relaxation occurs in the process of spin-current generation by a time-dependent gate.

Unlike the spin current (4) in a 1D system, in a 2DEG the current given by Eq. (14) has no specific direction. To clarify the spatial distribution of the spin flux induced by an ac gate, let us take the chiral component $\mathcal{J}_{\mathrm{chir}}(t)$ of the spin current

$$\mathcal{J}_{\mathrm{chir}}(t) = [\langle \mathcal{J}^x_y(t)\rangle - \langle \mathcal{J}^y_x(t)\rangle]/2. \quad (15)$$

It is easily seen that this chiral projection has the same form as the expression (4) for a 1D system, if n represents the electron density of the 2DEG. In Fig. 2 we illustrate the spin-current distribution for a circular gate which is marked as the gray area. The spin polarization at any point under the gate has two components parallel to the 2DEG. For any direction specified by the unit vector $\vec{N}$, the two spin-polarized fluxes with polarization directions parallel and antiparallel to $\vec{N}$ will oscillate out of phase by the amount of π along the direction perpendicular to $\vec{N}$. Such out of phase oscillation is schematically plotted in Fig. 2. The amplitude of the spin density flow in each of the opposite directions, as marked by the dashed-line arrows, is just $\mathcal{J}_{\mathrm{chir}}(t)$. In the 2DEG outside the gate area, the spin current can be supported only by spin diffusion. Therefore the chiral ac spin polarization is accumulated in the vicinity of the circumference of the gate, and from where diffuses away from the gate area. It can also diffuse under the gate. For small gates such back diffusion can diminish the efficiency of the spin generation. On the other hand, for large gates with the size larger than the spin-diffusion length the diffusion counterflow does not reduce much the total spin current.

The so-generated current amplitude can be easily estimated. With $\delta\alpha = 3\times 10^6$ cm/s,[4] for $\Omega = 2\pi\times 10^9$ s^{-1}, $n = 10^{12}$ cm^{-2}, and $\tau = 1$ ps, from (14) we derive $(2e/\hbar)\times\langle \mathcal{J}^i_j(\Omega)\rangle \simeq 10^{-3}$ Amp/cm. This ac spin current can be detected by various methods. For example, if holes can tunnel into the neighborhood of the gate edge, their recombination with spin-polarized electrons will produce the emission of circular-polarized light.[11]

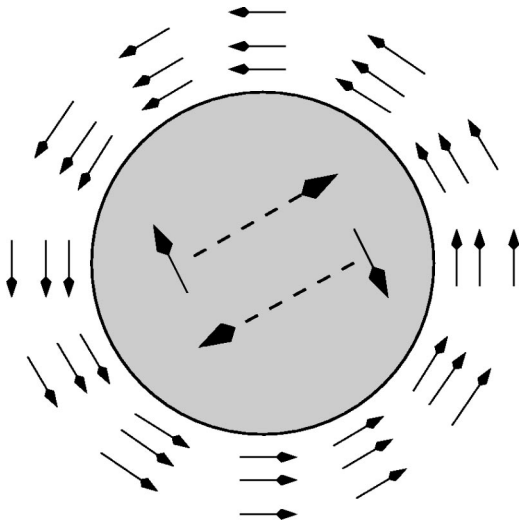

FIG. 2. Distribution of spin currents induced by a time-dependent circular gate which is marked as the gray region. Under the gate, electrons with opposite spins (solid arrows) move in opposite directions indicated by the dashed-line arrows. Arrows outside the gate area show the accumulated spin polarization during a half period of ac gate voltage oscillation.

However, here we will discuss a method of direct electric detection of the dc or the ac spin current. This method is based on a simple fact that the Rashba SOI couples the spin current to the gate voltage. We have shown in our above analysis that due to this coupling, spin current can be induced by a time-dependent gate voltage. In this case the voltage variation plays the role of a source which drives electrons out of thermodynamic equilibrium, and the spin current is the linear response to this perturbation. The reverse process is to create a spin current in a 2DEG by some source, and so inducing a voltage shift in a nearby gate. This is also possible to realize. We thus consider a model where the SOI constant $\alpha(U)$ is a function of the gate voltage $U(t) = U_0 + V(t)$. U_0 is the static equilibrium value in the absence of a spin current, while $V(t)$ is a dynamic variable. The mean value $\langle V\rangle$ of $V(t)$ has to be calculated as a linear response to the perturbation associated with the presence of the spin-polarization flow. The explicit form of this perturbation can be obtained by averaging the Hamiltonian of the system over an electronic state with the given time-dependent spin current.

Let $\langle\cdots\rangle_J$ be such type of average. To the lowest order with respect to SOI, the coupling of the gate voltage to the spin current is thus determined by the average of the Rashba interaction in Eq. (9) with $\alpha = \alpha(U)$. The coupling between the gate voltage $U(t)$ and the spin current $\mathcal{J}^i_j$ is via the kinetic current J^i_j. To derive the coupling Hamiltonian H_{int}, we use Eq. (6) to express J^i_j in terms of $\mathcal{J}^i_j$, and expand

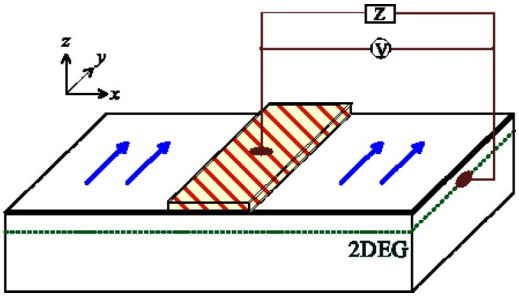

FIG. 3. Schematic illustration of spin current detection. ac spin current flows from the right to the left under the gate with spin polarized as shown by arrows. V denotes the voltmeter and Z is the outer circuit impedance.

$\alpha(U)=\alpha(U_0)+\alpha' V(t)$ for small $V(t)$. The coupling Hamiltonian is then derived from Eq. (9) as

$$H_{\rm int}=\frac{m^*\alpha'}{\hbar}V[\langle \mathcal{J}_y^x\rangle_J-\langle \mathcal{J}_j^y\rangle_J]. \tag{16}$$

The charging of the gate $Q=CV$ is related to the gate capacitance. Hence, Eq. (16) can be expressed in the convenient form $H_{\rm int}=Q\mathcal{E}$, where

$$\mathcal{E}=\frac{m^*\alpha'}{\hbar C}[\langle \mathcal{J}_y^x\rangle_J-\langle \mathcal{J}_j^y\rangle_J] \tag{17}$$

is the effective electromotive force.

To illustrate our proposed method of direct electric detection, let us consider a circuit connected to the gate. The principal scheme of the spin current detection is shown in Fig. 3. In it, an additional back gate can be utilized to tune the electron density (not shown). The circuit is characterized by a frequency-dependent impedance $Z(\Omega)$. The voltage induced on the gate by the electromotive force (17) is then easily obtained as

$$\langle V\rangle=\mathcal{E}\frac{i\Omega CZ(\Omega)}{1+i\Omega CZ(\Omega)}. \tag{18}$$

When the spin-current frequency is in resonance with the circuit eigenmode, the gate voltage becomes very large. In the limit of high impedance (open circuit), $\langle V\rangle=\mathcal{E}$. Using the spin current $(2e/\hbar)\langle \mathcal{J}_j^i(\Omega)\rangle\simeq 10^{-3}$ Amp/cm derived above, and the fact that $\langle \mathcal{J}_j^i\rangle_J=A\langle \mathcal{J}_j^i(\Omega)\rangle$, where A is the area under the gate, let us estimate the electromotive force induced in a probe gate by this spin current generated by a nearby source gate. For the reasonable parameter values $\alpha'=3\times 10^7$ cm/Vs,[4] $m^*=0.03\,m_e$, and $C=\kappa\epsilon_0 A/l$ with $\kappa=10$ and $l=10^{-5}$ cm, from Eqs. (14) and (18) we obtain $\mathcal{E}\simeq 10^{-5}$ V.

The generated ac spin current can be rectified with various methods. For example, one can use a shutter gate which is $\pi/2$ phase shifted with respect to the generation gate. The shutter gate can be placed in the neighborhood of the generation gate or between two such gates. The evaluation of the rectifying efficiency of such a setup requires a thorough analysis of spin relaxation and diffusion processes caused by the spin accumulation during the shutter cycle.

We would like to add one relevant piece of information which we became aware of after we completed this paper. The preprint of Governale *et al.* on the quantum-spin pumping in a 1D wire is also based on the idea of creating spin current via a time-dependent gate.[12] However, our results involving dissipative transport in 2DEG and 1DEG cannot be compared directly to those in Ref. 12.

This work was supported by the National Science Council of Taiwan under Grant Nos. 91-2119-M-007-004 (NCTS), 91-2112-M-009-044 (CSC), the Swedish Royal Academy of Science, and the Russian Academy of Sciences and the RFBR Grant No. 03-02-17452. A.G.M. acknowledges the hospitality of NCTS in Hsinchu where this work was initiated.

[1] S. Datta and B. Das, Appl. Phys. Lett. **56**, 665 (1990).
[2] Yu.A. Bychkov and E.I. Rashba, J. Phys. C **17**, 6039 (1984).
[3] J. Nitta *et al.*, Phys. Rev. Lett. **78**, 1335 (1997); G. Engels *et al.* Phys. Rev. B **55**, R1958 (1997).
[4] D. Grundler, Phys. Rev. Lett. **84**, 6074 (2000).
[5] A.G. Mal'shukov, V. Shlyapin, and K.A. Chao, Phys. Rev. B **66**, 081311(R) (2002); J.C. Egues, G. Burkard, and D. Loss, cond-mat/0209682 (unpublished); M. Governale *et al.*, Phys. Rev. B **65**, 140403(R) (2002).
[6] We ignored the bulk Dresselhaus contribution to SOI, which in narrow gap heterostructures is believed to be negligible in comparison with the Rashba effect. See discussion in Ref. 4.
[7] U. Zulicke and C. Schroll, Phys. Rev. Lett. **88**, 029701 (2002).
[8] A.G. Mal'shukov, K.A. Chao, and M. Willander, Phys. Rev. Lett. **76**, 3794 (1996); Phys. Scr. **T66**, 138 (1996).
[9] B. L. Altshuler and A. G. Aronov, in *Electron-Electron Interactions in Disordered Systems*, edited by A. L. Efros and M. Pollak (North-Holland, Amsterdam, 1985).
[10] M.I. D'yakonov and V.I. Perel, Fiz. Tverd. Tela **13**, 3581 (1971) [Sov. Phys. Solid State **13**, 3023 (1972)]; Zh. Éksp. Teor. Fiz. **60**, 1954 (1971) [Sov. Phys. JETP **33**, 1053 (1971)].
[11] R. Fiederling *et al.*, Nature (London) **402**, 787 (1999); Y. Ohno *et al.*, *ibid.* **402**, 790 (1999).
[12] M. Governale, F. Taddei, and R. Fazio, Phys. Rev. B **68**, 155324 (2003).

Transport spectroscopy in a time-modulated open quantum dot

C. S. Tang,[1] Y. H. Tan,[2] and C. S. Chu[2]
[1]*Physics Division, National Center for Theoretical Sciences, P.O. Box 2-131, Hsinchu 30013, Taiwan, Republic of China*
[2]*Department of Electrophysics, National Chiao-Tung University, Hsinchu 30010, Taiwan, Republic of China*
(Received 2 October 2002; published 30 May 2003)

We have investigated the time-modulated coherent quantum transport phenomenon in a ballistic open quantum dot. Conductance G and the electron dwell time in the dots are calculated by a time-dependent mode-matching method. Under high-frequency modulation, the traversing electrons are found to exhibit three types of resonant scatterings. They are intersideband scatterings into quasibound states in the dots, into true bound states in the dots, and into quasibound states just beneath the subband threshold in the leads. Dip structures or fano structures in G are their signatures. Our results show structures due to $2\hbar\omega$ intersideband processes. At the above scattering resonances, we have estimated, according to our dwell time calculation, the number of round-trip scatterings which the traversing electrons undertake between the two dot openings.

DOI: 10.1103/PhysRevB.67.205324 PACS number(s): 73.23.−b, 72.30.+q , 72.10.−d

I. INTRODUCTION

In the past decade, the quantum transport phenomenon in open quantum dots has received much attention.[1–11] The open quantum dot, consisting of a submicron sized cavity connecting via point contact leads to two end-electrodes, has become an important device for the investigation of phase-coherent processes and their various mechanisms. The size of the dot and the width of the leads can be controlled by split gates. In high electron mobility samples, and at sufficient low temperatures, the phase-coherent length may well exceed the dimension of the device, allowing electrons to remain coherent while traversing the dot.

Meanwhile, there has been growing interest in the high-frequency responses of mesoscopic nanostructures. The time-modulated fields invoked are either high-frequency electromagnetic fields[12–20] or time-modulated potentials.[21–25] A number of theoretical approaches have been developed to explore quantum transport under such time-modulated fields. The WKB approximation was employed in the study of photovoltaic effect[12] and photon-assisted quantum transport.[13] A mode-matching method was developed for δ-profile[21] as well as finite-range-profile time-modulated potentials.[22] Extension of this method to time-dependent field, represented by a vector potential $\vec{A}(t)$, was carried out by either neglecting[15] or including[18] the contribution of the $\vec{A}(t)^2$ term. This mode-matching method was further extended to accommodate spatial inhomogeneity. The time-modulated field is divided into piecewise potentials connected by either transfer matrices[17] or scattering matrices.[23] Recently, this latter approach has been applied to study a mechanism of nonadiabatic quantum pumping.[25] This pumping mechanism is due to resonances resulting from coherent inelastic scattering, which requires simultaneous changes in both the energy and momentum of the traversing electron, by, respectively, $\hbar\Omega$ and $\hbar K$. Here Ω and K characterize, respectively, the temporal and the spatial variation of the modulation field. Encouraged by the success of the time-modulated mode-matching method, we opt to apply the method to the very interesting case of time-modulated quantum dots.

In the absence of a time-modulated field, transmission of electrons through a quantum dot already shows resonance structures. For the case of a weakly coupled dot—a dot in which electrons are separated from the connecting leads by tunneling barriers—the resonance peaks in the transmission are due to the alignment of the incident electron energy with the quasi-bound-state (QBS) levels in the dot.[26–28] Interestingly, QBS's of a similar nature still exist in the case of an open quantum dot—where tunneling barriers between the dot and the lead are absent. These QBS's, again, give rise to resonances in the transmission. However, dip structures, rather than peaks, become the signatures for the resonances.

When acted upon by a time-modulated potential, the transmission of a weakly coupled dot was found to exhibit additional resonance peaks: peaks associated with ac sidebands.[29] This is due to the alignment, albeit shifted by $n\hbar\omega$, of the incident electron energy with the QBS levels in the dot. Other features found in a time-modulated weakly coupled dot are photon-assisted tunneling,[30] electron pumps,[31] and phase breaking.[32]

Recently, an open quantum dot, acted upon by a transversely polarized electromagnetic field, and connected adiabatically to the connecting leads, has been considered.[33,34] The adiabatic dot-lead connections allow an electron mode in the lead to evolve into an electron mode in the dot. Thus, situations occur when an electron in the lower mode in the dot can exit the dot without reflection, while an electron at the same energy, but in a higher mode in the dot, is trapped inside it. As such, intermode transitions between the above two modes in the dot, as induced by the transversely polarized electromagnetic field, were found to lead to giant mesoscopic conductance fluctuations[33] and microwave-induced resonant blocking in a mesoscopic channel.[34]

The adiabaticity of the dot-lead connection holds for large quantum dots. But, as the sizes of the open quantum dot shrink and approach the realm of the Fermi wavelength, the dot-lead connections can no longer remain adiabatic. More recent experimental findings in dc transport in open quantum dots—that transport occurs through individual eigenstates of the corresponding closed dot;[35] and that the conductance oscillations correlate to the recurrence of specific groups of

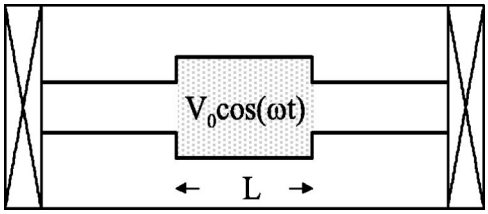

FIG. 1. Schematic illustration of an open quantum dot that is acted upon by a gate-induced time modulation with two leads connecting adiabatically to two end electrodes.

wave function scars in the dot[10]—indicate unequivocally that intermode scattering and backscattering are present, respectively, at the dot-lead connections. The effect of impurity should play no role here because of the high mobility of the sample used in these experiments.

Therefore, in this work, we consider a time-modulated open quantum dot with nonadiabatic dot-lead connections. We calculate the dc conductance G of a time-modulated open quantum dot and the dwell time $\tau_{\rm d}$ of the traversing electron in the dot. We have analyzed the resonance structures in G associated with the time modulation and are able to categorize them according to their respective dynamical processes involved. Of these three resonance types, one is analogous to that found in time-modulated weakly coupled dots. It is associated with the alignment of the incident electron energy with that of the ac sidebands of the QBS's inside the open dot. The second type is associated with the coherent inelastic scattering of the traversing electron into the true bound state in the open dot—bound state whose energy is lower than the threshold energy of the leads. The third type of resonance structures is most unexpected. It is associated with the coherent inelastic scattering of the traversing electron into the QBS in the lead—with energy just beneath the threshold energy of the lead. Also, from the dwell time $\tau_{\rm d}$, we estimate the number of scatterings that occur in the dot as the resonance structures establish themselves. In all, our results demonstrate the potential of establishing quantum transport as a spectroscopic probe for the QBSs and true bound states in the open dot—and possibly in other mesoscopic structures—through the coupling of a time-modulated field to the system.

In Sec. II, we present our theoretical method for the calculation of G and $\tau_{\rm d}$. The numerical results are presented and discussed in Sec. III. Finally, in Sec. IV, we present our conclusions.

II. MODEL AND METHOD

The system under investigation is sketched (top view) in Fig. 1, where the shaded area denotes the region acted upon by a time-modulated potential. The dot we consider has physical parameters typical to that in high mobility two-dimensional electron gas, formed in an AlGaAs-GaAs heterostructure. As such, mobility $\mu_e \sim 10^6$ cm^2/V s, mean free path $l \sim 1$ μm at sufficient low temperatures, and dots with submicron dot sizes would be in the ballistic regime. The Hamiltonian is given by

$$H = -\frac{\hbar^2}{2m}\left[\frac{\partial^2}{\partial x^2}+\frac{\partial^2}{\partial y^2}\right] + V_c(x,y) + V(x,t), \qquad (1)$$

where $V_c(x,y)$ is the confinement potential, chosen to be of hard-wall type, that defines the dot and the leads. It is given by $V_c=0$ if $|y|<W_1/2$ and $|x|>L/2$; $V_c=0$ if $|y|<W_2/2$ and $|x|<L/2$; and $V_c=\infty$ if otherwise. Here W_1, W_2 are, respectively, widths of the lead and the dot. The time-modulated potential

$$V(x,t) = V_0\cos(\omega t)\Theta(L/2-|x|)$$

acts only upon the dot.

For the sake of convenience, the physical quantities that appear in the following equations are dimensionless: with energy unit $E^*=E_F=\hbar^2k_F^2/2m$, wave vector unit $k^*=k_F$, length unit $a^*=1/k_F$, time unit $t^*=\hbar/E_F$, and frequency unit $\omega^*=1/t^*$. The scattering wave function for an electron incident upon the dot from the lth channel in the left lead is of the form

$$\psi_l(x,y,t) = \chi_l(y)e^{ik_l(0)x}e^{-i\mu t} + \sum_{n'}\sum_{m'}\chi_{n'}(y)r_{n'l}(m') \times \exp[-ik_{n'}(m')x - i(\mu+m'\omega)t] \quad \text{if } x<-L/2,$$

$$\psi_l(x,y,t) = \sum_{k'}\phi_{k'}(y)\int d\epsilon[\tilde{A}_{k'l}(\epsilon)e^{i\beta_{k'}(\epsilon)x} + \tilde{B}_{k'l}(\epsilon)e^{-i\beta_{k'}(\epsilon)x}] \times \exp\left[-i\epsilon t - i\frac{V_0}{\omega}\sin\omega t\right] \quad \text{if } |x|<L/2, \qquad (2)$$

$$\psi_l(x,y,t) = \sum_{n'}\sum_{m'}\chi_{n'}(y)t_{n'l}(m')\exp[ik_{n'}(m')x - i(\mu+m'\omega)t] \quad \text{if } x>L/2,$$

where the subscripts n' and k' are the subband indices in, respectively, the leads and the dot, and m' is the sideband index. In addition, $k_l(m')=[\mu+m'\omega-(l\pi/W_1)^2]^{1/2}$ and $\beta_{k'}(m')=[\mu+m'\omega-(k'\pi/W_2)^2]^{1/2}$ denote, respectively, the wave vectors in the lead and the dot. The normalized transverse subband states are $\chi_l(y)=(2/W_1)^{1/2}\sin[l\pi(y/W_1+1/2)]$ and $\phi_{k'}(y)=(2/W_2)^{1/2}\sin[k'\pi(y/W_2+1/2)]$.

The matching of the wave functions at the openings of the dot, and at all times, requires the coefficients in the dot to have the form

$$\tilde{\mathcal{F}}_{k'l}(\epsilon) = \sum_{m'}\mathcal{F}_{k'l}(m')\,\delta(\epsilon-\mu-m'\omega),$$

where $\tilde{\mathcal{F}}_{k'l}(\epsilon)$ refers to either $\tilde{A}_{k'l}(\epsilon)$ or $\tilde{B}_{k'l}(\epsilon)$. Performing the matching, and after some algebra, we obtain

$$\left[A_{kl}(m)\exp\left(-i\beta_k(m)\frac{L}{2}\right)+B_{kl}(m)\exp\left(i\beta_k(m)\frac{L}{2}\right)\right]$$
$$=\sum_{n'}\sum_{m'}J_{m'-m}\left(\frac{V_0}{\omega}\right)\left[a_{lk}\exp\left(-ik_l(m')\frac{L}{2}\right)\delta_{n'l}\delta_{m'0}+a_{n'k}r_{n'l}(m')\exp\left(ik_{n'}(m')\frac{L}{2}\right)\right], \quad (3)$$

$$\left[A_{kl}(m)\exp\left(i\beta_k(m)\frac{L}{2}\right)+B_{kl}(m)\exp\left(-i\beta_k(m)\frac{L}{2}\right)\right]$$
$$=\sum_{n'}\sum_{m'}J_{m'-m}\left(\frac{V_0}{\omega}\right)\left[a_{n'k}t_{n'l}(m')\exp\left(ik_{n'}(m')\frac{L}{2}\right)\right], \quad (4)$$

$$\sum_{k'}a_{nk'}\beta_{k'}(m)\left[A_{k'l}(m)\exp\left(-i\beta_{k'}(m)\frac{L}{2}\right)-B_{k'l}(m)\exp\left(i\beta_{k'}(m)\frac{L}{2}\right)\right]$$
$$=\sum_{m'}J_{m'-m}\left(\frac{V_0}{\omega}\right)k_n(m')\left[\delta_{nl}\delta_{m'0}\exp\left(-ik_l(m')\frac{L}{2}\right)-r_{nl}(m')\exp\left(ik_{n'}(m')\frac{L}{2}\right)\right], \quad (5)$$

and

$$\sum_{k'}a_{nk'}\beta_{k'}(m)\left[A_{k'l}(m)\exp\left(i\beta_{k'}(m)\frac{L}{2}\right)-B_{k'l}(m)\exp\left(-i\beta_{k'}(m)\frac{L}{2}\right)\right]$$
$$=\sum_{m'}J_{m'-m}\left(\frac{V_0}{\omega}\right)k_n(m')t_{nl}(m')\exp\left(ik_n(m')\frac{L}{2}\right), \quad (6)$$

where Eqs. (5) and (6) are obtained from matching the derivatives of the wave functions. The overlapping integral a_{lk} of the transverse subband states is given by

$$a_{lk}=\int_{-W_1/2}^{W_1/2}\chi_l(y)\phi_k(y)dy \quad (7)$$

and the identity $\exp(iz\sin\omega t)=\Sigma_p J_p(z)\exp(ip\omega t)$ has been invoked. We have solved Eqs. (3)–(6) for the coefficients $A_{kl}(m)$, $B_{kl}(m)$, $r_{n'l}(m')$ and $t_{n'l}(m')$. Furthermore, we note that the sole appearance of V_0 in Eqs. (3)–(6) is in the form V_0/ω and as an argument of the Bessel functions J_m. This shows a general trend that the effect of the time-modulated potential decreases with the raising of the frequency ω.

In the low drain-source bias regime, the dc conductance is given by

$$G=\frac{2e^2}{h}\sum_{l=1}^{N}T_l, \quad (8)$$

where N denotes the number of propagating channels in the leads. The current transmission coefficient T_l for an electron incident from the lth channel in the lead is

$$T_l=\sum_{n'}\sum_{m'}\frac{k_{n'}(m')}{k_l(0)}|t_{n'l}(m')|^2. \quad (9)$$

The current reflection coefficient R_l has a similar form and the current conservation condition $T_l+R_l=1$ is used to check on our numerical accuracy.

The stationary dwell time within one-dimensional system was well defined.[36] However, in a multichannel system, such as open quantum dots, we should consider not only the probability of finding the particle in the dot, but also that due to evanescent states in the vicinity of the dot. Hence, we define the dwell time as

$$\tau_d=\frac{\int\int_{\mathcal{A}'}\langle|\psi(x,y,t)|^2\rangle_{\text{t.a.}}dxdy}{\int dyj_{\text{inc}}}, \quad (10)$$

where j_{inc} denotes the incident electron flux. The subscript t.a. denotes time average. Here we note that the integral in the numerator and its region of interest $\mathcal{A}'$ include not only the region inside the quantum dot (region II), but also the evanescent modes on both the left-hand side (region I) and the right-hand side (region III) of the dot. Hence, the time-averaged probability density in the numerator of Eq. (10) can be separated into three integrals, expressed explicitly as

$$\int\int_{\text{I}}dxdy\langle|\psi(x,y,t)|^2\rangle_{\text{t.a.}}=\int_{-\infty}^{-L/2}dx\sum_{n'}\sum_{m'}|r_{n'l}(m')|^2e^{2\kappa_{n'}(m')x}, \quad (11)$$

$$\int\int_{\text{II}}dxdy\langle|\psi(x,y,t)|^2\rangle_{\text{t.a.}}=\int_{-L/2}^{L/2}dx\sum_{k'}\sum_{m'}\{A_{k'l}(m')A^*_{k'l}(m')\exp[i(\beta_{k'}(m')-\beta^*_{k'}(m'))x]+B_{k'l}(m')B^*_{k'l}(m')e^{-i(\beta_{k'}(m')-\beta^*_{k'}(m'))x}+2\text{Re}[A_{k'l}(m')B^*_{k'l}(m')e^{i(\beta_{k'}(m')+\beta^*_{k'}(m'))x}]\}, \quad (12)$$

and

$$\int \int_{\mathrm{III}} dxdy\langle|\psi(x,y,t)|^2\rangle_{\mathrm{t.a.}} = \int_{L/2}^{\infty} dx \sum_{n'} \sum_{m'} |t_{n'l}(m')|^2 \exp[-2\kappa_{n'}(m')x], \tag{13}$$

where the indices n' and m' in the summation for regions I and III include only the evanescent waves, and $\kappa_{n'}(m) = -ik_{n'}(m)$. Substituting Eqs. (11)–(13) into Eq. (10), we obtain the average dwell time of electrons in the open quantum dot system.

III. RESULTS AND DISCUSSION

In this section, we present our numerical examples for exploring the time-modulated effects on the quantum transport in open quantum dots—the conductance and the dwell time versus the incident electron energy μ. In the following, we choose energy unit $E^*=9$ meV, length unit $a^*=8$ nm, unit of angular frequency $\omega^*=13.6$ T rad/s, and the effective mass $m^*=0.067m_e$, where m_e is the free electron mass of an electron. The geometric parameters are chosen such that the width $W_1=10(\cong 80$ nm) for the leads, and the width $W_2=20(\cong 160$ nm) and the length $L=30(\cong 240$ nm) for the open quantum dot, which is typical for current experimental fabrication. It is convenient to define $X^2\equiv\mu/\varepsilon_1$ where $\varepsilon_1=(\pi/W_1)^2$ is the first transverse subband level in the leads. Then the integral values of X stand for the number of occupied subbands in the leads.

In the absence of time modulation, the quantum states of the open quantum dot associate closely with the bound states of the corresponding closed dot with the same geometry. For a closed dot with length L and width W_2, the bound-state energy $E_{\mathrm{b.s.}}=(n_x\pi/L)^2+(n_y\pi/W_2)^2$ is labeled by a pair of quantum number (n_x,n_y). Then we may obtain the rescaled bound-state levels $\underline{E}(n_x,n_y)\equiv E_{\mathrm{b.s.}}/\varepsilon_1=n_x^2/9+n_y^2/4$ inside the closed dot. For an open dot, the energy spectrum consists of both true bound states and QBS's corresponding either to electrons with energy μ less than or higher than the threshold energy ε_1 in the lead. As such, there are only two possible true bound states in the open dot: $E_{B1}\simeq\underline{E}(1,1)=0.361$ and $E_{B2}\simeq\underline{E}(2,1)=0.694$.

In Fig. 2, the conductance characteristic is studied as a function of incident electron energy: (a) in the absence of time modulation, as a comparative reference and (b)–(d) in the presence of time modulation with angular frequencies $\omega/\varepsilon_1=0.1$, 0.3, and 0.5, respectively, which also correspond to frequencies $f=\omega/2\pi\simeq 21.4$, 64.2, and 107 GHz. This frequency range is typical for current experiments.[37] In addition, the modulation amplitude is chosen to be $V_0=0.1\varepsilon_1$ ($\simeq 0.09$ meV). There are three dip structures common to all four plots. These dip structures occur at energies $\mu/\varepsilon_1=2.364(E_{Q1})$, $2.672(E_{Q2})$, and $3.208(E_{Q3})$. These are associated with the alignment of the incident electron energy with that of the QBS levels inside the open dot, as is indicated by the open triangle symbols locating the closed dot $\underline{E}(1,3)=2.361$, $\underline{E}(2,3)=2.694$, and $\underline{E}(3,3)=3.250$. The corresponding dwell time of these QBSs are, respectively, $\tau_d\simeq 73.5$, 26.7, and 69.0 ps, as shown in Fig. 3(a). These dwell time peak structures confirm the resonant nature of the states inside the dot.

Another interesting feature in Fig. 2(b) are the side-dip structures around the QBS's E_{Qi}, which are associated with electrons at incident energy μ that are able to make m-photon intersideband transitions into the ith QBS level. The condition is

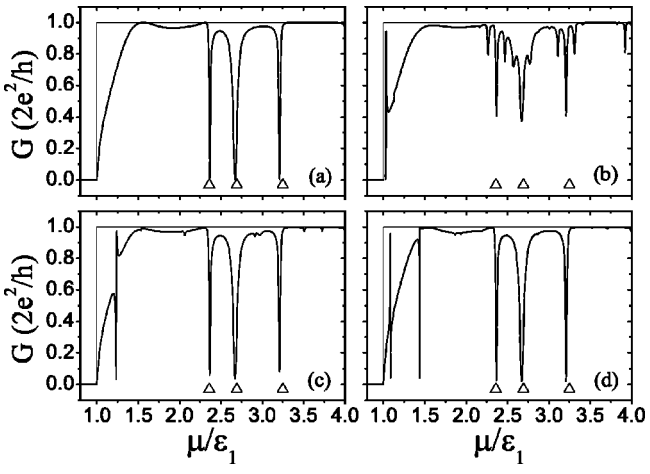

FIG. 2. Energy dependence of the quantum dot conductance G in the lowest subband as a function of incident electron energy μ, in units of ε_1, for cases of (a) no external modulation, (b)–(d) modulation amplitude $V_0=0.1\varepsilon_1$, with angular frequencies (b) $\omega=0.1\varepsilon_1$, (c) $0.3\varepsilon_1$, and (d) $0.5\varepsilon_1$.

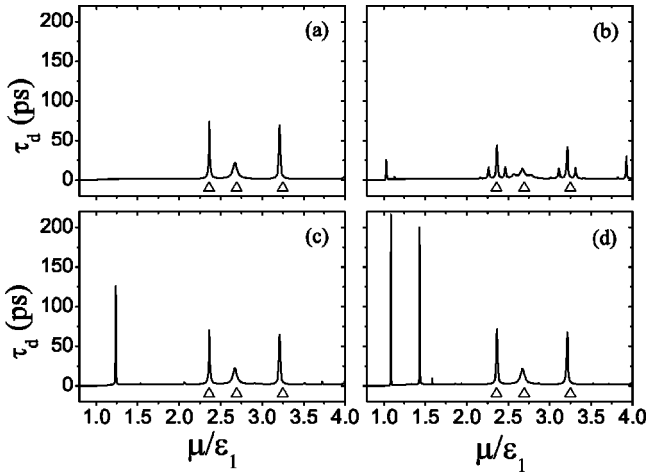

FIG. 3. The dwell time τ_d of the traversing electron is plotted as a function of the incident electron energy μ in units of ε_1. The parameters are the same as in Figs. 2(a)–2(d).

$$\mu + m\hbar\omega = E_{Qi}, \tag{14}$$

where the positive m and negative m indicate, respectively, the absorption and emission of m photons. Hence $m=-1$ side dips are at $\mu/\varepsilon_1=2.465$, 2.770, 3.309; $m=+1$ side dips are at $\mu/\varepsilon_1=2.165$, 2.574, 3.110; and $m=+2$ side dips are at $\mu/\varepsilon_1=2.266$, 3.008. The $m=-2$ process in the vicinity of the E_{Q3} state is barely identified and is at $\mu/\varepsilon_1=3.411$.

Two additional types of intersideband transition mechanisms are found in the low-energy regime in Fig. 2. As is shown in Fig. 2(d), where the frequency $\omega=0.5\varepsilon_1$ is high enough, the electrons with $\mu/\varepsilon_1=1.087$ may emit $\hbar\omega$ and make transitions into E_{B2}—the true bound state in the dot. The electron dwell time of this structure is $\tau_d\cong 216.6$ ps, see Fig. 3(d). In addition, electrons may also emit photons to make transitions into a QBS formed at energy just beneath a subband threshold in the lead. This mechanism is identified to be the fano structures at $\mu/\varepsilon_1=1.028$, 1.233, and 1.435, as shown in Figs. 2(b)–2(d), respectively, where $(\mu-\omega)/\varepsilon_1$ is close to 1 from below. Correspondingly, the dwell times of these structures are $\tau_d\simeq 23.0$, 125.5, and 200.2 ps, see Figs. 3(b)–3(d). More precisely, these structures correspond to electrons that emit $\hbar\omega$ to $\mu/\varepsilon_1=0.93$ and are trapped temporarily to form QBS's in the lead.

To provide further evidence for the above two transition mechanisms, we plot, in Fig. 4, the spatial dependence of the time-averaged probability density. The parameters are chosen to be the same as in Fig. 2(d). When the electron incident at energy $\mu=1.0854\varepsilon_1$, as shown in Fig. 4(a), we see that the time-averaged electron probability concentrates entirely within the dot and is like a (2,1) state. This supports the fact that the electron is trapped in a true bound state in the dot. Second, when the electron incident at energy $\mu=1.4353\varepsilon_1$, the electron probability has long exponential tails extending into the leads. The edges of the dot are at $x=\pm 15$. This demonstrates that the electron has made an intersideband transition, by emitting one photon, into a QBS in the lead whose energy is just below the threshold energy. We have also checked that a similar process can be found even in a time-modulated one-dimensional quantum well connecting to leads. A traversing electron can make intersideband transitions to QBS's in the leads or to true bound states in the well.[38]

To better appreciate the meaning of the dwell time, we define the number of round-trip scatterings, $N_{\rm sc}$, undertaken by the traversing electron. It is the ratio of the dwell time τ_d to the ballistic time τ_b the electron takes to go between the two dot-openings. The ballistic time for electrons traversing through the quantum dot is simply $\tau_b\sim L/v_e$, where v_e denotes the electron velocity and is given by $v_e=\hbar k_x/m$. We consider the electron incident in the lowest subband and then the electron ballistic time is given by $\tau_b=L/(\mu-\varepsilon_1)^{1/2}$ in units of t^*. Hence, in Fig. 3(d), the main peaks at $\mu/\varepsilon_1=1.085$, 1.435, 2.365, 2.673, and 3.210 correspond to the ballistic times $\tau_b\simeq 24.0$, 16.1, 6.01, 5.43, and 4.72 ps, respectively. The corresponding τ_d's are, respectively, 216.6, 200.2, 71.8, 21.8, and 67.9. Therefore, we obtain the number of round-trip scatterings, $N_{\rm sc}\equiv\tau_d/2\tau_b\sim 4.5$, 6.2, 6.0, 2.0, and 7.2, respectively. In light of the above analysis, we can see that two round-trip times are already sufficient to form a significant QBS level inside the open dot. The estimation for τ_b could be improved by considering the effective electron velocity in the dot, rather than in the lead. But we expect $N_{\rm sc}$ to remain of the same order of magnitude as shown here. Moreover, the $N_{\rm sc}$ obtained here is the lower bound to any such improved estimation.

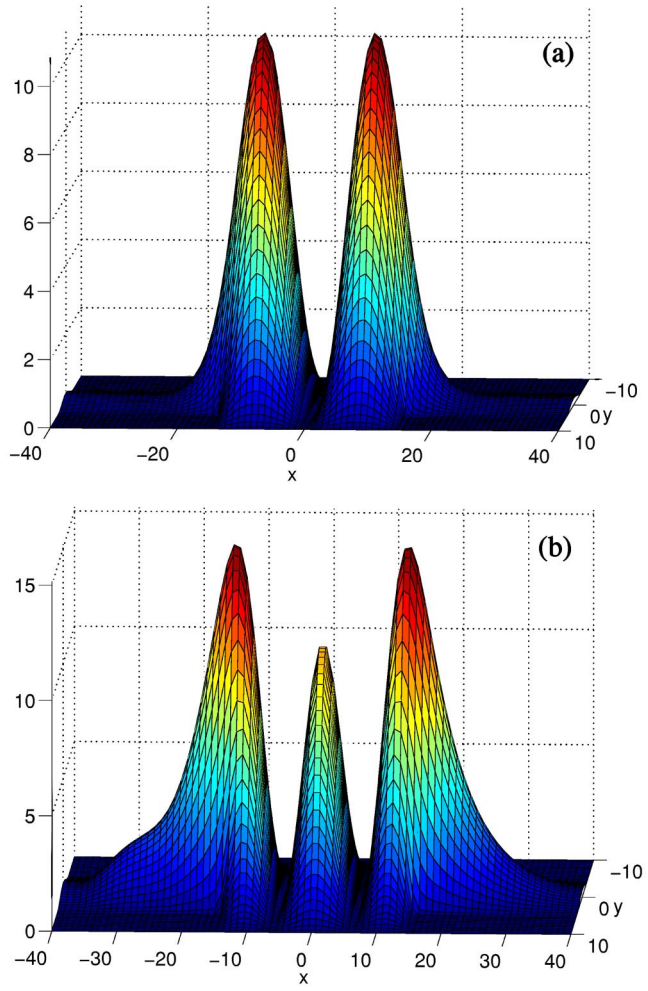

FIG. 4. (color online). The spatial dependence of the time-averaged electron probability density: (a) $\mu=1.0854\varepsilon_1$ and (b) $\mu=1.4353\varepsilon_1$. Other parameters are the same as in Fig. 2(d). The edges of the dot are at $L=\pm 15$.

It is known[22] that the strength of the time-modulated potential depends on the ratio of V_0 to ω. As a result, for a given amplitude V_0, the sideband dip features are suppressed with increase in the modulation frequency ω. This is illustrated in Figs. 2(c) and 2(d). On the other hand, if we fix $V_0/\omega=1$ in Fig. 5, and choose the modulation amplitude to be $V_0/\varepsilon_1=0.05$, 0.1, and 0.2 for Figs. 5(a)–5(c), respectively, we can see the side dips due to $2\hbar\omega$ intersideband processes in all the figures. This assures us that V_0/ω is an important index for photon absorption and emission processes. Furthermore, the QBS levels that associate with a fewer number of round-trip scatterings may be merged with its nearby sidebands, forming a broadened dip structure: such as the wide-dip structure at $\mu/\varepsilon_1=2.672$ in Fig. 5(a). In the

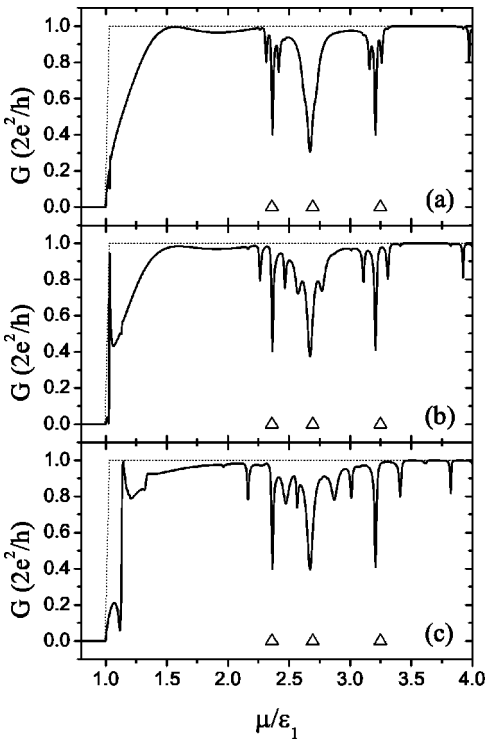

FIG. 5. Conductance is plotted as a function of electron energy μ for a fixed $V_0/\omega=1.0$. The values of V_0 (or ω) are (a) $0.05\varepsilon_1$, (b) $0.1\varepsilon_1$, and (c) $0.2\varepsilon_1$, respectively.

low-energy regime, again, electrons are able to undertake one-photon (or two-photon) emission processes into a subband threshold in the lead. This one-(or two-)photon mechanism is demonstrated by small dip structures in G at $\mu/\varepsilon_1=1.024$ (or 1.129) in Fig. 5(b) and $\mu/\varepsilon_1=1.118$ (or 1.317) in Fig. 5(c).

To conclude this section, we note in passing that despite of wide dot openings, electrons traversing through the dot are still effectively mediated by just a few bound states of the corresponding closed dot structure. Our results show that the conductance spectra for a time-modulated open dot show more intersideband structures than those associated with the bound states of the corresponding close dot. We believe that these mechanisms should find their way of manifestation in the time-modulated phenomena of other nanostructures.

IV. CONCLUSIONS

In this work we have extended the time-dependent mode matching approach to the study of quantum transport in open quantum dot systems. We have calculated the conductance, the dwell time, and the spatial distribution of the electron probability and their dependence on the modulation amplitudes and frequencies.

In conclusion, we have shown three types of coherent inelastic scatterings in a time-modulated open quantum dot. We have demonstrated the potential of establishing quantum transport as a spectroscopic probe for the QBS's and true bound states in an open dot through the coupling of a time-modulated field to the system.

ACKNOWLEDGMENTS

The authors wish to acknowledge the National Science Council of the Republic of China for financially supporting this research under Grants Nos. NSC90(91)-2119-M-007-004 (NCTS), NSC90-2112-M-262-001 (CST), and NSC90-2112-M-009-044 (CSC). Computational facilities supported by the National Center for High-Performance Computing are gratefully acknowledged.

[1] C.M. Marcus, A.J. Rimberg, R.M. Wetervelt, P.F. Hopkins, and A.C. Gossard, Phys. Rev. Lett. **69**, 506 (1992).
[2] A.M. Chang, H.U. Baranger, L.N. Pfeiffer, and K.W. West, Phys. Rev. Lett. **73**, 2111 (1994).
[3] H.I. Chan, R.M. Clarke, C.M. Marcus, K. Campman, and A.C. Gossard, Phys. Rev. Lett. **74**, 3876 (1995).
[4] M. Persson, J. Pettersson, B. von Sydow, P.E. Lindelof, A. Kristensen, and K.-F. Berggren, Phys. Rev. B **52**, 8921 (1995).
[5] M.W. Keller, A. Mittal, J.W. Sleight, R.G. Wheeler, D.E. Prober, R.N. Sacks, and H. Shrtikmann, Phys. Rev. B **53**, R1693 (1996).
[6] Y. Wang, N. Zhu, and J. Wang, Phys. Rev. B **53**, 16 408 (1996).
[7] R. Akis, D.K. Ferry, and J.P. Bird, Phys. Rev. Lett. **79**, 123 (1997).
[8] I.V. Zozoulenko and T. Lundberg, Phys. Rev. Lett. **81**, 1744 (1998).
[9] R. Akis, D.K. Ferry, and J.P. Bird, Phys. Rev. Lett. **81**, 1745 (1998).
[10] J.P. Bird, R. Akis, D.K. Ferry, D. Vasileska, J. Cooper, Y. Aoyagi, and T. Sugano, Phys. Rev. Lett. **82**, 4691 (1999).
[11] A.P.S. de Moura, Y.-C. Lai, R. Akis, J.P. Bird, and D.K. Ferry, Phys. Rev. Lett. **88**, 236804 (2002).
[12] F. Hekking and Y.V. Nazarov, Phys. Rev. B **44**, 11 506 (1991).
[13] S. Feng and Q. Hu, Phys. Rev. B **48**, 5354 (1993).
[14] L.Y. Gorelik, A. Grincwajg, V.Z. Kleiner, R.I. Shekhter, and M. Jonson, Phys. Rev. Lett. **73**, 2260 (1994).
[15] F.A. Maaø and L.Y. Gorelik, Phys. Rev. B **53**, 15 885 (1996).
[16] C.S. Chu and C.S. Tang, Solid State Commun. **97**, 119 (1996).
[17] M. Wagner and W. Zwerger, Phys. Rev. B **55**, R10 217 (1997).
[18] C.S. Tang and C.S. Chu, Phys. Rev. B **60**, 1830 (1999).
[19] Wenjun Li and L.E. Reichl, Phys. Rev. B **62**, 8269 (2000).
[20] C.S. Tang and C.S. Chu, Physica B **292**, 127 (2000).
[21] P.F. Bagwell and R.K. Lake, Phys. Rev. B **46**, 15 329 (1992).
[22] C.S. Tang and C.S. Chu, Phys. Rev. B **53**, 4838 (1996).
[23] C.S. Tang and C.S. Chu, Physica B **254**, 178 (1998).
[24] Wenjun Li and L.E. Reichl, Phys. Rev. B **60**, 15 732 (1999).
[25] C.S. Tang and C.S. Chu, Solid State Commun. **120**, 353 (2001).
[26] J. Wang and H. Guo, Appl. Phys. Lett. **60**, 654 (1992).
[27] S. Tarucha, D.G. Austing, T. Honda, R.J. van der Hage, and L.P. Kouwenhoven, Phys. Rev. Lett. **77**, 3613 (1996).

[28] L.P. Kouwenhoven *et al.*, in *Mesoscopic Electron Transport, Vol. 345 of Proceeding of a NATO Advanced Studies Institute, Series E: Applied Sciences*, edited by L.L. Sohn, L.P. Kouwenhoven, and G. Schön (Kluwer, Dordrecht, 1997).
[29] T.H. Oosterkamp, L.P. Kouwenhoven, A.E.A. Kooten, N.C. van der Vaart, and C.J.P.M. Harmans, Phys. Rev. Lett. **78**, 1536 (1997).
[30] T. Christen and M. Büttiker, Phys. Rev. B **53**, 2064 (1996).
[31] L.J. Geerlings, V.F. Anderegg, P.A.M. Holweg, J.E. Mooij, H. Pothier, D. Esteve, C. Urbina, and M.H. Devoret, Phys. Rev. Lett. **64**, 2691 (1990).
[32] M.P. Amatram and S. Datta, Phys. Rev. B **51**, 7632 (1995).
[33] L.Y. Gorelik, F.A. Maaø, R.I. Shekhter, and M. Jonson, Phys. Rev. Lett. **78**, 3169 (1997).
[34] S. Blom and L.Y. Gorelik, Phys. Rev. B **64**, 045320 (2001).
[35] I.V. Zozoulenko, A.S. Sachrajda, C. Gould, K.-F. Berggrem, P. Zawadzki, Y. Feng, and Z. Wasilewski, Phys. Rev. Lett. **83**, 1838 (1999).
[36] F.T. Smith, Phys. Rev. **118**, 349 (1960).
[37] H. Qin, F. Simmel, R.H. Blick, J.P. Kotthaus, W. Wegscheider, and M. Bichler, Phys. Rev. B **63**, 035320 (2001).
[38] C.S. Tang and C.S. Chu (unpublished).

計畫成果自評

本計畫已於 2005 年 12 月 31 日結束，在三年的計畫中共發表五＋多篇之論文，其中有三篇為 PRL 文章 (其中一篇被 PRL 列為 Focus of the Journal，另兩篇正審查中)，十六篇發表於 PRB，另有多篇發表在國外此領域知名期刊。由於本計畫實際參與人數不多(原來計畫有 3 個子題，但最後評審建議暫不執行第 3 主題-超導體—半導體奈米結構界面的量子效應，因此最後其實只有兩個研究群(褚德三及朱仲夏(許世英)研究群在執行兩個子題)實際參與，又因從事此領域研究的博士後人員甚少，因此三年中只有兩位博士後長期參與研究工作，在人員不足下，又由於儀器採購時，正值歐元大升值，導致第一、二年之設備經費不足，無法付足款額而導致延誤實驗儀器的進口，並因而嚴重延誤了建立完成實驗儀器之時間，目前實驗儀器大致已建立完成，預計完成之實驗測量正陸陸續續完成，成果亦已發表於國、內外舉辦之國際會議中，且獲得去年在中原舉辦之奈米國際會議的優良論文獎。正式論文目前正投稿中。因此考究此三年之研究內容，與原計畫所建議執行之項目均屬相符程度甚高，且研究成果亦已達成預期目標，研究成果又均發表於物理領域評價極高之期科中，尤其有關第一子題目前所得之研究成果已在量子資訊理論上佔有席之地，第 2 主題更發表了一篇被 PRL 當成當期焦點文章的論文，因此，在學術上的價值相當高，但因本計劃從事的研究問題是基本物理問題，目前之應用價值容或來能顯著，但如第一子題所發表之 PRL 文章，已提出一個能達遠距糾纏的機制，國內若能有元件及材料製作人員參與合作，以作成元件，則可造成單電子偵測器或單光子發射器來申請專利，未來將很有實際應用之價值。

附件二

可供推廣之研發成果資料表

□ 可申請專利　□ 可技術移轉　　日期：__年__月__日

國科會補助計畫	計畫名稱： 計畫主持人： 計畫編號：　　學門領域：
技術/創作名稱	
發明人/創作人	
技術說明	中文： （100~500 字）
	英文：
可利用之產業及可開發之產品	
技術特點	
推廣及運用的價值	

※　1.每項研發成果請填寫一式二份，一份隨成果報告送繳本會，一份送　貴單位

研發成果推廣單位（如技術移轉中心）。

※ **2.本項研發成果若尚未申請專利，請勿揭露可申請專利之主要內容。**

※ 3.本表若不敷使用，請自行影印使用。